UAB

Universitat Autònoma de Barcelona

Photoresponsive polar LuMnO$_3$ and nonpolar LaFeO$_3$ oxides in non-centrosymmetric structures

Yunwei Sheng

Doctoral Thesis

SUPERVISORS:

Prof. Josep Fontcuberta Griñó

Dr. Ignasi Fina Martínez

Laboratory of Multifunctional Oxides and Complex Structures

Institut de Ciència de Materials de Barcelona (ICMAB-CSIC)

Doctoral Program in Materials Science

Department of Physics, Faculty of Science

Universitat Autònoma de Barcelona

September 2022

Yunwei Sheng

ICMAB-CSIC

Campus de la UAB, Bell aterra, Barcelona, Spain

ysheng711@gmail.com

September 2022

Prof. Josep Fontcuberta Griñó, research professor, **and Dr. Ignasi Fina Martínez**, tenured scientist, at the Institut de Ciència de Materials de Barcelona - Consejo Superior de Investigaciones Científicas

CERTIFY

That **Yunwei Sheng** carried out under their direction the research work entitled "Photoresponsive polar $LuMnO_3$ and nonpolar $LaFeO_3$ oxides in non-centrosymmetric structures". This work has been developed within a PhD program in Materials Science at the department of physics of Universitat Autònoma de Barcelona.

For that record they sign the certificate.

Bellaterra, September 2022

Prof. Josep Fontcuberta i Griñó   Dr. Ignasi Fina Martínez

Acknowledgments

Four years in one moment. When looking back, I see enriching experience and precious memories that has only been possible accompanied by the help and support of all my colleagues, friends, and family. I would like to dedicate my sincere thanks to all of you, the people who has participated in this special journey of mine.

First, I would like to express my deepest gratitude to my supervisors, Prof. Josep Fontcuberta Griñó and Dr. Ignasi Fina Martínez, for always being there supportive. Pep has supported me throughout the whole PhD, leading, inspiring and helping me with his profound knowledge, innovative ideas, and boundless enthusiasm for science. Ignasi has been standing by all the time for discussions and any needs, guiding and helping me in the research lines and experimental details with his all-round skills and creative thoughts. I heartfeltly acknowledge the time, patience, encouragement, and guidance from them in all the fruitful discussions and every single step during my doctoral study.

In the same sense, sincere thanks to my colleagues from collaborations who sharing their professional knowledge and giving me precious advice. I want to acknowledge Prof. Marin Gospodinov who kindly offered the $LuMnO_3$ single crystals; Dr. Mathieu Mirjolet who helped with the sample characterization and shared every detail of $LaFeO_3$; Aaron Schankler and Prof. Andrew Rappe who contributed to the work from the theoretical point of view; Dr. Jaume Gazquez and Mario Villa Navas for their time and effort to obtain great STEM images and analysis of the results; Dr. José Santiso for his expertise on X-ray diffraction; Dr. Jordi Fraxedas, Dr. Guillaume Sauthier and Prof. Andreas Klein for their proficient contribution on X-ray photoemission measurements; Huan Tan for the piezoelectric force microscopy measurement and understanding.

I sincerely acknowledge Raul Solanas and Dr. Mengdi Qian for the growth of thin films and sample fabrication in pulsed laser deposition lab; Dr. José Caicedo at ICN2 for the supplement of target preparation; Dr. Alberto Quintana for the SEM images and discussions on hexagonal films. Special thanks to the support and help of the technicians from the scientific service at ICMAB, particularly Anna Crespi, Javier Campos and Joan Esquius for the XRD characterization, Dr. Bernat Bozzo and Dr. Ferran Vallès for low temperatures and

magnetometry measurements, and Maite Simón and Andrés Gómez for AFM measurements.

Last but not the least, I would like to extend my gratitude to my beloved family and friends, who accompanied me with their love all along this period. Thanks for the unconditional support, encourage and understanding from my family, particularly my mom 姜玉兰 and my cousins. Thanks for the company from my friends to make each day meaningful, especially Yi, Xiaowan and Alejandro. To all my officemates and other friends at ICMAB: Pengmei, Juri, Jordi... Thank you all for the good vibe at ICMAB and the nice memories we had in Barcelona!

Abstract

The low power conversion efficiency is an important limiting factor for extensive photovoltaic applications. Within this context, ferroelectric photovoltaics using ferroelectric materials, are receiving a new interest. Indeed, some unique properties that they display may contribute solving some current bottlenecks in photoconversion-related applications. For instance, the possible presence of an internal electric field (depoling) extending all over the material and the presence of bulk photovoltaic effect (BPE) associated to their inherent non-centrosymmetric character. While the first may lead to more efficient charge extraction from a photoresponsive material, the second can lead to new opportunities such as the achievement of open circuit voltage (V_{oc}) larger than the bandgap of the involved semiconductors. In recent years, the BPE research in ferroelectrics has been mainly focused on $BiFeO_3$ with a bandgap of 2.7 eV, which implies limited responsivity at the visible range. Obviously, ferroelectrics with narrower gap could lead to improved photoconversion and BPE can introduce additional benefit. Among those materials, a remarkably simple family are the hexagonal manganites h-$ReMnO_3$ (Re = Lu, Y, etc.), that having a narrower bandgap ($\approx$ 1.5 eV), could be promising candidates. In h-$ReMnO_3$, BPE had not been yet documented, and this is the first objective of this thesis. Non-centrosymmetry can be intrinsic to the photo absorber, as in photoferroelectrics, but it can also be engineered by the design of the photovoltaic cell. Still a narrow bandgap material is required. The nonpolar $LaFeO_3$ (bandgap $\approx$ 2.4 eV) is a good candidate to explore its photoresponsivity, to carefully analyze the role of electronic band alignment with electrodes on the short circuit current density (J_{sc}) and open circuit voltage and ultimately compare its photoresponsivity to that of polar materials.

With these goals in mind, we have systematically studied the photovoltaic response of hexagonal $LuMnO_3$ single crystals and thin films aiming at identifying fingerprints of BPE and evaluate their contribution to the overall photoresponse. Next, the transport properties in dark and under illumination of heterostructures containing $LaFeO_3$ thin films sandwiched between asymmetric electrodes, have provided the opportunity to identify the connection between the built-in potential at interfaces $LaFeO_3$ and their photovoltaic properties.

These systematic studies have first made apparent that the photoresponse of polar materials and thin films, contains a complex interplay of the conventional photovoltaic effect (CPE) contribution containing the diffusion (charge gradients) and drift (electric fields) photocurrents of various origins (interfacial electric fields, flexoelectric fields, etc.), superposed to a unique contribution arising from their non-centrosymmetric character (BPE). All these contributions can coexist and be intertwined challenging their analysis. Last but not least, the role of the air/electrode interface and any other interface modulating the light-polarization dependence of optical reflectance and transmittance of the devices adds a new ingredient that further enriches measurements.

In ferroelectric h-LuMnO$_3$ single crystals of polarization $\textbf{P}$, it is found that the photocurrent can be modulated by the applied electric field/voltage. Data were understood in terms of the voltage dependence of $P(V)$ and the $\textbf{P}$ modulated Schottky barriers. Later, measurements indicated that the polar domain back switching and the associated BPE may also contribute to the photocurrent modulation. When changing the polarization direction of the light polarization angle (φ) and its incidence angle (θ), an oscillatory behavior of $J_{sc}(\varphi, \theta)$ is observed. This would be a first fingerprint of BPE. However, the dichroism in h-LuMnO$_3$ could mask BPE in LuMnO$_3$. Cross check experiments using photons of different energy allowed to disregard dichroic contributions. The oscillatory behavior of $J_{sc}(\varphi, \theta)$ and $V_{oc}(\varphi, \theta)$ where thus taken as the first evidence of BPE in h-LuMnO$_3$. The drift and diffusion terms in J_{sc} preclude accurate extraction of the Glass coefficients (G_{ij}) characterizing the BPE, but only some bounds can be inferred. It was found, for instance, that the upper limits of G_{ij} are larger than other photoferroelectrics (e.g., BiFeO$_3$). When trying to reveal the drift contribution to the measured $J_{sc}(\varphi)$, it is discovered that the amplitude of $J_{sc}(\varphi)$ oscillations are affected by the polarization back-switching. This indicates that the accurate extraction of the Glass coefficients is even more challenging, due to not only the entangled CPE contributions but also the instability of the saturated ferroelectric state.

Aiming at minimizing diffusion contributions, h-LuMnO$_3$ thin film is introduced and its growth is optimized. It is found that the electrodes contribute to the imprint field and thus largely affect the sensitivity of J_{sc} to the written ferroelectric $\textbf{P}$ direction. In any event, our LuMnO$_3$ films are found to have a prominent photovoltaic response with a responsivity ($\leq$ 2 x 10^{-3} A/W) larger than other ferroelectric oxides (e.g., BiFeO$_3$) and earlier reported

LuMnO$_3$ films, and larger than in LuMnO$_3$ single crystals ($\approx 3 \times 10^{-4}$ A/W) suggesting more efficient charge extraction in thin films than in bulky single crystals. The grain boundaries observed in this thin film may boost the large responsivity, as known to occur in some II-VI semiconductors.

Finally, the Fresnel controlled transmittance and associated CPE, displays a (φ, θ) dependence similar to BPE and thus are entangled with BPE controlled $J_{sc}(\varphi)$. In attempts to discriminate between BPE and CPE contributions to the $J_{sc}(\varphi)$ oscillations, experiments have been designed to compare $J_{sc}(\varphi)$ oscillations in polar and nonpolar films where BPE should be absent. Nonpolar LaFeO$_3$ films has been selected to compare the $J_{sc}(\varphi)$ to polar materials. Preliminary results suggest that in polar materials the BPE appears to dominate $J_{sc}(\varphi)$ while Fresnel governs the nonpolar LaFeO$_3$ response.

The structures involving in LaFeO$_3$ offers the possibility to study in detail the role of electrodes in CPE. A close connection between the observed V_{oc} and the built-in potential is derived. Although some strain relaxation is observed in the LaFeO$_3$ films, it is argued that V_{oc} is mainly dictated by band alignment rather than from possible flexoelectric fields. The measured responsivity (2.6 x 10^{-4} A/W) is larger than earlier reports on LaFeO$_3$. It is proposed that the unavoidable grain boundaries between differently textured LaFeO$_3$ crystallites play a role on the observed large responsivity as found in LuMnO$_3$ films.

x

Resumen

La baja eficiencia es un factor limitante en algunas aplicaciones fotovoltaicas. En este contexto, los materiales ferroeléctricos están recibiendo un nuevo interés. El motivo es que algunas propiedades únicas que muestran pueden contribuir a resolver algunos de los cuellos de botella actuales en las aplicaciones relacionadas con la fotovoltaica. Por ejemplo, la presencia de un campo eléctrico interno (despolarización) que se extiende por todo el material y la presencia de efecto fotovoltaico másico (BPE, por sus siglas en inglés) asociado a su carácter no centrosimétrico inherente pueden ayudar a aumentar la eficiencia en la conversión fotovoltaica. Mientras que el primero puede conducir a una extracción de carga más eficiente, el segundo pueda ayudar a aumentar el voltaje en circuito abierto (V_{oc}) consiguiendo valores mayores que la banda prohibida de los materiales semiconductores involucrados. En los últimos años, la investigación de BPE en ferroeléctricos se ha centrado principalmente en el estudio de $BiFeO_3$ con una banda prohibida de 2.7 eV, lo que implica una capacidad de respuesta limitada en el rango visible. Obviamente, los ferroeléctricos con un ancho de banda más estrecho podrían mostrar mayor eficiencia y BPE puede presentar un beneficio adicional. Entre esos materiales, una familia de materiales potencialmente interesantes son las manganitas hexagonales h-ReMnO3 (Re = Lu, Y, etc.), que al tener una banda prohibida más estrecha ($\approx$ 1.5 eV) absorben una mayor parte del espectro visible. En h-ReMnO$_3$, el BPE aún no había sido estudiado en detalle, y este es el primer objetivo de esta tesis. La no centrosimetría que da lugar al BPE puede ser inherente del material pero también puede generarse mediante la ingeniería de dispositivos adecuados. En este caso el $LaFeO_3$ no polar de banda prohibida $\approx$ 2,4 eV es un buen candidato y también a centrado parte de las investigaciones de la presente tesis.

Con estos objetivos en mente, hemos estudiado sistemáticamente la respuesta fotovoltaica de monocristales y películas delgadas de $LuMnO_3$ en su fase hexagonal con el objetivo de identificar indicios de BPE y evaluar su contribución a su respuesta fotovoltaica. En la presente tesis, las propiedades de transporte bajo iluminación y sin ella de heteroestructuras que contienen películas delgadas de $LaFeO_3$ intercaladas entre electrodos asimétricos han brindado la oportunidad de identificar el papel de las intercaras de $LaFeO_3$ en sus propiedades fotovoltaicas.

Estos estudios sistemáticos primero han puesto de manifiesto que la fotorespuesta de materiales polares y películas delgadas contienen contribuciones de efecto fotovoltaico convencional, el cual resulta de la suma de las corrientes de difusión (gradientes de carga) y de deriva (campos eléctricos) el origen de las cuales puede ser variada (interfaz eléctrica campos, campos flexoeléctricos, etc.). Superpuesta a estas contribuciones existe la contribución única derivada de su carácter no centrosimétrico, esto es el BPE. Todos estas contribuciones pueden coexistir y entrelazarse dificultando su análisis. Por último, pero no menos importante, el papel de la interfaz aire/electrodo y cualquier otra interfaz que modula la dependencia de la fotorespuesta con polarización de la luz por cambios en la reflectancia también debe ser tenido en cuenta.

En monocristales ferroeléctricos de h-LuMnO$_3$ de polarización $\boldsymbol{P}$, se encuentra que la fotocorriente puede ser modulada por el campo/voltaje eléctrico aplicado. Los datos se entendieron en primera estancia en términos de la dependencia de las barreras de Schottky moduladas por P. Más tarde, los estudios llevados a cabo indicaron que la la conmutación espontanea de los dominios ferroeléctricos por acción de los campos eléctricos internos y el BPE asociado también pueden contribuir a la modulación de la fotocorriente. Al cambiar la dirección de polarización de la luz (φ) y su ángulo de incidencia (θ), se observa un comportamiento oscilatorio de $J_{sc}(\varphi, \theta)$. Este sería una primera indicación de la contribución del BPE a la corriente medida. Sin embargo, el dicroísmo intrínseco del material podría enmascarar la presencia de BPE en el mismo. Experimentos complementarios utilizando fotones de distinta energía permitió distinguir las contribuciones dicroicas concluyéndose que estas son pequeñas. Como se ha mencionado, el comportamiento oscilatorio de $J_{sc}(\varphi, \theta)$ y $J_{sc}(\varphi, \theta)$ se tomó como la primera evidencia de BPE en h-LuMnO$_3$. Los términos de deriva y difusión de la fotocorriente impiden la extracción precisa de los coeficientes de Glass (G_{ij}) que caracterizan el BPE, y solo se pueden inferir sus valores dentro de un amplio rango. Se encontró, por ejemplo, que los límites superiores del G_{ij} son más grandes que otros fotoferroeléctricos (por ejemplo, BiFeO$_3$). Cuando se intenta distinguir la contribución de la corriente deriva al $J_{sc}(\varphi)$ medido, se descubre que la amplitud de las oscilaciones de $J_{sc}(\varphi)$ se ven afectadas por la conmutación de la polarización mediante campos eléctricos internos haciendo la caracterización de la corriente generada por BPE aún más difícil.

Con el objetivo de minimizar las contribuciones de difusión, se estudian película delgadas de h-LuMnO$_3$ y se optimiza su crecimiento. Se concluye que los electrodos contribuyen a la magnitud y dirección de los campos eléctricos internos, por lo tanto, afectan en gran medida la sensibilidad de J_{sc} a la dirección de la polarización ferroeléctrica. En cualquier caso, se observa que películas de LuMnO$_3$ tienen una respuesta fotovoltaica prominente con una capacidad de respuesta ($\leq 2 \times 10^{-3}$ A/W) mayor que otros óxidos ferroeléctricos (p. ej., BiFeO$_3$) y que otras películas de LuMnO$_3$ examinadas por otros autores con anterioridad, y mayor que en los monocristales de LuMnO$_3$ estudiados. Esto sugiere que películas delgadas muestran una extracción de carga más eficiente que monocristales voluminosos. Se discute que los límites de grano observados en esta películas delgadas pueden aumentar su respuesta fotovoltaica, como se ha reportado en algunos semiconductores II-VI.

Finalmente, la transmitancia controlada por Fresnel y la fotocorriente resultante de los campos de difusión y deriva muestran una dependencia (φ, θ) similar a BPE y, por lo tanto, están entrelazados con $J_{sc}(\varphi)$ controlado por BPE. En un intento por discriminar entre las contribuciones de BPE y otras a las oscilaciones $J_{sc}(\varphi)$, se han diseñado experimentos para comparar las oscilaciones $J_{sc}(\varphi)$ en películas polares y no polares donde el BPE no debería existir. Se seleccionaron películas no polares de LaFeO$_3$ para comparar el $J_{sc}(\varphi)$ con materiales polares. Los resultados preliminares sugieren que en materiales polares el BPE parece dominar $J_{sc}(\varphi)$ mientras que Fresnel gobierna la respuesta en las láminas no polares de LaFeO$_3$.

Las estructuras involucradas en LaFeO$_3$ ofrecen la posibilidad de estudiar en detalle el papel de los electrodos en los campos eléctricos internos. Se concluye una estrecha relación entre el V_{oc} medido y el diagrama de bandas esperado del dispositivo. Aunque se observa cierta relajación de la tensión en las películas de LaFeO$_3$, se argumenta que la V_{oc} está dictada principalmente por el diagrama de bandas en las intercaras más que por posibles campos flexoeléctricos. La fotorespuesta del dispositivo ($2,6 \times 10^{-4}$ A/W) es mayor que las reportadas en anterioridad en LaFeO$_3$. Se propone que los límites de grano inevitables entre los cristalitos de LaFeO$_3$ de diferente textura desempeñan un papel en la gran capacidad de respuesta observada como ya se discute en base a los resultados obtenidos en películas de LuMnO$_3$.

Resum

La baixa eficiència de conversió d'energia és un factor limitant important per a algunes aplicacions fotovoltaiques. En aquest context, la conversió fotovoltaica emprant materials ferroelèctrics, està rebent un nou interès. De fet, algunes de les seves propietats son úniques i poden contribuir a resoldre alguns colls d'ampolla actuals en aplicacions relacionades amb la fotoconversió. Per exemple: la possible presència d'un camp elèctric intern (depolaritzant) que s'estén per tot el material i la presència l'anomenat *bulk photovoltaic effect* (BPE) directament associat al seu caràcter no centrosimètric inherent. Si bé el primer pot conduir a una extracció de càrrega més eficient d'un material fotoresponsiu, el segon pot donar lloc a noves oportunitats, com ara l'assoliment d'una tensió de circuit obert (V_{oc}) més gran que la banda prohibida (gap) dels semiconductors implicats. En els darrers anys, la investigació de BPE en ferroelèctrics s'ha centrat principalment en $BiFeO_3$ amb un amplada de band prohibida de 2,7 eV, la qual cosa implica una capacitat de resposta limitada en el rang visible. Òbviament, els ferroelèctrics amb una banda prohibida més estreta podrien conduir a una millor fotoconversió i el BPE podria introduir beneficis addicionals. Entre aquests materials, una família molt senzilla són les manganites hexagonals h-ReMnO$_3$ (Re = Lu, Y, etc.), que amb un interval de banda més estret ($\approx$ 1,5 eV), podrien ser candidats prometedors. En h-ReMnO$_3$, la BPE encara no s'ha documentat, i aquest és el primer objectiu d'aquesta tesi. La no-centrosimetria pot ser intrínseca en l'absorbent de fotons, com en els fotoferroelèctrics, però també es pot dissenyar mitjançant l'enginyeria de la cèl·lula fotovoltaica. Tot i així, es requereix un material de banda intercalada estreta. El $LaFeO_3$ no polar (banda prohibida $\approx$ 2,4 eV) és un bon candidat per explorar la seva fotoresponsivitat, per analitzar acuradament el paper de l'alineació de la banda electrònica amb els elèctrodes en la densitat de corrent de curtcircuit (J_{sc}) i la tensió de circuit obert i, finalment, comparar la seva fotoresponsivitat amb la de materials polars.

Tenint en compte aquests objectius, hem estudiat sistemàticament la resposta fotovoltaica de cristalls i pel·lícules primes de h-LuMnO$_3$ amb l'objectiu d'identificar la presència de BPE i avaluar la seva contribució a la fotoresposta global. A continuació, la mesura de les propietats de transport en foscor i sota il·luminació de les heteroestructures

que contenen pel·lícules primes de LaFeO$_3$ (centrosimètriques) intercalades entre elèctrodes asimètrics, han proporcionat l'oportunitat d'identificar la connexió entre els perfils de potencial a les interfícies LaFeO$_3$ i les seves propietats fotovoltaiques.

Aquests estudis sistemàtics han posat de manifest que la fotoresposta dels materials polars i les pel·lícules primes resulta d'una interacció complexa de la contribució de l'efecte fotovoltaic convencional (CPE) que conté la difusió (gradients de càrrega) i la deriva (camps elèctrics) fotocurrents de diversos orígens (elèctrics interfacials). camps, camps flexoelèctrics, etc.), superposats a una contribució única derivada del seu caràcter no centrosimètric (BPE). Totes aquestes aportacions poden conviure i estar entrellaçades i desafien la seva anàlisi. Finalment, però no menys important, el paper de la interfície aire/elèctrode i qualsevol altra interfície introdueix una dependència de la reflectància òptica i la transmitància òtica del dispositiu en la polarització de la llum i afegeix un nou ingredient que enriqueix encara més les mesures.

En els cristalls ferroelèctrics *h*-LuMnO$_3$ de polarització **P**, es va trobar que la fotocorrent es pot modular pel camp elèctric/tensió aplicats. Les dades es van entendre en termes de la dependència de la tensió de $P(V)$ i les barreres de Schottky **P** modulades. Més tard, les mesures van indicar que la commutació dels dominis polar i el BPE associat també poden contribuir a la modulació del fotocorrent. Quan es canvia la direcció de polarització de l'angle de polarització de la llum (φ) i el seu angle d'incidència (θ), s'observa un comportament oscil·latori de $J_{sc}(\varphi, \theta)$. Aquesta seria una primera empremta de BPE. Tanmateix, el dicroisme en *h*-LuMnO$_3$ podria emmascarar BPE. Experiments utilitzant fotons de diferent energia van permetre ignorar les contribucions dicroiques. El comportament oscil·latori de $J_{sc}(\varphi, \theta)$ i $V_{oc}(\varphi, \theta)$ es va prendre doncs com a primera evidència de BPE en *h*-LuMnO$_3$. Els termes de deriva i difusió que contribueixen a la J_{sc} impedeixen l'extracció precisa dels coeficients de Glass (G_{ij}) que caracteritzen el BPE, i només es poden inferir alguns límits. Es va trobar, per exemple, que els límits superiors de G_{ij} són més grans que altres fotoferroelèctrics (per exemple, BiFeO$_3$). Quan s'intenta analitzar la contribució de la corrent de deriva a la $J_{sc}(\varphi)$ mesurada, es descobreix que l'amplitud de les oscil·lacions de $J_{sc}(\varphi)$ es veu afectada pel canvi de polarització (commutació de dominis). Això indica que l'extracció precisa dels coeficients de vidre és encara més difícil,

a causa no només de les contribucions de CPE entrellaçades, sinó també de la inestabilitat de l'estat ferroelèctric saturat.

Amb l'objectiu de minimitzar les contribucions de difusió, s'han desenvolupat capes primes de h-LuMnO$_3$ i s'ha optimitzat el seu creixement. Es troba que els elèctrodes contribueixen al camp elèctric de *imprint* i, per tant, afecten en gran mesura la sensibilitat de J$_{SC}$ a la direcció **P** ferroelèctrica escrita. En qualsevol cas, es troba que les nostres pel·lícules LuMnO$_3$ tenen una resposta fotovoltaica important amb una resposta (≤ 2 x 10^{-3} A/W) més gran que altres òxids ferroelèctrics (per exemple, BiFeO$_3$) i pel·lícules de LuMnO$_3$ reportades anteriorment, i més gran que en els monocristalls de LuMnO$_3$ ($\leq 3 \times 10^{-4}$ A/W). Aquesta observació suggereixen que l'extracció de càrrega és més eficient en pel·lícules primes que en cristalls (més voluminosos). Els límits de gra observats en aquesta pel·lícula prima podrien ser els reponsables de la major respositivitat, tal i com s'observa en alguns semiconductors II-VI.

Finalment, la transmitància controlada per l'efecte Fresnel i el CPE associat, mostra una dependència (φ, θ) similar a BPE i, per tant, s'entrellaça amb $J_{sc}(\varphi)$ controlat per BPE. En un darrer intents de discriminar entre les contribucions BPE i CPE a les oscil·lacions $J_{sc}(\varphi)$, s'han dissenyat experiments per comparar les oscil·lacions $J_{sc}(\varphi)$ en pel·lícules polars i no polars on BPE hauria d'estar absent. Els resultats preliminars suggereixen que en materials polars el BPE sembla dominar $J_{sc}(\varphi)$ mentre que Fresnel governa la resposta LaFeO$_3$ no polar.

Les estructures implicades en LaFeO3 ofereixen la possibilitat d'estudiar en detall el paper dels elèctrodes en CPE. S'ha pogut evidenciar una estreta connexió entre el V$_{OC}$ observat i el potencial de interficies. D'altra banda, tot i que s'observa una certa relaxació de la tensió a les pel·lícules LaFeO$_3$, s'argumenta que V$_{oc}$ està dictada principalment per l'alineació de bandes en lloc de possibles camps flexoelèctrics. La resposta mesurada (2,6 x 10^{-4} A/W) és més gran que publicacions anteriors sobre LaFeO$_3$. Es proposa que els límits de gra inevitables entre cristal·lets de LaFeO$_3$ amb textura diferent tenen un paper en la gran capacitat de resposta observada tal com es troba a les pel·lícules de LuMnO$_3$.

Contents

Chapter 1. Introduction: bulk photovoltaic effect in non-centrosymmetric materials

Photovoltaic (PV) response appears when a semiconducting material is under suitable illumination ($h\upsilon$ > bandgap E_g) and photogenerated carries are extracted by electrodes generating a photocurrent. In non-centrosymmetric materials, such as ferroelectrics, the photocarriers can be driven towards electrodes by additional mechanisms. Precisely, the photovoltaic effect (PVE) originates from the conventional photovoltaic effect (CPE) which is mainly an interfacial driven response, and the so-called "bulk photovoltaic effect" (BPE) which is a genuine response of non-centrosymmetric materials and it is a bulk property. The CPE contains several contributions. First, a drift term photocurrent (J_E) associated with photocarriers separated by any build-in electric field (E_{bi}) or depoling field (E_d), etc. In metal-ferroelectric-metal junctions, E_{bi} is often found to originate from Schottky barriers (SBs) at electrode interfaces. The resulting J_E is controlled by the width and height of SBs, which are modulated itself by the ferroelectric polarization ($\boldsymbol{P}$) of the material. That is, J_E is modulable or even switchable by $\boldsymbol{P}$-controlled SBs. Second, the Dember effect caused by a nonuniform illumination/absorption, generating a diffusion term (J_D) associated to photoinduced carrier gradients.[1,2] The bulk photovoltaic effect (J_{BPE}) is genuinely related to the non-centrosymmetric nature of the structure.

1.1. Bulk photovoltaic effect and its fingerprints

The bulk photovoltaic effect occurs in homogeneous non-centrosymmetric materials (semiconductors and insulators, crystalline or polycrystalline) under a uniform illumination, in the absence of any inner field or spatial inhomogeneity (charge gradient), thus was named as "bulk" photovoltaic effect.[1,3,4] BPE is also a type of anomalous photovoltaic effect (APE), where the "anomalous" refers to the photovoltage (i.e., open circuit voltage V_{oc}) that can exceed the bandgap of the absorbing material (absorber) by several orders of magnitude,[5–7] which is not the case in CPE where the V_{oc} is limited by E_g of the device components. Thus, BPE opens new possibility towards efficient absorbers for photoelectric conversion application.

Fig. 1.1 illustrates the PVE in (a) centrosymmetric and (b) non-centrosymmetric crystals. The fundamental difference is that in occurrence of an asymmetric momentum distribution of nonthermalized carriers in the conduction band of non-centrosymmetric crystals. The asymmetric distribution can occur in the momentum space (giving rise to a so-called *ballistic current*) or the so-called *shift current*, which is of quantum-mechanical nature and refers to the virtual shift in the real space following the carrier band-band transition. Derailed description of these effects can be found elsewhere.[4,8–10] In any event, BPE produces a characteristic dependence of the photocurrent and photovoltage of light polarization, which are the topic of the present research.
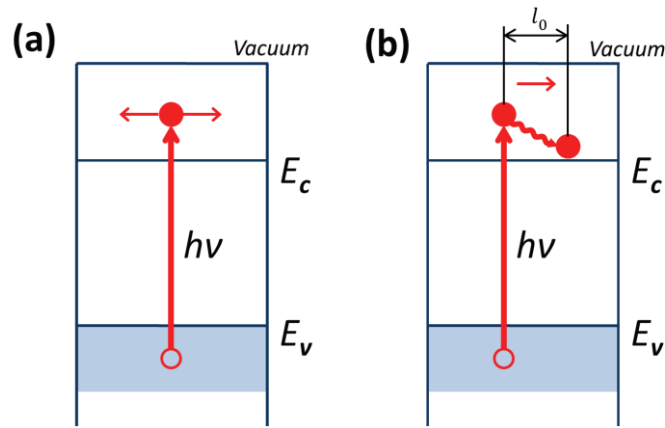
Fig. 1.1. (a) Isotropic and (b) anisotropic non-equilibrium carrier momentum distribution in centrosymmetric and non-centrosymmetric crystals corresponding to the classical and bulk photovoltaic effects, respectively. The photoexcited non-thermalized carriers lose their energy and descend to the bottom of the band, which results in the shift in space l_0. The figure is taken from Ref. 10.

In BPE, the short circuit current density (J_{sc}) is determined by the direction of light polarization (electric field ***E***) via a tensorial relation, given by:[1,4,11,12]

$$J_{\mathrm{BPE},i} = I_0\big[\beta^{\mathrm{L}}_{ijk} e_j e_k^* + \mathrm{i}\beta^{\mathrm{C}}_{ik}(\boldsymbol{e} \times \boldsymbol{e}^*)_k\big] \qquad [1.1]$$

where $J_{\mathrm{BPE},i}$ is the J_{sc} generated by BPE along the *i* direction; I_0 is the intensity of the light; e_j, e_k are the projection of the incoming light polarization vector along the *j*, *k* direction, respectively; ***e*** is the unit polarization vector; β_{ijk} is the photovoltaic tensor that depends on the symmetry of the material centers, its electronic properties and the photon energy.[4,6]

The real part of the photovoltaic tensor (β_{ijk}^{L}, third-rank piezo tensor) is symmetric under permutation of the latter subscripts and nonzero for the linear polarization ($e = e^*$), corresponding to the so-called linear BPE. While the imaginary part (β_{ik}^{C}, second-rank gyration tensor) is antisymmetric,[4,11] zero for the linear polarization and maximal for the circular polarization [$i(e \times e^*) = 1$], corresponding to the circular BPE. The suffixes *i*, *j*, *k* represent *x*-, *y*-, and *z*-axis in the Cartesian coordinate system for the light polarization components of the incoming light.

Within the scope of this thesis, only linear BPE is considered, that is:

$$J_{\mathrm{BPE},i} = I_0 \beta_{ijk} e_j e_k^*$$

[1.2]

where β_{ijk} denotes the linear piezo tensor determined by the symmetry nature of the material. The β_{ijk} tensor can be written as a matrix in reduced notation.[7] For example, in the extensively studied ferroelectric BiFeO$_3$ [BFO, space group *R*3c/3m ($\equiv$ C$_{3v}$)], the tensor contains only 4 non-zero independent elements and Eq. [1.2] can be written as:[4,13]

$$\begin{pmatrix} J_x \\ J_y \\ J_z \end{pmatrix} = I_0 \begin{pmatrix} 0 & 0 & 0 & 0 & \beta_{15} & -\beta_{22} \\ -\beta_{22} & \beta_{22} & 0 & \beta_{15} & 0 & 0 \\ \beta_{31} & \beta_{31} & \beta_{33} & 0 & 0 & 0 \end{pmatrix} \begin{pmatrix} e_x^2 \\ e_y^2 \\ e_z^2 \\ e_y e_z \\ e_z e_x \\ e_x e_y \end{pmatrix}$$

[1.3]

where $e_{x,y,z}$ depend on the specific optical geometry applied. For the ferroelectric hexagonal LuMnO$_3$ [*h*-LMO, space group *P*6$_3$cm/6mm ($\equiv$ C$_{6v}$)], materials to be investigated in this manuscript, the tensor contains only 3 non-zero independent elements and Eq. [1.2] is described by:[4,14]

$$\begin{pmatrix} J_x \\ J_y \\ J_z \end{pmatrix} = I_0 \begin{pmatrix} 0 & 0 & 0 & 0 & \beta_{15} & 0 \\ 0 & 0 & 0 & \beta_{15} & 0 & 0 \\ \beta_{31} & \beta_{31} & \beta_{33} & 0 & 0 & 0 \end{pmatrix} \begin{pmatrix} e_x^2 \\ e_y^2 \\ e_z^2 \\ e_y e_z \\ e_z e_x \\ e_x e_y \end{pmatrix}$$

[1.4]

When the material is thick enough to absorb all the penetrating light, the Glass coefficients G_{ijk} are introduced to include the effect of light attenuation due to absorption, as given by:[4,6,15]

$$\beta_{ijk} = \alpha_{jk} G_{ijk} \qquad [1.5]$$

Where α_{jk} is the absorption coefficient tensor; G_{ijk} is the Glass coefficient tensor characterizing the current excitation performance, which depends on the symmetry of the material, electronic structure and the absorbing properties of the material at a given photon energy.[6] When the absorption anisotropy is unimportant (i.e., $\alpha_{jk} = \alpha$), it is convenient to distinguish the absorbed power explicitly by:[4]

$$G_{ijk} = \alpha^{-1} \beta_{ijk} \qquad [1.6]$$

Within BPE scenario, V_{oc} can be expressed by [16–18]:

$$V_{\text{oc}} = \frac{J_{\text{sc}} l}{\sigma_{\text{d}} + \sigma_{\text{pv}}} + V_{\text{bi}} \qquad [1.7]$$

Where J_{sc} is the short circuit photocurrent l is the effective device length (distance between electrodes); V_{bi} is any built-in voltage apart from BPE; σ_{d} and σ_{pv} are the dark and photo conductivity, respectively ($\sigma_{\text{d}} \ll \sigma_{\text{pv}}$); σ_{pv} being:[19]

$$\sigma_{\text{pv}} = e I_0 \alpha \Phi (\hbar\omega)^{-1} (\mu\tau)_{pv} \qquad [1.8]$$

where ϕ is the quantum yield, $\hbar\omega$ is the incident photon energy, and μ and τ are the mobility and lifetime of the carriers responsible for photoconductivity and associated with thermalized nonequilibrium carriers, respectively. Then σ_{pv} can be assumed constant when rotating the light polarization plane φ [between the initial light polarization direction $\mathbf{E_1}$ and any intermediate $\mathbf{E_n}$, see Chapter 3 in Fig. 3.5]. From Eq. [1.7] it is clear that V_{oc} is also modulated by φ following the same rule as $J_{\text{sc}}(\varphi)$.

Eqs. [1.1, 1.7] describe the photocurrent and photovoltage and their dependence of the light polarization originating from BPE. Therefore, BPE can be examined by measuring the photocurrent (short circuit current I_{sc}) and/or photovoltage (V_{oc}) dependence on light polarization angle/helicity of a linearly/circularly polarized light to identify its tensorial

relation, which usually behaves as a sinusoidal oscillation. This angular dependence of photoresponse [$J_{sc}(\varphi)$, $V_{oc}(\varphi)$, $\approx \cos2\varphi$] is typically taken as the fingerprint of BPE, which were early seen in many non-centrosymmetric materials and used to evaluate their nonzero tensor elements , including the non-ferroelectric GaP,[20,21] ZnO^3 and ferroelectric $BaTiO_3$,[22,23] $LiNbO_3$,[24,25] etc.

1.2. The renaissance of BPE in bulk materials

Acentric materials with BPE have recently emerged as promising optoelectronic materials.[26] Ferroelectric photovoltaics which are non-centrosymmetric, fall into the category probably owning BPE in addition to drift and diffusion effects. Whereas the most common ferroelectrics, such as $Pb(Zr,Ti)O_3$ and $BaTiO_3$, have a large bandgap (≈ 3.6 eV) and thus their photo absorption and photocurrent in the visible range (about 1.8 - 3.1 eV) is rather limited. The discovery of large open circuit voltage in ferroelectric $BiFeO_3$ with a narrower bandgap[27,28] (about 2.7 eV) and a light polarization-dependent photocurrent suggested as significant BPE contribution to the photoresponse, triggered a renewed interest on photoferroelectrics aiming at applications for efficient photoconversion.[5,29–31]

In the following, the astonishing flow of results on $BiFeO_3$ and much modest in other narrow gap ferroelectric (hexagonal manganites or ferrites) are reviewed aiming at settling the state of the art.

1.2.1. Sate of the art in BiFeO₃

As an outstanding example among photoferroelectrics, $BiFeO_3$ has drawn much attention. Initial reports[5] attributed the anomalous photovoltaic effect (above bandgap open circuit voltage) in BFO to polarization-related carrier separation at the domain walls (DWs) but subsequent studies[7,17,32] revealed that the actual mechanism behind the APE is the bulk photovoltaic effect.

In 2009, T. Choi et al.[29] reported in $BiFeO_3$ single crystals (SC) a diode-like switchable photovoltaic effect associated with the direction of bulk electric polarization (**P**), and a substantial light polarization (**E**) dependent PV current induced by visible light, as shown in Fig. 1.2. The PVE becomes maximum when the light electric field is parallel to the in-plane

component of the ferroelectric polarization, and minimum when the *E* is perpendicular to it. This observation gave the first hint of bulk photovoltaic effect in a BFO single crystal.
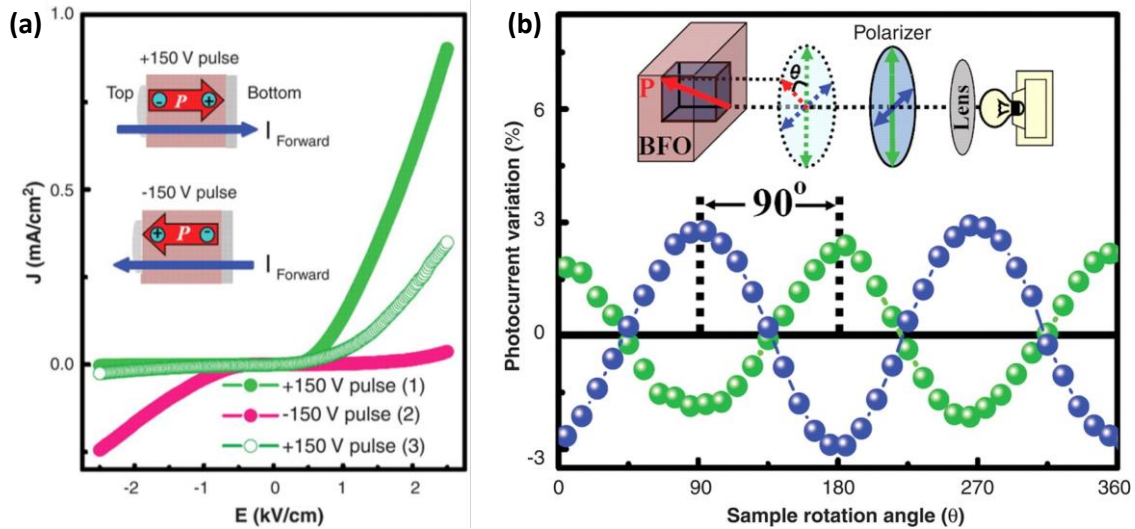
Fig. 1.2. (a) *J*(*E*) curves of BFO after +150 V, −150 V and +150V pulses, in sequence. The diode forward and reverse directions switch when the direction of out-of-plane polarization is reversed by ±150 V pulses. The diode forward direction turns out to be the same as the direction of electric pulses used for polarization flipping. (b) The variation of photocurrent with sample rotation under illumination with a linearly polarized light. The experimental sketch is shown in the inset. After the initial rotation experiment (blue circles), the polarizer was rotated by 90°, and light conditions were readjusted for an optimum photocurrent (green circles) where a 90° phase shift of is found in the photocurrent variation. Figure is adapted from Ref. 29.

In 2010, S. Yang et al.[5] showed a photovoltaic effect in BFO thin films. A large photovoltage (V_{oc} = 16 V) was measured and found to increase linearly in magnitude as the electrode spacing was increased (Fig. 1.3) and claimed to arise from steps of the electrostatic potential at domain walls. Data follows the characteristic V_{oc} dependence on thickness of bulk photovoltaic effect (Eq. [1.7]) although the authors ruled out BPE by the negligible V_{oc} in the single domain sample. In the same year, B. Kundys et al.[33] showed an angular dependence of the photostriction on the light polarization direction in BFO single crystal, this was not neither interpreted in terms of BPE.
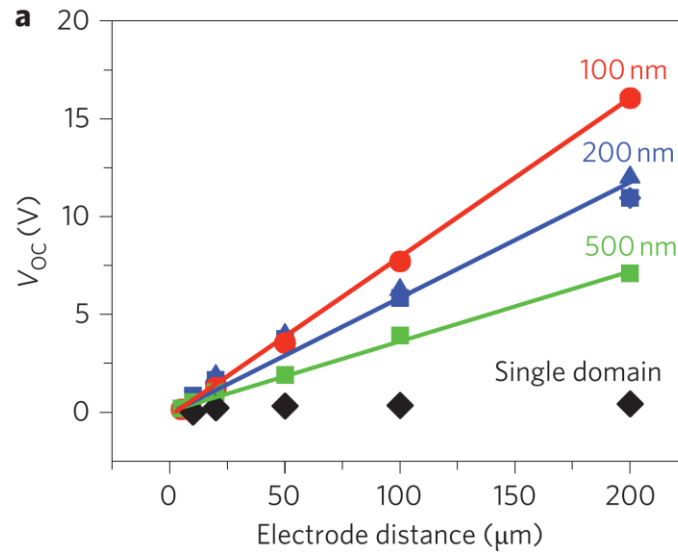
Fig. 1.3. The evolution of V_{oc} as a function of electrode spacing for four different samples: 71° domain-walls samples with thicknesses of 100 nm (red), 200 nm (blue) and 500 nm (green) as well as a monodomain BFO film having no domain walls (black). A clear correlation between the number of domain walls and the magnitude of V_{oc} is observed. Figure is taken from Ref. 5.
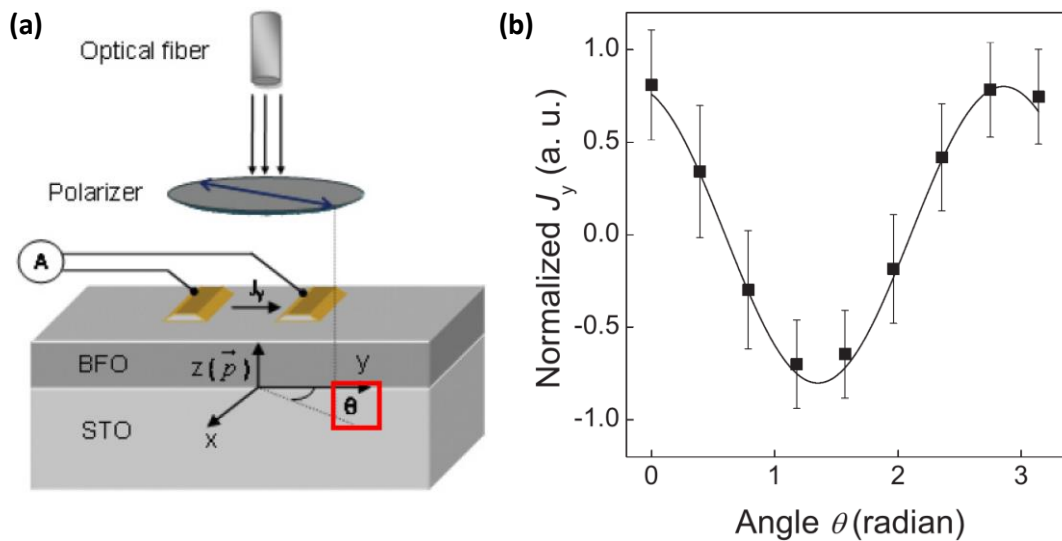
Fig. 1.4. (a) Schematic of the epitaxial BFO thin film with in-plane electrodes and polarization along thickness direction under polarized light. The angle between the polarizer transmission axis and the y axis is θ. (b) Normalized J_y at different polarizer angles. The error bar is one standard deviation of the readings from different samples. Figure is adapted from Ref. 34.

It was in 2011 that W. Ji et al.[34] measured the sinusoidal response of photocurrent on light polarization as shown in Fig. 1.4, which was taken as first direct evidence of BPE

contribution in epitaxial BFO films. The values of PV tensor element β_{22} and Glass coefficient G_{22} were obtained by considering nonuniform absorption of incident photons. The photocurrent was obtained using symmetric electrodes perpendicular to the ferroelectric polarization (***P***) in (111) BiFeO$_3$ thin films. Given the fact that this is a symmetric configuration with photocurrent measured perpendicular to ***P***, the contributions of interfacial barriers at electrodes and the depolarization field from the BPE could be neglected.

One year later, by using first principles shift current theory, S. Young et al.[9] computed the bulk photovoltaic effect in BiFeO$_3$ and found good agreement with experimental results. Moreover, they reconciled the significant BPE observed in monodomain samples in Refs. 34,35 with the apparent negligible contribution evinced in striped polydomain samples Ref. 5. That is, the domain-wall-driven response in striped polydomain samples is partially mitigated by BPE, suggesting that enhanced efficiency could be obtained in materials with cooperative rather than antagonistic interaction between the two mechanisms.

Inspired by the studies above, in 2013, A. Bhatnagar et al.[17] revisited the behavior of samples with stripe domains. Temperature-dependent PV studies using different geometries of the electrodes with respect to the DWs proved that the APE in BFO films originates from BPE, and all the PV tensor elements and corresponding Glass coefficients were calculated. Furthermore, large V_{oc} up to 50 V could be achieved by controlling the conductivity of DWs irrespective of the measurement geometry and the type of the DW. In fact, in 2016, H. Matsuo et al.[36] investigated the BiFeO$_3$ films with the single-domain and 71° domain structures, revealing a major contribution of the DWs superimposed on BPE, which explained the enhanced PV response in the multidomain film exhibiting photovoltages greater than E_g.

In 2014 and 2015, S. Nakashima et al.[32,37] investigated the origin of bulk photovoltaic effect by the dependence of PVE on the light polarization direction in epitaxial BiFeO$_3$ thin films with striped- and single-domain structures grown on cubic SrTiO$_3$ (STO) rather than on orthorhombic substrates.[5,17] Anomalous V_{oc} (of different values) was observed not only in striped domain-structured film with Pt electrodes fabricated parallel to domain walls but also in single-domain-structured film with Pt electrodes perpendicular to the in-plane

component of the spontaneous polarization (P_s) vector despite the absence of DW, plus a laser-rotation-angle sinusoidal dependence of I_{sc} and V_{oc}. This predicted an anomalous V_{oc} under randomly polarized light illumination, and further proved that the abnormal photovoltages originated from the PVE not at the domain walls but in bulk BFO (BPE). They[7] also explored the intrinsic APE in STO//Pt/single-domain BFO/Pt with sufficiently thick BFO films, by the influence of laser power, BFO film thickness, measurement direction, light polarization direction and sample rotation angle, on I_{sc} and V_{oc}. It was found that the measured I_{sc} and V_{oc} are affected by the low-resistance of the thin BFO layer and the photoconducance of the thick STO substrate. The BFO thickness dependence of APE was well explained by considering the light attenuation due to the absorption of BFO and the photoconductivity of STO. This revealed the importance of photon absorption process in APE of BFO thin films. It was concluded that the APE in BFO mostly aroused from the shift current of BPE and the corresponding tensor elements were evaluated.

In 2015, M. Yang et al.[38] also reported a work addressing the issue of the origin of the APE in BiFeO$_3$ single crystals by studying the spectral distribution of the photoconductivity and the temperature dependent PVE. An important sub-bandgap photoelectric response near 2.2 eV was observed, which allowed the tailoring of V_{oc} by modifying the occupancy of these sub-band levels with a controlled scheme of thermal and electrical treatments. In 2017, M. Yang et al.[39] characterized the local PV and photoconductive properties of 71° domain walls on BiFeO$_3$ thin films using the photoelectric atomic force microscopy (AFM) and piezoresponse force microscopy (PFM). Local PV current was proven to driven by the BPE and found to be significantly enhanced at DWs due to their higher photoconductivity rather than the internal electric field. Several months later, they[40] demonstrated the BPE of monodomain BiFeO$_3$ thin films originating from the non-centrosymmetry of ferroelectric semiconductors. Moreover, the photocurrent exhibited tunable direction and magnitude depending on the light polarization and temperature, suggesting that the BPE can be tailored by modifying the activity of sub-band levels via chemical doping hence enhancing the power conversion efficiency (PCE). In 2018, they[41] explored the full optical control in BiFeO$_3$ thin films at room temperature (RT). Namely, reversible switching of ferroelectric/ferroelastic domains can be achieved by the mediation of tip enhanced PVE. The enhanced J_{sc} at the tip generates a local electric field exceeding the coercive field (E_c),

enabling the switch of ferroelectric P. By tailoring the photocurrent direction via either tuning the illumination geometry or rotating the light polarization, full control of the ferroelectric P was achieved.

In 2018 and 2020, S. Nakashima et al.[13,42] investigated the bulk photovoltaic effect of Mn-doped $BiFeO_3$ thin films, whereby the light polarization dependent photovoltage was enhanced by Mn doping. A maximum V_{oc} of 209 V[13] and 852 V[42] (at 80 K) were observed. In addition, the optical strain of a cantilever was investigated by measuring the displacement of the edge of the cantilever under illumination. This edge displacement depended on light polarization, indicating that the optical strain was due to the coupling between the BPE and the inverse piezoelectric effect.

In 2019, T. Yang et al.[43] reported a design to realize the high photovoltaic output in $BiFeO_3$ films by manipulating its oxygen vacancy concentration through the alteration of the Bi content, further suggesting the BPE mechanism instead of the Schottky effect. Besides, oxygen vacancy migration dominated in determining the switchable PVE rather than the ferroelectric P.

Several months later, D. Knoche et al.[44] investigated the amplitude and angular dependence of I_{sc}, as the ferroelastic domain arrangement was varied by applying electric fields in planar devices of BFO films. Analysis of the PV response manifested in a mathematical model to estimate the proportion of switched and unswitched regions, which unraveled the potential utility of BPE to trace the orientation of the polarization vectors in areas much larger than that can be accommodated in probe-based techniques. In 2021, they[45] demonstrated the evolution of BPE in BFO thin films with stripe-domain pattern, by modulating the light polarization modulated from linear to elliptical to circular. Its V_{oc} under circularly polarized light exceeded ± 25 V. Analysis of the circular BPE with the associated tensors highlighted the necessity of helicity-dependent interaction between light and domain variants (P pointing along [111] or [1−11]). Appropriate positioning of electrodes introduced a switch-like (ON and OFF state) PVE by changing the helicity of circularly polarized light.

In November of 2021, Y. Heo et al.[46] showed enhanced piezoelectricity under illumination via BPE and SB contribution in $BiFeO_3$ single crystals by PFM and conductive

AFM, involving the role of V_{oc} and photocharge carrier density. In February of 2022, A. Abdelsamie et al.[47] demonstrated the crossover between bulk- and interface-dominant responses in vertical $BiFeO_3$ film based heterostructures when changing the photon energy. It revealed that well-above-bandgap excitation led to bulk PV response, but band-edge excitation required band bending at interface to separate the photocarriers. In April, A. Martínez et al.[48] reported direct evidence for bulk PV charge transport in ferroelectric polycrystalline BFO films. The photocurrent dependence on light polarization, poling state of the film and the light intensity, as well as the scaling of V_{oc} with electrode distance, indicated the charge carrier separation relying on BPE.

Up to now, experiments and calculations clearly evidenced that under visible illumination, V_{oc} in $BiFeO_3$ could be larger than the bandgap. Furthermore, the main origin of APE in BFO was identified as BPE by the oscillation of PVE dependence on light polarization angle φ [$J_{sc}(\varphi)$ and $V_{oc}(\varphi)$] in a particular geometry and single-domain BFO, along with the contribution of DWs. The four photovoltaic tensor elements and corresponding Glass coefficients were obtained. Nevertheless, it is worth mentioning that the BPE studies in BFO films and single crystals were performed mostly at normal incidence (light propagation along the normal to the sample surface) to avoid the possible role of the Fresnel (φ dependent transmitted light intensity, details see Chapter 6) and/or any dichroism (φ dependent light absorption, details see Chapter 4.2.4) controlled conventional photovoltaic effect (CPE).[34,49] The disentangling of CPE and BPE remains to be solved when both contribution exist.

1.2.2. Sate of the art in LuMnO₃

Interest of photoferroelectrics is now directed towards ferroelectrics having narrower bandgaps. Hexagonal rare-earth manganites and isostructural ferrites (ReMnO₃ and ReFeO₃, Re = Ho−Lu)[50–52] are particularly suitable candidates because they are uniaxial polar materials and chemically stable, with bandgap around 1.5 eV[53–55] and potential high open circuit voltage resulting from BPE. Responsivity ($\mathbf{R}$) accounts for the light sensitivity of photocurrent and it is defined as $\mathbf{R} = \frac{J_{sc} - J_{dark,V=0}}{I_p}$, where J_{sc} is the short circuit current density, $J_{dark,V=0}$ is the current in dark at zero bias and I_P is the incident light power density.[56,57] Possessing small bandgap, the photocurrent and responsivity observed in these

hexagonal ferroelectrics particularly manganites ($\approx 10^{-3}$ A/W)[58–60] are very attractive compared with other wide bandgap photoferroelectrics such as $BiFeO_3$ and $BaTiO_3$ (10^{-7} - 10^{-4} A/W).[57,61]
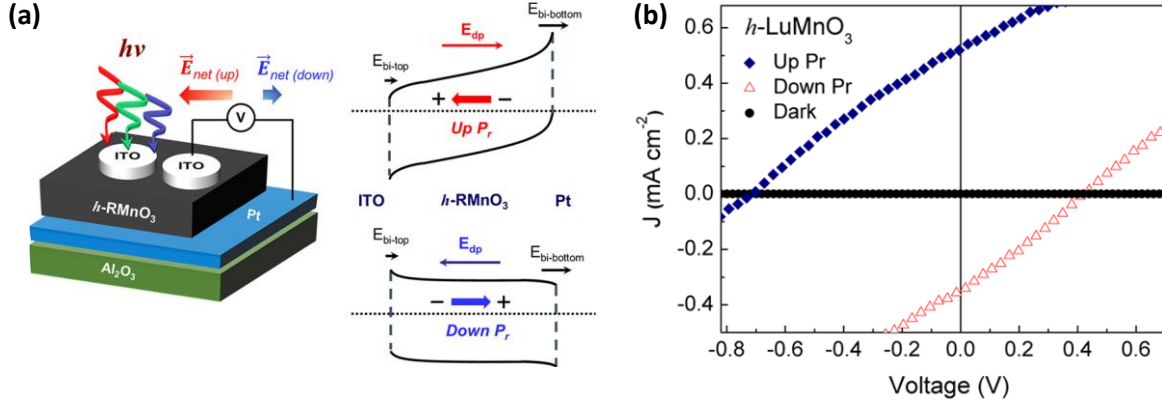
Fig. 1.5. (a) A schematic representation of the Al_2O_3//Pt/*h*-RMO/ITO heterojunction device. Two distinct energy band diagrams across the ITO/*h*-RMO(150 nm)/Pt heterojunction for the up-polarization state and the down-polarization state. (b) Current density (*J*)-voltage (*V*) characteristics of *h*-LMO devices in dark (black filled circles) and under AM 1.5G illumination. Here filled diamond squares denote data under the upward poling (Up remanent polarization P_r), and open triangles for the downward poling (Down P_r). Figure is adapted from Ref. 58.

In 2015 and 2018, H. Han et al.[58–60] reported on the growth and photoresponse of (Lu,Y)MnO$_3$ and (Lu,Tm,Yb)FeO$_3$ epitaxial films. It was found that J_{sc} and V_{oc} are switchable when reversing the ferroelectric polarization as shown in Fig. 1.5(b). It was argued that the band alignment and the corresponding SBs were altered as shown in Fig. 1.5(a) through the prepoling-induced switching of ferroelectric $\textbf{P}$ thus depolarization-field (E_d) modified Schottky barrier (SB). In addition, epitaxial strain in YbFeO$_3$[59] allows to modulate J_{sc}. In these cases, the switchable photovoltaic (PV) effect dominates over the unswitchable internal field effect mainly arising from the net built-in field developed in the ITO/*h*-Re(Mn,Fe)O3/Pt heterostructure. No reference was made to the possible BPE contribution.

In 2015, X. Huang et al.[54] using first-principles methods predicted a strong light absorption of *h*-TbMnO$_3$ in the solar spectrum range, resulting in a maximum light-to-electricity PCE of up to 33%. In 2020, L. Chen et al.[62] synthesized a series of rare earth manganates (polycrystalline ceramics) through the solid-state reactions. Among then, the

hexagonal YbMnO$_3$ has a direct bandgap near 1.35 eV. The Shockley-Queisser efficiency corresponding to a bandgap of 1.35 eV is up to about 33.7% for a single-pn-junction solar cell. No discussion was included on a possible BPE contribution.

In 2021, M. Tian et al.[61] studied polycrystalline hexagonal YMnO$_3$ thin film prepared by sol-gel method. A large J_{sc} of 3.92 mA/cm^2 under 1 sun illumination was achieved, much larger than that of other hexagonal manganites or ferrites epitaxial thin films.[58–60] The ferroelectric polarization within the grains, the high conductivity of grain boundary, and the grain boundary induced downward band bending that forms a new E_{bi}, were claimed to cooperatively promote the effective transport of carriers and PVE.

While these results undoubtedly demonstrate the presence of a prominent photocurrent in hexagonal rare earth ferroelectrics, and the direct impact of ferroelectric P direction on the photoresponse of the devices by modulating the SBs, there has never been any report that unveil the possible contribution of BPE to the observed PVE.

When comparing experiments in BiFeO$_3$ and hexagonal ferroelectrics, it is important to realize a significant geometrical difference. In rhombohedral BFO, the ferroelectric polarization aligns along [111],[44,63] Therefore, the oscillating $J_{BPE,z}$ (BPE current along z-axis) dependence on light polarization angle (φ) appears when illuminating along normal to the sample surface direction (incidence angle $\theta = 0°$). As in this configuration the angle between light E and ferroelectric P varies when changing φ, sinusoidal $J_{BPE,z}(\varphi)$ dependence can be observed. In BFO films grown with its polar axis along the sample z-axis, $J_{BPE}(\varphi)$ oscillations are detected by measuring the angular dependence of $J_{BPE,xy}$ (in-plane photocurrent) while illuminating the sample at normal incidence.[34]

In hexagonal manganites (RMO) and ferrites (RFO), the ferroelectric polar axis is oriented along the hexagonal c-axis.[51,64,65] Typically, RMO and RFO single crystals and films are c-oriented grown (polar c-axis along z-axis). It follows that when illumination at normal incidence, the light E keeps perpendicular to the ferroelectric P when rotating the light polarization for any angle. This leads to a constant dependence of $J_{BPE,z}$ on φ, and zero $J_{BPE,xy}$ due to its symmetry class (Supplementary information S4.7).[66] Consequently, $J_{BPE}(\varphi)$ oscillations should not be expected in h-RMO and h-RFO at normal incidence whether there is BPE or not. Therefore, the symmetry of RMO and RFO requires performing the angular

dependence of $J_{BPE}(\varphi)$ at oblique incidence or in-plane 90° incidence to inspect the oscillating BPE signature.

However, at oblique incidence, the contribution of Fresnel controlled transmittance variation with φ (φ dependent transmitted light intensity) follows the same light polarization angular dependence than BPE (details see Chapter 6), which challenge the experiments to distinguish BPE from Fresnel controlled CPE.[49,67] The in-plane incidence setup (illuminating normal to the lateral sample surface) could be a solution, but difficult to reach especially in thin films. Disentangling the relative contributions of BPE and Fresnel is challenging, which makes it harder to identify BPE signature in hexagonal ferroelectrics.

1.3. Engineered non-centrosymmetric structures

Apart from the non-centrosymmetric absorbing materials described in previous sections, the bulk photovoltaic effect may also be expected in artificially broken symmetry heterostructures. That is, the absorber itself (B) is centrosymmetric/nonpolar, but the asymmetric top and bottom electrodes layers form a structure (A/B/C) which lacks of center of symmetry.[68,69] Another case is that the nonpolar absorber grown on substrates with particularly engineered termination can be switched to display polar-like photoresponse because of the polar catastrophe (electronic reconstruction) at the interface of the heterojunction.[70,71]

LaFeO$_3$ (LFO) is known as a centrosymmetric Mott insulator with small bandgap (≈ 2.2 eV).[72] Structurally coherent and chemically abrupt interfaces formed between polar and nonpolar perovskite oxides provide an ideal platform for examining the purely polar catastrophe and the emergence of mobile or bound charges at the interface. It was reported by M. Nakamura et al.[70] in 2016 that nonpolar LaFeO$_3$ thin films grown on SrTiO$_3$ were converted to polar owing to the polar catastrophe, revealing the emergence of spontaneous polarization driven by the polar discontinuity in LaFeO$_3$/SrTiO$_3$ heterojunctions verified by PFM. The induced P_s evokes anomalous photovoltaic properties distinct from conventional pn junctions, such as a sign reversal of the photocurrent by changing the interfacial atomic sequence as shown in Fig. 1.6. It was considered that BPE could be the possible origin of photocurrent flowing opposite to E_{bi}. The results imply the control of the bulk polarization thus PVE in STO//LFO can be achieved by engineering the heterointerfaces. Subsequently,

K. Nakamura et al.[71] also investigated the polar-nonpolar interfaces between insulating LFO and semiconducting STO to elucidate effects of built-in potential on photocarrier dynamics, and observe that the photocurrent-voltage curves varied depending on the interface termination.
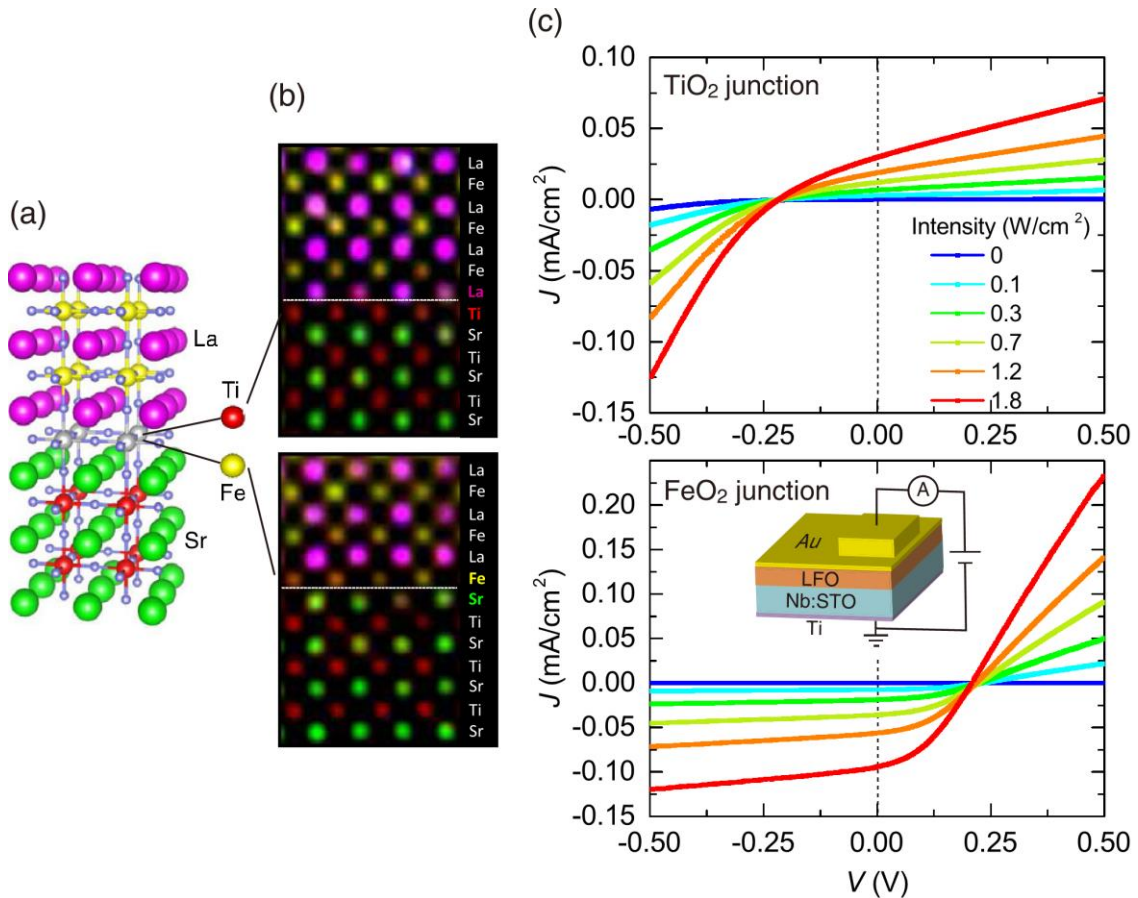
Fig. 1.6. (a) A schematic of the elemental stacking in the LFO/STO junctions. The interfacial atomic layers were controlled and were either TiO_2 or FeO_2 layers. (b) Elemental distribution mappings for a TiO_2 junction (upper panel) and a FeO_2 junction (lower panel) taken with a scanning transmission electron microscopy (STEM), where atomic resolution energy-dispersive x-ray spectroscopy images are superimposed on high-angle annular dark images. (c) Current density-Voltage *J-V* properties of the junctions upon shinning laser light (wavelength 473 nm). The positive direction of the applied voltage is defined by the schematics illustrated in the inset. Figure is taken from Ref. 70.

However, later in the same year, R. Comes et al.[73] performed an accurate XPS (high-energy-resolution X-ray photoelectron spectroscopy) study of $LaFeO_3/SrTiO_3$ interfaces and

failed to identify any built-in potential changing with the atomic termination of STO. They argued that the observed negligible effect of interface polarity on the potential gradient were not expected to produce dramatic differences in the photoresponse, in disagreement with the previously reported interface-controlled polarization in LFO.[70,71]

Nevertheless, there is a possibility to found BPE-like $J_{sc}(\varphi)$ oscillation in centrosymmetric LaFeO$_3$ with asymmetric electrodes[68,69] on non-engineered substrates or when termination engineered substrates are used[70,71]. Notice that the polar axis of this heterostructure, if any, is expected out-of-plane. Therefore, observation of $J_{BPE}(\varphi)$ oscillation are expected at oblique incidence, where $J_{BPE}(\varphi)$ is also entangled with Fresnel controlled (transmittance variation among φ) CPE dependence on φ, leading the results disputable.

In summary, CPE (J_E, J_D) and BPE coexist in ferroelectric photovoltaic materials in some cases. The drift term can be modulated or even switched by ferroelectric **P** modified Schottky barrier as shown in Fig. 1.5 (Chapter 4.1). The BPE can be switched by ferroelectric **P** reversal induced symmetry inversion (Chapter 4.3). The main differences of these two effects are: there is not photocurrent dependence on light polarization [$J_{sc}(\varphi)$] in CPE (unless a Fresnel and/or dichroism contribution appear), and the photovoltage is limited by the bandgap ($V_{oc} \leq V_g$); while an oscillatory $J_{BPE}(\varphi)$ behavior is expected in BPE, with above bandgap V_{oc}.

Bibliography

[1] V.M. Fridkin, Crystallogr. Reports **46**, 654 (2001).

[2] P. Würfel, *Physics of Solar Cells* (Wiley, 2005).

[3] V.M. Fridkin, E.P. Efremova, B.H. Karimov, V.A. Kuznezov, I.P. Kuzmina, A.N. Lobachev, V.G. Lazarev, and A.J. Rodin, Appl. Phys. **25**, 77 (1981).

[4] B. Sturman and V.M. Fridkin, *The Photovoltaic and Photorefractive Effects in Noncentrosymmetric Materials* (Gordon and Breach Science Publishers, Philadelphia, 1992).

[5] S.Y. Yang, J. Seidel, S.J. Byrnes, P. Shafer, C.-H. Yang, M.D. Rossell, P. Yu, Y.-H. Chu, J.F. Scott, J.W. Ager, L.W. Martin, and R. Ramesh, Nat. Nanotechnol. **5**, 143 (2010).

[6] V.M. Fridkin and B.N. Popov, Sov. Phys. Uspekhi **21**, 981 (1978).

[7] S. Nakashima, K. Takayama, T. Uchida, H. Fujisawa, and M. Shimizu, Jpn. J. Appl. Phys. **54**, 10NA16 (2015).

[8] S.M. Young and A.M. Rappe, Phys. Rev. Lett. **109**, 116601 (2012).

[9] S.M. Young, F. Zheng, and A.M. Rappe, Phys. Rev. Lett. **109**, 236601 (2012).

[10] A. Zenkevich, Y. Matveyev, K. Maksimova, R. Gaynutdinov, A. Tolstikhina, and V. Fridkin, Phys. Rev. B - Condens. Matter Mater. Phys. **90**, 1 (2014).

[11] B.I. Sturman, Uspekhi Fiz. Nauk **190**, 441 (2020).

[12] A.M. Burger, R. Agarwal, A. Aprelev, E. Schruba, A. Gutierrez-Perez, V.M. Fridkin, and J.E. Spanier, Sci. Adv. **5**, 1 (2019).

[13] S. Nakashima, R. Hayashimoto, H. Fujisawa, and M. Shimizu, Jpn. J. Appl. Phys. **57**, 11UF11 (2018).

[14] M. de Jong, W. Chen, H. Geerlings, M. Asta, and K.A. Persson, Sci. Data **2**, 150053 (2015).

[15] V.I. Belinicher and B.I. Sturman, Sov. Phys. Uspekhi **23**, 199 (1980).

[16] V.M. Fridkin, *Photoferroelectrics* (Springer Berlin Heidelberg, Berlin, Heidelberg, 1979).

[17] A. Bhatnagar, A. Roy Chaudhuri, Y. Heon Kim, D. Hesse, and M. Alexe, Nat. Commun. **4**, 2835 (2013).

[18] P. Lopez-Varo, L. Bertoluzzi, J. Bisquert, M. Alexe, M. Coll, J. Huang, J.A. Jimenez-Tejada, T. Kirchartz, R. Nechache, F. Rosei, and Y. Yuan, Phys. Rep. **653**, 1 (2016).

[19] J.E. Spanier, V.M. Fridkin, A.M. Rappe, A.R. Akbashev, A. Polemi, Y. Qi, Z. Gu, S.M. Young, C.J. Hawley, D. Imbrenda, G. Xiao, A.L. Bennett-Jackson, and C.L. Johnson, Nat. Photonics **10**, 611 (2016).

[20] R. Von Baltz and W. Kraut, Phys. Rev. B **23**, 5590 (1981).

[21] S.B. Astafiev, V.M. Fridkin, and V.G. Lazarev, Ferroelectrics **80**, 251 (1988).

[22] W.T.H. Koch, R. Munser, W. Ruppel, and P. Würfel, Solid State Commun. **17**, 847 (1975).

[23] S. Pal, S. Muthukrishnan, B. Sadhukhan, S. N. V., D. Murali, and P. Murugavel, J. Appl. Phys. **129**, 084106 (2021).

[24] A.M. Glass, D. von der Linde, and T.J. Negran, Appl. Phys. Lett. **25**, 233 (1974).

[25] F.S. Pilyak, A.G. Kulikov, V.M. Fridkin, Y. V. Pisarevsky, N. V. Marchenkov, A.E. Blagov, and M. V. Kovalchuk, Phys. B Condens. Matter **604**, 412706 (2021).

[26] Y. Dang and X. Tao, Matter **5**, 2659 (2022).

[27] S.R. Basu, L.W. Martin, Y.H. Chu, M. Gajek, R. Ramesh, R.C. Rai, X. Xu, and J.L. Musfeldt, Appl. Phys. Lett. **92**, 091905 (2008).

[28] D. Sando, C. Carrétéro, M.N. Grisolia, A. Barthélémy, V. Nagarajan, and M. Bibes, Adv. Opt. Mater. **6**, 1700836 (2018).

[29] T. Choi, S. Lee, Y.J. Choi, V. Kiryukhin, and S.-W. Cheong, Science (80-.). **324**, 63 (2009).

[30] R. Nechache, C. Harnagea, S. Li, L. Cardenas, W. Huang, J. Chakrabartty, and F. Rosei, Nat. Photonics **9**, 61 (2015).

[31] L. You, F. Zheng, L. Fang, Y. Zhou, L.Z. Tan, Z. Zhang, G. Ma, D. Schmidt, A. Rusydi, L. Wang, L. Chang, A.M. Rappe, and J. Wang, Sci. Adv. **4**, eaat3438 (2018).

[32] S. Nakashima, T. Uchida, D. Nakayama, H. Fujisawa, M. Kobune, and M. Shimizu, Jpn. J. Appl. Phys. **53**, 09PA16 (2014).

[33] B. Kundys, M. Viret, D. Colson, and D.O. Kundys, Nat. Mater. **9**, 803 (2010).

[34] W. Ji, K. Yao, and Y.C. Liang, Phys. Rev. B - Condens. Matter Mater. Phys. **84**, 094115 (2011).

[35] J. Seidel, D. Fu, S.-Y. Yang, E. Alarcón-Lladó, J. Wu, R. Ramesh, and J.W. Ager, Phys. Rev. Lett. **107**, 126805 (2011).

[36] H. Matsuo, Y. Kitanaka, R. Inoue, Y. Noguchi, M. Miyayama, T. Kiguchi, and T.J. Konno, Phys. Rev. B **94**, 214111 (2016).

[37] S. Nakashima, T. Uchida, K. Takayama, H. Fujisawa, and M. Shimizu, J. Korean Phys. Soc. **66**, 1389 (2015).

[38] M. Yang, A. Bhatnagar, and M. Alexe, Adv. Electron. Mater. **1**, 1500139 (2015).

[39] M.-M. Yang, A. Bhatnagar, Z.-D. Luo, and M. Alexe, Sci. Rep. **7**, 43070 (2017).

[40] M.M. Yang, Z.D. Luo, D.J. Kim, and M. Alexe, Appl. Phys. Lett. **110**, 183902 (2017).

[41] M.-M. Yang, M. Alexe, M. Yang, and M. Alexe, Adv. Mater. **30**, 1704908 (2018).

[42] S. Nakashima, T. Higuchi, A. Yasui, T. Kinoshita, M. Shimizu, and H. Fujisawa, Sci. Rep. **10**, 15108 (2020).

[43] T. Yang, J. Wei, Y. Guo, Z. Lv, Z. Xu, and Z. Cheng, ACS Appl. Mater. Interfaces **11**, 23372 (2019).

[44] D.S. Knoche, Y. Yun, N. Ramakrishnegowda, L. Mühlenbein, X. Li, and A. Bhatnagar, Sci. Rep. **9**, 13979 (2019).

[45] D.S. Knoche, M. Steimecke, Y. Yun, L. Mühlenbein, and A. Bhatnagar, Nat. Commun. **12**, 282 (2021).

[46] Y. Heo, M. Alexe, Y. Heo, and] M Alexe, Adv. Mater. **34**, 2105845 (2022).

[47] A. Abdelsamie, L. You, L. Wang, S. Li, M. Gu, and J. Wang, Phys. Rev. Appl. **17**, 024047 (2022).

[48] A. Blázquez Martínez, P. Grysan, S. Girod, S. Glinsek, and T. Granzow, Scr. Mater. **211**, 114498 (2022).

[49] M.-M. Yang, D.J. Kim, and M. Alexe, Science (80-.). **360**, 904 (2018).

[50] J. Fontcuberta, Comptes Rendus Phys. **16**, 204 (2015).

[51] B.B. Van Aken, T.T.M. Palstra, A. Filippetti, and N.A. Spaldin, Nat. Mater. **3**, 164 (2004).

[52] H. Lueken, Angew. Chemie Int. Ed. **47**, 8562 (2008).

[53] S.F. Wang, H. Yang, T. Xian, and X.Q. Liu, Catal. Commun. **12**, 625 (2011).

[54] X. Huang, T.R. Paudel, S. Dong, and E.Y. Tsymbal, Phys. Rev. B **92**, 125201 (2015).

[55] R.D. Kumar, R. Thangappan, and R. Jayavel, J. Nanosci. Nanotechnol. **19**, 2385 (2019).

[56] Q. Hong, Y. Cao, J. Xu, H. Lu, J. He, and J.-L. Sun, ACS Appl. Mater. Interfaces **6**, 20887 (2014).

[57] J. Chen, Z. Wang, H. He, J. Mao, Y. Zhang, Q. Zhang, M. Li, Y. Lu, and Y. He, Adv. Electron. Mater. **7**, 2100717 (2021).

[58] H. Han, S. Song, J.H. Lee, K.J. Kim, G.-W. Kim, T. Park, and H.M. Jang, Chem. Mater. **27**, 7425 (2015).

[59] H. Han, D. Kim, K. Chu, J. Park, S.Y. Nam, S. Heo, C.-H. Yang, and H.M. Jang, ACS Appl. Mater. Interfaces **10**, 1846 (2018).

[60] H. Han, D. Kim, S. Chae, J. Park, S.Y. Nam, M. Choi, K. Yong, H.J. Kim, J. Son, and H.M. Jang, Nanoscale **10**, 13261 (2018).

[61] M. Tian, Y. Li, G. Wang, and X. Hao, Sol. Energy Mater. Sol. Cells **224**, 111009 (2021).

[62] L. Chen, G. Zheng, G. Yao, P. Zhang, S. Dai, Y. Jiang, H. Li, B. Yu, H. Ni, and S. Wei, ACS Omega **5**, 8766 (2020).

[63] K.I. Doig, F. Aguesse, A.K. Axelsson, N.M. Alford, S. Nawaz, V.R. Palkar, S.P.P. Jones, R.D. Johnson, R.A. Synowicki, and J. Lloyd-Hughes, Phys. Rev. B **88**, 094425 (2013).

[64] Y.K. Jeong, J.-H. Lee, S.-J. Ahn, and H.M. Jang, Chem. Mater. **24**, 2426 (2012).

[65] M.-A. Oak, J.-H. Lee, H.M. Jang, J.S. Goh, H.J. Choi, and J.F. Scott, Phys. Rev. Lett. **106**, 047601 (2011).

[66] Y. Sheng, I. Fina, M. Gospodinov, A.M. Schankler, A.M. Rappe, and J. Fontcuberta, Phys. Rev. B **104**, 184116 (2021).

[67] J. Yu, Y. Chen, S. Cheng, and Y. Lai, Phys. E Low-Dimensional Syst. Nanostructures **49**, 92 (2013).

[68] H. Yamada, M. Kawasaki, Y. Ogawa, and Y. Tokura, Appl. Phys. Lett. **81**, 4793 (2002).

[69] Y. Ogawa, H. Yamada, T. Ogasawara, T. Arima, H. Okamoto, M. Kawasaki, and Y. Tokura, Phys. Rev. Lett. **90**, 217403 (2003).

[70] M. Nakamura, F. Kagawa, T. Tanigaki, H.S. Park, T. Matsuda, D. Shindo, Y. Tokura, and M. Kawasaki, Phys. Rev. Lett. **116**, 156801 (2016).

[71] K. Nakamura, H. Mashiko, K. Yoshimatsu, and A. Ohtomo, Appl. Phys. Lett. **108**, (2016).

[72] M. Imada, A. Fujimori, and Y. Tokura, Rev. Mod. Phys. **70**, 1039 (1998).

[73] R. Comes and S. Chambers, Phys. Rev. Lett. **117**, 226802 (2016).

[74] X. Hu, X. Li, G. Li, T. Ji, F. Ai, J. Wu, E. Ha, and J. Hu, Adv. Funct. Mater. **31**, 2011284 (2021).

[75] C. Ji, D. Dey, Y. Peng, X. Liu, L. Li, and J. Luo, Angew. Chemie **132**, 19095 (2020).

Chapter 2. Objectives and thesis outline

The low photovoltaic conversion efficiency of many narrow bandgap oxides is a severe drawback towards large scale application. To enhance the performance, materials like ferroelectrics appear as promising alternatives, owing to the possible presence of an internal electric field (depoling E_d) due to poor screening that may extend all over the material rather than in the narrow depletion layer as in the conventional pn junction. Therefore, it may be envisaged that more photo carriers can be extracted by the electrodes which enhances photocurrent. In addition, in ferroelectrics, the presence of BPE constitutes an additional toggle can potentially improve the photoresponse. Importantly enough, even if the mean free path of carriers in oxides (both electrons in narrow *3d* bands or holes on *2p*-bands) probably cannot compete with conventional semiconductors, the dramatic novelty is the possibility of obtaining V_{oc} exceedingly larger than the bandgap of the semiconducting ferroelectric. This opens new possibilities for applications. Self-powered devices could be one of them.[74,75] In any case, up to now, the research on BPE in narrow band ferroelectrics has been mainly limited to $BiFeO_3$ with a rather large bandgap of 2.7 eV. Ferroelectrics with narrower bandgaps would be a better option preferred for photo absorbing at all visible spectra.

Aiming to get a new understanding of the photoresponse of non-centrosymmetric materials and heterostructures comprising narrow bandgap oxides, in this PhD manuscript I have explored ferroelectric hexagonal oxides ($LuMnO_3$ and $YMnO_3$) either single crystals (SC) or thin films, as well as non-ferroelectric $LaFeO_3$. Central to the work has been my aim to reach deeper insight on the relevance of bulk photovoltaic effect (BPE) to the measured photoresponse, compared to conventional photovoltaic effect (CPE) contribution.

2.1. CPE and BPE in polar hexagonal oxides

As possible photoferroelectric candidates, hexagonal rare-earth manganites have drawn much attention owing to their narrower bandgap ($\approx$ 1.5 eV) than BFO, relatively high and switchable photocurrents. Motivated by the need of photovoltaics with high performance, this work is focused on investigating the photovoltaic properties of narrow bandgap ferroelectric *h*-$LuMnO_3$ single crystal and thin film based model system.

The objectives are a) exploring the switchable photovoltaic response and bulk photovoltaic effect in LuMnO$_3$ crystal and film based devices, b) untwining BPE contribution from light-polarization dependent photovoltaic response.

2.2. BPE and band alignment in non-centrosymmetric stacks of nonpolar oxides

To compare with the above ferroelectric devices and disentangle BPE from Fresnel controlled CPE, the light polarization dependent photoresponse of nonpolar LaFeO$_3$ thin films with narrow bandgap ($\approx$ 2.4 eV) is also studied. The LFO is probably not the optimal candidate to make comparison as the (La,Sr)MnO$_3$/LaFeO$_3$/Pt heterostructure could show some BPE, thus niobium doped SrTiO$_3$ (Nb:STO) and intrinsic Si which should only possess CPE are under preparation. Moreover, the band alignment and photovoltaic response of LFO-based devices are investigated. Inspired by this, further study of the influence of strain and strain gradients on the photoresponse of photo absorbing thin films are ongoing (details see Annex B).

2.3. Thesis outline

More precisely, this thesis is schematically organized as follows:

1. In Chapter 4.1, the ferroelectricity and PV response upon writing voltages of different sign and magnitude in LMO SC, measured at different configuration, are studied.
2. In Chapter 4.2, the light-polarization-dependent PV response and PV tensor elements in LMO SC are shown.
3. In Chapter 4.3, the BPE modulated by ferroelectric polarization back-switching in LMO SC, with possible spurious BPE due to Fresnel contribution, is investigated.
4. In Chapter 5.1, the growth and optimization of LMO thin films are presented.
5. In Chapter 5.2, the microstructure, ferroelectricity, retention, as well as PV response upon writing voltage, light intensity, and light polarization in LMO thin films, are explored.
6. In Chapter 6, methodology to distinguish BPE from Fresnel contribution, via measuring the dependence of photovoltaic response on light intensity (I_p), light polarization angle (φ) and light incidence angle (θ) of LMO SC, LMO thin film, isostructural YMnO$_3$ (YMO) film, as well as nonpolar LFO film, is introduced.

7. In Chapter 7, the band alignment determined by XPS, strain indicated from reciprocal space map (RSM) and STEM, and photovoltaic response of LFO-based heterojunctions, are combinedly studied.

Chapter 3. Materials and methods

In this chapter, an overview of the experimental techniques for sample preparation and characterization used in this thesis is given.

3.1. Materials

3.1.1. Single crystals of hexagonal LuMnO₃

The single crystals of h-LuMnO$_3$ (LMO SC) were grown by high-temperature flux technique.[1–5] The crystals are platelets of thickness around 100 μm and size around 1 mm^2, with the hexagonal c-axis along the normal of the largest faces. Crystals were chemically cleaned by 6.5 % HNO$_3$ solution to remove flux-growth residues from surfaces. For details about flux technique see Refs. 6,7. The pictures of one representative LMO crystal at pristine state and after chemical etching are shown in Fig. 3.1.
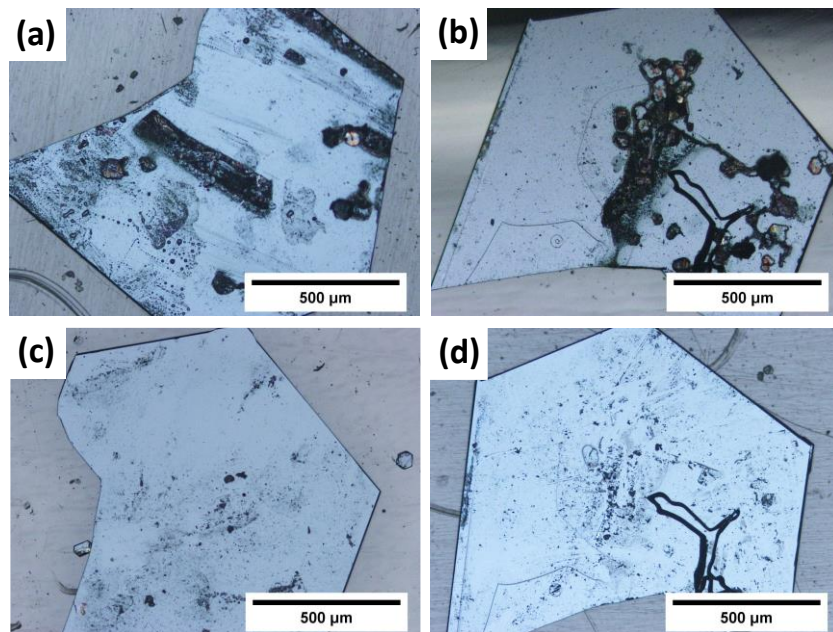
Fig. 3.1. Images of both faces of an LMO SC, (a,c) "face up" and (b,d) "reversed face down", obtained in the (a,b) pristine state and (c,d) after chemical etching by 6.5 % HNO$_3$.

3.1.2. Thin films of hexagonal (Lu,Y)MnO₃ and orthorhombic LaFeO₃

The thin films were grown by pulsed laser deposition (PLD). For details of PLD related methods see Refs. 8–10. The h-LuMnO$_3$ thin films were grown by PLD using laser fluence (F)

of 1.5 J/cm^2, a laser repetition rate (f) of 1 Hz, a dynamic oxygen pressure (PO_2) of 0.2 mbar, and a substrate temperature (T) of 825 °C. Details on the structural, morphological and transport properties on growth conditions (F, f, PO_2, T, substrates, and bottom contact) are given in Chapter 5.1. The h-YMnO$_3$ films were grown by PLD using F of 1.5 J/cm^2, f of 3 Hz, PO_2 of 0.1 mbar, and T of 825 °C. The explored growth conditions are similar with LMO and not shown in this thesis. The o-LaFeO$_3$ films were grown by PLD using F of 2 J/cm^2, f of 5 Hz, PO_2 of 0.01 mbar, and T of 700 °C. These conditions had been determined during the PhD of Dr. M. Mirjolet.[8] The films were cooled down at the end of deposition under static PO_2 of the corresponding dynamic PO_2 during the growth.

3.1.3. Target preparation of (Lu,Y)MnO$_3$

The targets used for PLD were prepared by solid-state reaction. The used chemicals (Lu$_2$O$_3$, MnO$_2$ and Y$_2$O$_3$, Table 3.1) were dried at 200 °C for 20 h to minimize the absorbed moisture. For each prepared target (LuMnO$_3$ and YMnO$_3$), oxide powders containing the elements needed were fully mixed in stoichiometric ratio by thoroughly grinding using hand-mortar for more than 2 h, then compacted into a pellet of 1 inch diameter at a load of 4 tons for 20 min. Afterwards, a thermal treatment (Fig. 3.2) in a tubular furnace in ambient air was performed.

Target	Chemicals	Purity (%)	Producer	Sintering T (°C)	Processing times
LuMnO$_3$	Lu$_2$O$_3$	99.99	Alfa Aesar	1100	3
	MnO$_2$	99.9			
YMnO$_3$	Y$_2$O$_3$	99.995		1250	4
	MnO$_2$	99.9			

Table 3.1. Description of the oxide powders used as precursors, the sintering temperature, and the number of processing times for the synthesis of PLD targets.

The quality of the target was probed by X-ray diffraction (XRD) and evaluated by the density of the pellet (reaching to around 60 % of the maximal theoretical density). If the target made after the first sintering process is not qualified (low density and/or too brittle), it is broken and ground into powder again, mixed with 5 % PVA as a binder, then re-pressed,

re-sintered to process another round. The process is repeated until obtaining an optimal quality pellet (the number of processing times is shown in Table 3.1).
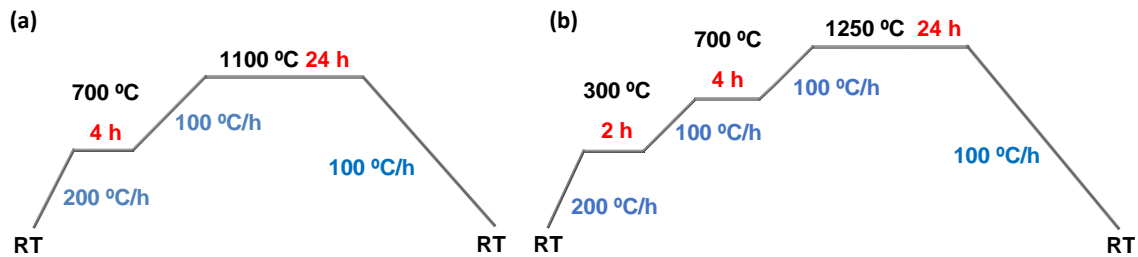
Fig. 3.2. Sintering thermal treatment process for (a) $LuMnO_3$ and (b) $YMnO_3$ targets.

Fig. 3.3 shows the XRD patterns of $LuMnO_3$ and $YMnO_3$ targets after the last sintering and the references of corresponding JCPDS (Joint Committee on Powder Diffraction Standards) cards of hexagonal phase. The pellets are of single hexagonal phase without presenting other phases, and therefore indicating the right A/B cationic ratio, with high density (around 60 % and 70 % of the maximum for LMO and YMO, respectively). The single hexagonal phase and high density indicate good homogeneity of the targets and hopefully a good reproducibility during the PLD deposition.
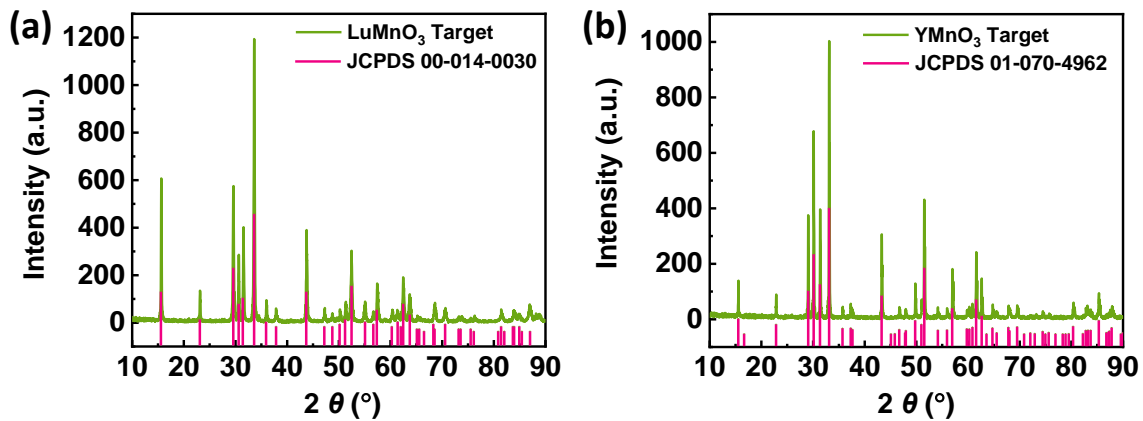
Fig. 3.3. XRD patterns of (a) $LuMnO_3$ and (b) $YMnO_3$ targets after the last sintering process (green curve). The pink spectra are taken as reference patterns from corresponding JCPDS cards.

3.1.4. Contact deposition

(a) LuMnO$_3$ single crystals

Pt electrical contacts were grown at room temperature by DC magnetron sputtering. A stencil mask (60 x 60 μm^2 square) was used to create top electrodes (TE, Pt$_{top}$) of 7 nm thick. The optical transparency of 7 nm Pt at 405 nm laser is of about 50 %.[11] The bottom side of the *h*-LMO crystals were either fully covered by a continuous Pt layer of 7 nm thick to be used as bottom electrode (BE, Pt$_{bot}$) when appropriate (Pt$_{bot}$/LMO/Pt$_{top}$), or left bare (Pt$_{top}$/LMO). The crystals were fixed on silicon substrates for better handling, using silver paste (Si//Pt/LMO/Pt) or insulating varnish (Si//LMO/Pt).

(b) (Lu,Y)MnO$_3$ thin films

Continuous Pt(111) layer, about 90 nm thick, used as bottom electrode (M$_B$ = Pt) was grown on Al$_2$O$_3$(0001) substrate ($\approx$ 5 × 5 mm^2) at 400°C using DC sputtering.[12] For electrical and photoresponse characterization, different top electrode metals (M$_T$ = Pt, Co and Ti) have been employed: (I) a layer of Pt (7 nm), (II) a layer of Co (20 nm) and (III) a layer of Ti (45 nm). Co and Ti electrodes were further covered by a protecting layer of Pt (10 nm) and Au (5 nm), respectively. Circular top electrodes were deposited ex-situ at room temperature by sputtering (Pt and Co-Pt) and electron-beam evaporation (Ti-Au) through stencil masks defining top electrodes of diameter around 20 μm. Device is denoted as: Al$_2$O$_3$//Pt/(L,Y)MO/M$_T$.

(c) LaFeO$_3$ thin films

Continuous La$_{2/3}$Sr$_{1/3}$MnO$_3$ (LSMO) layer of 27 nm as bottom electrode was deposited by PLD on LSAT(001) [(LaAlO$_3$)$_{0.3}$(Sr$_2$TaAlO$_6$)$_{0.7}$] and STO(110) substrates ($\approx$ 5 × 5 mm^2), using *F* of 2 J/cm^2 with *f* of 5 Hz, *P*O$_2$ of 0.1 mbar, and *T* of 725 °C, cooling under static *P*O$_2$ of 0.1 mbar. Details on the selected growth conditions are in Ref. 13. The semitransparent top Pt electrodes ($\approx$ 7 nm thick) were sputtered ex-situ at room temperature through a shadow mask (60 x 60 μm² square). The transparent top BLSO (Ba$_{0.95}$La$_{0.05}$SnO$_3$) electrodes ($\approx$ 40 nm thick) were deposited by PLD by using a suitable mask (200 x 200 μm^2) using the conditions of *F* = 2 J/cm^2, *f* = 5 Hz, *P*O$_2$ = 0.1 mbar, and *T* = 725°C, cooling under static *P*O$_2$ of 200 mbar.

These conditions had been determined during the PhD of Dr. M. Mirjolet.[8] Device is denoted as: LSAT,STO//LSMO/LFO/Pt,BLSO.

3.2. Measurement configuration and illumination installation

Measurement configuration refers to the electrical configuration used to characterize the single crystal or thin films. Illumination installation refers to the setup for illumination, which relevant parameters are related to the orientation of the beam used to illuminate the sample (SC/thin film absorber). In this thesis, two measurement configurations [top-bottom (t-b) and top-top (t-t)] and two illumination installations [out-of-plane (op) and in-plane (ip)] are used.
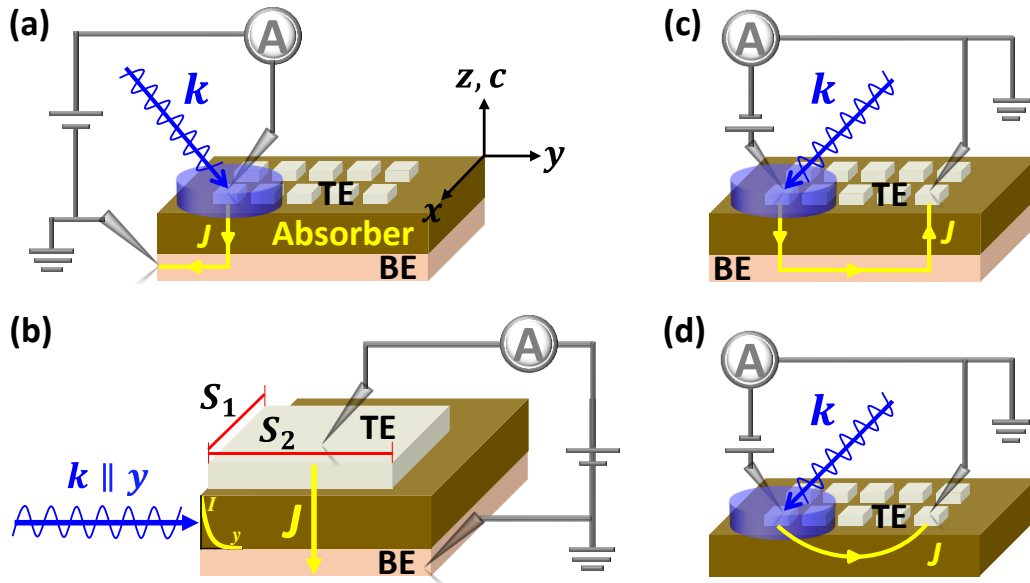
Fig. 3.4. Electrical measurements in t-b configuration (a) under op illumination and (b) ip illumination, and t-t configuration under op illumination (c) with BE and (d) without BE. The coordinate system is given by *xyz* with the *z*-axis along the polar *c*-axis. The yellow arrows denote the flow of positive carriers from *V*-biased towards the grounded electrode. The blue arrows denote the light propagation of wave vector $\boldsymbol{k}$. In (c), the electrode is placed exactly at the edge, the attenuation length of the light (intensity *I* vs. path *y*) and the contact size (S_1, S_2) are indicated.

In t-b configuration [Fig. 3.4(a)], which is used in most of the cases, the bottom and top electrodes are contacted, and out-of-plane electrical properties are measured. This configuration can be asymmetric because of different materials of the top/bottom

electrode, or discrepancy in top/bottom interfaces due to particular growth process (in-situ or ex-situ) and contact areas. The asymmetric contact can lead to asymmetric hysteresis $P(V)$ loops and current-voltage (I-V) characteristics as shown later.

In this t-b configuration, the top surface of the sample can be illuminated op [Fig. 3.4(a)], that is, at normal or oblique incidences. In this configuration, the inhomogeneous illumination should lead to a diffusion contribution to the measured photocurrent that shall be intertwined with any other contribution (f.i., drift and BPE). However, at oblique incidence, the BPE is entangled with the light polarization dependent Fresnel contribution [both can both contribute to the measured $J_{sc}(\varphi)$], as described in detail in Chapter 6. Alternatively, the sample can be illuminated ip, i.e., with light propagating along the y-axis of the sample [Fig. 3.4(b)]. Namely, at in-plane incidence ($\vartheta = 90°$), the sample lateral side is illuminated. In this case, the diffusion term is negligible in the t-b measuring configuration and the BPE oscillation $J_{sc}(\varphi)$ is preserved.[14] More importantly, the Fresnel contribution is fully prevented as the amount of light reflected and transmitted is always the same (light normal to the lateral surface) when rotating the light polarization angle (Chapter 6, Fig. 6.1). It is worth noting that the light intensity attenuates soon along y-axis (within 1 μm), thus the original Eq. [1.4] of J_{BPE} should be modified as the photocarriers generated will not increase with increasing the electrode size ($S_1 >$ spot diameter S_d, $S_2 \gg 1$ μm). For adapted details of the BPE Eqs. see Chapter 4.2 (Supplementary information S4.9). Nevertheless, it is hard to set a perfect ip illumination particularly in samples with thin film absorber.

In t-t configuration with bottom electrode [Fig. 3.4(c)], two top electrodes are contacted, forming a series connection of two identical capacitors through the bottom electrode, and the out-of-plane transport properties are measured. While in t-t configuration without bottom electrode [Fig. 3.4(d)], in-plane electrical properties are measured. In both configuration, op illumination is used, where the diffusion term becomes more prominent. Note that, in t-t configuration without bottom electrode [Fig. 3.4(d)], the drift term is canceled, and the diffusion term can be evaluated by varying the laser position from one top electrode to another (Chapter 4.1). There the in-plane J_{BPE} is also convoluted with the large diffusion current and can be hidden from it. The t-t configuration is not systematically studied in this thesis.

3.3. Ferroelectric characterization

Ferroelectric measurements were performed at room temperature by means of a TF Analyzer 2000 (AixACCT GmbH.). The $I(V)$ and $P(V)$ loops were obtained in the Dynamic Hysteresis Mode (DHM) at 1 kHz. Leakage contribution was compensated using the Dynamic Leakage Current Compensation (DLCC) standard procedure.[15,16] T-b configuration is applied in most of the cases. We grounded bottom contacts and applied a bias ($V^{+/-}$) to top contacts; accordingly, for V^+(> 0), $P^{\downarrow}$ is pointing downwards from top electrode (TE) towards bottom electrode (BE), and the upward $P^{\uparrow}$ is obtained for V^-(< 0).

3.4. Photoresponse and polarization-dependent photoresponse

3.4.1. Ferroelectric polarization dependent photoresponse
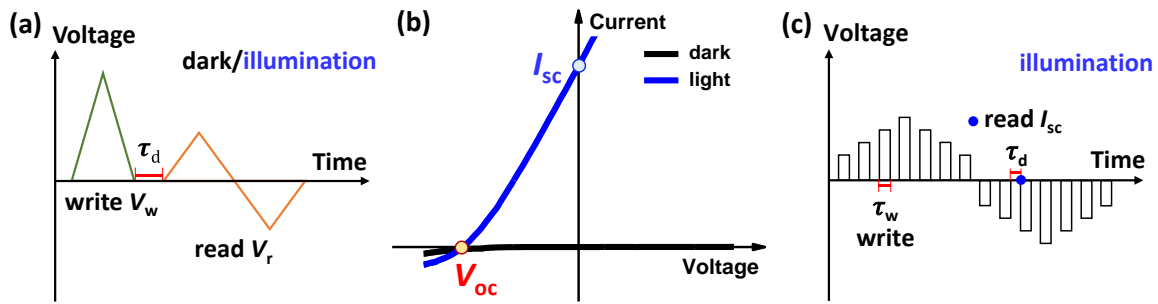
Fig. 3.5. (a) Writing (green) and reading (orange) voltage pulses of the *I-V* curves. (b) An example of the measured *I-V* curves in dark and under illumination, from which I_{sc} and V_{oc} can be extracted as indicated. (c) Pulse trains for the dependence of the I_{sc} on pre-polarization writing voltage V_w.

Current-Voltage (*I-V*) curves were recorded by a Keithley 6517B Electrometer, using bipolar triangular excitation signals [Fig. 3.5(a)] from $+V_{r,max}$ to $-V_{r,max}$ (V_{max} < coercive voltage V_c of the ferroelectric material) with ≈ 0.5 s integration time for each point. To investigate the possible role of ferroelectric $\boldsymbol{P}$ on the observed photovoltaic response, we pre-polarized the sample with a unipolar field (V_w) with $V_{w,max}$ larger than V_c, to set the polarization state. After a delay time (τ_d ≈ 5 s), the *I-V* curves at each poling state are recorded. The *I-V* (*J-V*) curves are plotted [Fig. 3.5(b)] taking the average current at each reading voltage [Fig. 3.5(a)]. To minimize the effect of $\boldsymbol{P}$ back-switching, I_{sc} has also been collected at zero bias directly in a continuous manner and using a shorter delay time (τ_d ≈ 1 s) after the sample pre-poling with V_w of different amplitudes and polarities [Fig. 3.5(c)].

When performed in top-bottom configuration, the bias $V^{+/-}$ was applied to the top electrode and the bottom electrode was grounded, where positive current corresponds to positive charges flowing from TE towards BE.

3.4.2. Light polarization dependent photoresponse
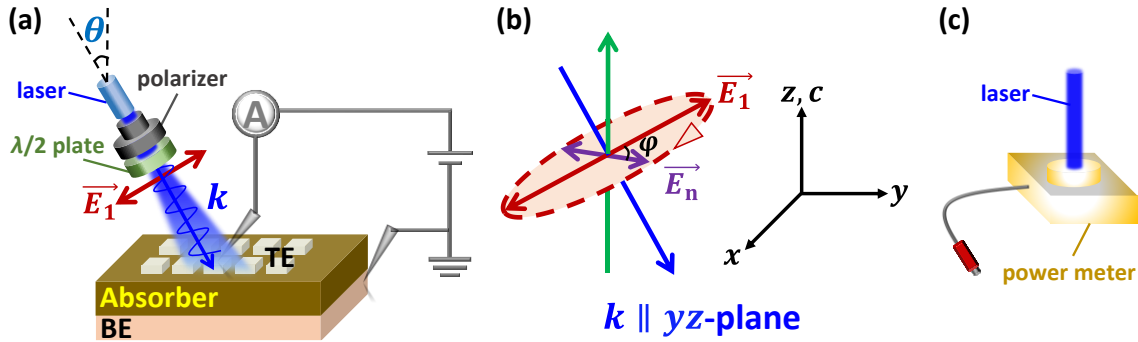
Fig. 3.6. (a) Photoresponse measurements under illumination of linearly polarized light at oblique incidence angle. (b) Definition of the light linearly polarized angle φ (angle between E_1 and E_n), where the dashed ellipse indicates the rotation plane of the polarization vector, and the coordinate system is given by *-xyz*. The blue arrows denote light propagation of wave vector k. Red arrows denote the light polarization at $\varphi = 0°$ (E_1, parallel with the incident plane). Purple arrow represents the light polarization at intermediate angle φ (E_n). (c) The schematic of the power meter (thermal sensor).

The photovoltaic response dependence on light polarization angle (φ) was performed while rotating φ using the optical setup in Fig. 3.6(a). A polarizer (Glan-Taylor GT5) was mounted after the laser to ensure a linearly polarized light and set the initial polarization direction of the light (E_1). That is, at $\varphi = 0°$, the initial polarization vector E_1 is in the incident plane (*p*-polarized light). A half wave ($\lambda/2$) plate (AHWP05M-600) driven by a Rotation Stage (KPRM1E/M) was used to rotate the polarization direction of the light (E_n) by an angle φ [Fig. 3.6(b)]. The laser, polarizer and $\lambda/2$ plate were installed in one aluminum post (TRA20/M) with their fast axes in alignment and parallel to the incident light polarization. This set up allows the incidence angle of light (wave vector k, with respect to the normal to the sample plane) varied between $\vartheta \approx 0°$ (normal incidence) to $\vartheta \approx 90°$ (in-plane incidence). The laser power was calibrated by a power meter (PM16-401 thermal sensor, Thorlabs), as shown in Fig. 3.6(c). The optical elements are from Thorlabs.

The short circuit current density (J_{sc}) dependence on light polarization angle (φ) was collected by a Keithley 6517B Electrometer at zero voltage source, and the open circuit voltage (V_{oc}) dependence on φ was collected by a digital multimeter (Mastech. M92A) or Keithley 2400 Sourcemeter, using the optical setup in Fig. 3.6(a) and the electrical arrangement in Fig. 3.7. This φ dependence was recorded in a continuous manner, not by values extracted from the *I-V* curves at each φ angle, to minimize artifacts. The sample, 6517B electrometer, and multimeter (or 2400 sourcemeter, or TF Analyzer) were connected through a commute device with the same ground. Therefore, different electrical properties can be measured through switching the connections, with one electrode/needle contact state and one illumination state (unless the optical setup is changed).
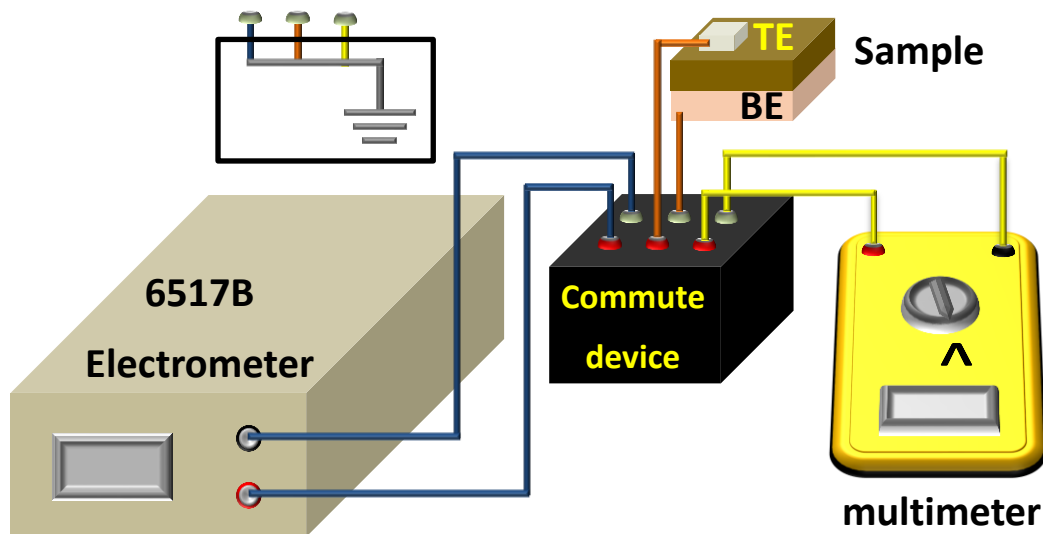
Fig. 3.7. A sketch of the electrical measurement arrangement. The sample, 6517B electrometer, and digital multimeter (or 2400 sourcemeter, or TF Analyzer) were connected through a commute device. The green connectors are connected to the same ground inside the commute device, as shown by the top left profile.

The V_{oc} measured with digital multimeter is smaller than the value obtained from the *I-V* curves [Fig. 3.5(b)] measured by 6517B Electrometer, related to the smaller system resistance of the multimeter. As verified by the 2400 sourcemeter, when V_{oc} is measured by the multimeter, the current flowing in the circuit is around 15 nA, which indicates an imperfect open circuit. Thus, the obtained V_{oc} is smaller than the real value due to the slight shift towards the short circuit. The V_{oc} measured by the 2400 sourcemeter is very close to

the value obtained by 6517B Electrometer. Nevertheless, the amplitude of $V_{oc}(\varphi)$ measured with the three equipment are very similar, as long as the measured V_{oc} is bigger than the amplitude of $V_{oc}(\varphi)$. Therefore, in this thesis, the V_{oc} measured by digital multimeter or 2400 sourcemeter was corrected in agreement with the value obtained by 6517B Electrometer (*I-V* curves).

3.4.3. Laser source and power calibration

Data were recorded in dark or under illumination mainly using a blue-violet laser source (M-14A405-20-G, MTO-laser) of 405 nm, with photon energy (3.06 eV) larger than the absorber bandgap [E_g(LMO, YMO) ≈ 1.5 eV; E_g(LFO) ≈ 2.2 eV). The spot diameter (S_d ≈ 280 µm) is larger than the electrode length (≈ 60 or 20 µm) and the inter-electrode distance (≈ 20 or 10 µm), allowing uniform top illumination of electrodes. The photoresponse dependence on wavelength (λ) was recorded by using a STEC multiwavelength system (Blue Sky Research), with a parallel laser beam of λ = 405, 450, 520, and 638 nm (S_d ≈ 1.7 mm). The lasers were fed by a CPX400SA DC power source (AimTTi Co.). By adjusting the magnitude of this voltage or current source, the laser power can be modulated.

The laser power was detected by a power meter [Fig 3.6(c)], with the sensor area (diameter of 3.5 mm) much larger than the laser beam (diameter of 280 µm or 1.7 mm). The laser area was determined by the picture taken with the camera (CMEX-3, DC.3000c, Euromex) above a microscope (Nexius Zoom, Euromex) [Fig. 3.8(a)]. Note that laser area accuracy can be affected by its Gaussian intensity distribution. The power density (I_p) ranging from 0.6 - 84 W/cm^2 is indicated in each case.

3.5. Precautions with photoresponse data collection and analysis

3.5.1. Beam adjusting before measuring

The measured photoresponse is very sensitive to the illumination state, i.e., laser source (wavelength, power), laser focus (beam size) and laser position. When the laser is fixed at a given λ and power, one should first pay attention to the laser focus every time before measuring, to make sure to get the same beam size and I_p especially when changing the whole optical setup (e.g., changing incidence angle ϑ). Besides, as mentioned, the photoresponse is very sensitive to the laser position and whether the laser spot is exactly

illuminated on the measured contact. For example, in Fig. 3.8(a), the laser in both cases is identical, well focused and in a similar position, but how the light shines above the measured contact/needle are different (light 1, 2). This leads to different results as shown in Fig. 3.8(b), where the shinier spot (light 2) results in much larger photocurrent. Therefore, before starting the formal test, photocurrent monitoring (I_{sc} vs. time) while adjusting the laser focus/position is used to get the maximal I_{sc}. This ensures the optimal illumination state and makes the results of different measurements comparable.
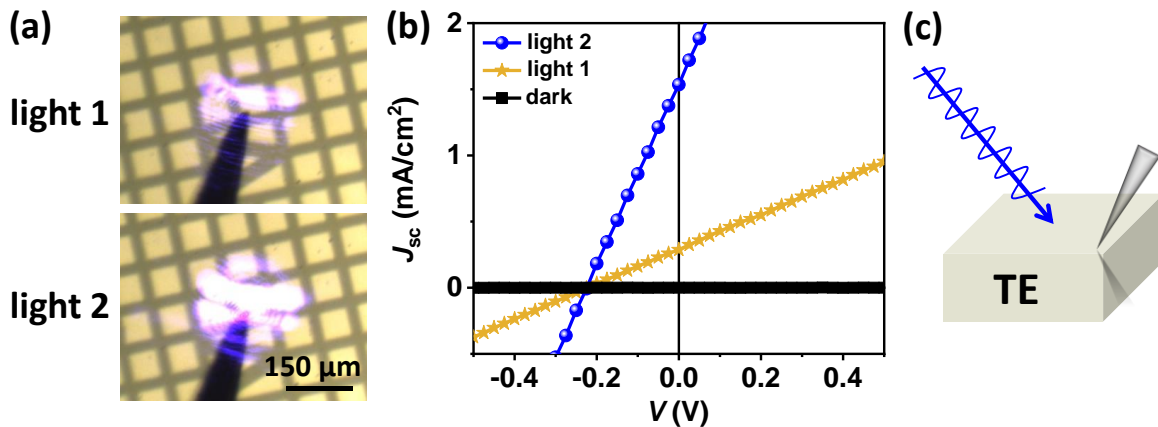
Fig. 3.8. (a) An example of the measured contact under illumination with "light 1" and "light 2" representing different but similar illumination state. (b) The corresponding *J-V* curves in dark and under illumination state "1" and "2". The data of "light 2" should be selected as effective and comparable results. (c) A sketch of the illumination and needle arrangement. The needle is contacted to the top electrode at the corner to minimize the effect of the needle shadow.

In addition, to minimize the possible influence of the needle shadow, the tungsten needle is always contacted at the edge/corner of the top electrode, with light illuminating from the opposite direction [Fig. 3.8(c)]. In fact, as identified by the *I-V* curves (not shown), the needle (tip of 5 μm radius) shadow has negligible influence on the measured photocurrent as long as the needle is well contacted with the intact top electrode (not scratched).

3.5.2. Normalization of light intensity

The light polarization dependent photoresponse is measured by rotating the λ/2 plate, which will not change the light intensity as identified by the power meter but can change

very slightly the laser position thus the illumination is deviated from the initial optimal state, as can be seen under the microscope. This is due to the inevitable artifacts/misalignments of optical setups. It causes a background photocurrent variation superimposed on the intrinsic sinusoidal $J_{sc}(\varphi)$, which affects more [Fig. 3.9(a)] when using the smaller electrode (20 μm) /laser (280 μm) and is imperceptible [Fig. 3.9(c)] when using the bigger laser (1.7 mm).
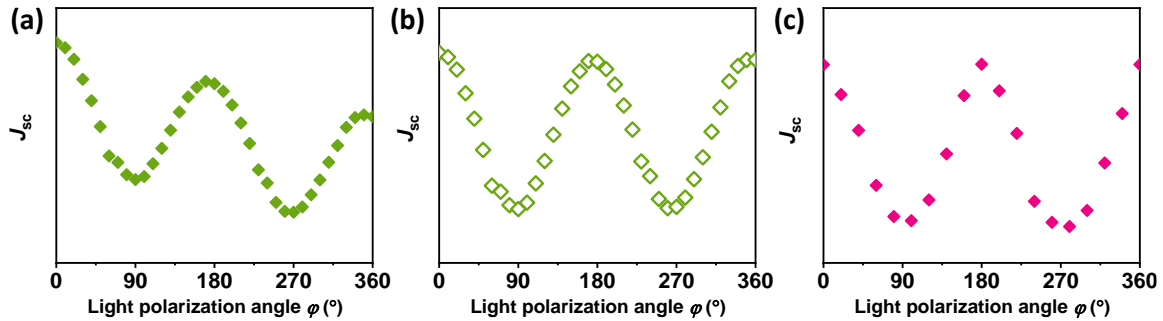
Fig. 3.9. An example of the (a) raw data and (b) normalized (slope subtracted) data of $J_{sc}(\varphi)$ using the 280 μm laser. (c) An example of the raw data of $J_{sc}(\varphi)$ using the 1.7 mm parallel laser.

In the range of φ = 0 - 360°, this background current decreases linearly with φ as the laser is gradually deviating from the optimal position, as shown for instance in Fig. 3.9(a). This is because the plane of the $\lambda/2$ plate surface is not perfectly aligned with the oscillating plane of laser polarization, resulting in a laser beam deviation while rotating the $\lambda/2$ plate. The J_{sc} values at any two points shifted by 180° should have been the same as the polarization plane are identical at this two φ angles, if there were no additional artifacts. Hence, the "standard" oscillation in Fig. 3.9(b) can be obtained by subtracting the background slope (evaluated by data points at φ = 90° and 270°) of the raw data shown in Fig. 3.9(a). In this thesis, plots of $J_{sc}(\varphi)$ and $V_{oc}(\varphi)$ measured using the 280 μm laser were all normalized using this slope subtraction.

However, when changing the incidence angle ϑ, the optical installation must be re-adjusted and the distance between the laser source and sample changes. The light fluence and the optimal illumination state in different experimental setups may vary even with careful refocusing. Thus, after solving the issue above caused by $\lambda/2$ plate rotation, there remains a problem of the distinct "effective I_p" reaching to the sample in each optical setup. This influence introduces additional artifacts to the background value of J_{sc}, which makes it

difficult to compare the values at different incidence ϑ and to distinguish BPE from Fresnel as will show in detail in Chapter 6 (Supplementary information 6.2).

Bibliography

[1] F. Yen, C. dela Cruz, B. Lorenz, E. Galstyan, Y.Y. Sun, M. Gospodinov, and C.W. Chu, J. Mater. Res. **22**, 2163 (2007).

[2] H.L. Yakel Jnr, W.C. Koehler, E.F. Bertaut, and E.F. Forrat, Acta Crystallogr. **16**, 957 (1963).

[3] C. Fan, Z.Y. Zhao, J.D. Song, J.C. Wu, F.B. Zhang, and X.F. Sun, J. Cryst. Growth **388**, 54 (2014).

[4] A.P. Litvinchuk, M.N. Iliev, V.N. Popov, and M.M. Gospodinov, J. Phys. Condens. Matter **16**, 809 (2004).

[5] T. Yu, P. Gao, T. Wu, T.A. Tyson, and R. Lalancette, Appl. Phys. Lett. **102**, 172901 (2013).

[6] K. Byrappa and T. Ohachi, 590 (2003).

[7] P.C. Canfield and Z. Fisk, Philos. Mag. B **65**, 1117 (1992).

[8] M. Mirjolet, Transparent Conducting Oxides Based on Early Transition Metals : - Dipòsit Digital de Documents de La UAB, n.d.

[9] M. Ohring, Mater. Sci. Thin Film. 357 (2002).

[10] D.B. Chrisey and G.K. Hubler, *Pulsed Laser Deposition of Thin Films* (John Wiley & Sons, New York, 1994).

[11] M.N. Polyanskiy, Refractive index database. https://refractiveindex.info. (accessed on Aug. 29, 2022).

[12] R. Bachelet, R. Muralidharan, F. Rigato, N. Dix, X. Martí, J. Santiso, F. Sánchez, and J. Fontcuberta, Appl. Phys. Lett. **95**, 181907 (2009).

[13] D. Pesquera, Strain and Interface-Induced Charge, Orbital and Spin Orderings in Transition-Metal Oxide Perovskites, Universitat Autònoma de Barcelona, 2014.

[14] Y. Sheng, I. Fina, M. Gospodinov, A.M. Schankler, A.M. Rappe, and J. Fontcuberta, Phys. Rev. B **104**, 184116 (2021).

[15] I. Fina, L. Fàbrega, E. Langenberg, X. Martí, F. Sánchez, M. Varela, and J. Fontcuberta, J. Appl. Phys. **109**, 074105 (2011).

[16] R. Meyer, R. Waser, K. Prume, T. Schmitz, and S. Tiedke, Appl. Phys. Lett. **86**, 1 (2005).

Chapter 4. Photovoltaic response of *h*-LuMnO₃ single crystals

As a model system, the photoresponse *h*-LuMnO₃ single crystals (LMO SC) have been explored first, which show less complex microstructure and better insulating properties owing to their lager thickness than films. Therefore, in this thesis, systematic study on LMO SC serves as a guide to better design experiments on thin films.

4.1. Ferroelectric polarization switchable photovoltaic response

In this section, we present ferroelectric and photocurrent characterization of Pt/LMO SC/Pt structures. Switchable photocurrent modulated up to 25 % by the direction of the ferroelectric polarization P is observed. The non-switchable photocurrent is attributed to arising from diffusion J_D and unswitchable drift J_{un-E}. The role of possible BPE J_{BPE} currents contribution is also discussed. The large optical absorption and accompanying optical dichroism in hexagonal manganites challenging to disentangle a genuine bulk photovoltaic effect is also observed to be relevant.

The work presented in this section was published in Appl. Phys. Lett. 118, 232902 (2021); https://doi.org/10.1063/5.0053379.

4.1.1. Introduction

The discovery of a substantial short circuit photocurrent density (J_{sc}) in ferroelectric BiFeO₃ (BFO)[1,2] was a hallmark that stimulated revisiting the photoresponse of narrow gap polar materials. In conventional semiconductor photovoltaic devices, electron-hole pairs created by photon absorption, are extracted by an internal electric field (E_{in}) present at device interfaces and/or by diffusion, and the resulting open circuit photovoltage (V_{oc}) is limited by the energy gap.[3] In recent years, attention is driven towards the so-called bulk photovoltaic effect (BPE), occurring in non-centrosymmetric materials, whose distinctive features are: the J_{sc} flows in absence of any E_{in}, the V_{oc} is not bounded by E_g and the J_{sc} is sensitive to the polarization direction of the incoming light.[4] Indeed, although in BFO, V_{oc} was observed to be larger than the bandgap and firstly attributed to domain walls,[5] subsequent experiments and the angular dependence of J_{sc} allowed to assess its BPE origin[6] with PV tensor elements and Glass coefficients that turned out to be in reasonable

agreement with first principle calculations,[7] although the detailed microscopic mechanisms of the observed photocurrent remain unsolved.[8,9]

On general grounds, other than J_{BPE}, the photocurrent contains drift (J_E) and diffusion (J_D) current contributions, being the first driven by the presence of E_{in} and the second by charge gradients whose origin is either inhomogeneous carrier generation and/or thermal gradients [see P. Würfel's book for details].[10] In ferroelectric capacitor structures, the Schottky barrier (SB) and the depoling field (E_d) contribute to E_{in}, giving rise to asymmetric conducting diode-like response, and permitting E_{in} to be modulated, and even reversed, upon ferroelectric polarization switching. Indeed, polarization-switchable diode-like response and photocurrent was reported in BiFeO₃ single crystals[1] and thin films[11] which were also consistent with earlier reports using wider bandgap ferroelectrics (BaTiO₃, Pb(Zr,Ti)O₃).[12,13] In strongly absorbing materials, gradients of photocarriers are unavoidable and, in presence of dichroism, J_D may display a dependence on the light polarization, entangled with BPE. In any event, the presence of non-switchable fields, either associate to the SB or to the presence of an imprint fields (E_{im}) or the occurrence of diffusion, may force J_{sc} to flow in a given direction thus allowing only an asymmetric modulation of the photocurrent upon ferroelectric switching.[12–14]

Nowadays attention focus on ferroelectrics having narrower bandgaps, such as the hexagonal ReMnO₃ and ReFeO₃ (L = Lu, Y, Tb, etc.)[15] having $E_g < 2$ eV.[16–20] Experiments in thin films of (Y,Lu)MnO₃ and (Tb,Yb)FeO₃ indicated that J_{sc} was switchable by the polarization direction. On the light of the discussion above, it appears that the response of the hexagonal films was dictated by the modulation of interfacial SB by the polarization direction, and any bulk photovoltaic contribution was not unveiled.

Herein, we aim at elucidating the photoresponse of *h*-LuMnO₃ single crystals, sandwiched between Pt electrodes (Pt/LuMnO₃/Pt) with focus on disentangling the different contributions to the measured photocurrent in the visible range. It is found that the J_{sc} is regulated by the polarization direction as a result of the modulation of the SB, mimicking the polarization loop $P(E)$. In addition, a non-switchable J_{sc} contribution exists. It is observed that the non-switchable J_{sc} response contains a large diffusion term which originates from the strong light attenuation within the LuMnO₃ crystal and the concomitant

charge gradients. Therefore, the optical dichroism of *h*-LuMnO₃ will entangle any bulk photovoltaic response compromising unravelling their relative weight. We shall argue that epitaxial thin films may constitute an appropriate alternative.

4.1.2. Samples and experiments

Data on several crystals are reported, named Cry-n (n = 1, 2, 3 and 4), all displaying similar features. The crystals with bottom Pt_{bot} (Cry-1, Cry-4), were fixed on silicon substrates using silver paste, while the crystals without Pt_{bot} (Cry-2, Cry-3) were fixed on a Si substrate using an insulating varnish.

The electrical measurement in t-b configuration is sketched in Fig. 4.1(a), where the excitation $V^{+/-}$ (non-grounded, NG) was applied to the Pt_{top}, while Pt_{bot} was grounded (G). Data were recorded in dark or under illumination using a blue-violet laser source (λ = 405 nm) of 3.06 eV photon energy, and power density $I_p \approx$ 32 W/cm².

4.1.3. Ferroelectricity and photoresponse
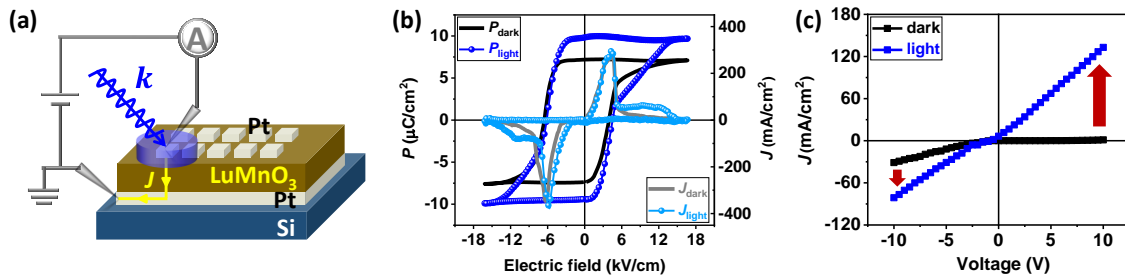
Fig. 4.1. (a) Electrical measurements in t-b configuration. The yellow arrow denotes the flow of positive carriers from *V*-biased towards the grounded electrode. The blue arrow denotes the light propagation of wave vector **k**. (b) The *J*(*E*) (right axis) and *P*(*E*) (left axis) loops of a Pt/LMO/Pt sample (Cry-1), recorded in dark and under illumination (45° incidence), at 1 kHz using DHM with DLCC. (c) The *J*-*V* characteristic of an unpolarized Pt/LMO/Pt sample (Cry-1) in dark and under illumination (45° incidence). The red arrows emphasize the photoresponse.

Fig. 4.1(b) shows the *J*(*E*) loops of the LMO sample measured in t-b configuration and the corresponding *P*(*E*) loops collected at 1 kHz in Cry-1. In *J*(*E*) loops the ferroelectric switching current peaks are visible as a result from the ferroelectric nature of the sample. Data in Fig. 4.1(b) indicates that, in dark, the *h*-LMO crystal has a remanent polarization P_r

$\approx 7.3\ \mu C/cm^2$, which is somewhat larger than in LMO films ($\approx 5\ \mu C/cm^2$)[18] and other *h*-RMO single crystals (*h*-YMnO$_3$ $\approx 4.5\ \mu C/cm^2$,[21] *h*-InMnO$_3$ $\approx 4.4\ \mu C/cm^2$,[22] *h*-HoMnO$_3$ $\approx 5.6\ \mu C/cm^2$).[23] The coercive field E_c is ≈ 5.3 kV/cm and displays a shift along the negative voltage direction, reflecting the $E_{im} \approx 1.3$ kV/cm pointing downwards. Although the top and bottom electrodes are both Pt, the presence of E_{im} is commonly observed when using *ex*-situ deposited electrodes. E_{im} is absent [Supplementary information S4.1, Fig. S4.1(a)] in the measurements collected using the top-top configuration in Fig. 3.3(c).

Fig. 4.1(b) also shows the *J*(*E*) and *P*(*E*) loops collected under illumination. Under illumination, the sample is more conductive and the *J*(*E*) loop become leakier compromising the accuracy of the corresponding *P*(*E*). However, the ferroelectric E_c and E_{im} and the height of the ferroelectric switching current peak remain almost constant, indicating that other ferroelectric properties, for instance due to heating effects, are not significantly modified. As shown in Fig. 4.1(b), E_{im} points downwards in Cry-1. It is worth noticing that the direction of E_{im} differs among the crystals, suggesting that the surface state of the crystals also differs after its chemical etching. For instance, in Cry-4, E_{im} is observed to point upwards [Supplementary information S4.1, Fig. S4.1(b)]. The absence of hysteresis in the leakage contribution of the measured *J*(*E*) loops disregard important contribution of ionic motion (f.i. oxygen) during the characterization.

Current-Voltage measurements were recorded using bipolar triangular excitation signals from +10 V to −10 V with ≈ 0.5 s integration time (the measurements takes ≈ 100 s, equivalent to 0.01 Hz, for 200 points). In Fig. 4.1(c) we show Current density-Voltage *J-V* data collected in the *V* = ± 10 V voltage range in Cry-1, in dark and under illumination. The maximum electric field used in the *J-V* excursion (E_{max} = 1 kV/cm at *V* = 10 V) is lower than E_c, which guarantees that the polarization is not switched by the applied voltage. It can be appreciated in Fig. 4.1(c), that in dark, there is substantial rectifying diode-like effect, blocking for *V* > 0 applied to the top Pt electrode (reverse bias). It indicates the presence of a SB at the top LMO/Pt$_{top}$ interface. Due to its larger area, the bottom Pt$_{bot}$/LMO interface has a lower resistance, and the *J-V* is governed by the more resistive LMO/Pt$_{top}$ interface. The rectification at *V* > 0 observed in dark, implies the existence of E_{in} pointing downwards either at the Pt/LMO interface (E_{bi}) and/or within LMO, most likely the E_d and a possible contribution from E_{im}, that we summarize as $E_{in} = E_{bi} + E_d + E_{im}$. In Cry-1, E_{im} and E_{in} are both

pointing downwards. In contrast, in Cry-4, E_{im} is upwards [Supplementary information Fig. S4.1(b)], while its rectifying behavior still indicates that E_{in} is downwards [Supplementary information S4.1, Fig. S4.1(c)]. This observation suggests that E_{im} does not dominate the rectifying character of the LMO/Pt$_{top}$ junction. It will be shown below (Fig. 4.2) that E_{in} is slightly modulated by E_d reflecting its contribution to the SB height.[24,25]

Under illumination [Fig. 4.1(c)], the strong rectifying behavior of the LMO/Pt$_{top}$ interface is suppressed and a large current flows in reverse bias. The photoresponse of Pt/LMO/Pt is governed by the photoresponse of the exposed LMO/Pt$_{top}$ interface. Indeed, light is fast attenuated and does not reach the bottom interface. The absorption coefficient of h-LMO at 405 nm is of about $\alpha \approx 5$ μm^{-1},[26] thus the absorption is about 99 % in 1 μm.

4.1.4. Switchable photovoltaic response

Searching for fingerprints of photovoltaic response and ferroelectric polarization effects, we focus on the low field region of the *J-V* data of Fig. 4.1(c), zoomed in Fig. 4.2(a). It can be appreciated that under illumination (blue lines and symbols), a photovoltaic response is apparent with J_{sc} (≈ 6.6 mA/cm^2) and V_{oc} (≈ -0.72 V). At $V = 0$ the photocurrent increases significantly under illumination ($\Delta J = \frac{J_{sc} - J_{dark,V=0}}{J_{dark,V=0}} \approx 1.1 \times 10^4$), and the responsivity ($R = \frac{J_{sc} - J_{dark,V=0}}{I_p} \approx 0.21$ mA/W) is comparable to that used in self-powered photodetectors.[27] To unravel a possible role of the E_d on the observed photovoltaic response, we pre-polarized the sample with a unipolar field (E_w) ($|E_{w,max}| = 15$ kV/cm higher than E_c) to set the polarization state. After a delay time $\tau_d \approx 5$ s, we recorded the *J-V* in each poling state. It can be seen in Fig. 4.2(a) that, whereas data recorded in dark (black line and symbols) does not show any perceptible dependence on the direction of pre-polarizing voltage, this is not the case under illumination. Indeed, it can be appreciated in Fig. 4.2(a) that for $E_w > 0$ ($P^{\downarrow}$), J_{sc} is larger than for $E_w < 0$ ($P^{\uparrow}$).
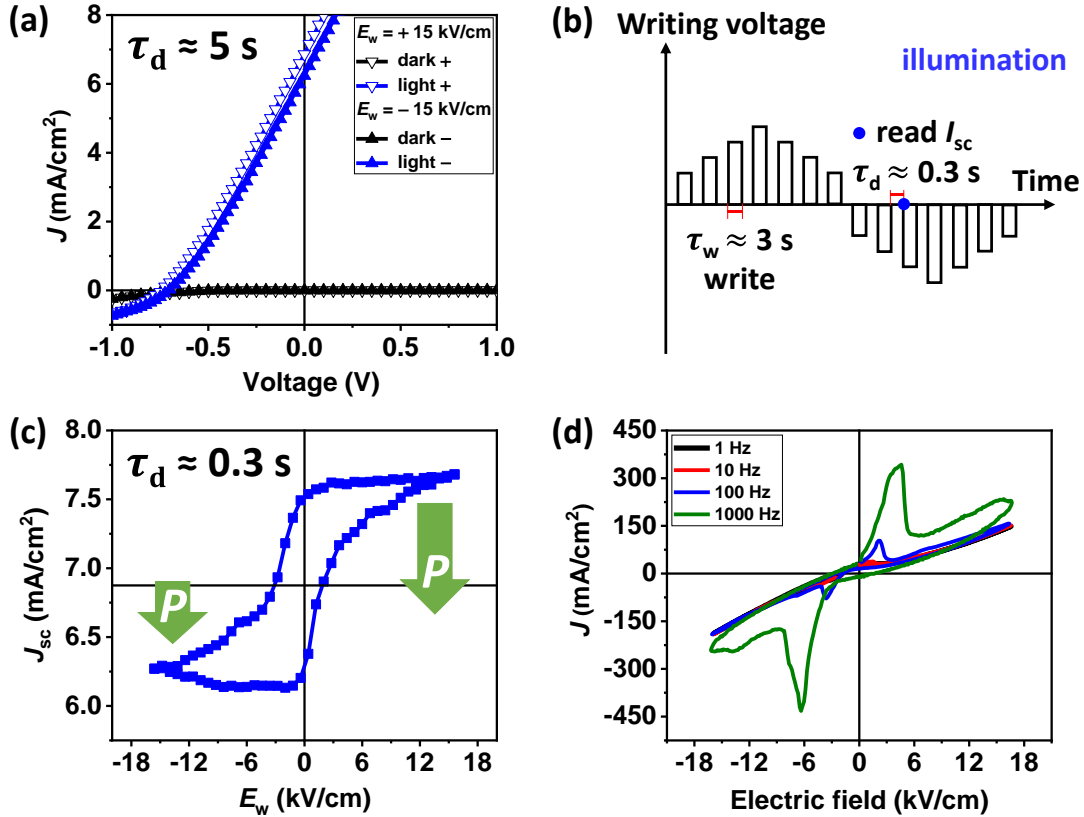
Fig. 4.2. (a) Enlarged view of the *J-V* curves of a polarized Pt/LMO/Pt sample (Cry-1), recorded in dark and under illumination (45° incidence); "+" and "−" signify the application of positive and negative pre-polarizing voltage. (b) Measuring protocol of the dependence of the short circuit J_{sc} on pre-polarization writing V_w amplitude; (c) Corresponding J_{sc}-E_w characteristic (Cry-1, normal 0° incidence). (d) The $J(E)$ hysteresis loops (Cry-1) recorded at various frequency (without DLCC).

The modulation of J_{sc} [Fig. 4.2(a)] is rather modest ($\frac{J_{sc}^+ - J_{sc}^-}{J_{sc}} \approx 10\,\%$, where J_{sc}^+ and J_{sc}^- are the short circuit current density after applying positive and negative pre-polarizing voltage). This is partially due to the back-switching of $P^\uparrow$ to $P^\downarrow$ occurring in a time scale shorter than 5 s [time delay τ_d of measurements in Fig. 4.2(a)], implying that actual measurements were done almost in one $P^\downarrow$ state.[13] Back-switching was already anticipated by the presence of downward imprint in this sample (Cry-1) and further confirmed by data in Supplementary information S4.2. The polarization-switchable (J_{sw}) and the unswitchable (J_{uns}) contributions to J_{sc} (V_{oc}) can be disentangled using:[14]

$$|J_{sw}| = \frac{|J_{sc}^+ - J_{sc}^-|}{2}; \quad |J_{uns}| = \frac{|J_{sc}^+ + J_{sc}^-|}{2} \qquad [4.1]$$

Open circuit voltages can be treated in the same way. Herein, $|J_{sw}| \approx 0.31$ mA/cm^2, $|J_{uns}| \approx$ 6.5 mA/cm^2; $|V_{sw}| \approx 0.017$ V, $|V_{un}| \approx 0.72$ V. These data show that polarization switching can only modulate J_{sc} and V_{oc} by some 10 % and 5 % ($\left|\frac{V_{oc}^+ - V_{oc}^-}{V_{oc}^-}\right|$) respectively, due to presence of the mentioned polarization back-switching process.

To minimize back-switching effects, we have measured out-of-plane J_{sc} in a continuous manner by using a shorter delay time ($\tau_d \approx 0.3$ s), after applying polarization-writing voltages (V_w) of different amplitudes and polarities. As schematized in Fig. 4.2(b), , J_{sc} is measured at zero bias directly after the application of each V_w pulse, allowing to trace the whole $P(E)$ loop.[12,13] The recorded J_{sc}-E_w curve [Fig. 4.2(c)] demonstrates that J_{sc} can be now modulated by the ferroelectric polarization by about ≈ 25 %. The switchable fraction increased to $|J_{sw}|$ ≈ 0.77 mA/cm^2, with $|J_{uns}| \approx 6.9$ mA/cm^2. The E_c (≈ 2.5 kV/cm) in Fig. 4.2(c), is somewhat smaller than in Fig. 4.1(b) due to the different measuring frequencies, which is lower (≈ 2 mHz) in the J_{sc}-E_w experiments of Fig. 4.2(c) than in Fig. 4.1(b) (1 kHz). We have assessed that the switching peaks of $J(E)$ loops and E_c, shift to higher electric fields when increasing frequency [Fig. 4.2(d)], as commonly observed in ferroelectrics.[28,29]

Finally, three features in J_{sc}-E_w loop [Fig. 4.2(c)] are worth noticing. First, J_{sc}-E_w is shifted towards $V < 0$, implying the presence of an internal electric field, such as imprint field, pointing downwards in agreement with the $P(E)$ loops [Fig. 4.1(b)]. Second, importantly, J_{sc} remains always positive, that is: charge (positive) flows towards the ground, irrespectively on the depoling E_d direction which switches with **P**. This contribution is $J_{sc\text{-}uns}$ (≈ 6.9 mA/cm^2 for Cry-1) as identified above. This offset photocurrent is found always positive for all tested crystals, i.e. samples with different signs of E_{im} show the same current offset sign (Supplementary information S4.3), which consequently, is not dictated by neither by E_{im} nor E_d. Therefore, J_{uns} shall originate from E_{bi} at the LMO/Pt$_{top}$ interface (unswitchable drift $J_{un\text{-}E}$) with a possible contribution from diffusion (J_D) and BPE (J_{BPE}). Third, the direction of the E_{im} determines the cycling direction of the hysteresis J_{sc}-E_w curve. For samples with E_{im} towards bottom electrode, as Cry-1 of Fig. 4.2(c), the hysteresis is clockwise [$J_{sc}^+ > J_{sc}^-$, Fig. 4.2(a)]. For samples with E_{im} towards top electrode, as Cry-4 of Fig. S4.3(b), the hysteresis is anticlockwise [$J_{sc}^+ < J_{sc}^-$, Fig. S4.3(a)].

4.1.5. In-plane photoresponse

To elucidate the origin of $J_{uns} > 0$, we explore in the following the role of a diffusive contribution and possible BPE to the photocurrent. Due to the geometry of the experimental setup [Fig. 4.1(a)] and the short penetration depth of light, we expect that in measurements described above, J_E and J_D will both contribute to the photocurrent. In contrast, in-plane photocurrent should minimize any J_E contribution and thus:

$$J_{sc} = J_{BPE} + J_D \qquad [4.2]$$
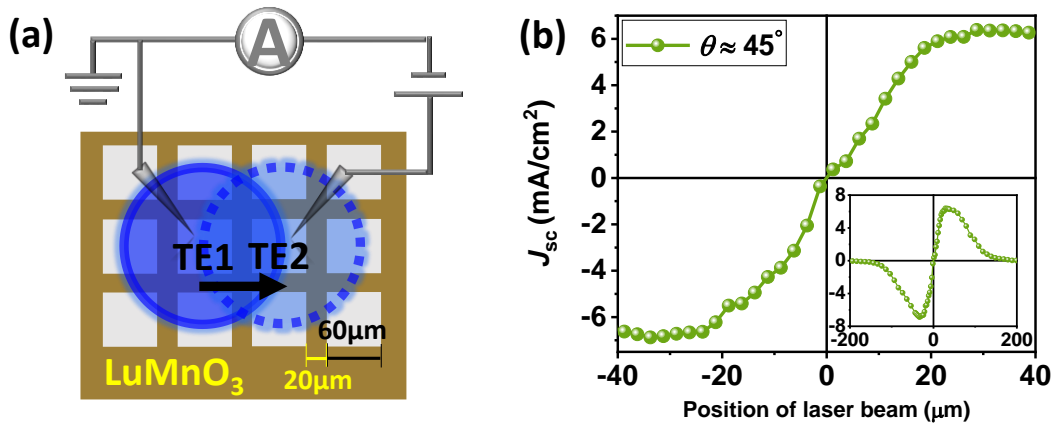
Fig. 4.3. (a) Measurement setup (top view) used to record the in-plane J_{sc} as a function of the beam position. (b) J_{sc} as a function of beam position (Cry-2, 45° incidence) by scanning the laser from the grounded electrode to the non-grounded electrode. Inset: photocurrent measured in a larger (400 μm) beam scan.

Accordingly, we have measured the in-plane phoresponse J_{sc} of a LMO single crystal, having only top electrodes without bottom electrode. Two adjacent electrodes separated by about 20 μm [Fig. 4.3(a), labelled TE1 and TE2] have been selected. Experimental evidence of the contribution of the diffusion term to J_{sc} is demonstrated in Fig. 4.3(b), where we show the J_{sc} measured using a pair of adjacent Pt$_{top}$ electrodes while scanning the laser beam from one electrode TE1 to the other TE2 [Fig. 4.3(a)]. Data in Fig. 4.3(b), displaying the recorded in-plane J_{sc} as a function of the position of laser beam (at 45° incidence), show that J_{sc} changes its sign form negative to positive when switching the illumination from grounded (G) to non-grounded (NG) electrode, as expected in presence of an excess of photo charges diffusing away from the illuminated spot. The inset in Fig. 4.3(b) indicates

that when the laser beam illuminates far away from both electrodes, the photovoltaic current detected tends to be zero.
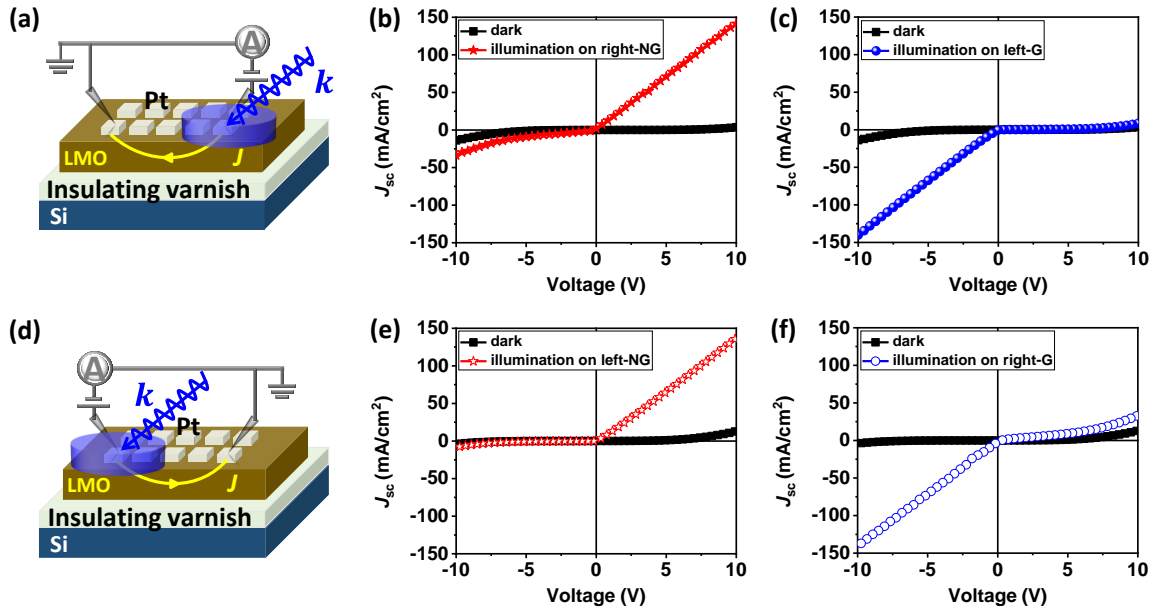
Fig. 4.4. (a) In-plane electric contacts configuration with the left electrode grounded. The *J-V* curves of a Pt/LMO sample (Cry-3) recorded in Fig. 4.4(a) configuration in dark and under illumination (45° incidence) of laser on (b) the right non-grounded electrode and (c) the left grounded electrode. (d) In-plane electric contacts configuration with the right electrode grounded. The *J-V* curves of a Pt/LMO sample (Cry-3) recorded in Fig. 4.4(d) configuration in dark and under illumination (45° incidence) of laser on (b) the left non-grounded electrode and (c) the right grounded electrode. The yellow arrows denote the flow of positive carriers from *V*-biased towards the grounded electrode. The blue arrow denotes the light propagation of wave vector $\boldsymbol{k}$.

To further assess that only the illuminated electrode plays a role in the photoresponse and to make sure only one top electrode is under illumination (spot diameter ≈ 280 µm), we have recorded the in-plane photoresponse using a pair of electrodes separated by ≈ 260 µm [Figs. 4(a,d)]. Note that the sample does not have bottom electrode and only top electrodes are deposited. Experiments have been performed by illuminating either the non-grounded electrode [red stars in Fig. 4.4(b,e)] or the grounded one [blue circles in Fig. 4.4(c,f)]. Data in Figs. (b,c) with the left electrode grounded clearly show that holes/electrons (photocarriers) always flow towards the lowest/highest potential, and are generated under the illuminated electrode. Consistently, when reversing the bias polarity

of two top electrodes [change from left-G in Figs. 4.4(a,b,c) to right-G in Figs. 4.4(d,e,f)], the response in dark and under illumination is fully reversed. It shows that the current increases for positive (negative) bias while illuminating the NG (G) electrode no matter how the electrodes are connected. This further proves that the photoresponse occurs mainly underneath the illuminated electrode.

Therefore, it follows that the diffusive contribution to the photocurrent dominates in-plane measurements in h-LuMnO₃ single crystals (Dember effect, see for instance the report of Ji et al.[30]). Moreover, in presence of dichroism, as in h-LuMnO₃ where the absorption coefficients ($\alpha \parallel c$ and $\alpha \perp c$) are large and anistropic,[26,31] the rotation of the polarization direction of the light at oblique incidence should give an angular dependence to J_D, leading to a polarization-dependent additional Dember effect contribution, that unavoidably will be convoluted with any BPE photorespose.

Before concluding, we mention that conductive domain walls has been reported to occur in h-manganites, potentially contributing to the observed photoresponse.[32–36] The number of domain walls is expected be at its maximum at E_c. However, data in Fig. 4.2(c) shows that at E_c, only monotonic change of J_{sc} occurs, which denies an important contribution of conductive domain walls in the present data.

4.1.6. Conclusions

In summary, we have measured the photoresponse of ferroelectric h-LuMnO₃ crystals using Pt electrodes. We have shown h-LuMnO₃ crystals display a photovoltaic response with an out-of-plane photocurrent J_{sc} that can be modulated by the ferroelectric polarization (up to 25 %), suggesting that depoling field contributes to modulate interface-Schottky barrier. The sign of the photocurrent cannot be switched by opposite writing voltages due to the presence of a non-switchable photocurrent contribution. Using in-plane photocurrent measurements we have evidenced the presence of a non-switchable diffusive photocurrent J_D, that originates from the large photoabsorption of h-LuMnO₃, that also contributes to the measured J_{sc}. The overruling presence of a diffusive term contributing to J_{sc}, associated to the large photoabsorption and the optical dichroism of h-LuMnO₃ may challenge to disentangle a genuine bulk photovoltaic contribution to J_{sc} in single crystals. Probably,

epitaxial thin films expected to have negligible J_d offer opportunities to disentangle bulk photovoltaic contributions in dichroic materials. The BPE remains to be identified with cautions and will be elucidated in the following sections 4.2 and 4.3.

Supplementary information

S4.1. Polarization loops and rectifying behavior of an LMO crystal

The electric coercivity is the ability of a ferroelectric material to withstand an external electric field without becoming depolarized. In Fig. S4.1(a), the loops of Cry-4 in top-top configuration are symmetric and the coercive field E_c' (12 kV/cm) is almost twice the value of E_c (8 kV/cm) in t-b configuration, which is attributed to the t-t configuration consists of two capacitors in series through the conducting Pt_{bot}, and the configuration is virtually independent of the distance between top electrodes. Note that in this configuration two Pt_{top} electrodes are contacted (one is grounded and the other is biased) and that the Pt_{bot} is acting as short circuit path between the mentioned two measured ferroelectric capacitors, which is not the case for the in-plane configuration in Fig. 3.3(d) used in the Figs. (4.3,4.4) of the main text.
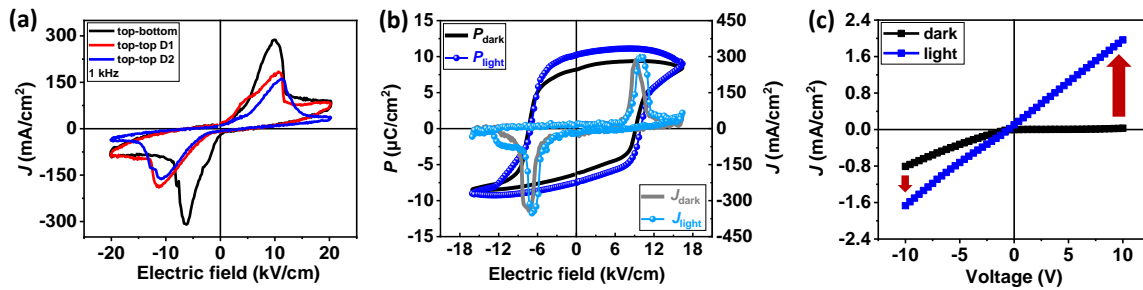
Fig. S4.1. (a) The $J(E)$ loops of a Pt/LMO/Pt sample (Cry-4) recorded in dark at 1 kHz without DLCC, where the black curve is measured in t-b configuration, the red and blue curves are measured in t-t configuration with different distance (D1 and D2, twice bigger than the sample thickness) between the two top electrodes. (b) The $J(E)$ and $P(E)$ loops of a Pt/LMO/Pt sample (Cry-4), in t-b, recorded in dark and under illumination (45° incidence) at 1 kH using DHM with DLCC. (c) The J-V characteristic of an unpolarized Pt/LMO/Pt sample (Cry-4), in t-b, in dark and under illumination (45° incidence). The red arrows indicate the prominent photoresponse under illumination.

In Fig. S4.1(b) we show the $P(E)$ and $I(E)$ loops recorded on the Cry-4, exemplifying a $P(E)$ loop with a different sign of E_{im} (upwards). Here the loops are right shifted, which is opposite to the behavior of Cry-1 [Fig. 4.1(a)]. We stress that crystals as taken from the growth bath are up/down randomly oriented. Therefore, in presence of a growth induced imprint, observation of E_{im} of opposite sign is to be expected. Interestingly, as show in Fig.

S4.1(c), the rectifying behavior is identical, that is blocking for $V > 0$, indicating downward E_{in} irrespectively on the direction of E_{im}.

S4.2. Back-switching of polarization in LMO crystals
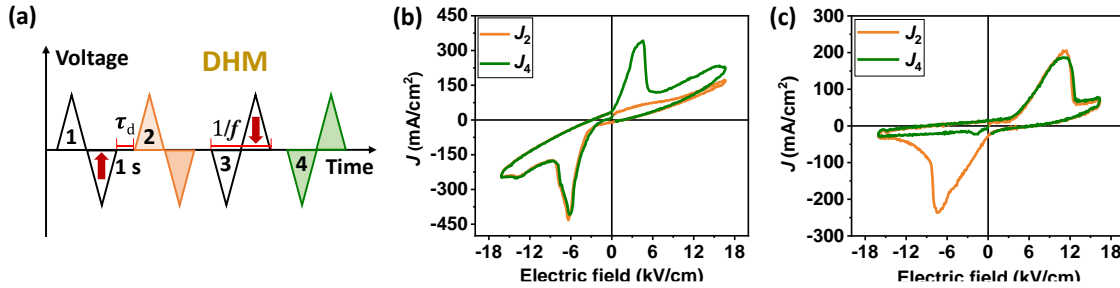
Fig. S4.2. (a) Voltage train pulses applied to write the polarization state and to read, where the shaded areas correspond to the measuring intervals, as the $J(E)$ curves shown in Figs. S4.2. (b,c). The J_2-E, J_4-E loops of Pt/LMO/Pt sample (b) Cry-1 and (c) Cry-4 recorded in dark at 1 kHz without DLCC, where the orange loop corresponds to the 2nd measuring pulse with upward initial $P^\uparrow$ state, and the green loop corresponds to the 4th measuring pulse with downward initial $P^\downarrow$ state.

Fig. S4.2(a) displays the $V(t)$ pulse sequence in DHM mode, four bipolar triangular excitation signals are applied to Pt$_{top}$ with a delay time τ_d (1 s) between them, which can be used to explore polarization switching back. Fig. S2(b) shows the $J(E)$ recorded on Cry-1 sample during two measuring pulses [labelled 2,4 in Fig S4.2(a)] following (τ_d = 1 s) the writing pulses [labelled 1,3 in Fig. S4.2(a)]. If the sample remains at $P_r^\uparrow$ state after the latter half V^- writing pulse 1, a positive switching peak should be visible during reading step 2 at $V > 0$; whereas a reverse current switching peak should be visible at $V < 0$ in step 4. However, the corresponding J_2-E loop [Fig. S2(b)] only contains a switching peak for $V < 0$ but not for $V > 0$, implying that after τ_d = 1 s, the written $P^\uparrow$ with $V < 0$ has already been switched back to $P^\downarrow$. This proves that the sample has short polarization retention (< 1 s) in $P^\uparrow$. The back-switching of $P^\uparrow$ to $P^\downarrow$ may be caused by the observed downward E_{im} existing inside LMO that can switch the oriented polarization back to downward in 1 s.[37,38] Consistent with the above observation, the J-V measurements of Fig. 4.3(a), collected with $\tau_d \approx 5$ s, do show a minimal dependence on polarization, because at the measurement time (τ_d) both pre-poled states are almost in an identical remanent polarization state ($P^\downarrow$).

Similarly, Fig. S4.2(c) shows the *J*(*E*) recorded on Cry-4 sample, where the corresponding *J₄*-*E* loop only contains an obvious switching peak for *V* > 0 but not for *V* < 0, implying that the sample has short polarization retention (< 1 s) in $P^{\downarrow}$ caused by the observed upward E_{im} existing inside LMO.

S4.3. Photocurrent of an LMO crystal

In Fig. S4.3(a) we show the *J*-*V* data recorded on Cry-4 together with the corresponding J_{sc}-E_w data [Fig. S4.3(b)] recorded during polarization cycles, measured using the protocol indicated in Fig. 4.3(b) (in the main text). It can be appreciated that E_{im} is pointing upward [Fig S4.1(b), Fig S4.3(b)] and LMO/Pt$_{top}$ is rectifying for *V* > 0 [Fig. S4.1(c)], as in any other crystal, irrespectively on the E_{im} direction.
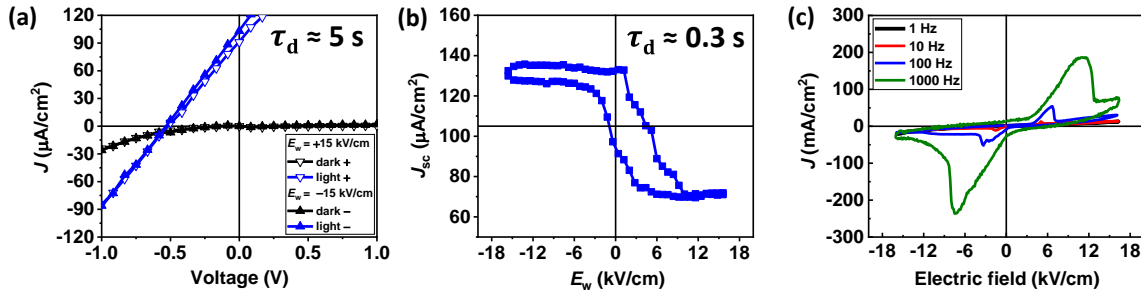
Fig. S4.3. (a) Enlarged view of the *J*-*V* curves of a polarized Pt/LMO/Pt sample (Cry-4), recorded in dark and under illumination (45° incidence). (b) The J_{sc}-E_w characteristic (Cry-4, 45° incidence). (c) The *J*(*E*) hysteresis loops (Cry-4) recorded at various frequency without DLCC.

Fig. S4.3(c) displays *J*(*E*) loops recorded at different frequencies. It can be appreciated that the coercive fields increase with frequency as commonly observed in ferroelectrics.

Bibliography

[1] T. Choi, S. Lee, Y.J. Choi, V. Kiryukhin, and S.-W. Cheong, Science (80-.). **324**, 63 (2009).

[2] S.Y. Yang, J. Seidel, S.J. Byrnes, P. Shafer, C.-H. Yang, M.D. Rossell, P. Yu, Y.-H. Chu, J.F. Scott, J.W. Ager, L.W. Martin, and R. Ramesh, Nat. Nanotechnol. **5**, 143 (2010).

[3] W. Shockley and H.J. Queisser, J. Appl. Phys. **32**, 510 (1961).

[4] B. Sturman and V.M. Fridkin, *The Photovoltaic and Photorefractive Effects in Noncentrosymmetric Materials* (Gordon and Breach Science Publishers, Philadelphia, 1992).

[5] J. Seidel, D. Fu, S.Y. Yang, E. Alarcón-Lladó, J. Wu, R. Ramesh, and J.W. Ager, Phys. Rev. Lett. **107**, (2011).

[6] A. Bhatnagar, A. Roy Chaudhuri, Y. Heon Kim, D. Hesse, and M. Alexe, Nat. Commun. **4**, 2835 (2013).

[7] S.M. Young, F. Zheng, and A.M. Rappe, Phys. Rev. Lett. **109**, 236601 (2012).

[8] A.M. Burger, R. Agarwal, A. Aprelev, E. Schruba, A. Gutierrez-Perez, V.M. Fridkin, and J.E. Spanier, Asian J. Chem. **31**, eaau5588 (2019).

[9] B.I. Sturman, Physics-Uspekhi **63**, 407 (2020).

[10] P. Würfel, *Physics of Solar Cells* (Wiley, 2005).

[11] D. Lee, S.H. Baek, T.H. Kim, J.G. Yoon, C.M. Folkman, C.B. Eom, and T.W. Noh, Phys. Rev. B - Condens. Matter Mater. Phys. **84**, (2011).

[12] Y.S. Yang, S.J. Lee, S. Yi, B.G. Chae, S.H. Lee, H.J. Joo, and M.S. Jang, Appl. Phys. Lett. **76**, 774 (2000).

[13] L. Pintilie, I. Vrejoiu, G. Le Rhun, and M. Alexe, J. Appl. Phys. **101**, 064109 (2007).

[14] W. Ji, K. Yao, and Y.C. Liang, Adv. Mater. **22**, 1763 (2010).

[15] J. Fontcuberta, Comptes Rendus Phys. **16**, 204 (2015).

[16] W.S. Choi, D.G. Kim, S.S.A. Seo, S.J. Moon, D. Lee, J.H. Lee, H.S. Lee, D.-Y. Cho, Y.S. Lee, P. Murugavel, J. Yu, and T.W. Noh, Phys. Rev. B **77**, 045137 (2008).

[17] V. V. Pavlov, A.R. Akbashev, A.M. Kalashnikova, V.A. Rusakov, A.R. Kaul, M. Bayer, and R. V. Pisarev, J. Appl. Phys. **111**, 056105 (2012).

[18] H. Han, S. Song, J.H. Lee, K.J. Kim, G.W. Kim, T. Park, and H.M. Jang, Chem. Mater. **27**, 7425 (2015).

[19] H. Han, D. Kim, K. Chu, J. Park, S.Y. Nam, S. Heo, C.H. Yang, and H.M. Jang, ACS Appl. Mater. Interfaces **10**, 1846 (2018).

[20] H. Han, D. Kim, S. Chae, J. Park, S.Y. Nam, M. Choi, K. Yong, H.J. Kim, J. Son, and H.M. Jang, Nanoscale **10**, 13261 (2018).

[21] S.H. Kim, S.H. Lee, T.H. Kim, T. Zyung, Y.H. Jeong, and M.S. Jang, Cryst. Res. Technol. **35**, 19 (2000).

[22] T. Yu, P. Gao, T. Wu, T.A. Tyson, and R. Lalancette, Appl. Phys. Lett. **102**, 172901 (2013).

[23] N. Hur, I.K. Jeong, M.F. Hundley, S.B. Kim, and S.W. Cheong, Phys. Rev. B - Condens. Matter Mater. Phys. **79**, 134120 (2009).

[24] A.H. Hubmann, S. Li, S. Zhukov, H. Von Seggern, and A. Klein, J. Phys. D. Appl. Phys. **49**, 295304 (2016).

[25] F. Chen and A. Klein, Phys. Rev. B - Condens. Matter Mater. Phys. **86**, 094105 (2012).

[26] R. Schmidt-Grund, S. Richter, S.G. Ebbinghaus, M. Lorenz, C. Bundesmann, and M. Grundmann, RSC Adv. **4**, 33549 (2014).

[27] Q. Hong, Y. Cao, J. Xu, H. Lu, J. He, and J.L. Sun, ACS Appl. Mater. Interfaces **6**, 20887 (2014).

[28] M.E. Hossain, S. Liu, S. O'Brien, and J. Li, Appl. Phys. Lett. **107**, 032904 (2015).

[29] A. Ruff, Z. Li, A. Loidl, J. Schaab, M. Fiebig, A. Cano, Z. Yan, E. Bourret, J. Glaum, D. Meier, and S. Krohns, Appl. Phys. Lett. **112**, 182908 (2018).

[30] Z. Ji, G. Liu, Z. Addison, W. Liu, P. Yu, H. Gao, Z. Liu, A.M. Rappe, C.L. Kane, E.J. Mele, and R. Agarwal, Nat. Mater. **18**, 955 (2019).

[31] A.M. Kalashnikova and R. V. Pisarev, JETP Lett. **78**, 143 (2003).

[32] M. Mostovoy, Nat. Mater. **9**, 188 (2010).

[33] T. Choi, Y. Horibe, H.T. Yi, Y.J. Choi, W. Wu, and S.W. Cheong, Nat. Mater. **9**, 253 (2010).

[34] D.R. Småbråten, Q.N. Meier, S.H. Skjærvø, K. Inzani, D. Meier, and S.M. Selbach, Phys. Rev. Mater. **2**, 114405 (2018).

[35] D. Meier, J. Seidel, A. Cano, K. Delaney, Y. Kumagai, M. Mostovoy, N.A. Spaldin, R. Ramesh, and M. Fiebig, Nat. Mater. **11**, 284 (2012).

[36] W. Wu, Y. Horibe, N. Lee, S.W. Cheong, and J.R. Guest, Phys. Rev. Lett. **108**, 077203 (2012).

[37] A. Picinin, M.H. Lente, J.A. Eiras, and J.P. Rino, Phys. Rev. B - Condens. Matter Mater. Phys. **69**, 064117 (2004).

[38] S. Pandya, G. Velarde, L. Zhang, and L.W. Martin, Phys. Rev. Mater. **2**, 124405 (2018).

4.2. Bulk photovoltaic effect evidenced by light polarization dependent photoresponse

In this section, the J_{sc} and V_{oc} dependence of Pt/LMO SC/Pt on the angle of the polarization of the linearly polarized light is presented. It is observed an oscillating angular dependence. This might be taken as a fingerprint of bulk photovoltaic effect in h-LuMnO₃. It is found that a switchable drift photocurrent also contributes to J_{sc}, which precludes accurate determination of the PV tensor elements and Glass coefficients. Some bounds of the Glass coefficients can be stablished and found to be significantly larger than those obtained in BiFeO₃.

The work presented in this section was published in Phys. Rev. B 104, 184116 (2021); https://doi.org/10.1103/PhysRevB.104.184116.

4.2.1. Introduction

Photoferroelectric materials are receiving a new attention towards efficient absorbers for photoelectric conversion. In conventional photovoltaic materials photogenerated electron-hole pairs are driven out of the absorbing material by a built-in electric field, engineered by doping gradients (pn junctions), work functions and electron affinity mismatch between different materials. In non-centrosymmetric materials photocarriers can be extracted from homogeneous materials, without any built-in electric field, with the additional advantage that the open circuit voltage is not limited by the bandgap (E_g) of the semiconducting absorber,[1,2] with promises of higher efficiency. This, is the so-called bulk photovoltaic effect (BPE).[3] Ferroelectric materials fall within this category. Whereas the most common ferroelectrics, such as Pb(Zr,Ti)O₃ and BaTiO₃, have a large bandgap (≈ 3.6 eV) and thus their photoabsorption in the visible range is rather limited, the discovery of a strong photoresponse in BiFeO₃ (BFO) ferroelectric with narrower bandgap (about 2.6 - 2.8 eV) constituted a hallmark that stimulated research on narrow gap photoferroelectrics.[4–7] The dependence of the short circuit photocurrent density (J_{sc}) and open circuit voltage (V_{oc}) on the polarization direction of the incoming light with respect to the crystal lattice[8] is commonly taken as a fingerprint of BPE, as identified in BFO.[9,10] Microscopic models have been developed to account for the BPE, and although still under some debate, have provided a rich insight, emphasizing the important role of wave functions of excited states [11] and allowed some predictive guidance.[12–15]

In BFO, the Fe^{3+} ions have a $3d^5$ electronic configuration and occupy an octahedral cage that breaks the degeneracy of the 3d levels in basically two spin-up subsets t_{2g} and e_g that are fully electron occupied. Hexagonal h-ReMnO₃ manganites, where Re indicates a lanthanide (Sc-Lu), are room-temperature ferroelectrics with their polar axis along the hexagonal axis. The high spin trivalent Mn^{3+} ions have a bipyramidal coordination and have a $3d^4$ electronic configuration.[16,17] The different crystal-field symmetry and the different electronic occupation accounts for the semiconducting behavior and lower bandgap of h-RMnO₃ (1.1 - 1.6 eV[18,19]). Importantly, the different nature of electronic ground and excited states in both materials anticipates a different BPE. The photoresponse of ferroelectric h-ReMnO₃ thin films has been explored in some detail. It has been shown, for instance, that J_{sc} can be switched by reversing the ferroelectric polarization (*P*) of the film, which indicates that the Schottky barriers at interfaces with electrodes play a major role.[20] However, to the best of our knowledge, no evidence of BPE has ever been reported neither in h-RMnO₃, nor in the isostructural h-ReFeO₃.[21,22] Here, we report on the photoresponse of h-LuMnO₃ (h-LMO) single crystals, aiming at determining its BPE response which may open new avenues beyond promising opportunities in conventional photovoltaics.[23]

As described in the previous section 4.1, the ferroelectric *P(E)* loops of these crystals display a remanent room-temperature polarization of $P_r \approx 7.3$ µC/cm² and the *J-V* characteristics clearly indicate a photovoltaic response.[24] However, the conventional photoresponse and the bulk photovoltaic effect are intertwined, as shown in the following, and disentangling their relative contributions is challenging. On the basis of general grounds, it is first argued that in absorbing materials displaying anisotropic absorption and in the presence of built-in electric fields, as typically found in ferroelectric capacitors, the short circuit photocurrent may contain drift and diffusion terms (J_E and J_D) in addition to any BPE contribution (J_{BPE}).[25] Importantly, drift and diffusion photocurrent contributions may display a dependence on light polarization that manifests entangled with BPE. It will be shown that h-LMO displays a remarkable J_{sc} and V_{oc} photoresponse both modulated by the polarization of the incoming light and its wavelength. It will be next argued that in the used experimental geometry, the diffusion term is negligible, and it is shown that the observed dependence of the measured short circuit photocurrent on light polarization is mainly governed by BPE. However, we observe the presence of a drift-related photocurrent that

also modulates J_{sc}. This contribution imposes bounds to the accuracy of the extracted Glass coefficients (G_{ij}) and tensor element (β_{ij}) of the BPE. The observed G_{ij} and β_{ij} values are found to be significantly larger than in BiFeO₃. It is concluded that *h*-LMO displays a stronger responsiveness than rhombohedral ferrites and related materials, and we describe a scenario to account for the differences and possible avenues.

4.2.2. Samples and experiments

Data on several crystals are reported here, Cry-n (n = 5, 6, 7 and 8), all displaying similar features. A stencil mask (≈ 58 x 58 μm²) was used to create top Pt (TE, Pt$_{top}$ ≈ 7 nm thick) electrodes on Cry-5 and Cry-8, while a mask of a rectangular aperture was used to prepare a single top electrode on Cry-6 and Cry-7 with 450 μm by 270 μm and 765 μm by 480 μm, respectively. The bottom side of the *h*-LMO crystals were fully covered by a continuous Pt layer (7 nm thick) to be used as bottom electrode (BE, Pt$_{bot}$). The crystals (Pt/LMO/Pt) were fixed on silicon substrates using silver paste.

Data were recorded in dark or under illumination as sketched in Figs. 3.5(a,b), using a blue-violet laser source (λ = 405 nm, I_p ≈ 27.6 − 45.5 W/cm²) or a STEC multiwavelength system (λ = 405, 450, 520, and 638 nm, I_p ≈ 1 W/cm²). The angle of incidence was varied between θ ≈ 0° (normal incidence) to ≈ 60°. Dedicated experiments were also conducted for in-plane incidence (θ ≈ 90°) measurements, and cross-check experiments have been done to exclude spurious misalignment contributions.

4.2.3. Angular dependent photoresponse at out-of-plane illumination

Figs. 4.5(a,b) show the normalized (Supplementary information S4.4) short circuit photocurrent [$J_{sc}(\theta, \varphi)$] and the open circuit photovoltage [$V_{oc}(\theta, \varphi)$] measured along the *z*-direction on a Pt/LMO/Pt sample (Cry-5), when varying the incidence angle (θ) and the polarization angle (φ) of the light.
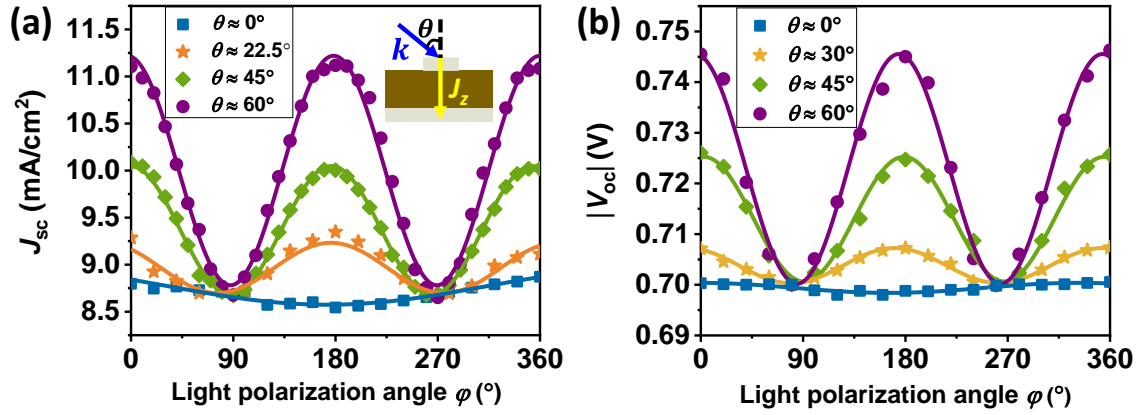
Fig. 4.5. Dependence of (a) short circuit current [$J_{sc}(\theta, \varphi)$)] and (b) the open circuit voltage [$V_{oc}(\theta, \varphi)$)], respectively, on the polarization angles (φ) of the light at different incident angles, of Cry-5. Solid lines are fits using Eq. [4.3] of experimental data (symbols). Light intensity I_0 after optical plates and the top Pt is around 15 W/cm². The sketch illustrates the experimental arrangement. Notice that the illumination is through the top electrode.

Data indicate that $J_{sc}(\theta, \varphi)$ and $V_{oc}(\theta, \varphi)$ both display an oscillatory dependence on the polarization angle of light, being both maxima at $\varphi = 0°$, that is when the **E** electric field is in the incident plane (*p*-polarization), and minimum for $\varphi = 90°$ (*s*-polarization). $J_{sc}(\theta, \varphi)$ can be well described by:

$$J_{sc}(\theta, \varphi) = A_z(\theta) \cos 2(\varphi - \varphi_0) + B_z(\theta) \qquad [4.3]$$

where the A_z and B_z coefficients are related to incoming light intensity, absorption coefficient and incidence angle, and may contain specific material-dependent parameters; φ_0 (< 4°) is a phase shift that account for unavoidable instrumental missalignements. A similar expressions holds for $V_{oc}(\theta, \varphi)$, as illustrated by the continuous line through data points in Fig. 4.5(b). In Fig. 4.5, experimental variation occurring when changing the incidence angle are mitigated by a vertical shift of data collected at different θ angle, to make J_{sc} coincide at $\varphi = 90°$ with reference to $J_{sc}(\theta = 90°)$ (Supplementary information S4.4). It can be appreciated that the amplitude of the $J_{sc}(\theta, \varphi)$ and $V_{oc}(\theta, \varphi)$ oscillations varies with the incidence angle, being null at normal incidence and increasing when approaching grazing incidence. Therefore, data in Figs. 4.5(a,b) indicate that J_{sc} and V_{oc} both increase with the projection of E_n along the *z*-axis increases.

This can be better seen in Fig. 4.6 displaying the dependence of $J_{sc}(\theta, \varphi = 0°)$ and the amplitude $A_z(\theta)$ on the incidence angle. Moreover, it can be appreciated that $A_z(\theta)$, $B_z(\theta)$ and consequently $J_{sc}(\theta, \varphi = 0°)$, are all linear on $\sin^2\theta$.
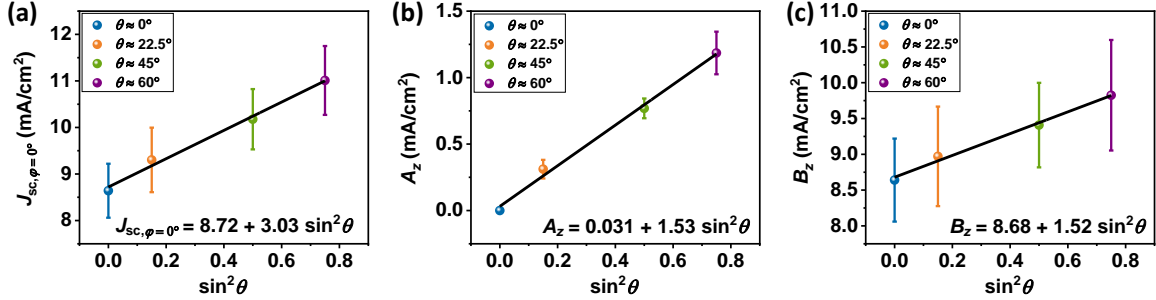
Fig. 4.6. Dependence of the (a) short circuit photocurrent recorded at $\varphi = 0$, (b) amplitude $A_z(\theta)$ and (c) background $B_z(\theta)$ on $\sin^2(\theta)$, of Cry-5. Solid lines are linear fits of experimental data (symbols) as indicated. Error bars in figures indicate the spread of values (standard deviation, SD) from data recorded in 6 capacitors. Light intensity I_0 after optical plates and the top Pt is around 15 W/cm².

Therefore, from data in Figs. 4.5,4.6 we conclude that

$$J_{sc}(\theta, \varphi) = A'_z \sin^2(\theta)\cos 2(\varphi - \varphi_0) + B'_z \sin^2(\theta) + C_z \qquad [4.4]$$

4.2.4. Dichroism contribution

In order to understand the observed dependence of $J_{sc}(\theta, \varphi)$ and $V_{oc}(\theta, \varphi)$ on the polarization of light, we first note that the measured short circuit photocurrent (J_{sc}) may contain contributions from drift (J_E) and diffusion (J_D) terms[25] and of bulk photovoltaic effect (J_{BPE}):

$$J_{sc} \approx J_E + J_D + J_{BPE} \qquad [4.5]$$

It is well known that the bulk photovoltaic effect (BPE) gives rise to a genuine polarization dependence of $J_{BPE}(\varphi)$. Indeed, the experimental observation of $J_{sc}(\varphi)$ is commonly taken as a fingerprint of BPE. This assumption is well grounded in materials with weak photo-absorption (α) and in absence of dichroism (i.e. $\alpha_x = \alpha_y = \alpha_z$), where observation of $J_{BPE}(\varphi)$ can be safely attributed to BPE. However, *h*-LMO is known to be strongly absorbing at visible wavelengths and *h*-manganites are known to be dichroic ($\alpha_\perp =$

$\alpha_x = \alpha_y \neq \alpha_\parallel = \alpha_z$, where the symbols "⊥" and "∥" indicate the direction perpendicular and parallel to *c*-axis, respectively).[26–28] In this case, polarization-dependent photo absorption may give rise to polarization-dependent drift and diffusion terms [$J_E(\varphi)$, $J_D(\varphi)$] in the measured photocurrent [$J_{sc}(\varphi)$].

In principle, owing to the geometry of the experiments in Fig. 3.5(a), the presence of interfacial electric fields, evident from the rectifying character of the measured *I-V* (Supplementary information S4.5), shall give rise to J_E. Moreover, the strong light absorption ($\alpha \approx 5$ μm⁻¹)[27] at the upper surface of the crystal (attenuation length < 1 μm) shall produce a gradient of photocarriers giving rise to a diffusion term, J_D. As mentioned, in presence of dichroism, these two contributions will be entangled with any BPE response and observation of $J_{sc}(\varphi)$ can no longer be taken as a fingerprint of BPE.

Aiming at disclosing if dichroism plays a relevant role on the polarization-dependence observed in Figs. 4.5, we recorded $J_{sc}(\varphi)$ at $\theta = 45°$ for different wavelengths and inspected the variation of $J_{sc}(\varphi)$ and then compared with the variations expected from the known dichroism ($\alpha_\parallel \neq \alpha_\perp$) of *h*-ReMO and its energy dependence. Although dichroism data of *h*-LMO is not available, optical measurements on isomorph *h*-YMnO₃ crystals[27] show that $\Delta\alpha = \alpha_\parallel - \alpha_\perp$ strongly depends on light energy and $\Delta\alpha$ changes its sign at about 2 eV. Accordingly, if dichroism were ruling the observed $J_{sc}(\varphi)$, one should expect that $J_{sc}(E_\parallel) > J_{sc}(E_\perp)$ and changing to $J_{sc}(E_\parallel) < J_{sc}(E_\perp)$ when using blue-violet (BV) or red (R) light, respectively, with their relative magnitudes dictated by $\frac{\alpha_\parallel}{\alpha_\perp} \approx 4$ (BV) and $\frac{\alpha_\parallel}{\alpha_\perp} \approx 0.2$ (R).

To test these predictions, we measured $J_{sc}(\varphi)$ when illuminating the sample ($\theta = 45°$, $0° \leq \varphi \leq 360°$) using different photon energies: 405 nm (3.06 eV) and 638 nm (1.95 eV). Data are displayed in Figs. 4.7(a,b). Data show the oscillations, as in Fig. 4.5, that can be similarly fitted using Eq. [4.3]. Notice that the background value and amplitude of the oscillations is smaller than in Fig. 4.5 due to the different laser source used in this experiment; here the laser intensity reaching the absorber is only of $I_0 \approx 0.6$ W/cm². We have verified that J_{sc} and the amplitude of the oscillations in the $J_{sc}(\varphi)$, both increase with power fluence (not shown). We note that the observation of polarization-dependent oscillations when using in-plane illumination (see Fig. 4.8 below) excludes a significant contribution of the polarization-

dependent reflectivity (Fresnel contribution) of the top electrode on the experimental results.
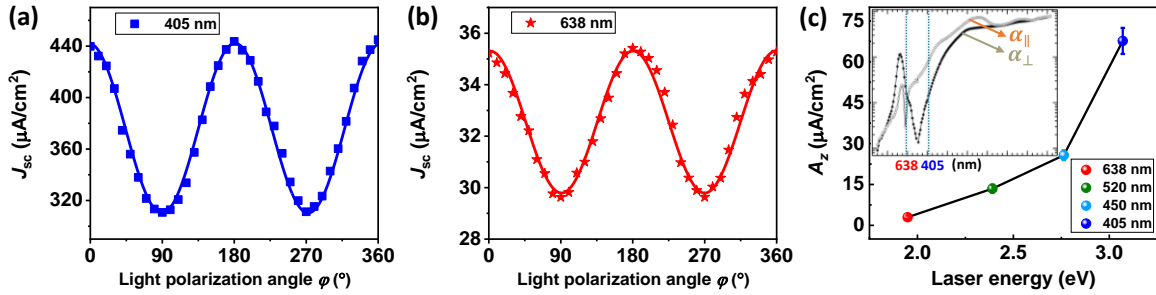

Fig. 4.7. $J_{sc}(\varphi)$ measured at $\theta \approx 45°$ incidence (Cry-5) recorded at (a) 405 nm and (b) 638 nm, respectively. Solid lines are fits using Eq. [4.3] of experimental data (symbols). (c) Dependence of the amplitude A_z of the oscillations $J_{sc}(\varphi)$ as a function of photon energy. Error bars in figures indicate the SD from data recorded in 4 capacitors. Light intensity I_0 after optical plates and the top Pt is around 0.6 W/cm². Note that absolute values of J_{sc} and A_z in (a,b,c) are smaller than in Fig. 2, due to the different laser fluence used in both cases (0.6 W/cm² and 15 W/cm², respectively). Inset in c) is adapted from Ref. 27.

Of relevance here is the observation that for blue-violet and red photons, the photocurrent is always maximal at ($\varphi = 0°$), although obviously its magnitude depends on the photon energy (see Supplementary information S4.6 for results measured at 450 nm and 520 nm laser). Indeed, $J_{sc}(\varphi)$ in Fig. 4.7(a) changes by about 42 % ($\Delta J = \frac{J_{\varphi=0°} - J_{\varphi=90°}}{J_{\varphi=90°}}$) when φ rotates from 0° (maximal $E_\parallel$) to 90° (only $E_\perp$) when using blue-violet light but only about 19 % [Fig. 4.7(b)] when using red light. Similar results measured at 90° in-plane incidence with 405 nm and 648 nm laser can be found in Supplementary information S4.6, which further indicates clearly $J_{sc}(\varphi = 0°, E_\parallel)$ always larger than $J_{sc}(\varphi = 90°, E_\perp)$ no matter how the dichroism varies ($\alpha_\parallel > \alpha_\perp$ or $\alpha_\parallel < \alpha_\perp$) with laser wavelength. These observations are in clear discordance with expectations from the dichroism of h-LMO and its energy dependence mentioned above. In fact, as shown in Fig. 4.7(c), the amplitude of $J_{sc}(\varphi)$ is found to vary monotonically ($\Delta J > 0$) with photon energy, which is not what should be expected from $\alpha(\lambda)$ and $\Delta\alpha(\lambda)$. For convenience we include in the inset of Fig. 4.7(c), the anisotropic absorption $\alpha(\lambda)$ reported for h-YMnO₃.[27] Therefore, experimental data demonstrate that dichroism does not play a dominant role of the polarization dependence

of $J_{sc}(\varphi)$. Consequently, in the following we analyze the $J_{sc}(\theta, \varphi)$ data within the BPE scenario.

4.2.5. BPE evidence

Within the BPE context, J_{BPE} is given by[8,10]

$$J_i = I_0 \cdot \alpha_{jk} \cdot G_{ijk} \cdot e_j e_k = I_0 \cdot \beta_{ijk} \cdot e_j e_k \qquad [4.6]$$

where J_i is the J_{BPE} along the i direction; I_0 is the intensity of the light of given λ; α_{jk} is the absorption coefficients tensor; e_j, e_k are the projection of the incoming light polarization vector along the j, k direction, respectively; G_{ijk} and β_{ijk} (= $\alpha_{jk}G_{ijk}$) are the Glass coefficients and the BPE tensor elements, respectively, that depend on the symmetry of the crystal centers, its electronic properties and the photon energy.[3,8] In Eq. [4.6], the suffixes i, j, k represent x-, y-, and z-axes in the Cartesian coordinate system for the electric field components of the incoming light; we take the z-axis along the polar c-axis of h-LMO.

For h-LMO [space group $P6_3cm$; symmetry class 6mm (≡ C₆ᵥ)], the β_{ijk} tensor contains only 3 non-zero independent elements.[29] When using Eq. [4.6] to analyze data, it is commonly assumed that the absorption is weak and isotropic ($\alpha_{ij} = \alpha$). We will first follow this simplifying assumption that will be released in a latter step. In this approximation and in the experimental arrangement (Fig. 3.5), the BPE (Eq. [4.6]) predicts an angular and polarization dependence of the short circuit photocurrent along the z-axis given by (Supplementary information S4.7):

$$J_{BPE} = I_0\alpha \left(\tfrac{G_{33}-G_{31}}{2}\sin^2\theta\cos2\varphi + \tfrac{G_{33}-G_{31}}{2}\sin^2\theta + G_{31}\right) \qquad [4.7]$$

In the following β_{ij} and G_{ij} are written here in the conventional reduced matrix notation of the β_{ijk} and G_{ijk} tensors.[30] According to Eq. [4.7], J_{BPE} has a $\cos(2\varphi)$ dependence on the light polarization, with an amplitude (A_z) and background (B_z) that depends on $\sin^2(\theta)$ with the same slope ($I_0\alpha\tfrac{G_{33}-G_{31}}{2}$). Note that at normal incidence, BPE contributes to the photocurrent with a term independent on light polarization neither incidence ($J_{BPE} = I_0\alpha G_{31}$). The angular dependence of J_{sc} in Fig. 4.5 and Fig. 4.6 as illustrated by the fitting function Eqs. [4.3, 4.4], closely follow predictions based on Eq. [4.7].

We also noted that the open circuit voltage $V_{oc}(\theta, \varphi)$ [Fig. 4.5(b)] displays a sinusoidal angular dependence, represented by Eq. [4.4] [$V_{oc}(\theta, \varphi) \approx A(\theta) \cos 2\varphi + B(\theta) + C$, solid lines through experimental data in Fig. 4.5(b)]. Within BPE, $V_{oc}(\theta, \varphi)$ can be expressed by:[9,31]

$$V_{oc} = \frac{J_{BPE} l}{\sigma_d + \sigma_{pv}} \qquad [4.8]$$

where σ_d and σ_{pv} are the dark and photo conductivity, respectively; l ($\leq$ mean free path) is the distance between electrodes; and J_{BPE} is the current generated under short circuit condition by BPE. Therefore, the angular dependence of $V_{oc}(\varphi)$ should follow that of J_{BPE} as observed here. Hence, both $J_{sc}(\theta, \varphi)$ and $V_{oc}(\theta, \varphi)$ angular dependences provide a strong indication that the BPE is ruling the light-polarization dependence of J_{sc}.

4.2.6. Angular dependent photoresponse at in-plane illumination

Finally, out-of-plane J_{sc} measurements have also been done at in-plane light incidence ($\theta \approx 90°$) by using dedicated samples (Cry-6 and Cry-7) and similar oscillation of $J_{sc}(\varphi)$ are observed when rotating the light polarization angle. Fig. 4.8(a) shows as illustrative example, data collected on Cry-6, 7 using electrodes of area $A_1 = 0.12$ mm^2 and $A_2 = 0.37$ mm^2 placed just at the edge of the crystal surface. Data collected to exclude spurious misalignment contributions (from grazing incidence illumination) are included in Supplementary information S4.8, Fig. S4.8(a). Data in Fig. 4.8(a) display $J_{sc}(\varphi)$ oscillations, similar to those observed at oblique incidence, reflecting how the photocurrent depends on the polarization direction of the light in relation to crystalline axis [Fig. 4.8(b)].

Notice that as mentioned in Chapter 3.2, at in-plane incidence, the light keeps normal to the lateral surface when rotating light polarization φ, in which case the reflectance at the side surface of p and s-polarized light remains the same. In the absence of polarization-dependent Fresnel contribution, the sinusoidal waveform is still observed, which excludes important role of the Fresnel contribution to the experimental results.
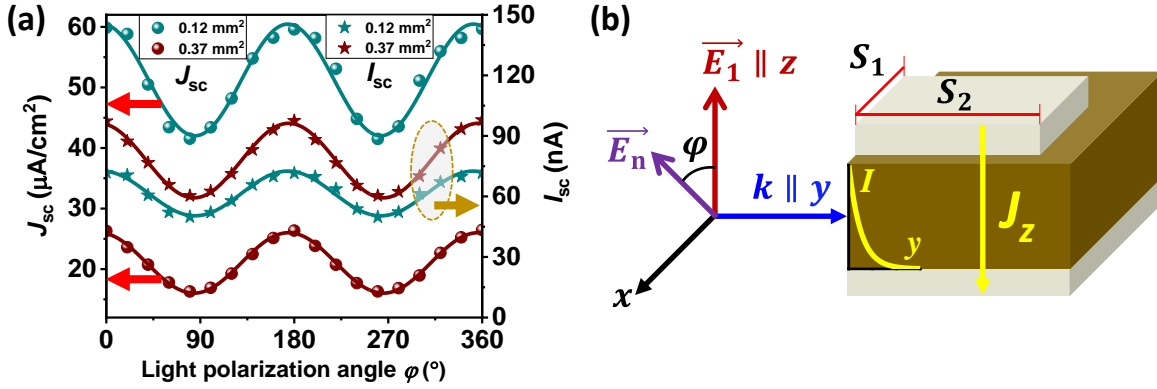
Fig. 4.8. (a) Left axis: $J_{sc}(\varphi)$ (solid circles) measured at $\theta \approx 90°$ incidence using a top electrodes of area S_1 x S_2 = 450 μm x 270 μm = $A_1 \approx 0.12$ mm² (Cry-6) and S_1 x S_2 = 770 μm x 480 μm = $A_2 \approx 0.37$ mm² (Cry-7), placed up to the edge of the crystal surface. Right axis: $I_{sc}(\varphi)$ =$J_{sc}(\varphi)$ x A) (solid stars). Light intensity I_0 after optical plates is around 27.6 W/cm². (b) Sketch of the experimental arrangement. The light attenuation length along y-axis (yellow I-y curve) and the contact size (S_1, S_2) are indicated. In this sketch, the edge-electrode distance ($D = 0$) is not shown.

All available data, particularly the in-plane incidence data, show that the out-of-plane photocurrent is maximal when light polarization axis coincides ($\varphi = 0°$) with the optical axis of h-LMO. However, comparison of current density data collected at oblique incidence [Figs 4.5(a) and 4.7(a)), with that obtained using in-plane incidence experiments [Fig. 4.8(a)], reveal two major differences. First, the collected photocurrent (I_{sc} = J_{sc} x A) is largely insensitive to contact area [Fig. 4.8(a), right axis]. As a matter of fact, as the illuminated spot size (diameter $S_d \approx 280$ μm) is smaller than the lateral sizes of the electrode ($S_1 \approx 450$ μm for Cry-2 and 770 μm for Cry-3), no additional photocurrent should be collected by increasing S_1, as illustrated by data in Fig. 4.8(a) (right axis). Consequently, it is observed in Fig. 4.8(a) (left axis) that the measured current density appears to depend on the contact area. Indeed, when reducing the contact area by about $\approx 1/3$ (= A_1/A_2), the measured current density is not constant but increases by about a factor ≈ 2.4. Moreover, out-of-plane J_{sc} recorded on Cry-8 using in-plane incidence measurements, reduces and eventually vanishes, when the collecting electrodes are placed at increasing distances (D) from the crystal edge where light impinges the crystal and most of the photo-absorption takes place [see photocurrent gathered at edge-distant electrode in Supplementary information S4.8,

Fig. S4.8(b)]. These observations indicate that: a) photocarrier generation is limited to a narrow region at the edge of the crystal of depth $\approx 1/\alpha < 1$ μm, much smaller than the lateral size of the electrodes and, b) recombination limits charge collection at distant electrodes (no additional photocurrent should be collected by increasing $S_2 \gg 1$ μm). Both effects indicate that derivation of Eq. [4.7] should be revised when photo absorption is relevant.

4.2.7. Values of Glass coefficients

Next task is to evaluate the Glass coefficients of *h*-LMO. Two sets of data are available to determine G_{33} and G_{31}: a) data extracted at oblique incidence (Figs. 4.5 and 4.6), and b) data collected from in-plane incidence (Fig. 4.8).

The photocurrent collected at oblique incidence, under the assumption of weak absorption, is given by:

$$J_{sc} = J_{BPE} + J_E + J_D = I_0\alpha \left(\frac{G_{33}-G_{31}}{2}\sin^2\theta\cos2\varphi + \frac{G_{33}-G_{31}}{2}\sin^2\theta + G_{31} \right) + J_E + J_D \ [4.9]$$

Using the linear fits in Fig. 4.6 and Eqs. [4.4, 4.9] we deduce: $I_0\alpha(G_{33} - G_{31}) \approx 3.03$ mA/cm² and $I_0\alpha G_{31} + J_E + J_D \approx 8.72$ mA/cm².

Equation [4.9] emphasizes that in presence of diffusion and drift terms, even in absence of any dichroic absorption contribution, the G_{31} and G_{33} coefficients cannot be disentangled. However, as argued above, in the measuring configuration used here, the diffusion term can be neglected. Indeed, the penetration depth of visible light in LMO crystal (< 1 μm) is much shorter than the crystal thickness ($t \approx 100$ μm), and both lengths are expected to be large compared the mean free path of carriers in LMO (< 1 μm).[32] We thus take $J_D \approx 0$. Assuming J_D and J_E are both negligible, we obtain as upper bound values: $G_{31} \approx 116$ pm/V and $G_{33} \approx 157$ pm/V [$I_0 \approx 15$ W/cm², $\alpha \approx 5$ μm⁻¹ (Table I)].

However, Eqs. [4.7, 4.9] are appropriate to describe BPE contribution in weakly absorbing materials, where the light attenuation and its tensorial character are not relevant. Obviously, this is not the case of *h*-LMO as dramatically shown by the in-plane incidence data in Fig. 4.8. In case of strongly absorbing and dichroic materials, derivation of appropriately modified $J_{sc}(\theta = 90°, \varphi)$ expression (along the *z*-axis) for in-plane incidence (Supplementary information S4.9) leads to Eq. [4.10]:

$$J_{sc} = \frac{I_0}{2S_2} \cdot \frac{S_d}{S_1} [(G_{33} - G_{31})\cos 2\varphi + (G_{33} + G_{31})] + J_E \qquad [4.10]$$

where S_d is the spot diameter; S_1, S_2 is the length along *x, y*-axis of the electrode, respectively; and the J_D is assumed again to be negligible. We note that Eq. [4.10] predicts that the current density decreases when increasing the length of the electrode, which is in agreement with the experimental evidence in Fig. 4.8(a). Moreover, it follows form Eq. [4.10] that the measured current (and the current density) are independent on the absorption length ($\approx 1/\alpha$), as far as $S_2 \gg 1/\alpha$, reflecting that all photoelectrons are created in a depth much smaller than the electrode size. Two limiting cases of Eq. [4.10] are of interest:

At $\theta \approx 90°$; $\varphi = 0°$ $\qquad\qquad\qquad J_{sc} = \frac{I_0}{S_2} \cdot \frac{S_d}{S_1} \cdot G_{33} + J_E$ $\qquad\qquad\qquad$ [4.11]

At $\theta \approx 90°$; $\varphi = 90°$ $\qquad\qquad\qquad J_{sc} = \frac{I_0}{S_2} \cdot \frac{S_d}{S_1} \cdot G_{31} + J_E$ $\qquad\qquad\qquad$ [4.12]

Using J_{sc} ($\theta \approx 90°$; φ) data of Fig. 4.8, collected with the indicated two different electrodes [J_{sc} ($\theta \approx 90°$; $\varphi = 0°$, A_1) ≈ 60 µA/cm², J_{sc} ($\theta \approx 90°$; $\varphi = 90°$, A_1) ≈ 42 µA/cm², $S_1 \approx 450$ µm, $S_2 \approx 270$ µm (Cry-2); and J_{sc} ($\theta \approx 90°$; $\varphi = 0°$, A_2) ≈ 26 µA/cm², J_{sc} ($\theta \approx 90°$; $\varphi = 90°$, $A2$) ≈ 16 µA/cm², $S_1 \approx 770$ µm, $S_2 \approx 480$ µm (Cry-3); $I_0 \approx 27.6$ W/cm², $S_d \approx 280$ µm], we obtain upper bounds assuming $J_E \approx 0$: $G_{31} \approx 660 - 765$ pm/V and $G_{33} \approx 943 - 1243$ pm/V. The corresponding average values are: $G_{31} \approx 713 \pm 53$ pm/V and $G_{33} \approx 1093 \pm 150$ pm/V. Taking into account the light attenuation, as expected, the bounds of Glass coefficients obtained using the strong-absorption limit are larger than those obtained above under the weak-absorption condition. In Table I we include the Glass coefficients G_{ij} together with the corresponding BPE tensor elements β_{ij} deduced in the weak-absorbing (WA) and strong-absorbing (SA) cases.
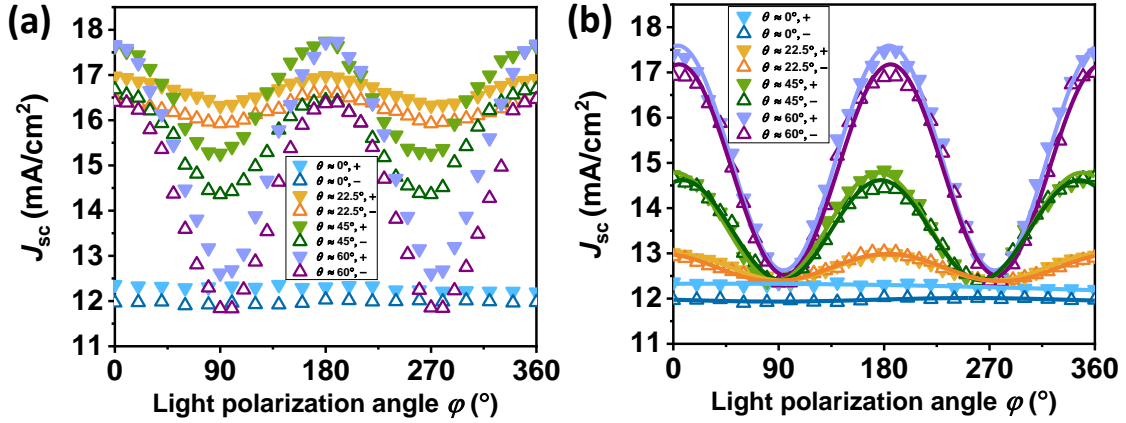
4.2.8. Switchable drift contribution

Fig. 4.9. Dependence of short circuit photocurrent $J_{sc}(\theta, \varphi)$ on the polarization of light (φ), at various incident angles (θ), of Cry-5 at pre-polarized to *P*-down and *P*-up states using (V_w^+/ V_w^- = ± 150 V)). Signs "+" and "−" signify positive and negative pre-polarizing voltage. Solid lines are fits using Eq. [4.3] to experimental data (symbols). Light intensity I_0 after optical plates and the top Pt is around 22.5 W/cm². Data for J_{sc} ($\theta \neq 0°$, φ) have been vertically shifted such as J_{sc} ($\theta \neq 0°$, $\varphi = 90°$) to coincide with J_{sc} ($\theta \neq 0°$, $\varphi = 90°$; V_w^+ = + 150 V)

We address in the following the contribution of J_E to the measured J_{sc}, that we have so far neglected. We first note that J_E is related to the presence of internal electric fields (depoling E_d) and others (imprint E_{im}, etc.) that give rise to a switchable J_E contribution (denoted here J_{E-sw}) and a unswitchable component respectively (denoted here J_{E-usw}) as discussed in Ref. 24. The J_{E-sw} contribution can be evaluated by performing and comparing J_{sc} measurements after pre-polarizing the sample up or down. With this aim, we recorded $J_{sc}(\theta, \varphi)$ as a function of the ferroelectric polarization (***P***) state of the sample to unravel the contribution of E_d to J_{sc}. A unipolar pre-poling voltage ($V_{w,max} > V_c$ coercive voltage of LMO) of different sign was applied to the top Pt electrode with a duration of ≈ 50 s, that is long enough to saturate the polarization of the sample [$P(E)$ loops were measured at 1 kHz].[24] After a delay time τ_d = 5 s, the short circuit photocurrent was recorded at various light polarization direction (φ) and incidence angle (θ). In Fig. 4.9(a), we show the raw J_{sc} data recorded as a function of θ and φ and measured after pre-poling the sample (Cry-5) with V_w = ± 150 V. Data for θ = 0° most clearly illustrate the dependence of J_{sc} on polarization direction, as expected in presence of J_{E-sw}, that modulates J_{sc} being J_{sc} slightly larger for V_w^+ ($P^\downarrow$) than for V_w^- ($P^\uparrow$) polarization. The same trend can be appreciated at any θ.

At normal incidence, the polarization vector of light ($E \perp c$) is perpendicular to the ferroelectric polarization ($P \parallel c$) and J_{sc} varies by about 3 % upon polarization reversal. When increasing the incidence angle (θ), that is when increasing the component of the light polarization along the z-axis, the P-dependence of the photocurrent slightly differ (3 % - 6 %), although being in all cases somewhat larger in P-down than in P-up. This difference is a signature of a switchable J_{E-sw} term, that at remanence and depends on the direction of ferroelectric polarization which affects the internal electric field in h-LMO and thus J_{sc}. As already reported, polarization-modulated Schottky barriers at LMO/electrode interfaces[24] allow to modulate the photocurrent upon P switching. As observed, at remanence, J_{sc} is modified by less than 10 %, and thus the BPE coefficient extracted using Eq. [4.9, 4.10] above is only accurate within a 10 %.

To discern any possible effect of the ferroelectric polarization direction on the amplitude of the $J_{sc}(\theta, \varphi)$ oscillations, while minimizing experimental artifacts occurring when changing the incidence angle, the slope subtracted data of Fig. 4.9(a) has been normalized, as in Fig. 4.5, by a vertical shift to coincide at $\varphi = 90°$ with $J_{sc}(\theta = 0°, \varphi = 90°)$ data collected at $V_w = +150$ V and shown in Fig. 4.9(b). It appears that the amplitude of the $J_{sc}(\varphi)$ oscillations are also slightly modulated by the P direction (4 % - 7 %), which can only be attributed to the J_{BPE} but not the J_{E-sw}. However, available data does not allow to discern if this variation is genuine or results from spurious effects, which will be discussed in detail in the next section 4.3.

In summary, the switchable component of the drift photocurrent (J_{E-sw}) is only about (3 - 6) % of the measured J_{sc}. It follows that the photocurrent in these LuMnO₃ crystals is governed by the contributions of J_{BPE} and J_{E-usw}. At normal incidence, both contributions cannot be disentangled and thus J_{BPE} can be any value within (0 - 100 %) of J_{sc}. Nevertheless, at oblique incidence, the observation of obvious oscillations depending on the polarization angles, allows to set minimal values for J_{PBE}, that reaches up to 34 % at grazing incidence (Supplementary information S4.10).

We end by comparing the Glass coefficients (G_{ij}) and the corresponding tensor elements ($\beta_{ij} = \alpha_{jk}G_{ij}$) of h-LMO determined above (summarized in table I) with the corresponding data reported in the weakly absorbing and isostructural ZnO and in the

intensively studied strongly absorbing $BiFeO_3$. It can be appreciated in table I that the Glass coefficients of *h*-LMO, having the same symmetry class than ZnO, are much larger. This fact is likely related to the different nature of valence and conduction bands and the corresponding optical transitions. Being the symmetry classes of *h*-LMO and *r*-$BiFeO_3$ different (6*mm* and 3*m*, respectively), the corresponding tensor elements cannot be easily compared. However, the observation of larger β_{ij} and G_{ij} values in *h*-LMO than in $BiFeO_3$ reflects the important role of the trigonal and octahedral crystal field splitting setting the corresponding excited states and their impact on BPE.

Material	S.G./S.C.	Method	β_{ij} (kV^{-1})	G_{ij} (pm/V)	α (μm^{-1})
$LuMnO_3$ (λ = 405 nm)	$P6_3cm$/ 6mm	Oblique incidence WA	$\beta_{31} \leq 0.581$ $\beta_{33} \leq 0.783$	$G_{31} \leq 116$ $G_{33} \leq 157$	≈ 5[27]
		In-plane incidence SA	$\beta_{31} \leq 1.283$ $\beta_{33} \leq 8.744$	$G_{31} \leq 713$ $G_{33} \leq 1093$	$\alpha_\perp \approx 1.8$[27] $\alpha_\parallel \approx 8$[27]
ZnO (λ = 460 nm)	$P6_3cm$/ 6mm			$G_{31} \approx 2$ $G_{33} \approx 20$[33]	0.0002[33]
$BiFeO_3$ (λ = 405 nm)	$R3c$/ 3m		$\beta_{15} \approx 0.05 - 0.07$[9,12,34] $\beta_{22} \approx 0.11 - 0.2$[12,34] $\beta_{31} \approx 0.1 - 0.18$[9,12,34] $\beta_{33} \approx 0.1 - 0.3$[9,12,34]	$G_{15} \approx 0.5 - 4$[9,12] $G_{22} \approx 4.5 - 7.8$[10,12] $G_{31} \approx 6 - 6.5$[9,12] $G_{33} \approx 5 - 16$[9,12]	6.04[30] (λ = 405 nm) 25[10] (λ = 435 nm)

Table I. The photovoltaic tensor elements (β_{ij}) and the Glass coefficients (G_{ij}) of *h*-$LuMnO_3$, evaluated in weak-absorbing (WA) and strong-absorbing limits (SA), determined using 58 x 58 μm^2 electrodes, from data collected at normal incidence and extrapolated grazing incidence. Data for $BiFeO_3$ and ZnO are also included. The corresponding absorption coefficients at the indicated wavelength (λ) indicated. The "≤" symbol in β_{ij} and G_{ij} data of $LuMnO_3$ indicates that J_E contribution may be higher.

4.2.9. Conclusions

We have measured the photoresponse of ferroelectric *h*-$LuMnO_3$ crystals along the hexagonal *c*-axis using Pt electrodes, using oblique and in-plane light incidence. The analysis of the dependence of J_{sc} on the polarization direction of the incoming light and its incident

angle $J_{sc}(\theta, \varphi)$ at different wavelength, have provided consistent data revealing a clear contribution arising from BPE. It turns out that J_{sc} is the largest when the polarization axis of the light is parallel to the polar hexagonal axis. Short circuit photocurrent measurements using in-plane light incidence, have also provide evidence of the impact of the strong optical absorption on the out-of-plane photocurrent density, most noticeable in the inverse dependence on the electrode area. The presence of a contributions to J_{sc} that does not originate from BPE but are related to drift currents implies that only bounds for the Glass coefficients and tensor elements can be given. In spite of these caveats, the BPE coefficients β_{ij} and G_{ij} are significantly larger than other photoferroelectrics, such as $BiFeO_3$, suggesting possible advantages for photoconversion.

Supplementary information

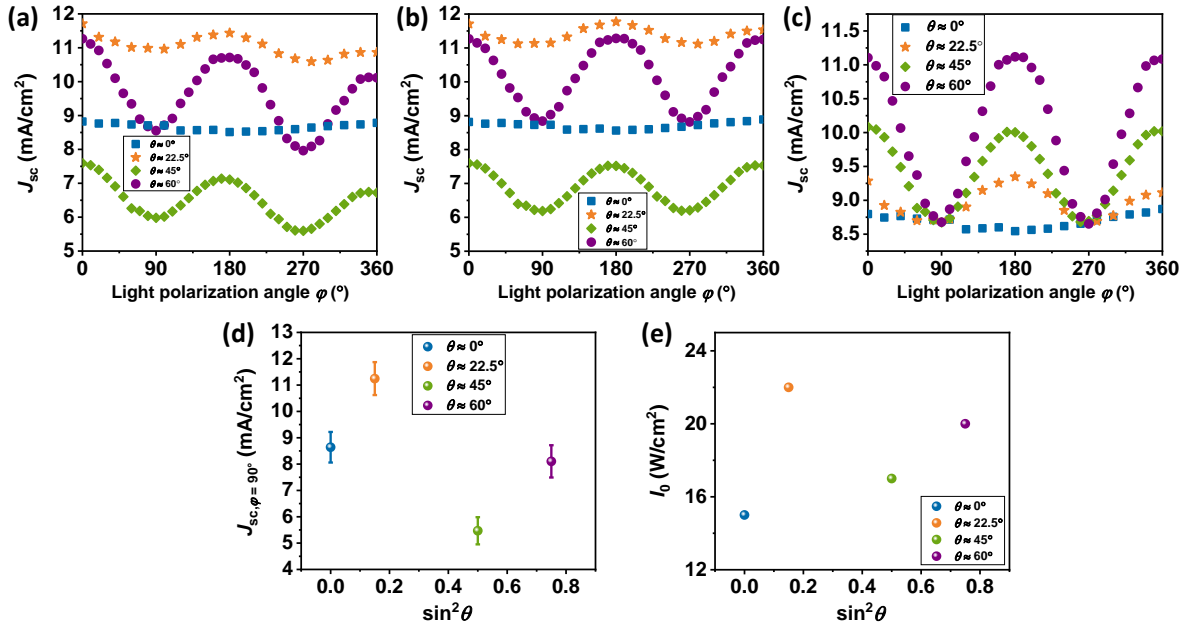## S4.4. Normalization of the angular dependence of short circuit current

Fig. S4.4. The (a) raw data of $J_{sc}(\theta, \varphi)$, (b) slope subtracted $J_{sc}(\theta, \varphi)$ and (c) vertical shifted $J_{sc}(\theta, \varphi)$ with respect to $J_{sc}(\varphi = 90°, \theta = 90°)$, respectively, along the z-axis versus the polarization angles (φ) of the light at different incident angles, of Cry-5. Dependence of the (d) raw data of $J_{sc}(\theta, \varphi = 90°)$ and (e) light intensity I_0 reached to the crystal on $\sin^2(\theta)$. Error bars in Fig. S1(d) indicate the spread of values (SD) from data recorded in 6 capacitors.

Fig. 4.5(a) is obtained by subtracting the slope extracted by points at $\varphi = 90°$ and $\varphi = 270°$ of the raw data in Fig S4.4(a), because the conditions (polarization and intensity) of light and the J_{sc} values at any two points shifted by 180° should be the same, if there is no deviation of plate fast axes of optical setups. This slope exists due to small misalignments of optical plates that result in a small variation of the light intensity while rotating φ, which results in a variation of the background current. The slope-subtracted result is shown in Fig. S4.4(b)

At $\varphi = 90°$, there is only perpendicular $\alpha_\perp$ being constant with increasing θ. Based on Eq. [4.9], at $\varphi = 90°$, J_{sc} (= $I_0\alpha G_{31}$+ J_E + J_D) should be constant and irrelevant to θ, thus Fig S4.4(c) is obtained by vertical shifting the data in Fig S4.4(b) with reference to $J_{sc}(\varphi = 90°, \theta = 0°)$. In Fig. S4.4(d) the original $J_{sc}(\varphi = 90°, \theta = 0°)$ before subtraction is plotted as a function

of the $\sin^2\theta$. This value is expected to be constant for any $\sin^2\theta$ value, as mentioned. In Fig. S4.4(e), the value of the light fluence as a function $\sin^2\theta$ is also plotted. It can be observed that the trend in Figs. S4.4(d,e) are similar pointing to the fact that the found variations on $J_{sc}(\varphi = 90°, \theta = 0°)$ result from unavoidable variation of effective light fluence in different experimental set-up at each incidence. The small discrepancy between Figs. S4.4(d,e) results from the artifacts and intrinsic error present in the measurement of the laser fluence. Here the Fresnel contribution is fully neglected, note that if Fresnel dominates, the $J_{sc}(\varphi = 45°)$ but not $J_{sc}(\varphi = 90°)$ should be constant, thus this background shift is not accurate and may hide the Fresnel contribution as will show in detail in Chapter 6. However, as mentioned in Chapter 3.5, the discrepant illumination state at different optical installation prevents easy comparison of the absolute B_z (J_{sc}) values between them.

Similarly, the V_{oc} values in Fig. 4.5(b) are also normalized to make the $J_{sc}(\theta)$ overlap at $\varphi = 90°$ with reference to $J_{sc}(\varphi = 90°, \theta = 0°)$.

S4.5. Rectifying response of the Pt/LMO/Pt device

Fig. S4.5 show the *J-V* of the Pt/LMO/Pt device. It can be observed that for negative bias the current is larger. This is expected for a *p*-type/metal junction. Thus, LMO acts as a *p*-type semiconductor as expected.[35] This disregards the important contribution of the Pt bottom electrode, which covers the whole crystal back surface.
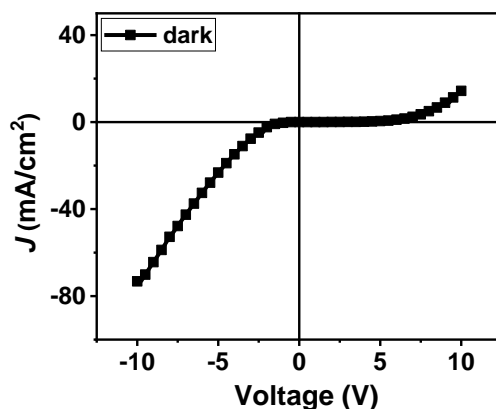
Fig. S4.5. *J-V* curves of Cry-5 in dark.

S4.6. $J(\varphi)$ measured under illumination of multiwavelength
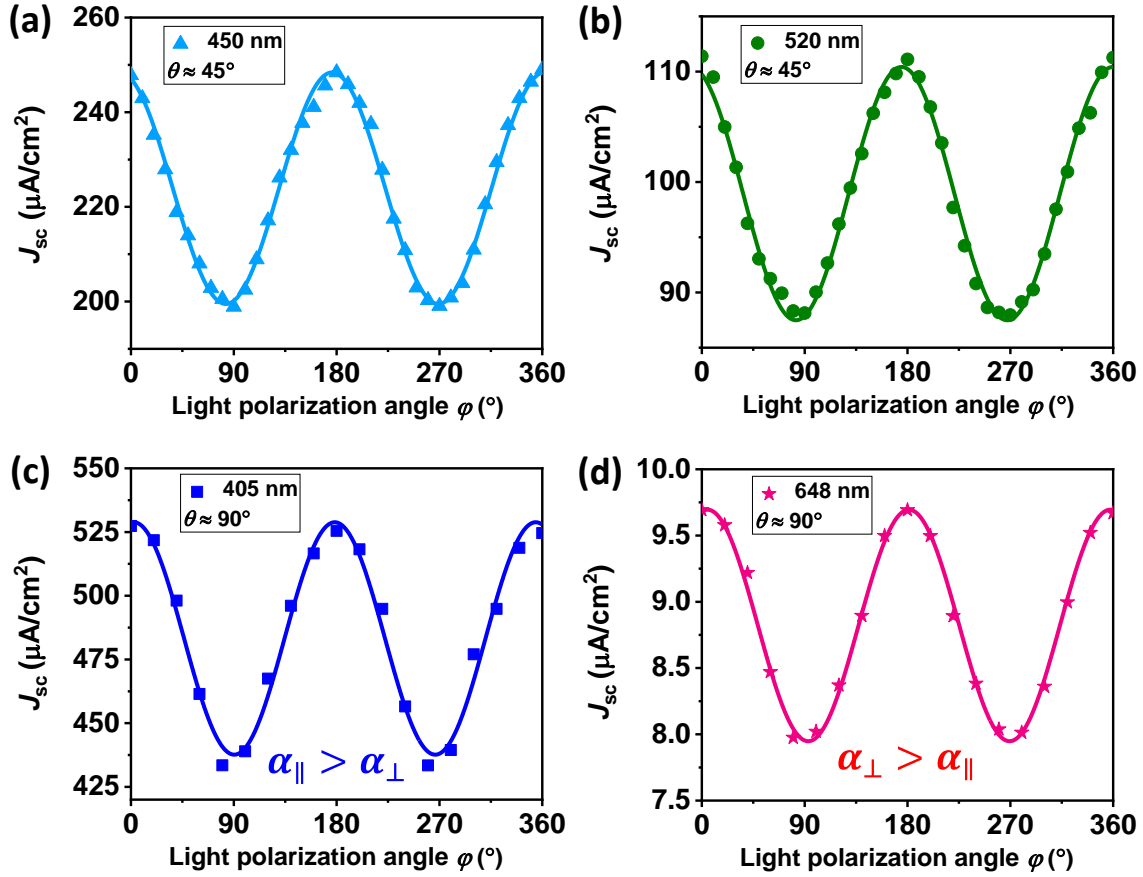
Fig. S4.6. $J_{sc}(\varphi)$ measured at $\theta \approx 45°$ incidence (Cry-5) recorded at (a) 450 nm and (b) 520 nm; light intensity I_0 after optical plates and the top Pt is around 0.6 W/cm². $J_{sc}(\varphi)$ measured at $\theta \approx 90°$ in-plane incidence (Cry-8) recorded at (c) 405 nm and (d) 648 nm; light intensity I_0 after optical plates is around 27.6 W/cm² and 6 W/cm² respectively. Solid lines are fits using Eq. [4.3] of experimental data (symbols).

S4.7. Derivation of $J_{BPE}(\theta, \varphi)$ in a non(weak)-absorbing material with $P6_3cm$ symmetry

The dependence of the J_{sc} on the light polarization is a fingerprint of a contribution of the bulk photovoltaic effect (BPE) to the short-circuit photocurrent. In the BPE scenario, the short circuit photocurrent effect ($J_{sc,BPE}$) is given by Eq. [4.6], here repeated for convenience as Eq. [S4.1]:

$$J_{BPE,i} = I_0 \cdot \alpha_{jk} \cdot G_{ijk} \cdot e_j e_k = I_0 \cdot \beta_{ijk} \cdot e_j e_k \qquad [S4.1]$$

For *h*-LMO (space group *P*6$_3$cm), assuming a relatively weak absorption anisotropy (i.e., $\alpha_{jk} \approx \alpha$) and an uniform absorption in the crystal[10], Eq. [S4.1] can be written as:

$$\begin{pmatrix} J_x \\ J_y \\ J_z \end{pmatrix} = I_0 \begin{pmatrix} 0 & 0 & 0 & 0 & \beta_{15} & 0 \\ 0 & 0 & 0 & \beta_{15} & 0 & 0 \\ \beta_{31} & \beta_{31} & \beta_{33} & 0 & 0 & 0 \end{pmatrix} \begin{pmatrix} e_x^2 \\ e_y^2 \\ e_z^2 \\ e_y e_z \\ e_z e_x \\ e_x e_y \end{pmatrix} = I_0 \alpha \begin{pmatrix} G_{15} e_z e_x \\ G_{15} e_y e_z \\ G_{31} e_x^2 + G_{31} e_y^2 + G_{33} e_z^2 \end{pmatrix}$$

[S4.2]

where ($e_{x,y,z}$) are the components of the light polarization incoming along $\boldsymbol{k}$. In our experimental arrangement [Fig. 3.5(a,b)]: $e_x = \sin(\varphi)$, $e_y = \cos(\varphi)\cos(\theta)$ and $e_z = \cos(\varphi)\sin(\theta)$, thus BPE (Eq. [S4.2]) predicts an angular and polarization dependence of $J_{\text{BPE}}(\theta, \varphi)$ given by

$$\begin{pmatrix} J_x \\ J_y \\ J_z \end{pmatrix} = I_0 \alpha \begin{pmatrix} \frac{1}{2} G_{15} \sin\theta \sin 2\varphi \\ \frac{1}{4} G_{15} \sin 2\theta \ (1 + \cos 2\varphi) \\ \frac{G_{33} - G_{31}}{2} \sin^2\theta \cos 2\varphi + \frac{G_{33} - G_{31}}{2} \sin^2\theta + G_{31} \end{pmatrix}$$

[S4.3]

According to Eq. [S4.3] J_{BPE} along the *z*-axis has a cos(2φ) waveform as

$$J_{\text{BPE}} = I_0 \alpha \ (\frac{G_{33} - G_{31}}{2} \sin^2\theta \cos 2\varphi + \frac{G_{33} - G_{31}}{2} \sin^2\theta + G_{31})$$

[S4.4]

S4.8. In-plane illumination J_{sc} (φ) measurements

In Fig. S4.8 (a), the J_{sc} (φ) dependence for in-plane illumination of bare and capped electrode is shown. The brown circles display the photocurrent measured using the bare A_2 = 0.37 mm^2 electrode (as in main text), while the red circles depict the photocurrent measured after capping the A_2 = 0.37 mm^2 top electrode by suitable photo absorbing cover (even though the perfect overcover cannot be assured). It can be appreciated that the measured photocurrent is basically constant, as expected from exclusively lateral illumination.
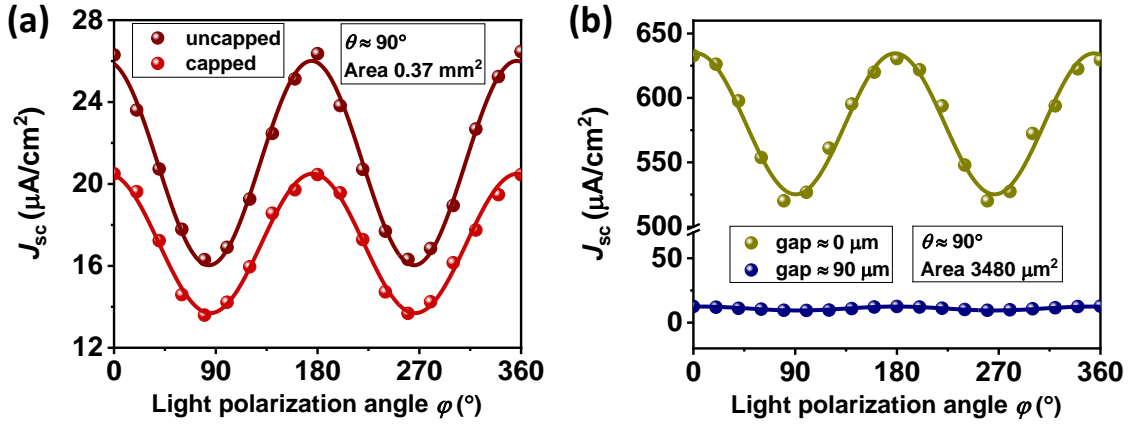
Fig. S4.8 (a) Dependence of the short circuit photocurrent on polarization angles (φ) of the light with in-plane incidence ($\theta \approx 90°$, Cry-7) of uncapped and capped top electrode with gap $D = 0$. (b) Dependence of the short circuit photocurrent of the light with in-plane incidence ($\theta \approx 90°$, Cry-8) on the distance of electrodes to the sample edge. Solid lines are fits using Eq. [1] of experimental data (symbols). Light intensity I_0 after optical plates is around 27.6 W/cm².

In Fig. S4.8 (b), the J_{sc} (φ) dependence for in-plane illumination with different edge-electrode distance (gap D) is shown. It can be seen that the photocurrent measured with a 90 μm gap is near zero. This results from the fact that the photocarrier generation is limited to a narrow region of depth < 1 μm and recombination limits charge extraction at distant electrodes. Note that here the absolute photocurrent is around 3 - 4 times smaller than that of Fig. 4.8. Using Eq. [S4.14] and J_{sc} ($\theta \approx 90°$, φ) data of Fig. S4.8(b) collected for 0 gap [J_{sc} ($\theta \approx 90°$; $\varphi = 0°$) ≈ 635 μA/cm², J_{sc} ($\theta \approx 90°$; $\varphi = 90°$) ≈ 520 μA/cm², $S_1 = S_2 \approx 59$ μm, $I_0 \approx 27.6$ W/cm²], Glass coefficients (upper bounds) of $G_{31} \approx 1112$ pm/V and $G_{33} \approx 1357$ pm/V are obtained. These values are comparable with the in-plane SA case in the main text.

S4.9. Derivation of $J_{BPE}(\theta, \varphi)$ in an anisotropic strongly absorbing material with $P6_3cm$ symmetry

We attempt in the following to derive the BPE response of LuMnO₃ by taking into account the strong anisotropic (dichroism) of LuMnO₃.

For uniaxial system along the *z*-axis, optical absorption is given by:

$$\alpha_\perp = \frac{2\kappa_\perp \omega}{c} = \frac{4\pi\kappa_\perp}{\lambda}; \ \alpha_\parallel = \frac{2\kappa_\parallel \omega}{c} = \frac{4\pi\kappa_\parallel}{\lambda} \qquad \text{[S4.5]}$$

where $\alpha_\perp$ and $\alpha_\parallel$ denote the absorption for the different component of the light electric field, namely: $\overrightarrow{E_{\perp z}}$ and $\overrightarrow{E_{\parallel z}}$, respectively.
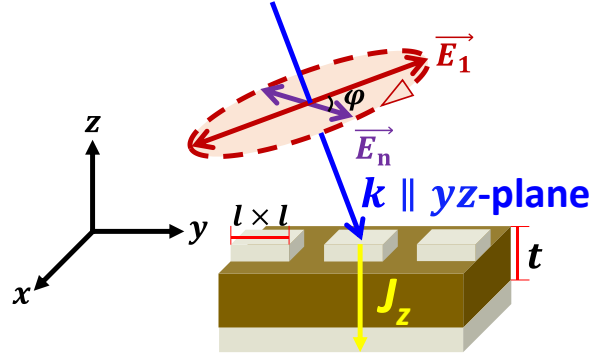
Fig. S4.9.1. Sketch illustrates the experimental arrangement of oblique incidence (θ). The length of the top electrode square ($l \times l$) is $l \approx 58$ μm; the thickness of the crystal is $t \approx 100$ μm.

In general, $(\overrightarrow{e_{x,y,z}})$ are the components (unit vectors) along *x,y,z*-axes of the light polarization of amplitude $|E_0|$ incoming along $\boldsymbol{k}$, that will suffer different absorption. In our experimental arrangement (Fig. S4.9):

$$\overrightarrow{e_1} = \overrightarrow{e_x}|E_0|\sin\varphi\, e^{-\left(\frac{\alpha_\perp x}{2}\right)}e^{i(kx-\omega t)} \qquad \text{[S4.6]}$$

$$\overrightarrow{e_2} = \overrightarrow{e_y}|E_0|\cos\varphi\cos\theta\sin\varphi\, e^{-\left(\frac{\alpha_\perp y}{2}\right)}e^{i(ky-\omega t)} \qquad \text{[S4.7]}$$

$$\overrightarrow{e_3} = \overrightarrow{e_z}|E_0|\cos\varphi\sin\theta\sin\varphi\, e^{-\left(\frac{\alpha_\parallel z}{2}\right)}e^{i(kz-\omega t)} \qquad \text{[S4.8]}$$

In the present case, having LuMnO$_3$ a strong absorption, $\left|E_{x,y,z}(r)\right| = g(\theta,\varphi)|E_0|e^{-\left(\frac{\alpha_{\parallel,\perp} r}{2}\right)}$ with the angular dependence $g(\theta,\varphi)$ identified in [S4.6-S4.7], becomes a function of penetration depth. Therefore, the Eq [S4.2] needs to be modified by explicitly expressing the depth-dependence of the light intensity.

$$\begin{pmatrix} J'_x \\ J'_y \\ J'_z \end{pmatrix} = I_0 \begin{pmatrix} \beta_{15}e_1 e_3^* \\ \beta_{15}e_2 e_3^* \\ \beta_{31}e_1 e_1^* + \beta_{31}e_2 e_2^* + \beta_{33}e_3 e_3^* \end{pmatrix} \qquad \text{[S4.9]}$$

According to the experimental arrangement used in which we have measured J_z, for simplicity we limit the derivation only at one specific case: in-plane incidence, that is θ = 90°.
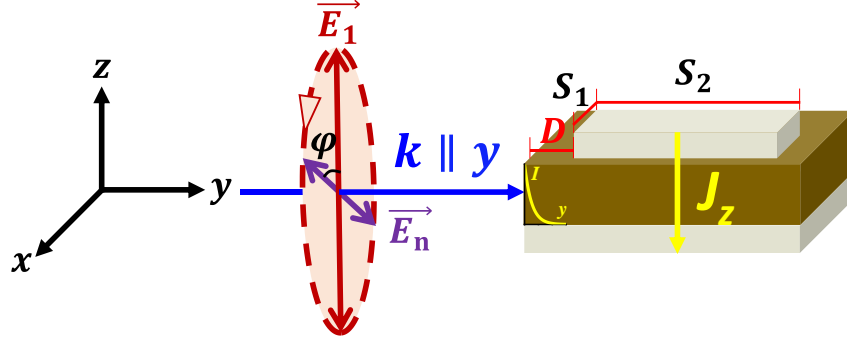
Fig. S4.9.2. Sketch of the experimental arrangement used to measure the photocurrent along the z-axis (J_z), when the sample is illuminated in-plane (k ∥ y; θ = 90°). The profile (decay) of light intensity is indicated by the yellow *I-y* curve. The length of the top electrode (S_1 x S_2) along the propagation direction of light is S_2; the gap between the crystal lateral surface and the top electrode is D (<< 1 µm).

According to Eqs. [S4.6, S4.8], the electric field of the light propagating along k ∥ y is:

$$\overrightarrow{E_{k\|y}} = |E_0|\left[\overrightarrow{e_x}\sin\varphi\, e^{-\left(\frac{\alpha_\perp y}{2}\right)}e^{i(ky-\omega t)} + \overrightarrow{e_z}\cos\varphi\, e^{-\left(\frac{\alpha_\| y}{2}\right)}e^{i(ky-\omega t)}\right] \qquad \text{[S4.10a]}$$

$$\equiv |E_0|[\overrightarrow{e_x}e_1 + \overrightarrow{e_z}e_3] \qquad \text{[S4.10b]}$$

By Eqs. [S4.9, S4.10], the current density produced by photoabsorption in a differential volume $dxdydz$ is[10]:

$$J_z' = I_0(\beta_{31}e_1e_1^* + \beta_{33}e_3e_3^*) = I_0\left[\beta_{31}\sin^2\varphi\, e^{-(\alpha_\perp y)} + \beta_{33}\cos^2\varphi\, e^{-(\alpha_\| y)}\right] \qquad \text{[S4.11]}$$

The current through a differential area *dxdy* is:

$$I_z' = J_z'dxdy$$

In our experimental setup, the electrode widths $S_1 \approx$ 450 µm and 770 µm of Cry-2 and Cry-3 (in the main text) are bigger than the spot diameter $S_d \approx$ 280 µm, thus the interval of integration along *dx* should be [0, S_d]. The total current through the lateral face S_1t is:

$$I_z = \int_{0,0}^{x=S_{\mathrm{d}}, y=S_2} J_z' \, dxdy$$

Assuming that the electrode is at the sample edge ($D \approx 0$), the current density is:

$$J_z = \frac{I_0 \int_{0,0}^{x=S_{\mathrm{d}}, y=S_2} \left[\beta_{31}\sin^2\varphi\, e^{-(\alpha_{\perp}y)} + \beta_{33}\cos^2\varphi\, e^{-(\alpha_{\parallel}y)}\right]dxdy}{S_1 \cdot S_2}$$

$$= \frac{I_0}{2S_2} \cdot \frac{S_{\mathrm{d}}}{S_1}\left\{\left[\beta_{33}\frac{1-e^{-(\alpha_{\parallel}S_2)}}{\alpha_{\parallel}} - \beta_{31}\frac{1-e^{-(\alpha_{\perp}S_2)}}{\alpha_{\perp}}\right]\cos2\varphi + \left[\beta_{33}\frac{1-e^{-(\alpha_{\parallel}S_2)}}{\alpha_{\parallel}} + \beta_{31}\frac{1-e^{-(\alpha_{\perp}S_2)}}{\alpha_{\perp}}\right]\right\}$$

[S4.12]

In the limit of large electrodes: $\alpha_{\parallel}S_2 \gg 1$ and $\alpha_{\perp}S_2 \gg 1$:

$$J_z = \frac{I_0}{2S_2} \cdot \frac{S_{\mathrm{d}}}{S_1}\left\{\left[\beta_{33}\frac{1}{\alpha_{\parallel}} - \beta_{31}\frac{1}{\alpha_{\perp}}\right]\cos2\varphi + \left[\beta_{33}\frac{1}{\alpha_{\parallel}} + \beta_{31}\frac{1}{\alpha_{\perp}}\right]\right\}$$

$$= \frac{I_0}{2S_2} \cdot \frac{S_{\mathrm{d}}}{S_1}\left[(G_{33} - G_{31})\cos2\varphi + (G_{33} + G_{31})\right]$$

[S4.13]

When the electrode width $S_1 = S_2 \approx 59$ µm of Cry-8 (in Supplementary information S4.8) is smaller than $S_{\mathrm{d}} \approx 280$ µm, thus the interval of integration along dx should be $[0, S_1]$ and Eq. [S4.13] becomes:

$$J_z = \frac{I_0 \int_{0,0}^{x=S_1, y=S_2} \left[\beta_{31}\sin^2\varphi\, e^{-(\alpha_{\perp}y)} + \beta_{33}\cos^2\varphi\, e^{-(\alpha_{\parallel}y)}\right]dxdy}{S_1 \cdot S_2}$$

$$= \frac{I_0}{2S_2}\left[(G_{33} - G_{31})\cos2\varphi + (G_{33} + G_{31})\right]$$

[S4.14]

Note: In Eq. [S4.13, S4.14] the size of the electrode appears explicitly at the denominator.

S4.10. The contribution of drift and bulk photovoltaic effect

The upper limits of $J_{\mathrm{BPE}}(\theta, \varphi)$ (or alternatively the upper limits of G_{ij} indicated in Table I) can be obtained by assuming J_E, $J_D = 0$ (B_z only comes from J_{BPE}). On the premise of ignoring the Dichroism and Fresnel contribution identified by the multiwavelength and in-plane incidence measurements, the well visible oscillations ($G_{33} - G_{31}$) of J_{sc} are only ascribed to BPE. Therefore, J_{BPE} cannot be zero, by assuming $G_{31} = 0$ (B_z only comes from J_E, J_D), the

lower bounds of $J_{BPE}(\theta, \varphi)$ can be derived from the amplitudes of J_{sc} oscillations (Figs. 4.5 and 4.8).

Therefore, at 405 nm, the correlation of the three contributions in $J_{sc}(\theta, \varphi = 0°)$ can be deduced as below:

θ	(J_E+J_D) (mA/cm^2)	J_{BPE} (mA/cm^2)	$(J_E+J_D)/J_{sc}$	J_{BPE}/J_{sc}
0°	0 - 8.72	0 - 8.72	0 - 100 %	0 - 100 %
22.5°	0 - 8.72	0.44 - 9.16	0 - 95.2 %	4.8 % - 100 %
45°	0 - 8.72	1.52 - 10.24	0 - 85.2 %	14.8 % - 100 %
60°	0 - 8.72	2.27 - 10.99	0 - 79.3 %	20.7 % - 100 %
90°	0 - 0.029	0.015 - 0.044	0 - 65.9 %	34.1 % - 100 %

Bibliography

[1] A.M. Glass, D. von der Linde, and T.J. Negran, Appl. Phys. Lett. **25**, 233 (1974).

[2] W.T.H. Koch, R. Munser, W. Ruppel, and P. Würfel, Solid State Commun. **17**, 847 (1975).

[3] V.M. Fridkin and B.N. Popov, Sov. Phys. Uspekhi **21**, 981 (1978).

[4] T. Choi, S. Lee, Y.J. Choi, V. Kiryukhin, and S.-W. Cheong, Science (80-.). **324**, 63 (2009).

[5] S.Y. Yang, J. Seidel, S.J. Byrnes, P. Shafer, C.-H. Yang, M.D. Rossell, P. Yu, Y.-H. Chu, J.F. Scott, J.W. Ager, L.W. Martin, and R. Ramesh, Nat. Nanotechnol. **5**, 143 (2010).

[6] R. Nechache, C. Harnagea, S. Li, L. Cardenas, W. Huang, J. Chakrabartty, and F. Rosei, Nat. Photonics **9**, 61 (2015).

[7] L. You, F. Zheng, L. Fang, Y. Zhou, L.Z. Tan, Z. Zhang, G. Ma, D. Schmidt, A. Rusydi, L. Wang, L. Chang, A.M. Rappe, and J. Wang, Sci. Adv. **4**, eaat3438 (2018).

[8] B. Sturman and V.M. Fridkin, *The Photovoltaic and Photorefractive Effects in Noncentrosymmetric Materials* (Gordon and Breach Science Publishers, Philadelphia, 1992).

[9] A. Bhatnagar, A. Roy Chaudhuri, Y. Heon Kim, D. Hesse, and M. Alexe, Nat. Commun. **4**, 2835 (2013).

[10] W. Ji, K. Yao, and Y.C. Liang, Phys. Rev. B **84**, 094115 (2011).

[11] B.M. Fregoso, T. Morimoto, and J.E. Moore, Phys. Rev. B **96**, 075421 (2017).

[12] S.M. Young, F. Zheng, and A.M. Rappe, Phys. Rev. Lett. **109**, 236601 (2012).

[13] L.Z. Tan, F. Zheng, S.M. Young, F. Wang, S. Liu, and A.M. Rappe, Npj Comput. Mater. **2**, 16026 (2016).

[14] R. Fei, W. Song, and L. Yang, Phys. Rev. B **102**, 035440 (2020).

[15] B.I. Sturman, Physics-Uspekhi **63**, 407 (2020).

[16] J. Fontcuberta, Comptes Rendus Phys. **16**, 204 (2015).

[17] B. Lorenz, ISRN Condens. Matter Phys. **2013**, 1 (2013).

[18] C. Degenhardt, M. Fiebig, D. Fröhlich, T. Lottermoser, and R.V. Pisarev, Appl. Phys. B **73**, 139 (2001).

[19] W. Wang, H. Wang, X. Xu, L. Zhu, L. He, E. Wills, X. Cheng, D.J. Keavney, J. Shen, X. Wu, and X. Xu, Appl. Phys. Lett. **101**, 241907 (2012).

[20] H. Han, S. Song, J.H. Lee, K.J. Kim, G.-W. Kim, T. Park, and H.M. Jang, Chem. Mater. **27**, 7425 (2015).

[21] H. Han, D. Kim, K. Chu, J. Park, S.Y. Nam, S. Heo, C.-H. Yang, and H.M. Jang, ACS Appl. Mater. Interfaces **10**, 1846 (2018).

[22] H. Han, D. Kim, S. Chae, J. Park, S.Y. Nam, M. Choi, K. Yong, H.J. Kim, J. Son, and H.M. Jang, Nanoscale **10**, 13261 (2018).

[23] X. Huang, T.R. Paudel, S. Dong, and E.Y. Tsymbal, Phys. Rev. B **92**, 125201 (2015).

[24] Y. Sheng, I. Fina, M. Gospodinov, and J. Fontcuberta, Appl. Phys. Lett. **118**, 232902 (2021).

[25] P. Würfel, *Physics of Solar Cells* (Wiley, 2005).

[26] A.F. Lima and M.V. Lalic, Opt. Mater. (Amst). **64**, 406 (2017).

[27] R. Schmidt-Grund, S. Richter, S.G. Ebbinghaus, M. Lorenz, C. Bundesmann, and M. Grundmann, RSC Adv. **4**, 33549 (2014).

[28] A.M. Kalashnikova and R. V. Pisarev, J. Exp. Theor. Phys. Lett. **78**, 143 (2003).

[29] M. de Jong, W. Chen, H. Geerlings, M. Asta, and K.A. Persson, Sci. Data **2**, 150053 (2015).

[30] S. Nakashima, K. Takayama, T. Uchida, H. Fujisawa, and M. Shimizu, Jpn. J. Appl. Phys. **54**, 10NA16 (2015).

[31] V.M. Fridkin, *Photoferroelectrics* (Springer Berlin Heidelberg, Berlin, Heidelberg, 1979).

[32] L. Wang, Y. Li, A. Bera, C. Ma, F. Jin, K. Yuan, W. Yin, A. David, W. Chen, W. Wu, W. Prellier, S. Wei, and T. Wu, Phys. Rev. Appl. **3**, 064015 (2015).

[33] V.M. Fridkin, E.P. Efremova, B.H. Karimov, V.A. Kuznezov, I.P. Kuzmina, A.N. Lobachev, V.G. Lazarev, and A.J. Rodin, Appl. Phys. **25**, 77 (1981).

[34] M.-M. Yang, A. Bhatnagar, Z.-D. Luo, and M. Alexe, Sci. Rep. **7**, 43070 (2017).

[35] S.H. Skjærvø, E.T. Wefring, S.K. Nesdal, N.H. Gaukås, G.H. Olsen, J. Glaum, T. Tybell, and S.M. Selbach, Nat. Commun. **7**, 13745 (2016).

4.3. Bulk photovoltaic effect modulated by ferroelectric polarization back-switching

It is found in the last section 4.2 that the amplitudes of $J_{sc}(\varphi)$ oscillations appear to depend on the polarization state of the sample. In this section, how the ferroelectric polarization direction in h-LuMnO₃ crystals affects the oscillating photocurrent $J_{sc}(\varphi)$ is explored. It is shown that after pre-poling the crystal at saturation, at remanence, the direction and amplitude of photocurrent oscillations are no longer dictated by pre-poling voltage but are largely modulated by polarization back-switching, here ruled by the imprint field. Thus, the light polarization dependence of photocurrent is also ruled by the imprint field. The impact of these effects on the determination of the Glass coefficients of the material is discussed.

The work presented in this section was published in Appl. Phys. Lett. 120, 242901 (2022); https://doi.org/10.1063/5.0094837.

4.3.1. Introduction

Bulk photovoltaic effect (BPE) occurs in non-centrosymmetric materials.[1-4] In recent years, interest on BPE has been renewed mainly because the open circuit voltage is not limited by the band gap of the absorber, but can be orders of magnitude larger.[5] BPE is governed by optically induced excitations between ground and excited states, most commonly assumed to be the valence and conduction bands, although contribution of in-gap states to BPE has been reported.[6] The BPE photocurrent under illumination of a linearly polarized light is given by $J_{BPE,i} \approx \boldsymbol{G_{ijk}e_je_k}$, where $J_{BPE,i}$ denotes the BPE photocurrent density measured along i direction, and $e_{j,k}$ are the light polarization components along j, k directions.[7] The symmetry of Glass tensor $\{\boldsymbol{G_{ijk}}\}$ collects the point symmetry of the studied material[8] and the values of its elements which depend on photon energy, are dictated by specific features of the electronic band structure.[9] As a result, there is a genuine dependence of short circuit current density (J_{sc}) on the polarization of the incoming photons.

The determination of the G_{ijk} elements involves measuring J_{sc} along different directions (i,j,k) when the sample is illuminated with light of a given wavelength (λ) at different incidence angles (θ) with respect to the normal to sample surface and different polarization

angles (φ). Typically, an oscillating $J_{sc}(\theta, \varphi)$ behavior is observed, whose details depend on the symmetry-related structure, illumination configuration and the values of the G_{ijk} elements.

When measuring the J_{sc} in ferroelectric materials, several contributions may exist and be entangled. Other than J_{BPE}, drift photocurrent (J_E) arising from internal fields of various sources [i.e Schottky (E_{bi}), depoling (E_d), imprint (E_{im}), etc.] and a diffusion term (J_D) associated to photoinduced charge gradients, may coexist and contribute to the measured J_{sc}.[10,11] Discerning these different contributions to J_{sc} (= J_{BPE} + J_E + J_D), particularly J_{BPE} and J_E requires to know the ferroelectric polarization $\boldsymbol{P}$ state when J_{sc} is measured.[12] This seemingly a simple requirement at first sight, in practice could be difficult to achieve. Indeed, the presence of E_d and E_{im} may hinder keeping the polarization at saturated state,[13,14] and at remanence when J_{sc} is measured, polarization back-switching may have occurred leading to a ferroelectric multidomain state or even reversing the overall polarization.[15] As reversing the ferroelectric $\boldsymbol{P}$ is equivalent to a spatial inversion, the J_{BPE} should change its sign with equal magnitude because the {$\boldsymbol{G_{ijk}}$} tensor is odd (see details in Supplementary information S4.11).[8,16,17] Similarly, J_E can be changed upon reversing $\boldsymbol{P}$ as the depoling field/Schottky barriers is modulated.[18,19] Therefore, the amplitude of the observed J_{BPE} oscillations may not be described as expected for fully polarized sample. Moreover, in general, at oblique incidence the intensity of light transmitted and reflected at any interface should also depend on the polarization state (p or s) of the incoming light (Fresnel coefficients), thus producing a modulation of J_{sc}[20,21] irrespectively of the origin of the photocurrent.

Here we address this issue of $\boldsymbol{P}$ influence on J_{BPE} by measuring J_{sc} in uniaxial ferroelectric single crystals. Hexagonal h-LuMnO₃ is a room-temperature narrow-gap ferroelectric,[22,23] where the polarization axis is along the hexagonal c-axis, either pointing up or down. It will be shown that the J_{sc} magnitude and its dependence on light polarization $J_{sc}(\varphi)$ are largely affected by the back-switching effect. More precisely, imprint governs the back-switching as evidenced by polarization retention measurements, performed on crystals displaying opposite imprint directions, which translates into the amplitude of $J_{sc}(\varphi)$. Consequently, the quantitative extraction of the Glass coefficients can be severely hampered.

4.3.2. Samples and experiments

We report data on two single crystals (Cry-9,10) of h-LuMnO$_3$ (LMO) around 100 μm thick. Cry-9 and Cry-10 were selected to display opposite imprint direction (see below). Pt contacts were deposited on top of the crystals (Pt$_{top}$ of 7 nm) forming capacitor structures labelled as E$_n$ (n =1, 2, 3...). The crystals were fixed on silicon substrates by silver paste.

Data were recorded in dark or under illumination by using a linearly polarized blue-violet laser (λ = 405 nm) of 3.06 eV photon energy, and power density after optical plates $I_p \approx 47$ W/cm^2. The light propagation direction ($\boldsymbol{k}$) is fixed at $\theta \approx 45°$ of the normal to the crystal surface. A unipolar triangular prepoling $V^{+/-}$ pulse (V_{max} = 60 V) larger than the corresponding coercive voltage (V_c), was applied to the top Pt electrode with a duration of $\tau_w \approx 10$ s, long enough to saturate the polarization of the sample. After a delay time $\tau_d \approx 5$ s, the short-circuit photocurrent was collected while rotating φ (step 20°) with a dwell time of 6.5 s at each step; the complete φ sweep from 0 to 360° took around 162 s.

4.3.3. Ferroelectricity and polarization dependent oscillation

Fig. 4.10(a) depicts the $I(V)$ curves recorded on illustrative capacitors (E$_1$, E$_2$, and E$_3$) on Cry-9. Data show obvious current peaks indicating polarization switching at coercive voltages (V_c^+ and V_c^-). The polarization $P(V)$ loops are shown in Fig. 4.10(b). The saturation polarization is about 9 μC/cm^2, which is somewhat larger than typically found in hexagonal manganites.[18,24,25] Of interest here is that the I-V loops clearly reflect an imprint field (loops are shifted towards negative voltages), which indicates the presence of an internal field pointing downwards [Fig. 4.10(c)]. From Fig. 4.10(b), we obtain V_{im} [= (V_c^+ + V_c^-)/2)] of: -2.22 V, -3.21 V, and -4.26 V, for E$_1$, E$_2$ and E$_3$, respectively. It is worth noticing that the loops in Figs. 4.10(a,b) have been collected at 1 kHz without delay time.
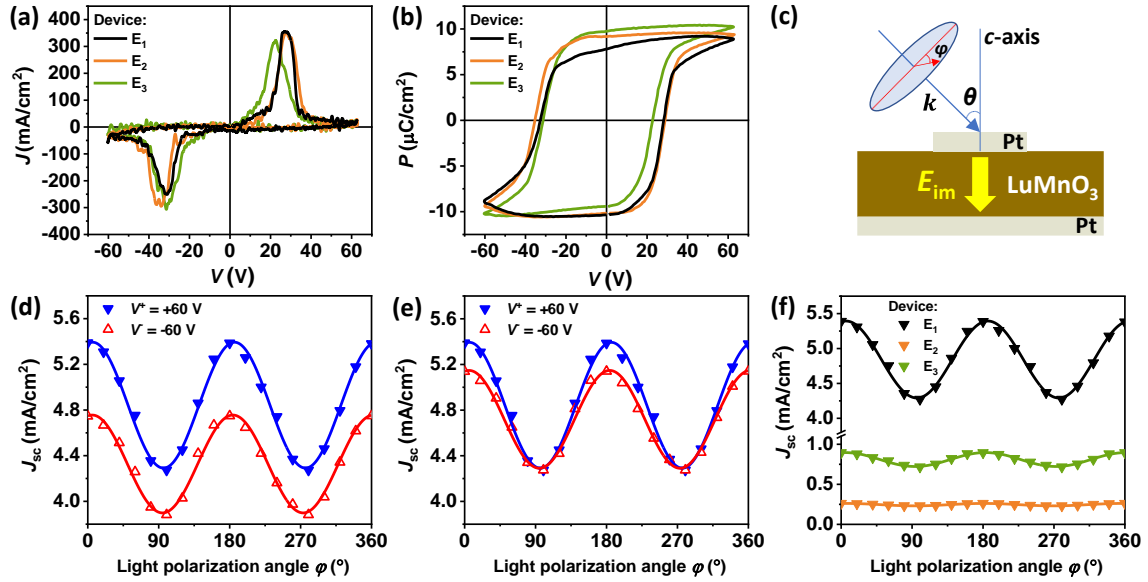
Fig. 4.10. (a) *I-V* curves and (b) corresponding polarization *P(V)* loops collected using DLCC mode at 1 kHz, in capacitors $E_{1,2,3}$ (Cry-9). (c) Sketch of the Pt/LMO/Pt sample, the illumination geometry and the direction of the imprint field. (d) Dependence of the J_{sc} on the light polarization angle φ and on the sign of the prepoling voltage $V^{+/-}$ (Cry-9). (e) Data from (d) vertically shifted to emphasize the dependence of the amplitude of oscillations on $V^{+/-}$. (f) J_{sc} measured after V^+, in capacitors $E_{1,2,3}$ (Cry-9). In Figs (d,e,f), solid lines are fits using Eq. [4.13] to experimental data (symbols).

The short-circuit photocurrent along the hexagonal axis is monitored while rotating the light polarization angle φ, with an incidence angle of $\theta \approx 45°$ (Fig. 4.10c). Data corresponding to electrode E_1 [Fig. 4.10(d)] have been collected after prepoling the sample with $V^{+/-} = \pm 60$ V. We first note in Fig. 4.10(d) the characteristic oscillations of $J_{sc}(\varphi)$ that are typically but disputably, taken as fingerprints of BPE. Data can be fitted using Eq. [4.13] below, as predicted by BPE theory:[8,26,27]

$$J_{sc}(\varphi) = A_z \cos 2(\varphi + \varphi_0) + B_z \qquad [4.13]$$

where the subindex "z" signals that photocurrent is measured along *z*-axis (out of plane) and φ_0 ($\leq 5°$) is a phase shift related to experimental uncertainties. Data in Fig. 4.10(d) also evidences a dependence of background current $[B_z(V^+) > B_z(V^-)]$ and of amplitude (A_z) of the $J_{sc}(\varphi)$ oscillations on the sign of the voltage $V^{+/-}$ used to write the capacitor. The amplitude variation $[A_z(V^+) > A_z(V^-)]$ can be better appreciated in Fig. 4.10(e) where data have been vertically shifted to match at $\varphi = 90°$. In Fig. 4.10(f) we show the J_{sc} recorded in three

capacitors after prepoling with V^+. Clearly the background current and the amplitude of oscillations vary similarly among electrodes but with $A_z/B_z \approx 0.1$ almost constant among various capacitors.

In Fig. 4.10(d) the sign of J_{sc} is independent on the sign (+/−) of the prepoling voltage. We notice that the observed E_{im}, evident in the $I(V)$ and $P(V)$ loops in Figs. 4.10(a,b), may have promoted a fast-preferential back-switching of the polarization before J_{sc} is recorded. We remark that recording the whole $J_{sc}(\varphi)$ [Figs. 4.10(d,e,f)] sweep takes $\tau \approx 162$ s, which may be much longer than the required polarization back-switching time. To get information on the dynamics of the back-switching process, we have recorded polarization loops with a delay time $\tau_d = 1$ s, between polarization writing and reading as shown in Fig. 4.11.

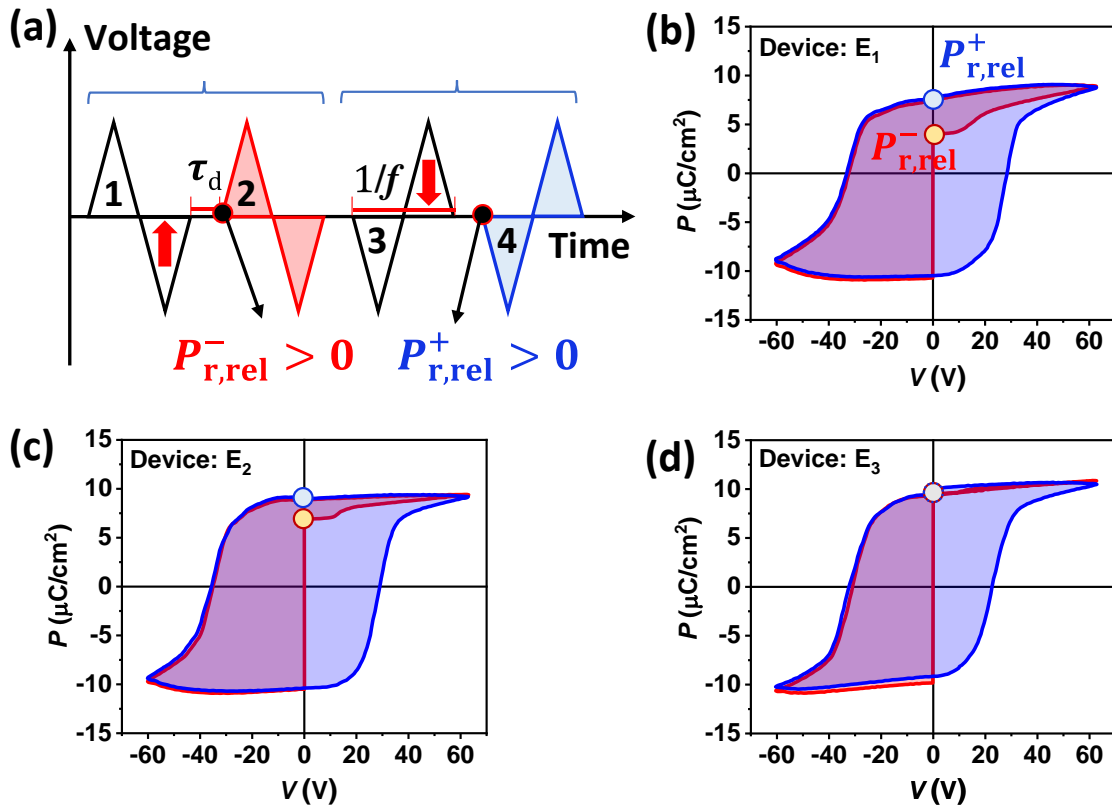### 4.3.4. Relaxation polarization at remanence

Fig. 4.11. (a) Voltage pulse trains used to determine the relaxation polarization in $\tau_d = 1$ s, after V^- or V^+ writing pulses. (b,c,d) Polarization loops and retention in $\tau_d = 1$ s in capacitors $E_{1,2,3}$ (Cry-9), respectively.

The methodology to measure the remanent relaxation polarization $P_{r,rel}^-$ and $P_{r,rel}^+$ (retention) after saturation with V^- and V^+, is illustrated in Fig. 4.11(a). A $V(t)$ pulse sequence consisting of four bipolar triangular excitation signals (1 & 2, 3 & 4) are applied to Pt$_{top}$ with a delay time τ_d (1 s) between them. $P_{r,rel}^-$ is the polarization value after 1 s delay of negative prepoling, determined from the $P(V)$ loop recorded during pulse 2. Similarly, $P_{r,rel}^+$ is the polarization after 1 s delay of positive prepoling, determined from the $P(V)$ loop recorded during pulse 4. Positive values of polarization correspond to polarization pointing down (towards Pt$_{bot}$) and negative for polarization pointing up (towards Pt$_{top}$). Similar information is extracted from Positive-Up-Negative-Down (PUND) measurements (Supplementary information S4.13).

Data for devices E$_{1,2,3}$ [Figs. 4.11(b,c,d)] reveal that in all cases, $P_{r,rel}^-$ has the same sign as $P_{r,rel}^+$, implying that polarization written with V^- has switched back to downward within τ_d = 1 s, mimicking $P_{r,rel}^+$. As expected, E_{im} increases from E$_1$ to E$_3$ while the polarization difference of $P_{r,rel}^+$ and $P_{r,rel}^-$ decreases. Additional experiments indicate that longer delay (up to 1000 s) does not reveal further switching back (see Supplementary information S4.14). Therefore, when $J_{sc}(\varphi)$ is recorded, the polarization always points downwards irrespectively on the writing voltage, as dictated by E_{im}. Accordingly, $A_z(V^+) > A_z(V^-)$ and $B_z(V^+) > B_z(V^-)$, and J_{sc} is positive as observed.

4.3.5. Modulated polarization dependent oscillation

Crosscheck experiments have been performed using Cry-10 where the $P(V)$ loops indicate that E_{im} is pointing upwards [Fig. 4.12(a)], and consistently, back-switching favors upward $P_{r,rel}^-$ [Fig. 4.12(b)]. The $J_{sc}(\varphi)$ data [Fig. 4.12(c,d)] show that the impact of polarization is reversed compared to data of Cry-9 (Fig.1), that is: $A_z(V^-) > A_z(V^+)$ and $B_z(V^-) > B_z(V^+)$. The fact that here, J_{sc} is still positive also denotes the presence of additional terms, probably related to a diffusion term due to non-homogenous illumination and/or a non-switchable drift contribution due to the pinned electric field.
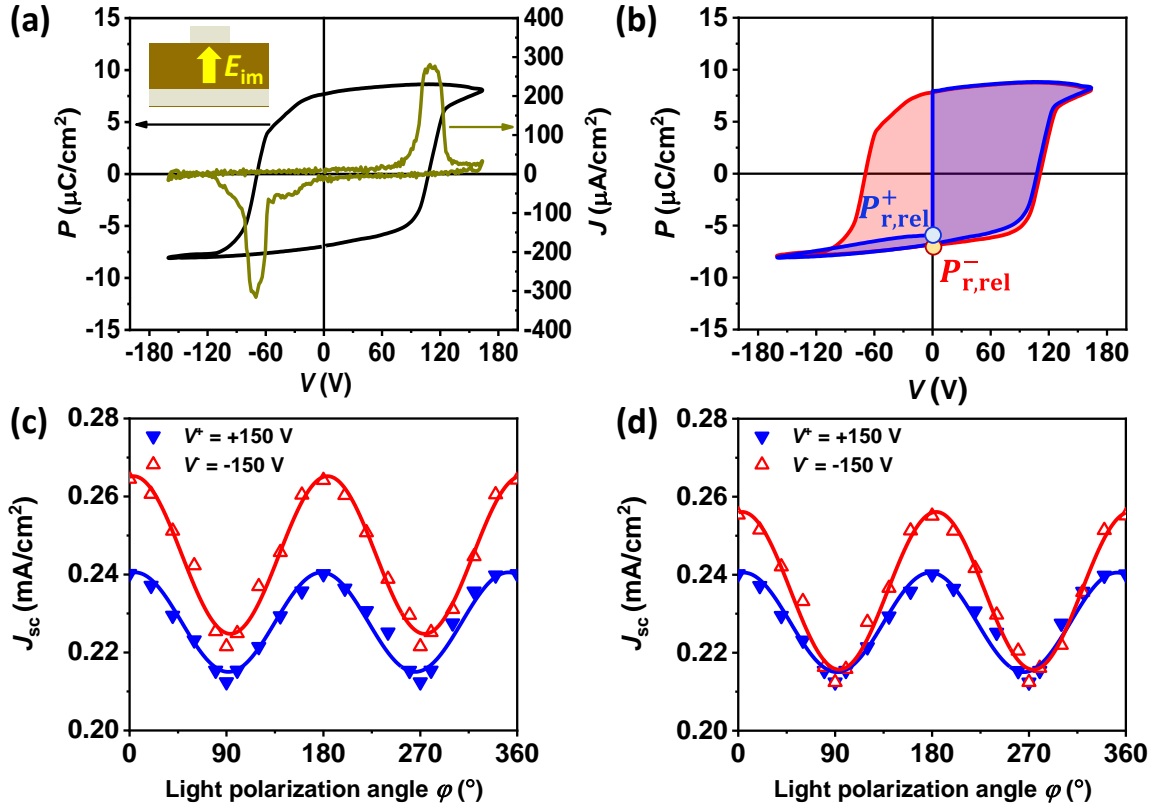
Fig. 4.12. (a) $I(V)$ and $P(V)$ loops and (b) retention in $\tau_d = 1$ s in Cry-10. (c) Raw $J_{sc}(\varphi)$ and (d) the same data shifted to better visualize the change of amplitude; solid lines are fits using Eq. [4.13] to experimental data (symbols).

The $\delta P_{r,rel} = \left| \frac{(P^+_{r,rel} - P^-_{r,rel})}{2} \right|$ is the difference of polarization measured at remanence after writing with $V^{+/-}$. It is to be expected that any polarization contribution to A_z and B_z should be encapsulated by $\delta P_{r,rel}$. To assess this hypothesis, we plot in Fig. 4.13(a) the $\delta A_z = |A_z(P^+_{r,rel}) - A_z(P^-_{r,rel})|$ vs. $\delta P_{r,rel}$ collected from 20 capacitors (Cry-9) all having the same imprint sign. Data show that the contrast of amplitude (δA_z) of $J_{sc}(\varphi)$ oscillations increases when reducing the back-switching (larger $\delta P_{r,rel}$). A similar trend can be appreciated in Fig. 4.13(b) where $\delta B_z = |B_z(P^+_{r,rel}) - B_z(P^-_{r,rel})|$ vs. $\delta P_{r,rel}$ is plotted. In short, both A_z and B_z change when reversing the polarization and the stronger the retention of the pre-polarized states (bigger $\delta P_{r,rel}$) the larger the contrasts in δA_z and δB_z.
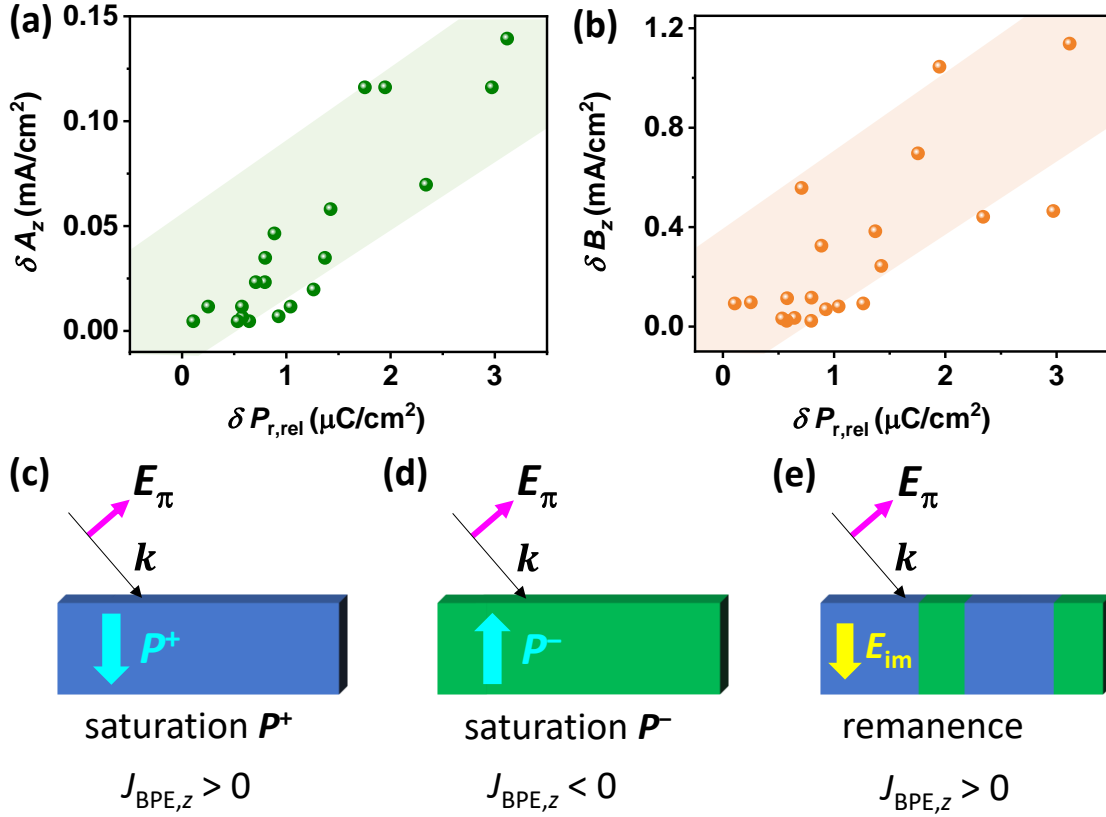
Fig. 4.13. Contrast of the oscillation (a) amplitudes (δA_z) and (b) backgrounds (δB_z) of $J_{sc}(\varphi)$ *vs.* the difference of relaxation polarization ($\delta P_{r,rel}$) after $V^{+/-}$ writing, collected in 20 capacitors in Cry-9. Sketches represent the polarization at saturation of (c) P^+ (blue), (d) P^- (green) domains in absence of back-switching and (e) the polarization at remanence in presence of back-switching, favoring P^+ state. Blue arrows indicate the polarization direction, yellow arrow denotes the imprint direction, black arrows represent the propagation direction (k) of the light and red arrows illustrates a p-polarized light (E_π).

Several mechanisms may contribute to the photocurrent as observed in both in *h*-LuMnO₃[12] and other materials.[28] As the background term B_z may contain all these contributions, the role of ferroelectric P on B_z is difficult to discern. In contrast, understanding the dependence of the amplitude of oscillations on P appears at first sight simpler. Indeed, A_z reflects the sensitivity of the photoresponse to light polarization and it is expected to provide a genuine fingerprint of BPE weighted by any Fresnel contribution. However, the observation that A_z depends on writing voltage [Figs. 4.10, 4.12], implies that it is not simply determined by the symmetry of the crystal, but it is also affected by fine details of the polarization state of the sample when measurements are performed. As

different capacitors on a given crystal have slightly different imprint fields [(Figs. 4.10(a,b)],
it is expected that the polar state of the sample under the electrodes, when J_{sc} is measured
at remanence, may differ from one capacitor to another. If so, the differences of A_z after
$V^{+/-}$ writing: $\delta A_z = A_z(V^+) - A_z(V^-)$), could be a fingerprint and a reflection of the polarization
retention, or in other words, a measure of the fraction of domains that may have switched
back.

To better understand the rationale behind, we recall that BPE photocurrent is given by

$$J^+_{\text{BPE},i} = I_0 \alpha_{jk} G^+_{ijk} e_j e_k \qquad [4.14]$$

where I_0 is the light intensity of a given wavelength; α_{jk} is the absorption coefficient; G_{ijk} is
the third rank Glass tensor.[8,26] The suffixes (i, j, k) refer to (x, y, z) cartesian coordinates of
the polarization components of the incoming light. We take the z-axis along the polar c-axis
of h-LMO. As reported elsewhere,[12,27] the oscillations of $J_{\text{BPE}}(\varphi)$ in h-LuMnO₃ of Fig. 4.10 can
be well described by Eq. [4.14]. The super index $(^+)$ emphasizes that the actual values of the
tensor elements correspond to a net shift of positive ionic charges along the negative
direction of z-axis, say $\boldsymbol{P^+}$, and under this circumstance $J^+_{\text{BPE},z}$ is measured.

When polarization is fully reversed $(\boldsymbol{P^-})$, preserving illumination conditions, Eq. [4.14]
transforms to:

$$J^-_{\text{BPE},i} = I_0 \alpha_{jk} G^-_{ijk} e_j e_k \qquad [4.15]$$

and $J^-_{\text{BPE},z}$ is measured. Polarization reversal in h-LuMnO₃ corresponds to a spatial inversion
like a mirror (M ⊥ c) symmetry transformation. Therefore (see Supplementary information
S4.11):

$$G^-_{ijk} = -G^+_{ijk} \qquad [4.16]$$

Eqs. [4.15, 4.16] imply that under $\boldsymbol{P}$ reversal, $J^-_{\text{BPE},z}$ should display similar oscillations of the
same amplitude but reversed sign than $J^+_{\text{BPE},z}$, that is: $J_{sc}(\varphi)$ should be phase-shifted by 90°.
Under partial polarization back-switching, where the sample is in a mix state of polarization,
the $J_{\text{BPE},z}$ would be the weighted sum of the $J^{+/-}_{\text{BPE},i}$ contributions.

Data of Cry-9 [Figs. 4.10(d,e)] show that after $V^{+/-}$ writing the current direction remains unperturbed. Only a relatively small change of amplitude ($\approx$ 5 %) is observed. This implies that when J_{sc} is measured ($\tau_d > 1$ s), the polarization written with V^- has been partially switched back to $\boldsymbol{P^+}$ state, in which case $\boldsymbol{P_r^-}$ is also downwards but with a smaller magnitude than the fully stable $\boldsymbol{P_r^+}$ (Fig. 4.11), thus the measured J_{sc}^- written with V^- keeps the same sign but smaller value than J_{sc}^+ written with V^+. This process is sketched in Figs. 4.13(c,d,e). It is expected to have opposite J_{sc} for downward and upward polarization state, respectively [Fig. 4.13(c,d)]. Instead, due to the presence of imprint, the final state can be a mixture of up and down domains impacting on the J_{sc} sign and magnitude. Thus, the presence of E_{im} is instrumental triggering the switching-back process and accounts for the observed dependence of $J_{sc}(\varphi)$ on the polarization state of crystal.

On the contrary, in Cry-10, where the upward E_{im} favors $\boldsymbol{P^-}$, J_{sc}^+ is smaller than J_{sc}^-, because the magnitude of real upward $\boldsymbol{P_r^+}$ is smaller than fully switched $\boldsymbol{P_r^-}$. However, the measured $J_{sc}^{+/-}$ is always positive (Fig. 4.12) and data show that the BPE-predicted phase shift of $J_{sc}(\varphi)$ compared with Cry-9 is absent. Therefore, it follows that an additional contribution to $J_{sc}(\varphi)$ that does not change its sign under a mirror transformation should also coexist. As shown in BiFeO₃,[29] defect-related in-gap states in the ferroelectric may conspicuously affect the actual symmetry of $\boldsymbol{G_{ijk}}$[7] while preserving the cosinusoidal cos2φ dependence. The observation that the measured photocurrent differs among electrodes on the sample already indicates the importance of defects and/or impurities in the photovoltaic response, as already found in BiFeO₃.[30] Finally, additional contributions to $J_{sc}(\varphi)$ may originate from dichroism, as recently reported in BiFeO₃[31] although earlier experiments indicated that this is not the case in LuMnO₃.[27] Even more, the polarization-dependent light transmittance (Fresnel) at the interfaces could impact both the BPE and drift or diffusion currents by adding a cos2φ contribution to the measured $J_{sc}(\varphi)$ photovoltaic current. Its inspection is beyond the scope of this work.

Finally, we recall that extraction of the Glass coefficients from the measured magnitude of $J_{sc}(\varphi)$, relies on the assumption that the measured photocurrent is dominated by bulk photovoltaic response, potentially affected by polarization back switching as demonstrated above. However, other effects such as drift photocurrent associated to band alignment at interfaces and/or diffusion photocurrent associated to photocarrier gradients

both contribute to the light-polarization insensitive background J_{sc}. Their presence, which precludes accurate extraction of some of the G_{ijk} elements, can be minimized by using engineered metallic electrodes and thin films.

4.3.6. Conclusions

In summary, the short circuit photocurrent J_{sc} in ferroelectric materials, measured at zero *V*-bias and thus at remanence, is largely affected by the polarization history of the sample and the presence of polarization back-switching and depoling processes. By measuring the dependence of $J_{sc}(\varphi)$ ($\approx \cos2\varphi$) on the light polarization, we have observed that the amplitude of $\cos2\varphi$ oscillations depends on the polarization state of the ferroelectric at remanence, and thus it is sensitive to the polarization back-switching. It follows that the accurate extraction of the intrinsic Glass coefficients of the material, related to the amplitude of $J_{sc}(\varphi)$ oscillations, is challenging. As back-switching is typically more relevant in thin films, dedicated attention is required towards quantitative understanding of BPE. Moreover, data have been analyzed based on the assumption that BPE controls $J_{sc}(\varphi)$. However, it is worth noticing that a similar $J_{sc}(\varphi)$ oscillations ($\approx \cos2\varphi$) depending on the light polarization could be expected in case of Fresnel controlled transmittance of *p*- and *s*-polarized light at top interfaces, and thus a similar ferroelectric polarization dependent $J_{sc}(\varphi)$ could appear since the Schottky barriers at interfaces and depoling field are related to ferroelectric polarization. Disentangling both effects remains to be solved.

Supplementary information

S4.11. Photovoltaic tensor by reversing the ferroelectric **P**

h-LuMnO$_3$ belongs to space group $P63cm$ (C_{6v}), whose photovoltaic tensor is given by:

$$\boldsymbol{\beta_{ijk}} = \begin{array}{cccccccccc} & 11 & 12 & 13 & 21 & 22 & 23 & 31 & 32 & 33 & \\ & \begin{pmatrix} 0 & 0 & \beta_{113} & 0 & 0 & 0 & \beta_{131} & 0 & 0 \\ 0 & 0 & 0 & 0 & 0 & \beta_{223} & 0 & \beta_{232} & 0 \\ \beta_{311} & 0 & 0 & 0 & \beta_{322} & 0 & 0 & 0 & \beta_{333} \end{pmatrix} & \begin{array}{c} 1 \\ 2 \\ 3 \end{array} \end{array}$$

The $\boldsymbol{\beta_{ijk}}$ tensor contains only three nonzero independent elements:

$$\beta_{333}, \beta_{311} = \beta_{322}, \beta_{113} = \beta_{131} = \beta_{223} = \beta_{232}$$

The transformation rule for a third-rank tensor is:[32]

$$\beta'_{ijk} = a_{il} a_{jm} a_{kn} \beta_{lmn}$$

where β'_{ijk} is the tensor element after transformation; β_{lmn} is a tensor element in the original system; and a_{il}, a_{jm}, a_{kn} are the matrix elements of the transformation; the indices l, m, n = 1, 2, 3 are summed over as noted by Einstein summation convention.

Fully reversing ferroelectric **P** can be considered as operating a transformation of mirror (M) perpendicular to the z = [0 0 1], where the matrix for this mirror plane is:[32]

$$M(\perp z) = \begin{pmatrix} 1 & 0 & 0 \\ 0 & 1 & 0 \\ 0 & 0 & -1 \end{pmatrix} = \begin{pmatrix} a_{11} & a_{12} & a_{13} \\ a_{21} & a_{22} & a_{23} \\ a_{31} & a_{32} & a_{33} \end{pmatrix}$$

which includes only three non-zero elements (a_{11}, a_{22}, a_{33}). Thus, the BPE tensor elements can be transformed as:[32]

$$\beta'_{333} = a_{3l} a_{3m} a_{3n} \beta_{lmn} = a_{31} a_{31} a_{31} \beta_{111} + a_{31} a_{31} a_{32} \beta_{112} + a_{31} a_{31} a_{33} \beta_{113} + \cdots$$
$$= \boldsymbol{a_{33} a_{33} a_{33}} \beta_{333} = -\beta_{333}$$

$$\beta'_{311} = a_{3l} a_{1m} a_{1n} \beta_{lmn} = \boldsymbol{a_{33} a_{11} a_{11}} \beta_{311} = -\beta_{311}$$

$$\beta'_{131} = \beta'_{113} = a_{1l} a_{3m} a_{1n} \beta_{lmn} = \boldsymbol{a_{11} a_{33} a_{11}} \beta_{333} = -\beta_{131}$$

Therefore, the whole PV tensor changes its sign upon fully reversing $\boldsymbol{P}$, that is $\boldsymbol{\beta}_{ijk}^- = -\boldsymbol{\beta}_{ijk}^+$, similarly, $\boldsymbol{G}_{ijk}^- = -\boldsymbol{G}_{ijk}^+$ as $\boldsymbol{\beta}_{ijk} = \alpha_{jk}\boldsymbol{G}_{ijk}$. Consequently, the corresponding BPE current at each fully polarized $\boldsymbol{P}$ state changes its sign with equal magnitude ($J_{\mathrm{BPE}}^- = -J_{\mathrm{BPE}}^+$) as J_{BPE} is given by $J_{\mathrm{BPE},i} = I_0\boldsymbol{\beta}_{ijk}\boldsymbol{e}_j\boldsymbol{e}_k = I_0\alpha_{jk}\boldsymbol{G}_{ijk}\boldsymbol{e}_j\boldsymbol{e}_k$.

Accordingly, for the geometry used in these experiments, it turns out the BPE contribution to $J_{sc}(\varphi)$ for saturated P^+ is given by:[27]

$$J_{\mathrm{BPE},z}^+ = A_z'\cos2\varphi + B_z'$$

and for saturated P^-:

$$J_{\mathrm{BPE},z}^- = A_z'\cos2(\varphi + \pi/2) - B_z'$$

S4.12. Retention identified by PUND measurements

In Figure S4.12(a), the train pulses used to perform PUND measurements is sketched. In Figure S.12(b), the measured current versus voltage is plotted. The observation of absence of ferroelectric switching peak in the positive voltage branch and the fact that ferroelectric switching peak is visible for the negative branch for the N and D pulses indicate that the polarization state, with τ_d = 1 s, is always down.
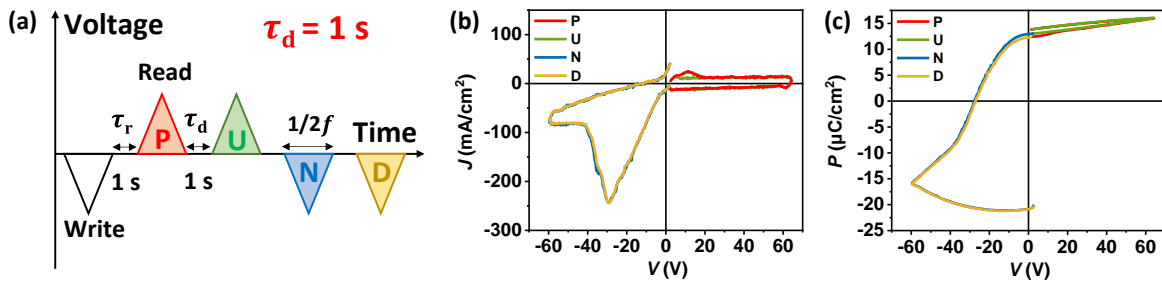

Fig. S4.12. (a) Voltage pulse trains applied for PUND (Positive Up Negative Down) measurements with a delay to read time τ_r = 1 s and a delay time τ_d = 1 s between consecutive reading pulses, where the shaded areas correspond to the measuring intervals. (b) $J(V)$ and (c) $P(V)$ loops measured with PUND at 1 kHz, in capacitor E₃ (Cry-9).

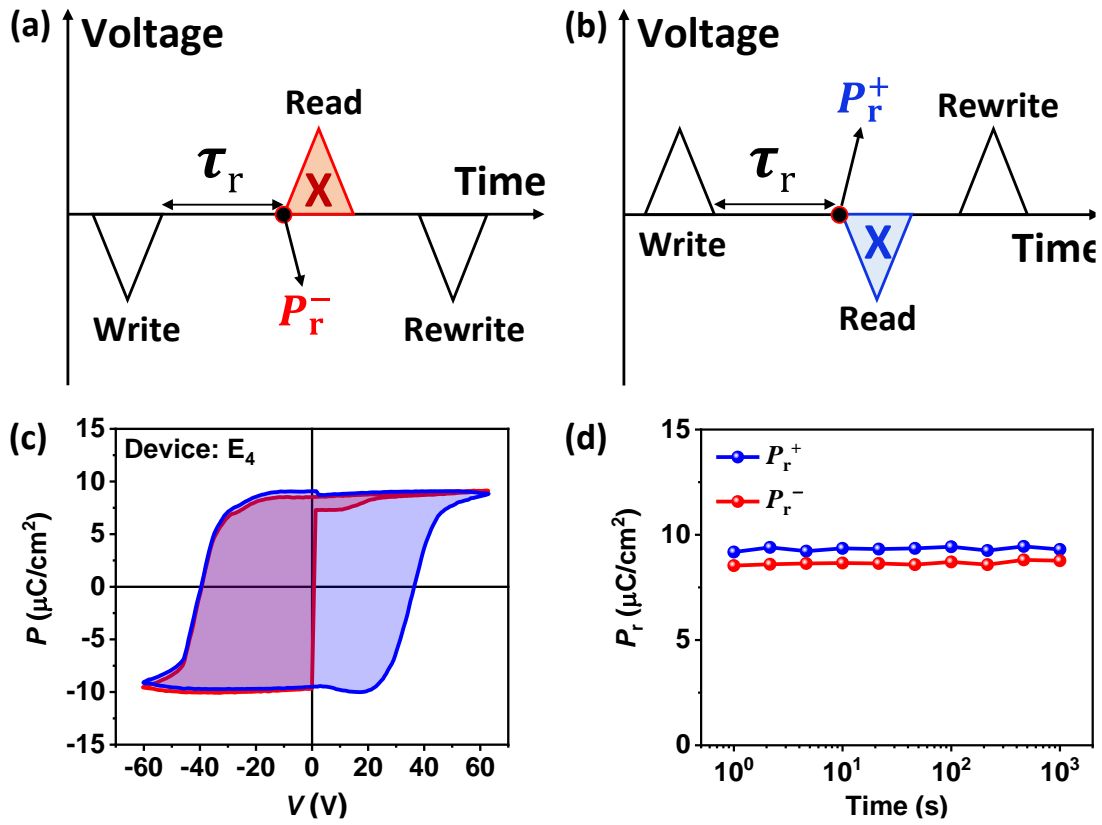S4.13. Retention identified by PUND measurements

Fig. S4.13. Voltage pulse trains used to determine the retention in a delay to read time τ_r, after (a) V^- and (b) V^+ writing pulses. (c) Polarization loops and retention in $\tau_d = 1$ s in capacitor E₄ (Cry-9). (d) Retention P_r^+ and P_r^- *vs*. time τ_r after V^- and V^+ writing pulses (Cry-9).

Bibliography

[1] V. M. Fridkin, Crystallogr. Rep. **46**, 654 (2001).

[2] V. M. Fridkin, *Photoferroelectrics*. (Springer-Verlag Berlin Heidelberg, New York, 1979).

[3] A. M. Glass, D. von der Linde, D. H. Auston, and T. J. Negran, J. Electron. Mater. **4**, 915 (1975).

[4] V. M. Fridkin and B. N. Popov, Sov. Phys. Usp. **21**, 981 (1978).

[5] S. Y. Yang, J. Seidel, S. J. Byrnes, P. Shafer, C. H. Yang, M. D. Rossell, P. Yu, Y. H. Chu, J. F. Scott, J. W. Ager, L. W. Martin, and R. Ramesh, Nat. Nanotech. **5**, 143 (2010).

[6] M. Yang, A. Bhatnagar, and M. Alexe, Adv. Electron. Mater. **1**, 1500139 (2015).

[7] V. I. Belinicher and B. I. Sturman, Sov. Phys. Usp. **23**, 199 (1980).

[8] B. Sturman and V. M. Fridkin, The Photovoltaic and Photorefractive Effects in Noncentrosymmetric Materials (Gordon and Breach, Philadelphia, 1992).

[9] L. Z. Tan, F. Zheng, S. M. Young, F. Wang, S. Liu, and A. M. Rappe, Npj Comput. Mater. **2**, 16026 (2016).

[10] P. Würfel, *Physics of solar cells: from basic principles to advanced concepts*. (John Wiley and Sons, 2005).

[11] K. Buse, Appl. Phys. B: Lasers O **64**, 273 (1997).

[12] Y. Sheng, I. Fina, M. Gospodinov, and J. Fontcuberta, Appl. Phys. Lett. **118**, 232902 (2021).

[13] V. Koval, G. Viola, and Y. Tan, *Ferroelectric Materials-Synthesis and Characterization*, edited by A. P. Barranco (IntechOpen, 2015).

[14] A. Picinin, M. H. Lente, J. A. Eiras, and J. P. Rino, Phys. Rev. B **69**, 064117 (2004).

[15] Z. Tan, J. Tian, Z. Fan, Z. Lu, L. Zhang, D. Zheng, Y.g Wang, D. Chen, M. Qin, M. Zeng, X. Lu, X. Gao, and J. Liu, Appl. Phys. Lett. **112**, 152905 (2018).

[16] V. I. Belinicher, Zh. Eksp. Teor. Fiz. **75**, 641 (1978).

[17] C. Paillard, X. Bai, I. C. Infante, M. Guennou, G. Geneste, M. Alexe, J. Kreisel, and B. Dkhil, Adv. Mater. **28**, 5153 (2016).

[18] H. Han, S. Song, J. H. Lee, K. J. Kim, G. W. Kim, T. Park, and H. M. Jang, Chem. Mater. **27**, 7425 (2015).

[19] H. Han, D. Kim, S. Chae, J. Park, S. Y. Nam, M. Choi, K. Yong, H. J. Kim, J. Son, and H. M. Jang, Nanoscale **10**, 13261 (2018).

[20] J. Yu, Y. Chen, S. Cheng, and Y. Lai, Physica E **49**, 92 (2013).

[21] M. Yang, D. J. Kim, and M. Alexe, Science **360**, 904 (2018).

[22] H. L. Yakel, W. C. Koehler, E. F. Bertaut, and E. F. Forrat, Acta Cryst. **16**, 957 (1963).

[23] A. M. Kalashnikova and R. V. Pisarev, Jetp Lett. **78**, 143 (2003).

[24] S. H. Kim, S. H. Lee, T. H. Kim, T. Zyung, Y. H. Jeong, and M. S. Jang, Cryst. Res. Technol. **35**, 19 (2000).

[25] T. Yu, P. Gao, T. Wu, T. A. Tyson, and R. Lalancette, Appl. Phys. Lett. **102** (17), 172901 (2013).

[26] W. Ji, K. Yao, and Y. C. Liang, Phys. Rev. B **84**, 094115 (2011).

[27] Y. Sheng, I. Fina, M. Gospodinov, A. M. Schankler, A. M. Rappe, and J. Fontcuberta, Phys. Rev. B **104**, 184116 (2021).

[28] M. Nakamura, S. Horiuchi, F. Kagawa, N. Ogawa, T. Kurumaji, Y. Tokura, and M. Kawasaki, Nat. Commun. **8**, 281 (2017).

[29] M. Yang, Z. Luo, D. J. Kim, and M. Alexe, Appl. Phys. Lett. **110**, 183902 (2017).

[30] T. Choi, S. Lee, Y. J. Choi, V. Kiryukhin, and S. W. Cheong, Science. **324**, 63 (2009).

[31] A. Abdelsamie, L. You, L. Wang, S. Li, M. Gu, and J. Wang, Phys. Rev. Appl. **17**, 024047 (2022).

[32] R. E. Newnham, in *Properties of Materials*, Oxford University Press, 2004.

Chapter 5. Growth and photovoltaic response of *h*-LuMnO₃ thin films

In this chapter, the growth conditions of *h*-LuMnO₃ thin films are explored to select the optimal samples grown by optimized growth parameters, to conduct the characterization and electrical photoresponse measurements.

5.1. Growth and optimization

In this section, a series of LMO samples grown by PLD with different substrate temperature (T), dynamic oxygen pressure (PO_2), laser fluence (F), laser repetition rate (frequency, f), and substrate is presented, to investigate their influence on the quality of the obtained films, by X-ray diffraction (XRD) and X-ray reflectometry (XRR). The films were cooled down at the end of deposition under static PO_2 of the corresponding dynamic PO_2 during the growth.

5.1.1. Films grown on Al₂O₃

First, we grow the LMO films directly on Al₂O₃(0001) without bottom electrode, with one parameter varying and the others fixed (using 4000 pulses). The studied parameters are indicated below in Table 5.1, which are adapted from the previous Refs. 1–8 and preliminary trials. In our case, 0.3 mbar is the maximum dynamic flowing PO_2 can be controlled, and 825°C is the maximal temperature the PLD equipment can tolerate.

T (°C)	PO_2 (mbar)	F (J/cm²)	f (Hz)
750	0.1	1.5	3
800	0.2	2	5
825	0.3	-	-

Table 5.1. Investigated PLD growth parameters.

As seen by θ-2θ scans in Fig. 5.1(a), except for the film grown at 750 °C, the hexagonal LMO (0004) reflections ($P6_3cm$) around $2\theta \approx 31.4°$ are all clearly visible in all the other films. The oscillation width and decay of XRR scans in Fig. 5.1(b) indicate the thickness of the film and the roughness of the internal interfaces, respectively. The rapid decay of film grown at

750 °C reflects a poor quality of film with rough interfaces. Relatively, the 825 °C film (green lines) shows both larger LMO peak intensity and more clear oscillations.
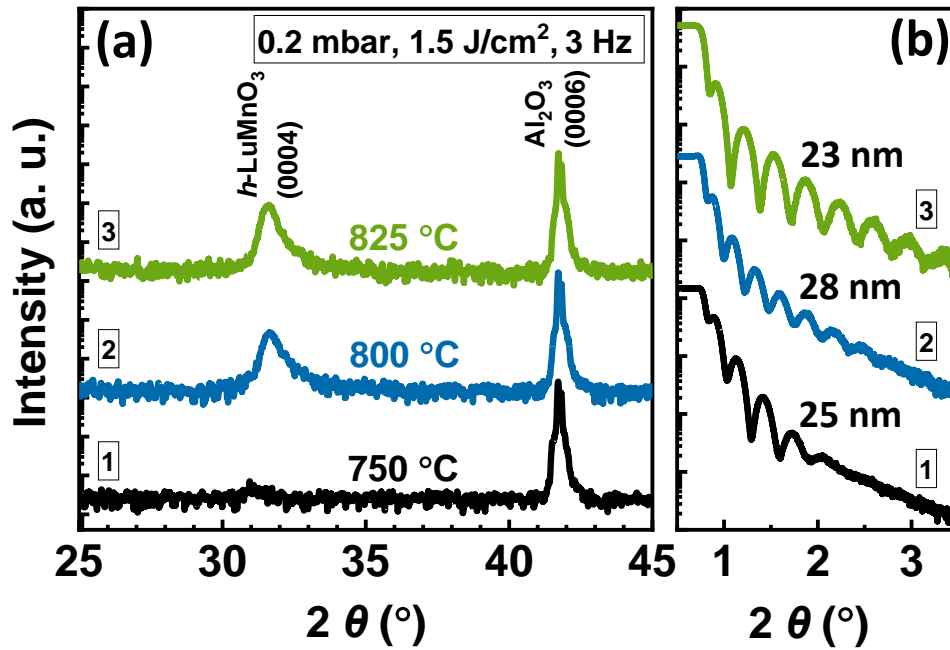

Fig. 5.1. (a) θ-2θ XRD and (b) XRR scan of Al_2O_3//LMO with different PLD growth T.

By fitting the XRR results, the film thickness and roughness (R) can be quantified, as shown in Fig. 5.2. The thicknesses (nm) are indicated in the XRR plots, and the roughness is summarized in Fig. 5.6.
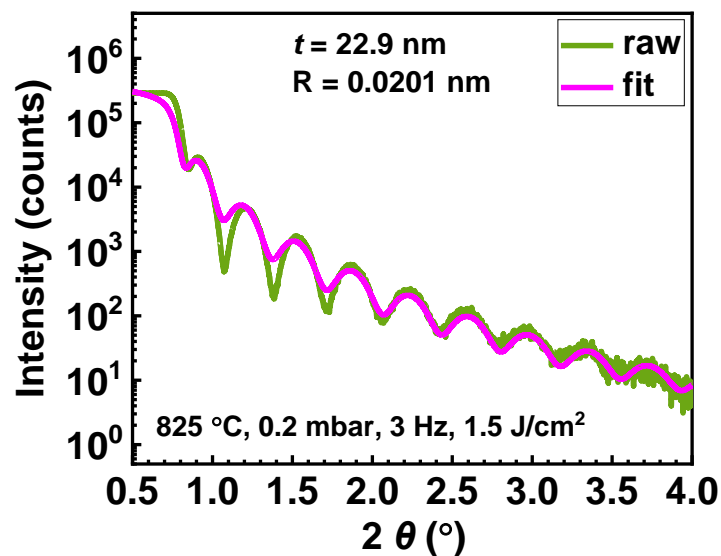

Fig. 5.2. An example of fitting of XRR data using LEPTOS software.

Fig. 5.3 shows the θ-2θ XRD and XRR scans of films grown at various oxygen pressures. The LMO peak intensity increases slightly with decreasing the PO_2 but probably owing to the increasing film thickness as identified by the narrower oscillations with lower PO_2 [Fig. 5.3(b)]. For the 0.2 mbar sample (green lines), the XRR oscillations are better so the roughness is expected to be less [Fig. 5.5(b)].
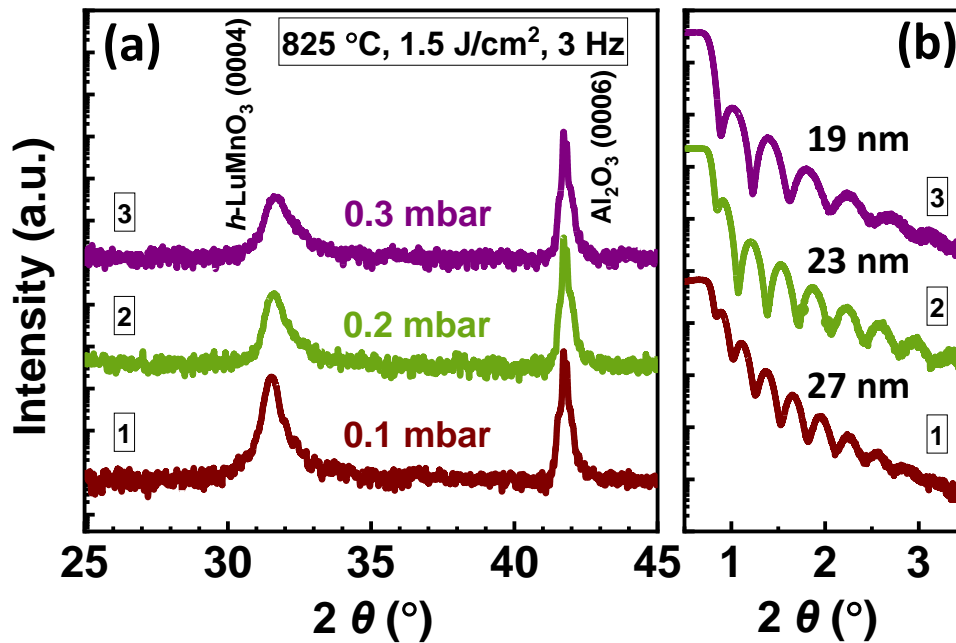

Fig. 5.3. (a) θ-2θ XRD and (b) XRR scan of Al_2O_3//LMO with different PLD growth PO_2.

Fig. 5.4 illustrates the θ-2θ XRD and XRR scans of the films grown at 800 °C, 0.2 mbar, 3 Hz, and varying the laser fluence (1.5 and 2 J/cm²). The sample grown with 1.5 J/cm² (blue lines) possesses higher LMO peak intensity although with smaller film thickness, and it shows slower decay in XRR scan. Similarly, Fig. 5.5 shows the θ-2θ XRD and XRR scans of the films grown at 825 °C, 0.2 mbar, 1.5 J/cm² when varying the laser frequency (3 and 5 Hz). It can be appreciated that the 3 Hz sample shows slightly better oscillations, although the influence of laser frequency on the film quality is marginal.
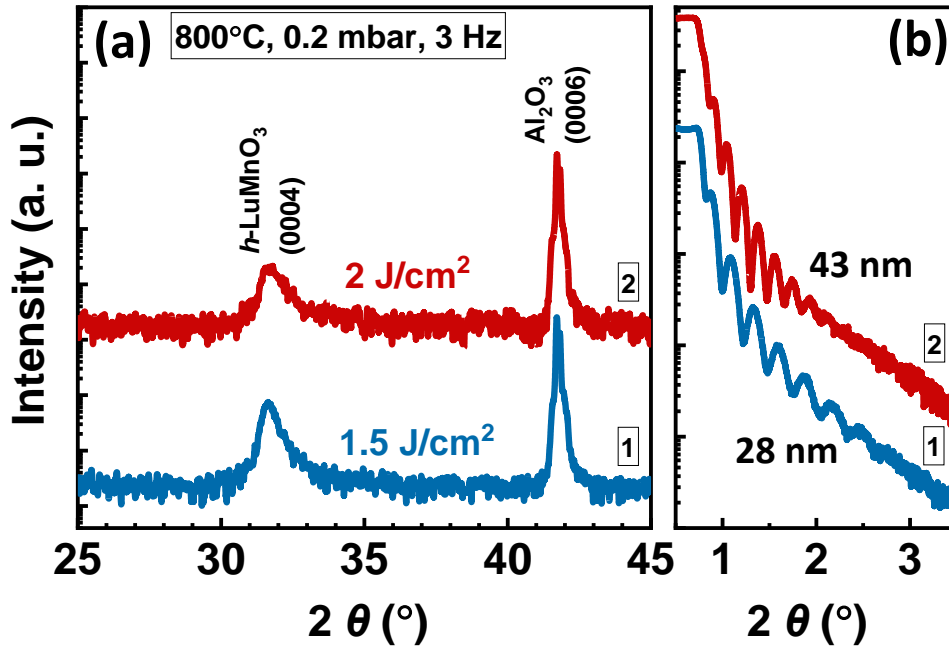
Fig. 5.4. (a) θ-2θ XRD and (b) XRR scan of Al_2O_3//LMO with different PLD laser fluence.
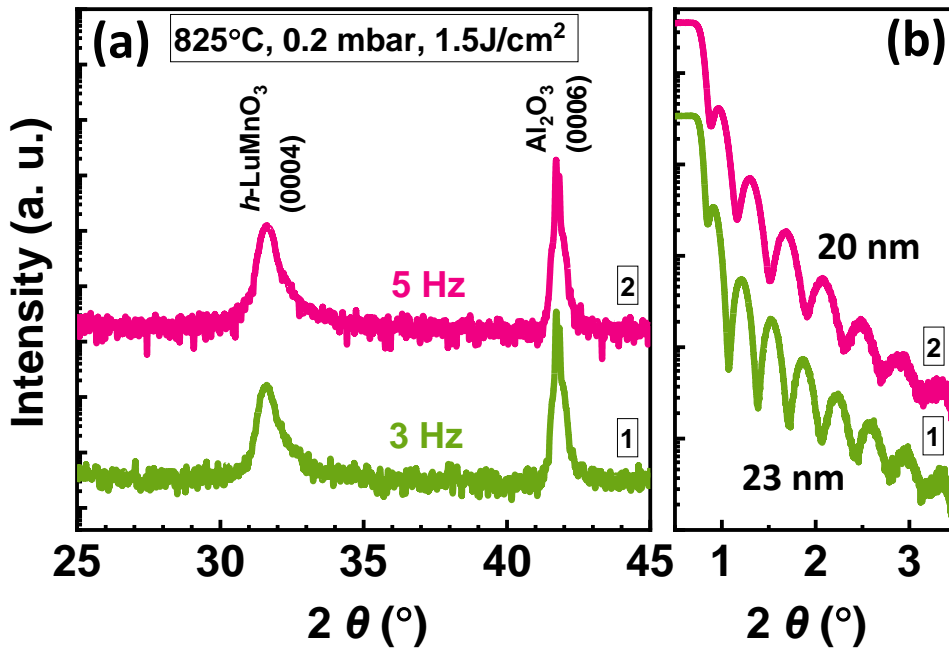

Fig. 5.5. (a) θ-2θ XRD and (b) XRR scan of Al_2O_3//LMO with different PLD laser frequency.

Fig. 5.6 summarized the roughness extracted by fitting the XRR results of Figs. 5.1, 5.3-5.5. In agreement with the observed decay/oscillation quality above, film grown at 825 °C,

0.2 mbar, 1.5 J/cm² and 3 Hz shows relatively strong LMO peak intensity and the smallest roughness, thus these parameters are determined as the optimal growth conditions.
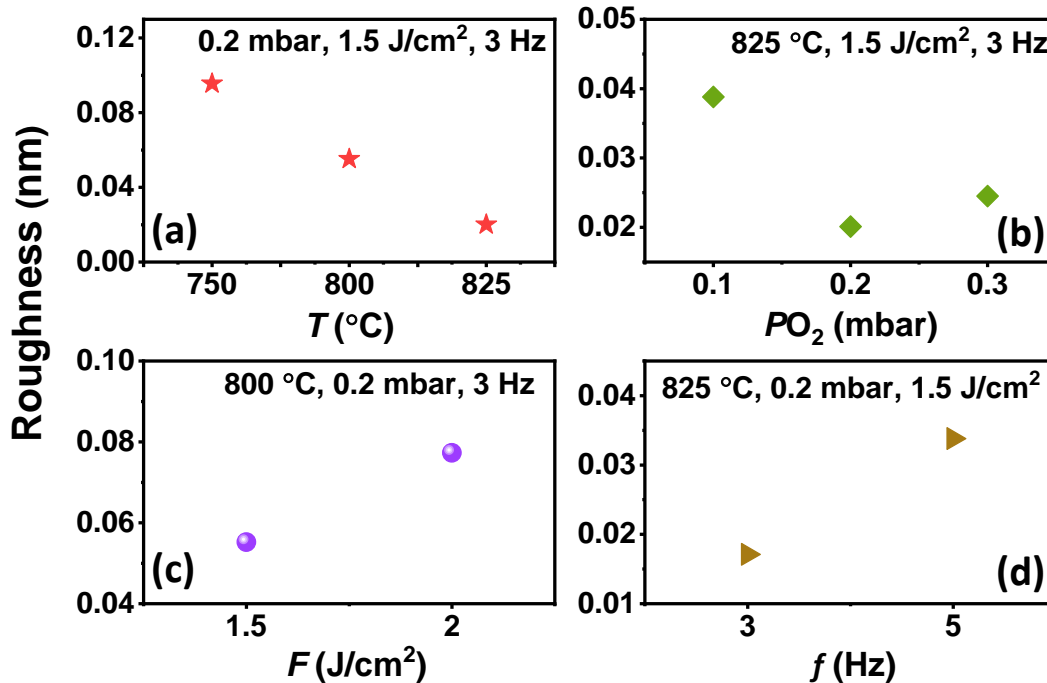

Fig. 5.6. Roughness dependence on PLD growth (a) temperate, (b) dynamic oxygen pressure, laser (c) fluence and (d) frequency, respectively. Roughness is extracted by fitting the XRR results of Al₂O₃//LMO.

Additionally, note that higher growth rate is obtained with lower PO_2 and higher laser fluence, thus thicker film can be obtained with less growth time (which is limited by the equipment threshold). Lower frequency also brings higher growth rate but requires more growth time. It will be found in Fig. 5.10 that, for our hexagonal films grown on Pt bottom electrode, thicker LMO film (> 60 nm) is beneficial for reducing leakage and performing electrical measurements. While under the selected optimal conditions, to obtain films thicker than 80 nm requires a time beyond the equipment limit, hence we must compromise the optimal conditions like reducing the PO_2 or increasing the laser fluence. In the work of section 5.2, simply one optimal sample was selected, grown under the optimal conditions (825 °C, 0.2 mbar, 1.5 J/cm²) using 1 Hz to compensate the thickness with expectation of higher growth rate from Fig. 5.5 (see later the text for Fig. 5.9).

5.1.2. Films grown on YSZ

Similar investigations were conducted with films grown on yttria-stabilized zirconia YSZ(111), and 825 °C, 0.2 mbar, 1.5 J/cm^2 and 3 Hz were also found to be the optimal growth conditions. However, it shows worse quality compared to films grown on Al$_2$O$_3$ (Fig. 5.7, 4000 pulses).
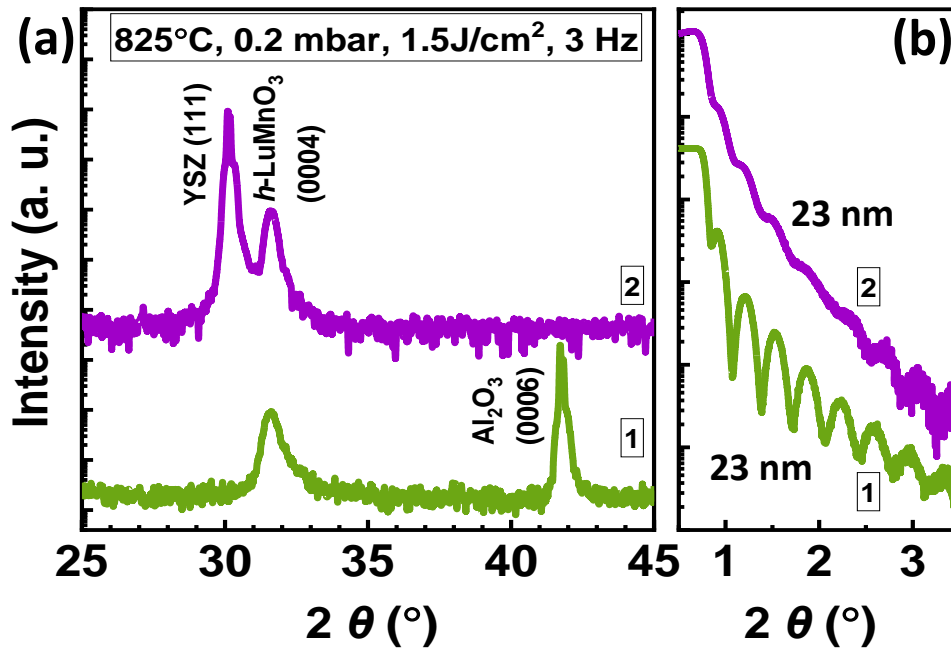
Fig. 5.7. (a) θ-2θ XRD and (b) XRR scan of Al$_2$O$_3$//LMO (1) and YSZ//LMO (2).

5.1.3. Films grown on Pt-buffered substrates

The bottom contacts were grown by ex-situ sputtering. We tried first to use a thin Pt layer (20 nm), however, it was found that the samples are easy to get dewetting during subsequent high temperature process of LMO growth [Figs. 5.8(a,b)]. Then it was found that a thick Pt layer (> 90 nm) solves the dewetteing problem both on Al$_2$O$_3$ [Figs. 5.8(c,d)] and on Si(100), where the Pt ($\approx$ 120 nm) buffered Si(100) is a commercial available substrate. Nevertheless, for YSZ(111), the film layers peel off from the substrate even with 100 nm thick Pt (YSZ//Pt/LMO).
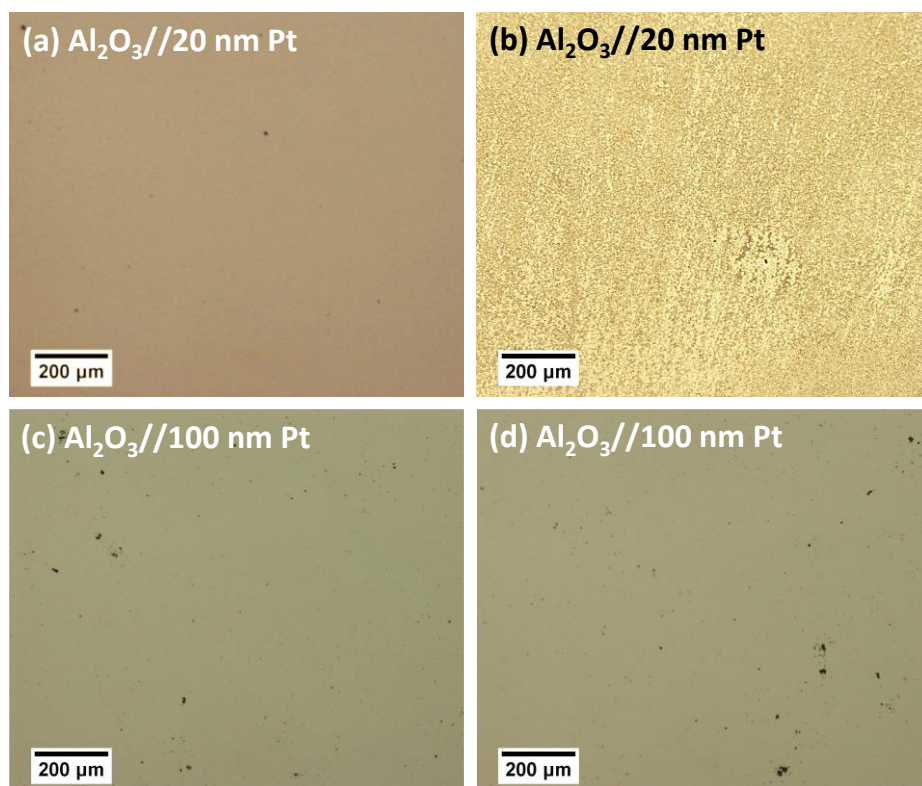
Fig. 5.8. Pictures of samples Al₂O₃//Pt (a,c) before and (b,d) after the dwell process (825 °C, 0.2 mbar, 60 min) in PLD chamber without depositing any further layer. It clearly shows when introducing thick Pt (100 nm), the dewetting phenomena is effectively suppressed.

It is worth noting that the θ-2θ XRD scans show a pure *c*-oriented LMO along hexagonal (0001) before introducing the Pt layer. While on the Pt-buffered substrate [Fig. 5.9(a)], there appears other characteristic peaks of LMO(11–22) plane and a tinny reflection of Mn_3O_4 (see detail in Chapter 5.2.3). As shown in Fig. 5.9(b), the Si//Pt/LMO samples show worse XRR results than Al₂O₃//Pt/LMO. Therefore, Al₂O₃//Pt (100 nm) is preferable substrate for LMO film. The red arrow denotes the critical angle of Pt, before which there are only oscillations of LMO, after which there exist oscillations of both LMO and Pt. The growth rate using 1 Hz (0.0584 Å/pulse) is slightly larger than using 3Hz (0.0575 Å/pulse), although it is hard to determine the accurate thickness by the unclear LMO oscillations in XRR when introducing the Pt layer.

Fig. 5.9. (a) θ-2θ XRD and (b) XRR scan of Si//Pt/LMO (1) and Al_2O_3//Pt/LMO (2) (12000 pulses).
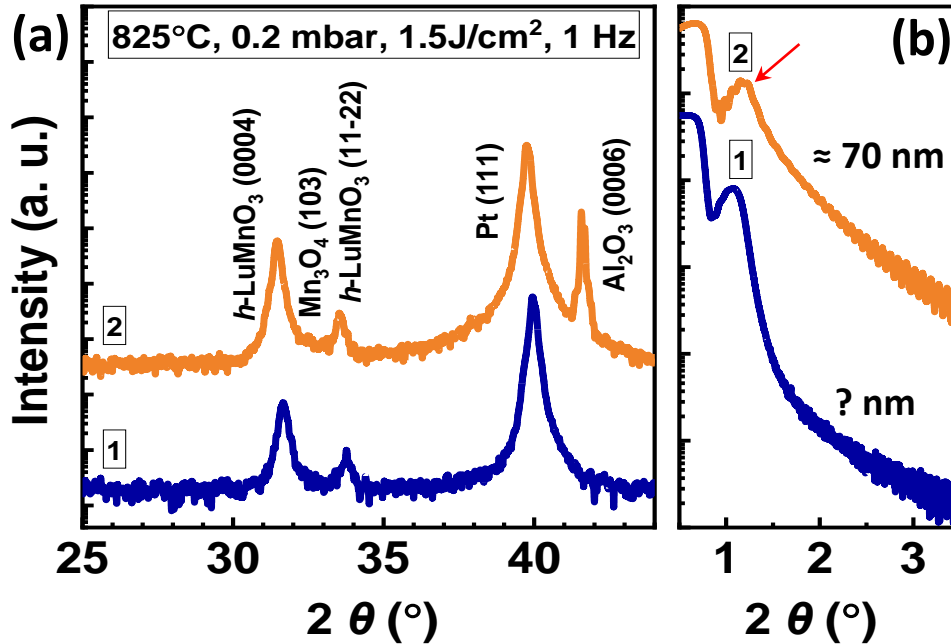
Based on above studies, 20 nm LMO was first deposited on Al_2O_3//Pt (100 nm), it shows good ferroelectricity by piezoresponse force microscopy (PFM) phase image [Fig. 5.10(c)], which exhibits almost 180° contrast between domains of opposite polarity as expected in ferroelectric materials. Despite that, the sample is too conducting (short-circuited) to be measured [Fig. 5.10(c)]. In contrast, when the LMO film thickness is larger than 60 nm, the LMO samples are more insulating and can be measured. For example, Figs. 5.10(b,d) show the results of 70 nm LMO based device, it also shows ferroelectricity although with higher surface roughness [Figs. 5.10(b)], more importantly, the leakage issue is significantly improved ($\approx$ 50 % effective Pt/LMO/Pt capacitors are not short-circuited) as seen by the green line in Figs. 5.10(d). For thicker LMO ($\approx$ 150 nm) sample, shown by the red line in Fig. 5.10(d), the more effective capacitors can be easily found ($\approx$ 80 % effective Pt/LMO/Pt capacitors). This 150 nm LMO was grown at 825 °C, 0.1 mbar, 2 J/cm^2 and 5 Hz to increase the growth rate, where even with less PO_2, the possible oxygen vacancies do not bring more leakage as the thickness increases.
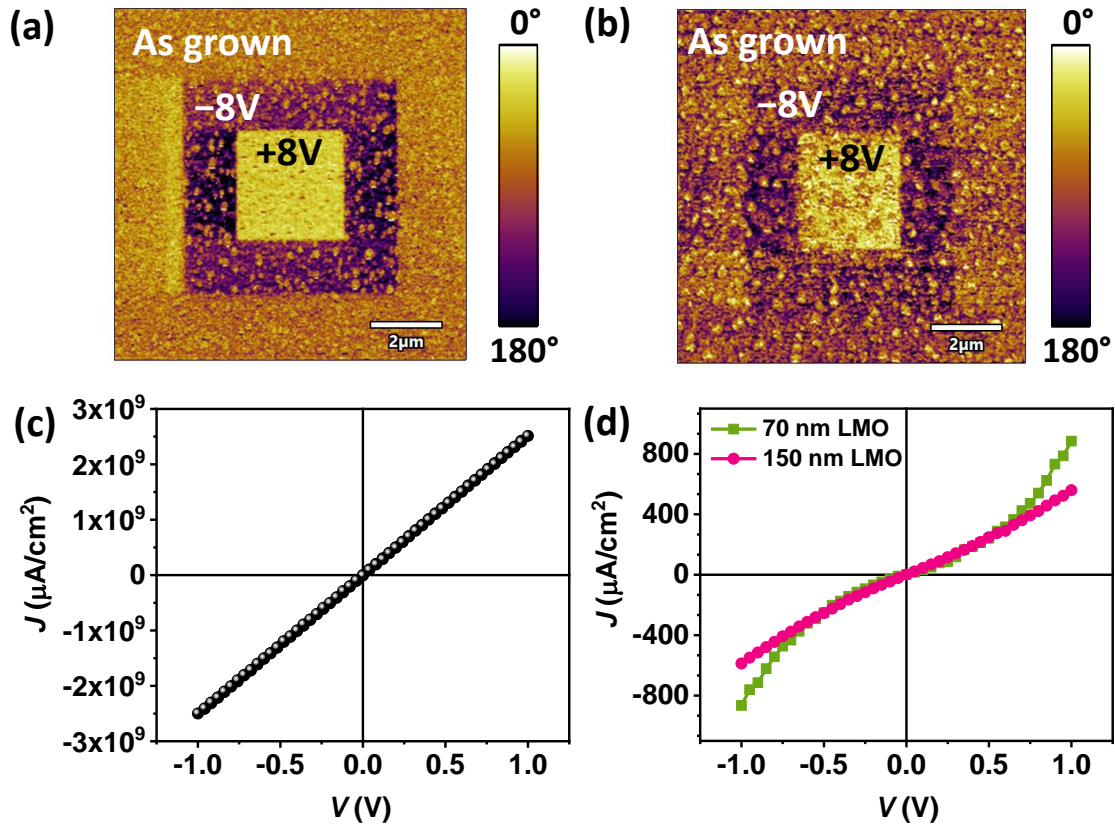
Fig. 5.10. PFM phase images of sample Al$_2$O$_3$//Pt/LMO with (a) 20 nm LMO and (b) 70 nm LMO, recorded at pristine state and after electrical lithography using ±8 V in the inner bright/dark areas as indicated. *J-V* characteristics in dark of device Al$_2$O$_3$//Pt/LMO/M$_T$ with (a) 20 nm LMO (top 50 nm Pt) and (b) 70 nm (top 20 nm Co covered by 10 nm Pt), 150 nm LMO (top 7 nm Pt).

5.1.3. Conclusions

In summary, according to the θ-2θ XRD and XRR scans, the optimal PLD conditions for growing hexagonal LuMnO$_3$ thin films are 825 °C, 0.2 mbar, 1.5 J/cm^2, where the laser frequency is insignificant. In addition, Al$_2$O$_3$(0001) is preferable substrate than YSZ(111) and Si(001). Thicker bottom electrode layer (> 90 nm Pt) prevents the films from dewetting, and thicker LMO layer (> 60 nm) improves the ratio of effective capacitors (not short-circuited Pt/LMO/Pt). Consequently, one optimal sample (70 nm LMO) was selected, grown on Pt(94 nm) coated Al$_2$O$_3$ under the optimal conditions, to perform further characterizations in the next section.

5.2. Polarization dependent photovoltaic response of LuMnO₃ thin films

In this section, the photovoltaic response of vertical capacitors of ferroelectric hexagonal LuMnO₃ films sandwiched between semitransparent top electrodes (Pt, Co, Au) and a common bottom electrode (Pt) is present. Our results show that the presence of electrodes, other than their optical transparency, crucially determines the imprint in the ferroelectric layer and ultimately the sensitivity of short circuit current density (J_{sc}) to the ferroelectric polarization direction. The use of ultrathin (7 nm) Pt top electrodes allows to obtain a large J_{sc} (up to 100 mA/cm^2) and an open circuit voltage of $V_{oc} \approx -0.52$ V, with a responsivity of 2 x 10^{-3} A/W. Polarization back-switching due to imprint largely washes out the dependence of J_{sc} on the direction of the polarization and thus, at first sight, J_{sc} seemingly appears to be ruled by conventional photovoltaic response. However, a pioneering analysis of the light-polarization dependent photosensitivity, allowed to disentangle for the first time, a genuine contribution of BPE from a ubiquitous Fresnel controlled contribution arising from interfaced optical media.

The work presented in this section was submitted to Acta. Mater.

5.2.1. Introduction

Photovoltaic conversion appears as the greenest energy source and as such it is receiving attention, both in the development of materials and fundamental understanding. Beyond the conventional photovoltaic materials and the dramatic progress achieved in halides, the recognition that light-matter interaction in non-centrosymmetric materials, which may give rise to rich phenomenology and open new opportunities, is also gaining momentum.[9–11] The photoresponse of non-centrosymmetric materials, the ferroelectrics among them, is one example of an emerging symmetry-related responsivity that may find applications in many areas (sensing, actuators, self-powered devices, data storage, etc.) [12] and, particularly, on photovoltaics.[13,14] Conventional photovoltaic materials rely on photon absorption on suitable semiconductors to create electron-hole pairs and their subsequent dissociation and extraction using built-in electric fields in non-homogenous electronic structures, for instance a pn-diode. While the physics and engineering of these devices are nowadays well understood, this is not the case of the photoresponse in ferroelectric materials.[15] Practical devices made using ferroelectric photo-absorbers (FE) would probably

require capacitor-like structures where the dielectric FE layer is sandwiched between top and bottom metallic electrodes (M_T and M_B), in which interfacial asymmetric Schottky barriers will be most generally formed. The electronic characteristics of these barriers primarily depend on the work function of the electrodes and the electronic nature of the dielectric layer. Their response (i.e., change of conductivity) upon illumination in the absorber determines the characteristics of M_B/FE/M_T capacitors. Besides, the ferroelectric polarization (*P*) of the ferroelectric layer, constitutes a new parameter to tune the photoconductivity conductivity of the capacitor as the surface charge associated to *P* modulates the height of the Schottky barriers, with reversed effect upon *P* reversal.[16] While at first sight these mechanisms appear to be simple, in practice the situation is more complex for several reasons. For instance: *P* reversal is commonly achieved by applying a suitable external electric field, although the fraction of switched ferroelectric domains, their localization within the capacitors or the presence of non-switchable regions is hardly known. It follows that the electric field distribution within the capacitor may largely differ from the simple two-plate capacitor model, and consequently its impact on the Schottky barrier shape may become intricate. In any event, the photovoltaic response driven by non-homogenous electric field of the devices, most notably the open circuit voltage (V_{oc}), is limited by the built-in voltage (V_{bi}) in the junction, typically < 1 V.

An added contribution to photoresponse arises from the non-centrosymmetric nature of the dielectric material, other than the mentioned *P*-related modulation of the interface electronic energy profiles. It turns out that, in electronically homogeneous non-centrosymmetric materials, there is a genuine photo response (so called bulk photovoltaic effect, BPE), a photocurrent is generated in absence of any built-in electric field.[17] BPE generated excitement as it offers new opportunities because V_{oc} is no longer limited by V_{bi} but can be orders of magnitude larger.[18] Of course, photoresponse at visible range, including BPE, requires photoabsorption and thus narrow bandgap semiconductors are beneficial. The observation of this large V_{oc} in the narrow gap BiFeO₃ ($E_g \approx 2.67$ V) boosted renewed research in photoferroelectrics. The interface-related contributions to the short circuit current density (J_{sc}) and V_{oc} were soon identified and it was also observed that, as suspected, *P* reversal had a direct impact on J_{sc} via modulation of Schottky barriers. Interestingly a dependence of J_{sc} on light polarization angle (φ) was discovered in BiFeO₃

single crystals[16], later understood as owing to BPE, and concomitantly a much larger V_{oc} than bandgap was also observed.[19] Wrapping up, several experimental evidences that are commonly taken as originating from BPE in photoferroelectrics are switchable photovoltaic outputs,[6–8,16,20] above-bandgap photovoltage,[18,19,21,22] and light polarization dependence.[9,19,22–24] Among those, light polarization dependence appears to be the most indisputable and pervasive fingerprint of BPE.[16,19,25,26]

Interest is now directed towards ferroelectric materials having narrower bandgaps (E_g). Hexagonal manganites (ReMnO₃) and ferrites (ReFeO₃) are particularly suitable candidates because they are uniaxial polar materials and chemically stable, with E_g < 2 eV. Epitaxial films of (Lu,Y)MnO₃ [6] and (Lu,Tm)FeO₃ films [8] were explored. It was shown that J_{sc} can be reversed (charge flow reversed) when reversing the polarization of the ferroelectric layer. While these results undoubtedly demonstrate that the polarization direction ***P*** has a direct impact on the performance of the devices by modulating the Schottky barriers and subsequently their photoconductance, they did not provide any information of the possible contribution of BPE to the observed photoresponse. Attempts to disclose any possible role of BPE on the photoresponse of LuMnO₃ were first reported by Y. Sheng et al.[23] who reported data on single crystals. They identified that drift and diffusion photocurrent terms can contribute to a non-switchable portion of the photoresponse that add to a Schottky modulated transport. Drift current arises from any built-in electric field, either at interfaces or within the ferroelectric layer (depoling field), and thus it is expected to be affected by the selection of the electrode (M_T, M_B) and the ***P*** direction. The diffusion term is associated to photogenerated charge gradients that are unavoidable when using thick single crystals of strongly absorbing materials. Interestingly, Sheng et al. reported that the magnitude of J_{sc} was dependent on the polarization direction (φ) of the linearly polarized light used in the experiments, with an angular dependence fully consistent with expectations based on the symmetry class of hexagonal LuMnO₃, suggesting that BPE also contributes to J_{sc}.[23] However, they also discovered that, contrary to BPE expectations, the signs of J_{sc} and $J_{sc}(\varphi)$ in LuMnO₃ single crystals could not be reversed by poling the ferroelectric in opposite direction.[20,27] This apparent difficulty was solved by the demonstration that back-switching of polarization due to imprint fields precluded stable polarization reversed states.

Herein, we focus on the photoresponse of capacitors using ferroelectric hexagonal LuMnO$_3$ thin films as photoabsorbers, with the expectation that the use of thin films will reduce diffusion contributions to the photocurrent. After confirming the ferroelectric character of the fabricated films, we show that the selected metallic electrodes (M$_T$) have twofold important effects on the photoresponse. First, not surprisingly, the optical absorption at electrodes limits the observed short-circuit photocurrent (J_{sc}). Second, we show that the electrodes not only affect the Schottky barriers at interfaces but also have an important role on stablishing an imprint field within the ferroelectric that imbalances the equilibrium distribution of polar domains. In the presence of imprint, polarization back-switching occurs and translates into a weak dependence of the J_{sc} on the initial polarization direction, set by the pre-polarization of the ferroelectric layer, that washes out the most obvious fingerprints (switchable photoresponse) of the polar nature of LuMnO$_3$ on the photoresponse. Still, it is shown that photoinduced carriers further contribute to polarization back-switching. Lastly, the ferroelectric contribution to J_{sc}, which as mentioned remains largely invisible in presence of back-switching, may still be present and enhanced by the existence of bulk photovoltaic effect (BPE). [27]

Moreover, a dependence of $J_{sc}(\varphi)$ on the light-polarization direction (φ is the angle between the initial light polarization and the polarization axis) is commonly taken as a genuine fingerprint of BPE. Indeed, reports exist attributing $J_{sc}(\varphi)$ in LuMnO$_3$ to BPE,[23,27] as in BiFeO$_3$ or BaTiO$_3$, to mention few earlier examples.[16,19,25,26] However, in vertical capacitors, the polarization-dependent light transmission at oblique incidence (Fresnel contribution) at top electrodes may introduce a spurious Fresnel-related contribution to $J_{sc}(\varphi)$ oscillation [9,28] that mimics and may conceal a genuine BPE contribution. Here, a pioneering comparative analysis of $J_{sc}(\varphi)$ and related open-circuit voltages $V_{oc}(\varphi)$, together with the dependence of J_{sc} and V_{oc} on light intensity allows to disentangle and disclose for the first time a minor BPE contribution to J_{sc} in hexagonal manganite thin films. All in all, our LuMnO$_3$ films which although being mostly epitaxial contain obvious grain boundaries, display a photocurrent and responsivity that rivals and even exceed those of epitaxial films of related materials, i.e., BiFeO$_3$.[29,30]

5.2.2. Samples and experiments

A sketch of the sample is shown in Fig. 5.11(a). To minimize possible spurious difference among samples, all electrodes reported here were grown on the very same film. Devices are denoted as: Pt/LMO/Pt, Pt/LMO/Co (Co-Pt) and Pt/LMO/Ti (Ti-Au), electrode details see Chapter 3.1.4.

Structural characterization was performed by X-ray diffraction (XRD) with Cu K_α radiation using a Siemens D5000 diffractometer equipped with a point detector. X-ray reflectometry and suitable calibration were used to infer the thicknesses of the different layers. The morphology was characterized by scanning electron microscopy (SEM) QUANTA FEI 200 FEG-ESEM. Cross-sectional scanning transmission electron microscopy (STEM) analyses have been performed using a probe aberration corrected microscope, a Jeol ARM 200cF STEM with a cold field emission source operated at 200 kV, at Universidad Complutense de Madrid (Spain). Specimens for TEM observations were prepared by conventional methods: grinding, dimpling and Ar ion milling. Piezoresponse force microscopy (PFM) measurements were performed with an MFP-3D Asylum Research microscope (Oxford Instrument Co.) using BudgetSensors silicon (n-type) cantilevers with Cr/Pt coating (Multi75E-G). To achieve better sensitivity, the dual AC resonance tracking (DART) method was employed.[31] PFM voltage hysteresis loops were performed at remanence, using a dwell time of 5 ms.

Current density-Voltage (*J-V*) characteristics were recorded by a Keithley 6517B Electrometer, using bipolar triangular excitation signals from +1 V to −1 V with ≈ 0.5 s integration time; the recording time is: $\tau_r \approx 50$ s for 100 points. See details of photoresponse measurements in Chapter 3.4, illumination was done by a blue-violet laser source (λ = 405 nm). The angle of incidence of the light (with respect to the normal to the sample surface) was fixed at 45°. All the electrical measurements were performed in top-bottom configuration with the bias $V^{+/-}$ applied to the top contacts (Pt, Co and Ti) and the bottom contact (Pt) grounded. Magnetic data were obtained by using a QD SQUID magnetometer.

5.2.3. Ferroelectric h-LuMnO₃ thin films

The XRD θ-2θ scan of the Al_2O_3//Pt/LMO heterostructure is shown in Fig. 5.11(b). The highest intensity peaks correspond to Al_2O_3 and Pt reflections. The hexagonal LMO(0004) reflection ($P6_3cm$) is clearly visible. The small peak of the LMO(11−22) plane, indicates a minor fraction misoriented LMO crystallites. A tinny reflection perceptible at $2\theta \approx 32.5°$ can be attributed to Mn_3O_4 crystallites embedded within the film, which have also been observed using STEM. Full angular range θ-2θ and 2θ-χ scans (see Supplementary information S5.1) confirm that LMO films are mostly textured along (0001). χ-ϕ frames around the indicated reflections are shown in Fig. 5.11(c). They signal an epitaxial growth of the bottom Pt layer and LMO(0001) on Al_2O_3. There are 6 peaks of Al_2O_3, representing a single domain of Al_2O_3. Instead, 12 peaks for LMO are visible, indicating the presence of 2 crystallographic domains of LMO rotated by 30°. Pt shows 9 peaks implying the presence of three in-plane Pt domains rotated by 30°.
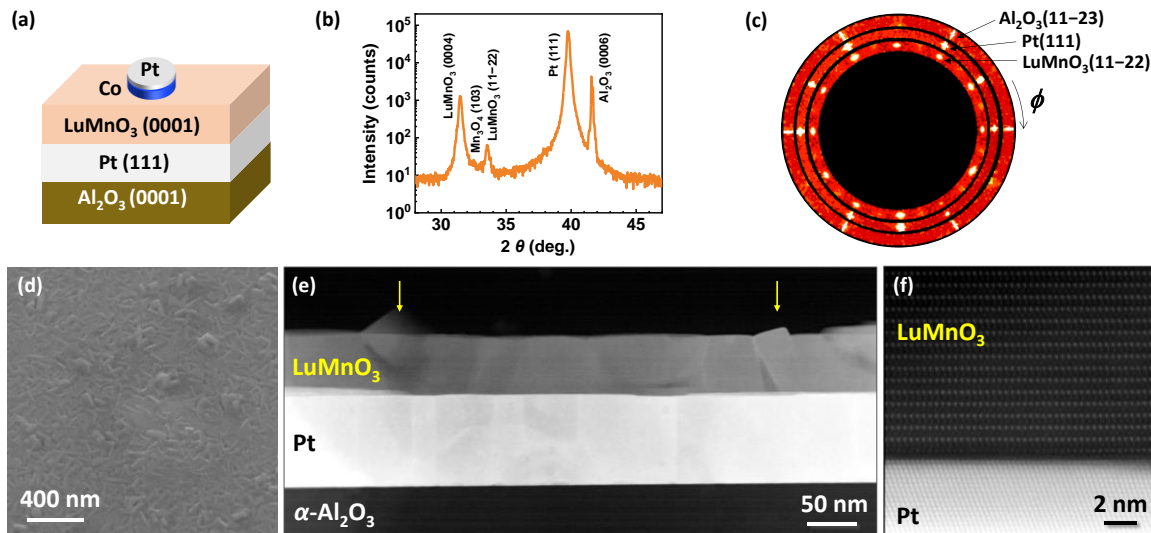

Fig. 5.11. (a) Sketch of the sample structure and vertical capacitors. Here Al_2O_3//Pt/LMO/Co is displayed. (b) θ-2θ XRD scan and (c) χ-ϕ pole figures around the indicated reflections of Al_2O_3//Pt/LMO. (d) SEM images of the Al_2O_3//Pt/LMO top surface using secondary electrons. (e) Low HAADF-STEM image of the Al_2O_3//Pt/LMO heterostructure acquired along the [11−20] α-Al_2O_3 zone axis. The yellow arrows mark two misoriented LMO grains among the majority of *c*-textured ones. (f) Atomic resolution HAADF-STEM image of the Pt/LMO interface acquired the [1−10] and [11−20] zone axes, respectively.

The SEM image of the top surface [Fig. 5.11(d)] shows its morphology and reveals the presence of crystallites at the film surface. The low magnification HAADF-STEM image shown in Fig. 5.11(e) allows to get a deeper insight into the microstructure of the films in section view. The contrast of the HAADF imaging mode is sensitive to the atomic number, the brightness scales approximately as Z^2, which means that the heavier element has brighter contrast. Thus, this image shows a clear contrast among the LMO film, the bottom Pt electrode, and the Al_2O_3 substrate. The image also shows a continuous film with a uniform columnar grain structure, with lateral sizes ranging from 50 to 100 nm. The coalesced grains have a rectangular shape and a flat surface, although they present a small grooving at the grain boundaries. Notice that there are regions within the film that present a darker contrast, indicative of a different composition, Lu-poor, which coincides with the Mn_3O_4 reflection observed above. Moreover, a careful analysis of the LMO microstructure reveals that most of the LMO grains are epitaxially grown and *c*-textured, whereas there are others that present a different orientation, e.g. (11−22) in Fig. 5.11(b), which outgrow from the Mn_3O_4 crystallites located deep into the film and emerge at the film surface, as anticipated by SEM images [Fig. 5.11(d)]. The magnetization data confirms the presence of intergrowths of ferromagnetic Mn_3O_4 (Annex A).[32,33] Fig. 5.11(e) shows two of such grains signaled with yellow arrows. As a result, the LMO films grown on a thick Pt layer (94 nm) have a complex network of grain boundaries (see Supplementary information S5.2 for further details). Higher resolution HAADF-STEM images probed the high quality of the epitaxial LMO crystallites in the film. Fig. 5.11(f) shows a high resolution HAADF image of the Pt/LMO interface along the [1−10] and [11−20] zone axes, respectively. This Z-contrast image shows the expected sequence of manganese and lutetium monolayers of a *c*-textured grain, and reveal a Al_2O_3[11−20]//Pt[1−10]/LMO[11−20] in plane and a Al_2O_3[0001]//Pt[111]/LMO [0001] out of plane epitaxial relationship, in agreement with χ-ϕ frames.

Figs. 5.12(a,b) show amplitude and phase PFM images of the bare surface of LMO at pristine state (outer region) and after electrical lithography using +/−8 V (inner regions). It can be appreciated in Fig. 5.12(a) that the PFM amplitude at the poled regions is constant while at the boundary between regions of opposite polarization the PFM amplitude signal zeroes. The phase image [Fig. 5.12(b)] shows a 180° contrast between domains of opposite

polarity as expected in ferroelectric materials. The pristine polarization direction is upward (outer region), indicating the presence of upward imprint field. In Fig. 5.12(c), the PFM amplitude and phase loops are displayed. The amplitude loop shows the characteristic butterfly-shape and the phase loop shows a hysteretic 180° switchable signal. Note that the loops are shifted towards positive voltage, which is consistent with data in Figs. 5.12(a,b), indicating the presence of a upwards imprint field (V_{im} ≈ +0.53 V). All these features are signatures of the ferroelectric character of the sample and exclude a significant contribution of extrinsic effects.[34]
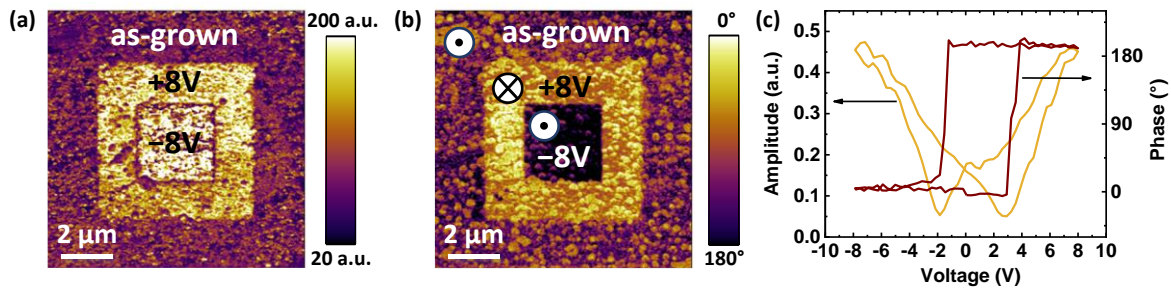

Fig. 5.12. PFM (a) amplitude and (b) phase images recorded at the bare surface of Pt/LMO at pristine state and after electrical lithography using ±8 V in the inner bright/dark areas [of Fig. 5.11(b)] as indicated. (c) PFM amplitude and phase loops of Pt/LMO.

5.2.4. Dependence of LuMnO₃-based capacitors photoresponse on top electrodes

The photoresponse of LMO-based capacitors using the different electrodes are summarized in Fig. 5.13(a), where we depict the *J-V* curves collected in dark and under illumination (I_p = 50, 84 and 70 W/cm² for Pt, Co and Ti, respectively). The zoom of *J-V* curves for Pt/LMO/Pt is included in Supplementary information S5.3. The dark *J-V* curves, which cannot be appreciated in Fig. 5.13(a) as the current is comparatively much smaller (see zoom in Supplementary information S5.4), display a weak non-linearity resulting from the presence of distinctive interfacial barriers which are determined by the electrode selection that led to different conductance: $J_{V=0.2V}$ ≈ 250 μA/cm², 50 μA/cm² and 10 μA/cm², for Pt, Ti and Co, respectively. Under illumination, a remarkably large J_{sc} is measured, and it turns out that J_{sc}(Pt) > J_{sc}(Co) >> J_{sc}(Ti). In Fig. 5.13(b) we plot the responsivity ($R = \frac{J_{sc} - J_{dark,V=0}}{I_p}$, where $J_{dark,V=0}$ is the current in dark at zero bias) as a function of the electrode optical transparency calculated at λ = 405 nm.[35,36] It is obvious that J_{sc} and R are mainly governed by the optical

transparency of the electrode, as it primarily determines the light intensity reaching to the LMO absorbing layer. For comparison, data on LMO single crystal (SC) using 7 nm top Pt electrode [20,23] has also been included to emphasize the relatively larger R of the LMO films reported here.
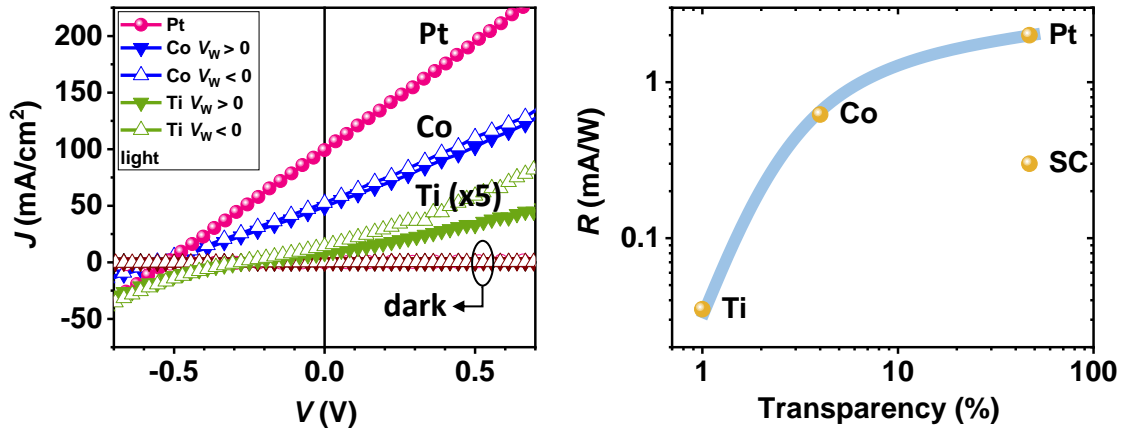

Fig. 5.13 (a) *J-V* characteristics of Pt/LMO/M (M = Pt, Co and Ti) capacitors ($V_w^{+,-}$ = ± 12 V). A zoom of the dark data is shown in Supplementary information S5.4. (b) Photoresponsivity (R) as a function of electrode optical transparency. LMO single crystal (SC) data is from refs. 20,23. The blue line is a guide to eyes.

5.2.5. Imprint in LuMnO₃-based capacitors

Next, we address the existence of imprint fields and their relation with the selected M_T electrode and the polarization back-switching. Capacitors having top Co electrodes (Pt/LMO/Co) are fully described here. Data for Pt/LMO/Ti capacitor are in Supplementary information S5.5. Ferroelectric polarization and current loops collected using Pt/LMO/Co electrodes are shown in Fig. 5.14(a). The presence of current switching peaks (indicated by red arrows) confirms the ferroelectric character of the Pt/LMO/Co capacitor. Note that the loops of Fig. 5.14(a) are strongly shifted towards positive voltage (V_{im} = +5.76 V, from the current loop), implying an upward imprint field, as observed by PFM in the bare LMO films (Fig. 5.12), but here, it is found much stronger. As LMO film is the same as the one used in the PFM experiments performed at the bare LMO surface and in the electric experiments on the Pt/LMO/Co capacitors, the observed different imprint results from the deposition of the top electrode.
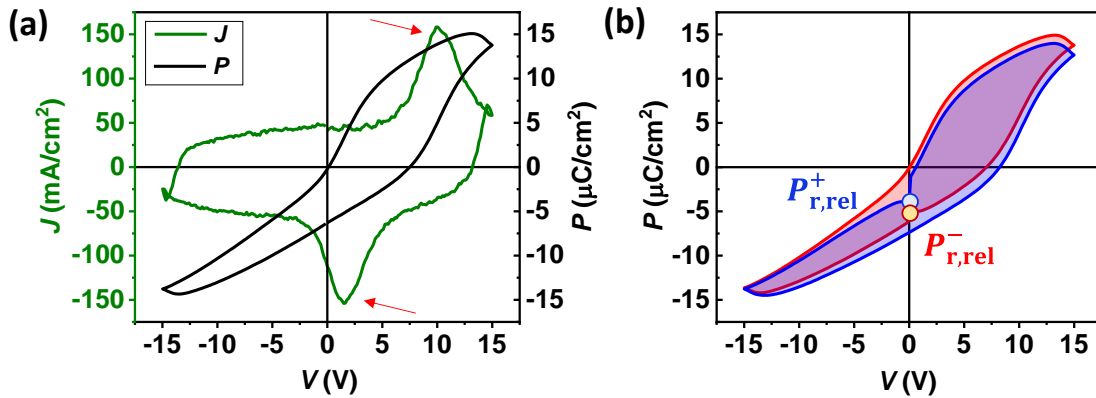
Fig. 5.14 (a) $J(V)$ and integrated $P(V)$ loops; (b) Retention measured by $P(V)$ loops at remanence (delay time τ_d = 1 s) of Pt/LMO/Co.

A practical consequence of the absence of a significant imprint field in the PFM images of the bare sample (Pt/LMO) is that there is not obvious back-switching. This is not the case in Pt/LMO/Co capacitors. In Fig. 5.14(b), we show the so-called relaxed polarization curves collected in Pt/LMO/Co. The red curve corresponds to the application of a negative triangular voltage pulse of 1 kHz and the measurement of the loop after a delay time $\tau_d \approx 1$ s. The loop is measured by first increasing the voltage from V_w = 0 V until the maximum voltage then decreasing to the minimum and coming back to V_w = 0 V (anticlockwise). Then, the polarization indicated as $P^-_{r,rel}$ corresponds to the remanent polarization state after τ_d ≈ 1 s, set by the negative pre-poling. The same protocol is applied to obtain $P^+_{r,rel}$ (the blue curve) using a positive pre-poling . Further experimental details can be found elsewhere.[27] Remarkably, it is observed that irrespectively of the sign of the writing voltage, the polarization is always found with the same sign (negative here, implying upward polarization) which evidences the back-switch of downward polarization. Thus, the final polarization state is always upward and the difference between $P^+_{r,rel}$ and $P^-_{r,rel}$ is only ≈ 1.08 $\mu C/cm^2$, reflecting a small polarization contrast. Similar results are obtained using Pt/LMO/Ti capacitor (Supplementary information S5.5), while leakage current in Pt/LMO/Pt precluded obtaining reliable $P(E)$ loops and evaluation imprint fields.

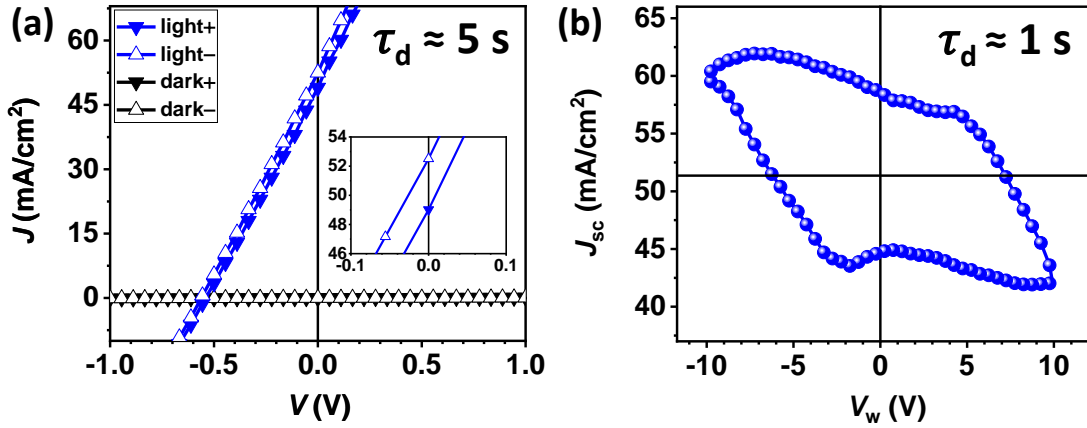*5.2.6. Role of imprint on the polarization-dependent photoresponse*

Fig. 5.15. (a) J(V) curves of Pt/LMO/Co collected in dark and under illumination ($I_p \approx 84$ W/cm^2) after pre-poling the capacitor with writing voltages: $V_w^{+,-} = \pm 12$ V (inset shows the zoom of photocurrent near zero bias). (b) J_{sc} of Pt/LMO/Co measured after pre-poling the capacitor with indicated writing voltage V_w.

We now concentrate on the polarization-dependent photoresponse and how it is affected by polarization back-switching. We first note that J(V) data collected under illumination after pre-polarizing the samples with $V_w > 0$ (+), or $V_w < 0$ (−) ($|V_{w,max}| = 12$ V larger than the coercive voltage $V_c^+ \approx 10$ V) remains always in the same quadrant implying that pre-poling direction does not reverse the current flow. Fig. 5.15(a) shows an expanded view of J(V) data of the Pt/LMO/Co capacitor [Fig. 5.13(a)], collected in dark and under illumination. Measurements were done with $\tau_d \approx 5$ s after applying pre-poling voltages ($V_w^{+,-}$) of opposite sign to set the initial polarization state. The J_{sc} and V_{oc} values are $\approx + 52$ mA/cm^2 and $\approx - 0.56$ V, respectively. The current offset (≈ 52 mA/cm^2) results from the presence of an unswitchable drift current contribution related to built-in electric fields. Superimposed, it can be appreciated that $J_{sc}^{+,-}$ and $V_{oc}^{+,-}$ slightly vary depending on the sign (+,−) of V_w. The variation is quantified by: $J_{sc\text{-switch}} = \frac{J_{sc}^- - J_{sc}^+}{J_{sc}^-} \approx 7$ % and $\frac{V_{oc}^- - V_{oc}^+}{V_{oc}^-} \approx 4$ %. The small value of switchable photocurrent $J_{sc\text{-switch}}$ is mostly a manifestation of back-switching of ferroelectric domains which, in presence of imprint, occurs shortly ($\tau < \tau_d \approx 5$ s) after application of pre-poling voltage V_w.[20] To minimize its effect, J_{sc} has been collected at zero bias directly in a continuous manner and using a shorter delay time ($\tau_d \approx 1$ s) after the sample pre-poling. The experimental protocol is further described in Supplementary information S5.6. The

collected $J_{sc}(V_w)$ dependence [Fig. 5.15(b)] nicely mimics the hysteresis of a ferroelectric loop. The J_{sc} variation upon polarization switching is now found to be larger ($J_{sc\text{-switch}} \approx 32$ %) than in the experiment shown in Fig. 5.15(a), owing to the shorter delay time used in the latter and the continuous J_{sc} data collection process that reduce the impact of polarization back-switching. It can be also observed in Fig. 5.15(b) that the imprint voltage is reduced under illumination ($V_{im} \approx + 0.6$ V) although its sign is preserved (Figs. 5.12, 5.14). Similar results are obtained using Pt/LMO/Ti capacitor (Supplementary information S5.7).
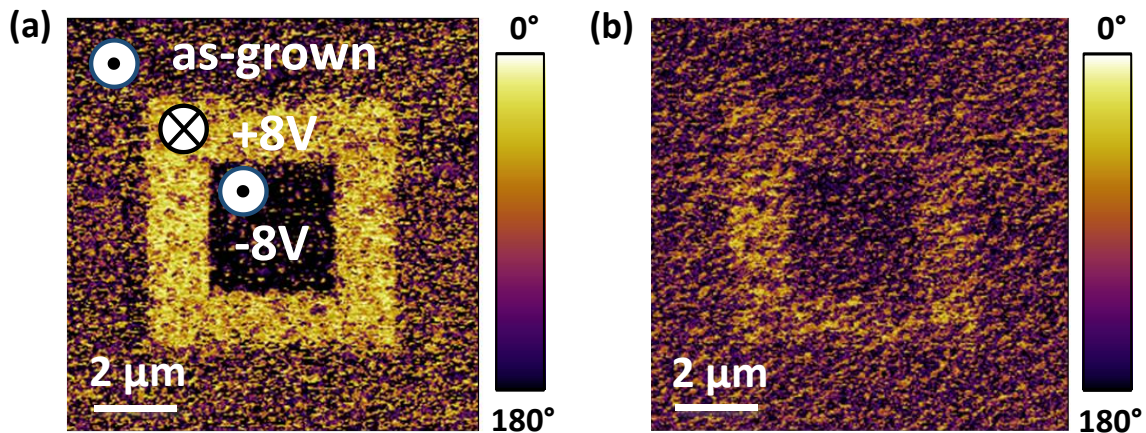

Fig. 5.16. PFM phase images at the bare surface of Pt/LMO heterostructure and after electrical lithography using ±8 V in the inner dark/bright areas recorded: (a) in dark and (b) after illumination with 405 nm laser of $I_p \approx 20$ W/cm² for 1 min.

While data in Figs. 5.14, 5.15 conclusively demonstrate the impact of imprint-enhanced polarization reversal, occurring within $\tau < \tau_d$ ($\approx$ 1s) in Pt/LMO/Co capacitors, its relevance should be much weaker when imprint is reduced. As shown in Fig. 5.12, the bare Pt/LMO devices are weakly imprinted and correspondingly, their retention should be larger. Bare Pt/LMO have been biased with $V_w^{+,-} = \pm 8$ V (corresponding to $P^\downarrow$ and $P^\uparrow$ polarization, respectively) as shown in Fig. 5.12(b), to write domains of opposite polarity [Fig. 5.16(a)]. The phase contrast in Fig. 5.16(a) does not show any perceptible time evolution within one hour, implying negligible back-switching in dark. However, it is found that after 1 min illumination (λ = 405 nm, $I_p \approx 20$ W/cm²) the phase contrast disappears [Fig. 5.16(b)]. The resulting yellow contrast indicates that most of the $P^\downarrow$ domains have switched back to $P^\uparrow$, that is: parallel to the pristine polarization direction as dictated by imprint.

Fig. 5.17(a) sketches the back-switching process in presence of a large imprint and its effect on the polarization retention and the measured J_{sc}. Fig. 5.17(b) sketches the light-induced polarization reversal under weak imprint.
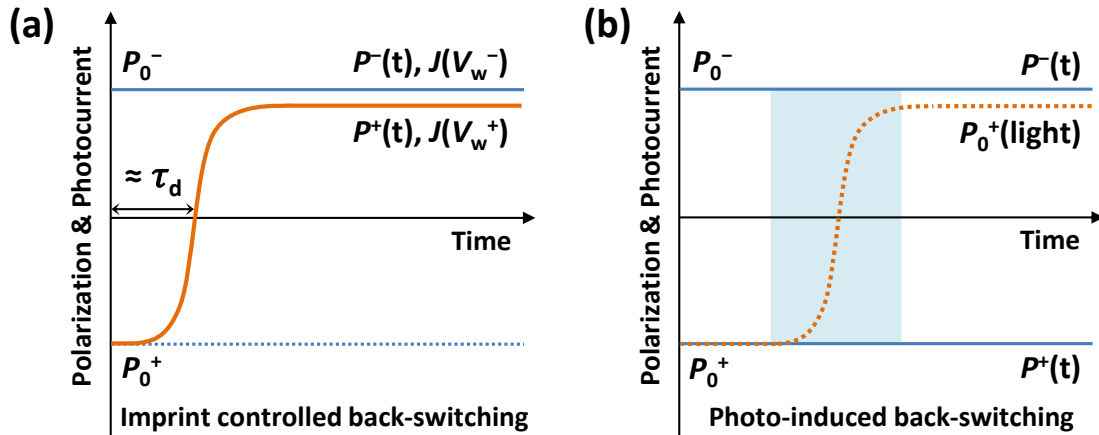

Fig. 5.17. Polarization retention and its impact on: (a) the measured photocurrent J_{sc} [as in Fig. 5.15(a)] and, (b) the contrast in PFM images [as in Fig. 5.16]. (a) Horizontal (blue) lines at P_0^- and P_0^+ indicate the written polarization by $V_w^{+,-}$ pre-poling in absence of back-switching, and $P^+(t)$ is its actual temporal evolution of polarization and the corresponding photocurrent $J(V_w^+)$ (solid blue line and orange line), after V_w^+ when a large imprint imposes a fast polarization switching (< 1 s) as observed in Pt/LFO/Co capacitors. (b) A weak imprint is assumed as observed in bare Pt/LMO devices where no polarization reversal occurs in dark and the written polar state is preserved (blue lines). Under illumination (blueish box) polarization reversal is promoted (dashed orange line).

Light-induced polarization reversal,[37–40] as observed in Fig. 5.16 and sketched in Fig. 5.17(b), has been earlier reported in BaTiO₃ films and attributed to photocarrier-induced transient suppression of the polarization and subsequent poling in the direction of imprint field [37] Returning to the photoresponse of LMO capacitors, in spite the fact that imprint largely cancels the dependence of photocurrent on the polarization direction, the photocurrent observed in Figs. 5.15, S5.3 clearly indicate a substantial responsivity of Pt/LMO/Co and Pt/LMO/Pt capacitors (6.2 × 10⁻⁴ and 2 x 10⁻³ A/W, respectively), that exceeds that reported for LMO single crystals (3 × 10⁻⁴ A/W).[20,23] The comparison with other hexagonal ferroelectrics [6–8,29,41] thin films is hampered by different illumination conditions and electrodes.

5.2.7. Light intensity dependence and role of light polarization: BPE vs. Fresnel

The *J-V* curves collected in dark and under illumination [Fig. 5.18(a)] recorded with a λ = 405 nm laser of various intensities I_p, show a steady increase of $J(I_p)$. As shown in Fig. 5.18(b) the photocurrent with light switching on and off at different light intensity is stable and repeatable. Data also show that the photocurrent increases in a step-like manner indicating the fast response at the measurement timescale. Data extracted from Fig. 5.18(a) indicate that J_{sc} increases almost linearly with I_p [Fig. 5.18(c), left axis] while V_{oc} increases rapidly first then tends to saturate [Fig. 5.18(c), right axis] [see zoom of Fig. 5.18(a) near V_{oc} in Supplementary information S5.8], roughly mimicking the V_{oc} [$\propto \ln(I_p)$] dependence of conventional photovoltaic devices.[42–44]
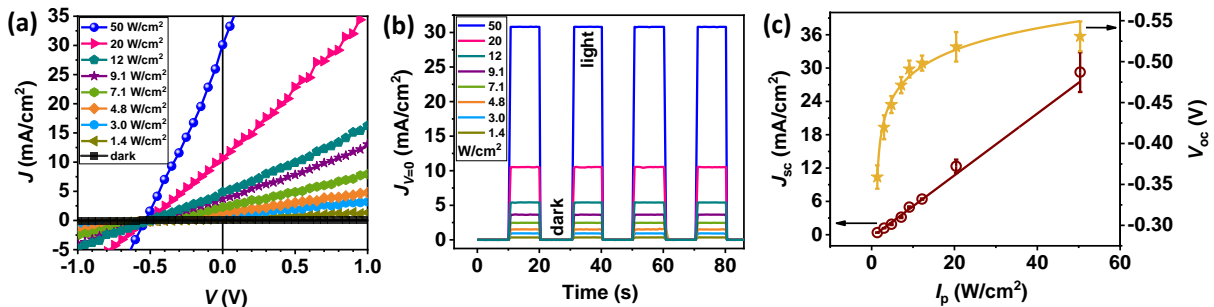

Fig. 5.18. (a) The *J-V* curves of Pt/LMO/Co collected in dark and under illumination of various light intensities and (b) the corresponding time-dependent current response of recorded at zero bias recorded during repeated on/off light cycles. (c) Average values of J_{sc} and V_{oc} extracted from the *J-V* curves of three capacitors as a function of light intensity. Dark and yellow solid lines are linear ($J_{sc} \propto I_p$) and logarithm [$V_{oc} \propto \ln(I_p)$] fits of the experimental data (symbols), respectively; error bars indicate the spread of values (standard deviation).

A fingerprint of a possible BPE contribution to J_{sc} can be in principle inferred from a measurement of J_{sc} as a function of polarization angle of light $J_{sc}(\varphi)$, when the sample is illuminated at oblique incidence. As shown in Fig. 5.19(a), $J_{sc}(\varphi) \approx A\cos(2\varphi) + B$, which is in agreement with the predicted $J_{sc}(\varphi)$ for hexagonal LMO. [23] Similar results with smaller oscillation amplitude and background are obtained when Ti top electrodes are used (see Supplementary information S5.9). However, Fresnel contributions due to light polarization (*p* or *s*) dependence on the transmitted light (I_T) at various interfaces (i.e., air/top electrode) display a similar $I_T(\varphi)$ oscillation [$I_T(\varphi) \approx I_p\cos(2\varphi)$] [9] as well, and consequently conventional

photovoltaic response (i.e., drift) should lead also to a similar oscillation of $J_{sc}(\varphi)$. Therefore, at oblique light incidence, both effects are entangled and challenging twined. To circumvent this difficulty we notice that in standard pn junction, V_{oc} is given by:[45]

$$V_{oc} = n\frac{kT}{q}\ln(1+\frac{J_{sc}}{J_0})$$ [5.1]

where J_0 is the reverse saturation current of the junction and n (the so-called ideality factor) measures the relative contribution of recombination or diffusion and typically $1 \leq n \leq 2$.[46] On the other hand, within BPE scenario, V_{oc} is given by:[19,47]

$$V_{oc} = \frac{J_{sc}l}{\sigma_d+\sigma_{pv}}$$ [5.2]

where σ_d and σ_{pv} are the dark and photo conductivity, respectively; l is the distance between electrodes. In this case, σ_d is relatively small and negligible, even though both J_{sc} and σ_{pv} increases linearly with I_p, V_{oc} can still be modulated by I_p if J_{sc} and σ_{pv} would increase with a different growth rate.

Data in Fig. 5.19(b) reveal that V_{oc} also displays a $\cos(2\varphi)$ dependence, which can originate from Eq. [5.1] and/or [5.2] and thus taken alone it cannot discriminate between BPE and Fresnel. In Fig. 5.19(c) we plot the measured dependence of $V_{oc}(I_p)$ vs. $\ln[J_{sc}(I_p)]$ (orange spheres) derived from data in Fig. 5.18(c). Data show a clear logarithmic dependence of V_{oc} on J_{sc} as expected from Eq. [5.1] above. The measured slope is ≈ 0.041, which according to Eq. [5.1] indicates that $n \approx 1.58$ (if there is not contribution from BPE), which is within the expected range. Therefore, most of J_{sc} in the present capacitors can be well described within the conventional photovoltaic framework. However, in case the $J_{sc}(\varphi)$ and $V_{oc}(\varphi)$ oscillations in Figs. 5.9(a,b) were due to Fresnel, according to Eq. [5.1], it should be expected that $V_{oc}(\varphi) \propto \ln[J_{sc}(\varphi)]$, with an identical slope that determined above. To assess this prediction, we also depict $V_{oc}(\varphi)$ vs. $\ln[J_{sc}(\varphi)]$ (blue rhombi) in Fig. 5.19(c). It is obvious that data extends on a limited range of values exemplifying the minor modulation of photocurrent with the light polarization. However, more interesting is to notice that the slope of $V_{oc}(\varphi)$ vs. $\ln[J_{sc}(\varphi)]$ (≈ 0.15) is definitely larger (≈ 366 %) than that of $V_{oc}(I_p)$ vs. $\ln[J_{sc}(I_p)]$, implying that the modulation of the light intensity reaching the photoabsorber by the Fresnel effect is definitely insufficient to account for the observed modulation of $V_{oc}(\varphi)$.

Therefore, we take the observed joint cos(2φ) dependences of $J_{sc}(\varphi)$ and $V_{oc}(\varphi)$ as first fingerprints of BPE in hexagonal ferroelectric thin films, although accompanied with the Fresnel contribution.
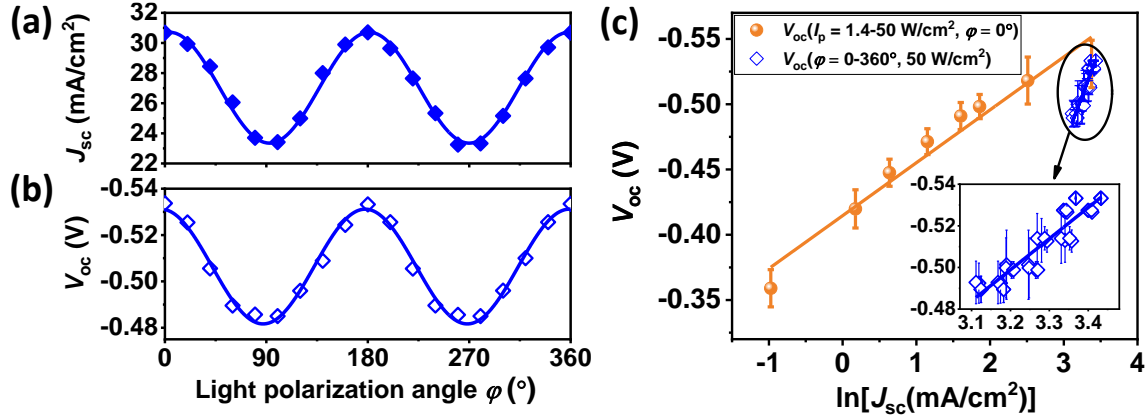

Fig. 5.19. Dependence of the (a) $J_{sc}(\varphi)$ and (b) $V_{oc}(\varphi)$ of Pt/LMO/Co on the light polarization angles (φ); solid lines are fits using a sine function of experimental data (symbols); the illumination is through the top electrode and the I_p after optical plates is around 50 W/cm². (c) Average values of V_{oc} among three capacitors as a function of ln(J_{sc}) at various power [orange spheres, data taken from Fig. 5.18(c)] and light polarization angle φ [blue rhombi, data taken from Figs. 5.9(a,b) of three capacitors], where the inset shows the zoom of $V_{oc}(\varphi)$ vs. ln[$J_{sc}(\varphi)$]. Solid lines are linear fits of experimental data (symbols), error bars indicate the spread (SD) of values.

5.2.8. Discussions and conclusions

Ferroelectricity and photovoltaic response have been identified in hexagonal LuMnO₃ thin films. A short circuit photocurrent up to ≈ 100 mA/cm² is observed, which is larger than observed in other ferroelectric oxides[29] but, probably, still too small for energy harvesting applications. The comparison of J_{sc} data reported here with available data in literature shows that our J_{sc} values exceed by more than two orders of magnitude than those reported for epitaxial LuMnO₃ films and isostructural ferroelectric ferrites.[6–8] However, the detailed comparison of responsivity is hampered by the use of different electrodes and different illuminations conditions.[6–8] The photocurrent and responsivity reported (≤ 2 × 10⁻³ A/W) here are also definitely larger than those obtained from measurements on LuMnO₃ single crystals (≈ 3 × 10⁻⁴ A/W [20]), using similar illuminations/conditions, probably due to the more efficient charge extraction in thin films than in bulky single crystals. The responsivity is also

larger than in BiFeO₃ thin films where a maximum responsivity 6.56×10^{-4} A/W was reported (using ITO top electrode measured at 66.1 °C with 365 nm laser).[48] The presence of a minor concentration of grain boundaries among differently oriented crystallites observed in the present LuMnO₃ films does not impede reaching a larger responsivity. While at first sight this may seem surprising as in conventional silicon or related III-V semiconductors, the performance of polycrystalline materials is definitely beaten by their crystalline counterparts, other materials display the opposite trend. For instance, samples containing mixed Bi-Mn-O phases or CdTe-based solar cells, display better efficiency than related single crystalline phases [49,50] where grain boundaries boost photovoltaic conversion, in some cases assisted by associated strain-gradients.[51] In this scenario it cannot be excluded that grain boundaries in hexagonal ferroelectrics may similarly enhance photo carrier extraction.

We have shown that electrodes used in vertical Pt/LuMnO₃/M capacitors (M = Pt, Co and Ti) have intricate effects on the photoresponse of polar materials. Beyond an obvious role by partially absorbing the incoming light and producing a first modulation of photocurrent, the presence of electrodes has a subtler impact by modifying the relative stability of the ferroelectric domains via the imprint field. Subsequently, the interfacial Schottky barriers in ferroelectric capacitors, their conductance and ultimately the short-circuit photocurrent are affected by imprint. We have demonstrated that in vertical Pt/LuMnO₃/M_T structures, the imprint field is largely strengthened when the metal electrode (M_T = Pt, Co, Ti) is deposited on top, and its presence or absence, critically determine that the observed *J-V* curves change of quadrant upon polarization reversal or not. More precisely, it has been shown that Co electrodes promote a large imprint that, after poling the ferroelectric layer with $V_w^{+,-}$, stimulates a rapid back-switching of polarization towards the direction favored by imprint. Naturally, in this circumstances the *J-V* curves remain in a given quadrant and display only minute photocurrent changes after $V_w^{+,-}$ pre-poling. On the contrary, when imprint is weaker, as in the case of bare LuMnO₃ surface (that is: without top electrode), the polarization retention is long. In these cases, polarization reversal is facilitated by photon absorption as reported earlier in other ferroelectrics (i.e., BaTiO₃). [37]

The J_{sc} photocurrent is found to increase linearly with light intensity ($I_p \approx 1.4 - 50$ W/cm²), while V_{oc} increases from −0.36 eV and saturates to −0.53 eV as $I_p \approx J_{sc}$ increases,

following a logarithmic dependence of $V_{oc}(J_{sc})$ [$V_{oc} \propto \ln(J_{sc})$], with an ideality factor $n \approx 1.5$, as found in conventional photodiodes. This observation implies that photoresponse in the present capacitors is mainly dictated by photoabsorption and band alignment at interfaces. At first sight this observation appears to deny a significant contribution of BPE to the photoresponse of ferroelectric Pt/LMO/M capacitors. However, we have also observed a dependence of the photoresponse $J_{sc}(\varphi)$ and $V_{oc}(\varphi)$ on the polarization angle of light that is best interpreted arising from BPE, as demonstrated by the larger slope of $V_{oc}[\ln(J_{sc})]$ when deduced from $V_{oc}[J_{sc}(\varphi)]$ than from $V_{oc}[J_{sc}(I_p)]$. This could be the first direct evidence of the contribution of BPE at oblique incidence to the photoresponse of hexagonal manganites. In summary, a large photovoltaic responsivity has been obtained in vertical capacitors using ferroelectric LuMnO₃ absorbers and suitable electrodes, resulting from a synergetic contribution of conventional photovoltaic and bulk photovoltaic effects.
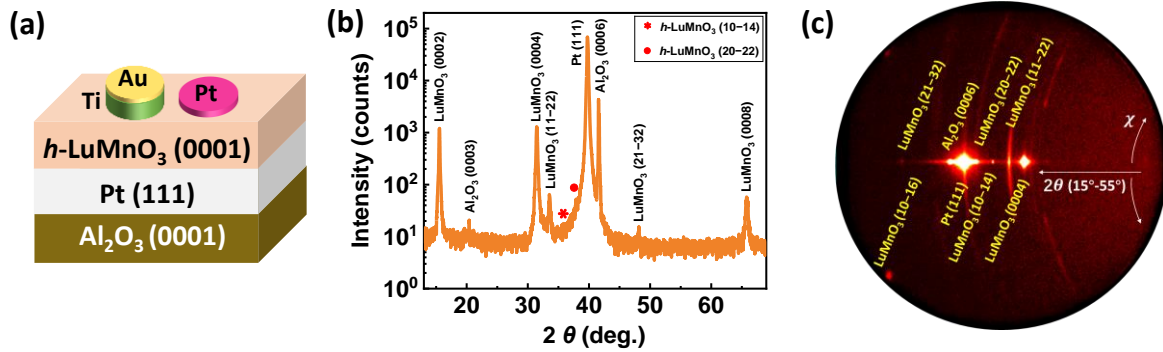
Supplementary information

S5.1. Full angular range θ-2θ and 2θ-χ scans

Fig. S5.1. (a) Sketch of the Al₂O₃//Pt/LMO/Ti (Pt) structures. (b) Full range of XRD θ-2θ scans and (b) 2θ-χ maps of LMO film on Pt//Al₂O₃ substrate.

S5.2. STEM images near the grain boundaries
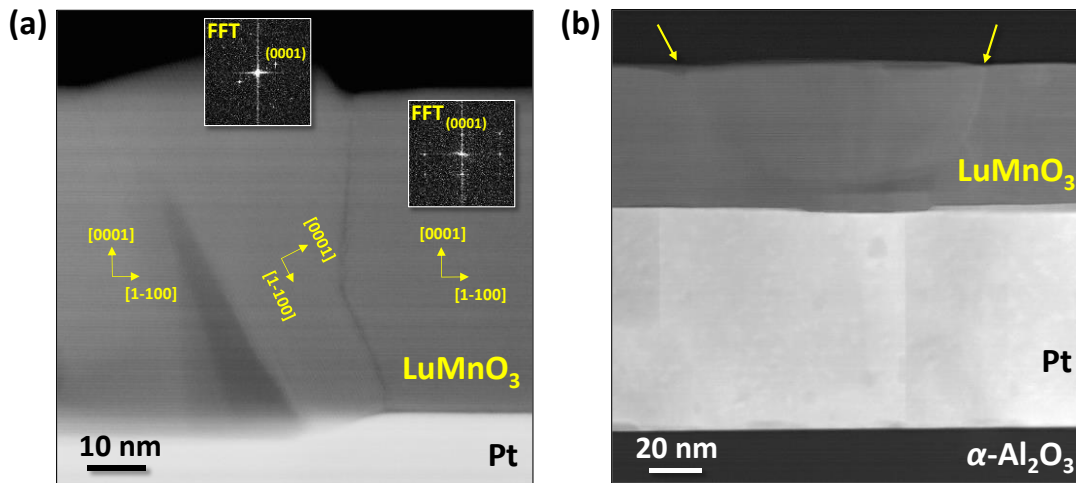
Fig. S5.2. (a) Low HAADF-STEM images of the heterostructure acquired along the [11−20] α-Al₂O₃ zone axis, which shows a misoriented LMO grain. The Fast Fourier Transforms of two grains (inset) show the tilting of the (0001) plane of the central grain with respect to the others. (b) The HAADF image shows three coalesced *c*-textured LMO grains grown on the Pt(111) layer. The yellow arrows mark the respective grain boundaries.

S5.3. *J-V* characteristics of Al₂O₃//Pt/LMO/Pt
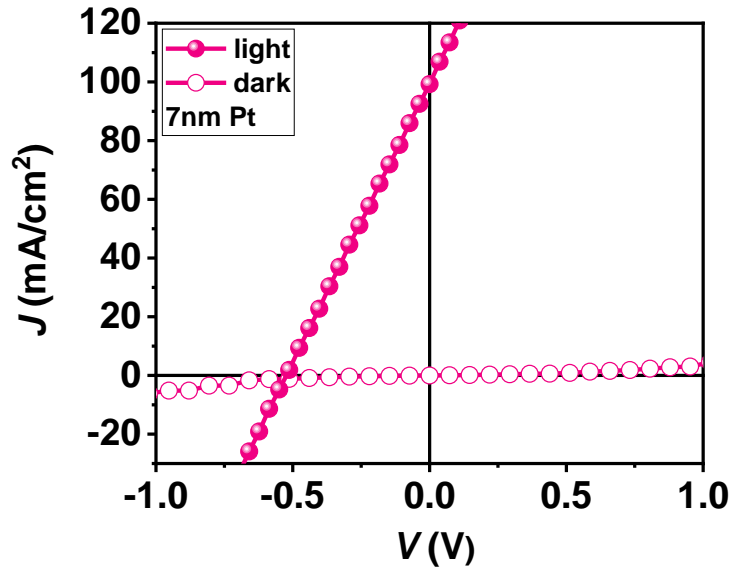
Fig. S5.3. (a) *J-V* characteristics collected in dark and under illumination of capacitor Al₂O₃//Pt/LMO/Pt. Light intensity I_p is around 50 W/cm^2.

S5.4. *J-V* characteristics in dark of Pt/LMO/M capacitors
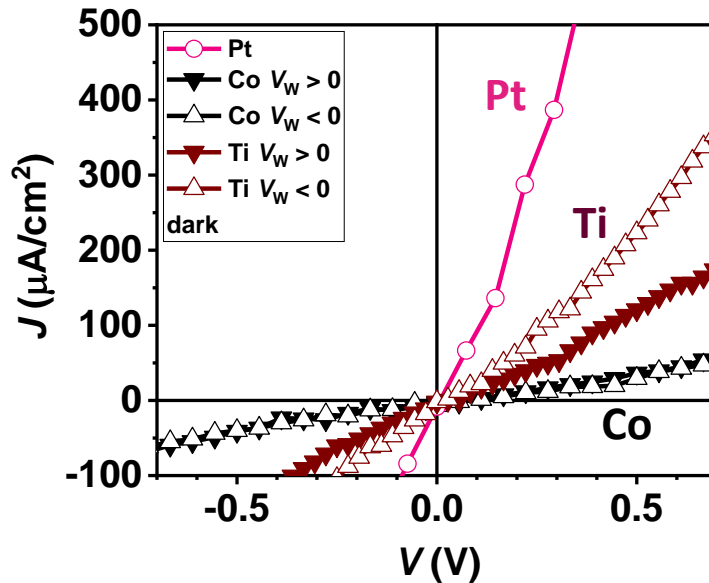
Fig. S5.4. The *J-V* characteristics of the Pt/LMO/M capacitors (M = Pt, Co and Ti) recorded in dark [zoom of dark curves in fig. 5.13(a)].

S5.5. Ferroelectricity and retention of Pt/LMO/Ti
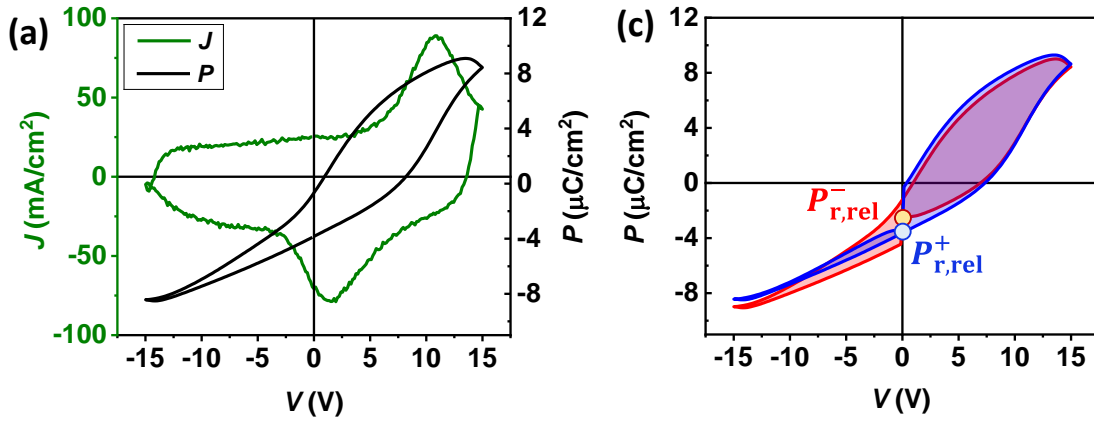
Fig. S5.5. (a) $J(V)$ and integrated $P(V)$ loops; (b) Retention measured by $P(V)$ loops at remanence in $\tau_d = 1$ s; of capacitor Pt/LMO/Ti

S5.6. Pulse train of the writing voltage dependence
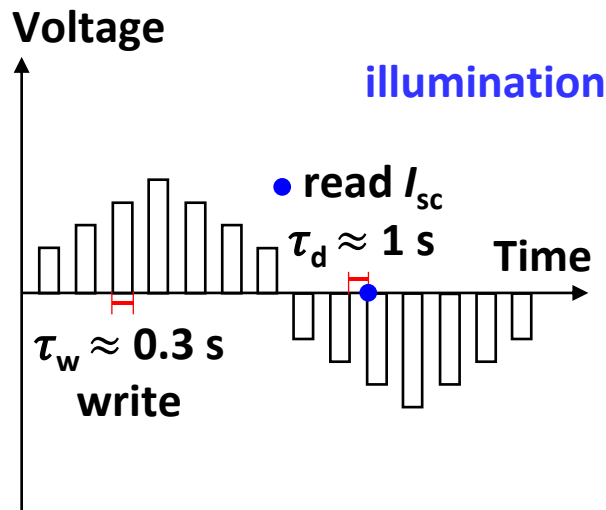
Fig. S5.6. Pulse train of the dependence of the J_{sc} on pre-polarization writing voltage V_w.

S5.7. Ferroelectric polarization dependence of Pt/LMO/Ti
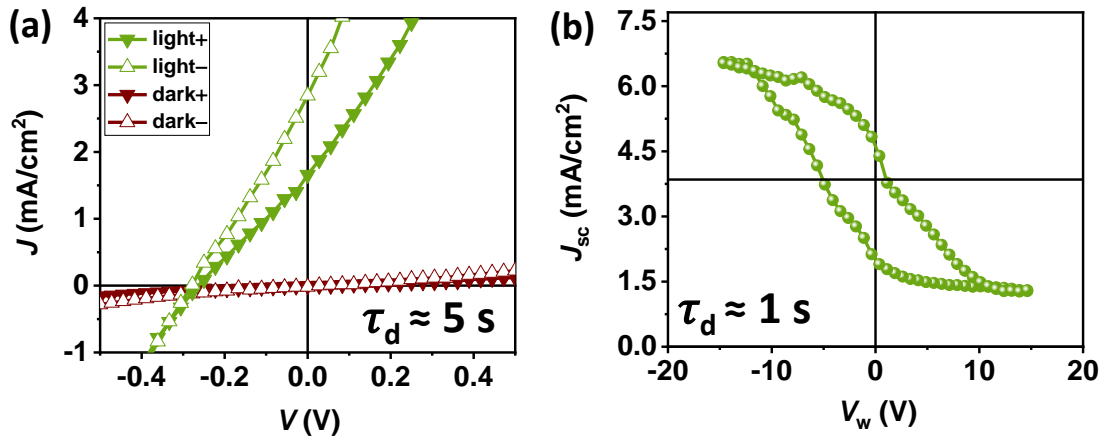
Fig. S5.7. (a) *J-V* curves collected in dark and under illumination after pre-poling the capacitor with positive (+) or negative (−) 12 V. (b) J_{sc} measured after pre-poling the capacitor with indicated writing voltage V_w. Light intensity I_p is around 70 W/cm², of capacitor Pt/LMO/Ti.

S5.8. Zoom of the *J-V* curves of Pt/LMO/Co
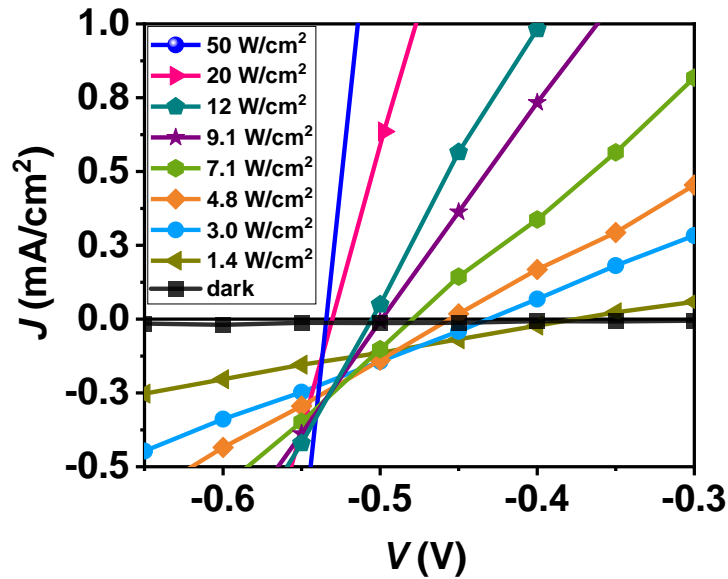
Fig. S5.8. The *J-V* curves of Pt/LMO/Co recorded in dark and under illumination of various light intensity [zoom near V_{oc} in fig. 8(a)].

S5.9. Light polarization dependence $J_{sc}(\varphi)$ of Pt/LMO/Ti
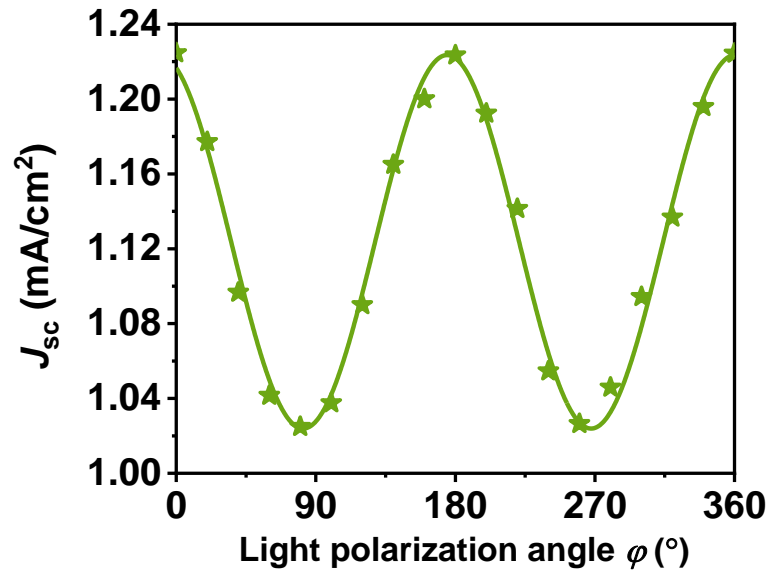
Fig. S5.9. Dependence of short circuit current $J_{sc}(\varphi)$ on light polarization angles (φ) of Pt/LMO/Ti. Solid line is fit using a sine function of experimental data (symbols), light intensity I_p after optical plates is around 50 W/cm².

Annex A: Magnetization properties of LuMnO₃ based samples

Fig. A1(a) shows the magnetic moment of a Al_2O_3/Pt/LuMnO₃(120 nm)/Pt sample recorded in a ZFC (zero-field-cooled) and FC (field-cooled) temperature dependence using a magnetic field of 100 Oe (7958 A/m). Data show distinct behavior between ZFC and FC, and a clear magnetic transition at about 41 K that closely coincides with that reported for Mn_3O_4.[32,33] Inset in Fig. A1(a) displays the magnetic moment in the 60 - 100 K temperature range where the antiferromagnetic transition of bulk LuMnO₃ is expected (Néel temperature $T_N \approx 90$ K) but not visible here.[52,53] Moreover, the ZFC and FC data are not fully overlapped, indicating a contribution from other possible magnetic source. The perceptible negative magnetization observed in the 60 - 300 K temperature range (about -1.5×10^{-6} emu) arises from the diamagnetic susceptibility of the substrate. Not corrected in the raw data displayed in Fig. A1(a) but well evident in Fig. A1(b) where the $m(H)$ loop recorded at 5 K is displayed. The measured high field slope in Fig. A1(b) (-1.67×10^{-8} emu/Oe) is the magnetic susceptibility of the Al_2O_3 substrate, that corresponds to a magnetic moment of -1.67×10^{-6} emu when measured at 100 Oe in agreement with data in Fig. A1(a). In Fig. A1(c) displays the hysteretic region of the $m(H)$ loop in Fig. A1(b) after subtracting the diamagnetic contribution of the substrate. This is a fingerprint of the ferromagnetic and coercive character of Mn_3O_4.

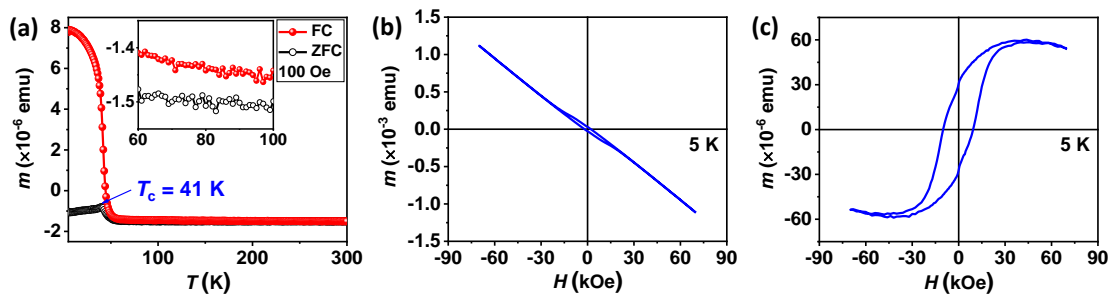Fig. A1. Magnetic properties of a sample Al_2O_3//Pt/LuMnO₃/Pt (LMO of 120 nm). (a) Zero-field cooled (ZFC) and field cooled (FC) temperature-dependent magnetic moment *m-T* recorded under 100 Oe field. (b) Raw magnetic moment versus magnetic field *m(H)* loop recorded at 5 K with the field applied in the plane of the sample. (c) The *m(H)* loop after subtracting the substrate contribution in (b).

Assuming that a saturation magnetization of $Mn_3O_4 \approx 240$ emu/cm^3 as reported,[54,55] the measured magnetic moment of the film [$\approx 60 \times 10^{-6}$ emu in Fig. A1(c)], would correspond to volume of $v(Mn_3O_4) = 0.25 \times 10^{-6}$ cm^3. That is roughly 8 % of the sample volume [v(LMO) ≈ 5 mm x 5 mm x 120 nm $= 3 \times 10^{-6}$ cm^3]. Although this value is exceedingly large, may be due to the presence of a larger amount of uncompensated Mn-spins in the Mn_3O_4 inclusions, the data clearly show that a significant magnetic impurity phase exist in the LuMnO₃ films. Of course, non-magnetic compensation in otherwise antiferromagnetic LuMnO₃ can itself contribute to the measured moment but marginal as the Néel transition is invisible in the *m-T* dependence.

When LuMnO₃ samples having electrodes containing magnetic materials, the measurements of the magnetic moment of the samples lead to distinct behavior. Below we show the data corresponding to a Al_2O_3//Pt/LMO(70 nm)/M_T (M_T = Pt, Co and Ti) sample.
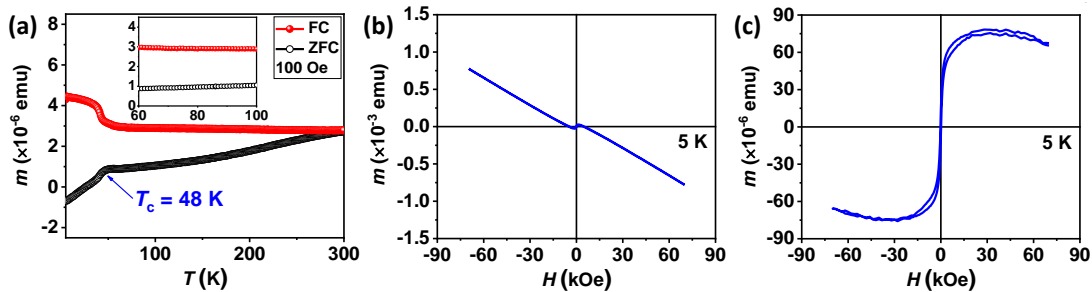
Fig. A2. Magnetic properties of the sample Al_2O_3//Pt/LMO(70 nm)/M (M = Pt, Co and Ti) extensively described in Chapter 5.2, without any magnetic field preparation of the magnet nor the sample (not demagnetization process was employed) before measuring with the SQUID. (a) ZFC-FC temperature-dependent magnetic moment recorded under 100 Oe field, after proper demagnetization process. The magnetization abruptly varies at about 48 K, again this is a fingerprint of the presence of a magnetic contribution developing at this temperature. As argued in Chapter 5.2, this phase is the residual Mn_3O_4 phase identified by STEM. The magnetic contribution of the Co electrode is also evident at $T > 48$ K. Naturally, this magnetic contribution is also perceptible in the (b) $m(H)$ data and more evident in (c) after subtraction of the diamagnetic contribution of the substrate.

In Fig. A2(a), we show the magnetic moment of the sample recorded in a ZFZ and FC measuring process using $H = 100$ Oe field. In this preliminary experiments it can be appreciated that the magnetization of ZFC and FC data, abruptly varies at about 48 K, which

is a fingerprint of the presence of a magnetic contribution developing at this temperature. Moreover, the behavior of the FC and ZFC are clearly different over all temperature range. The FC data show a large positive magnetization exists at 300 K, only slightly increasing upon lowering the temperature until the transition at 48 K is observed, where the magnetization largely increases due to the claimed Mn_3O_4 contribution. The presence of a positive residual, almost temperature independent, magnetic contribution in the 48 - 300 K temperature range, is unique to samples with M (= Pt, Co and Ti) electrodes. It is therefore attributed to the presence of the hard magnetic Co contribution of the electrodes to the magnetic response of the sample. The room magnetic moment is $m > 0$ which indicates that either the field (100 Oe) is enough to saturate Co along the field direction or that accidentally the remnant magnetic moment of Co (which in bulk is a hard material with a coercivity larger than 100 Oe) is along the field direction.

Inspection of the ZFC data allows to distinguish among two possibilities. The ZFC data (recorded at 100 Oe) at the lowest temperature is $m < 0$, indicating that either the diamagnetic contribution of the substrate overrules the contribution from Mn_3O_4 and Co, which is not a surprise as the volume of the substrate is orders of magnitude larger than these "spurious" ferromagnetic contributions; or that the Co is negatively magnetized during the ZFC process, either due to the presence of a residual $H < 0$ in the magnet chamber or the remnant magnetization of Co, that cannot be switched by the applied field ($H = 100$ Oe $< H_c$).

In ZFC, upon heating m-T starts increasing (become less negative) with a slope larger (faster variation) than observed in the FC process due to the Mn_3O_4 contribution. This may indicate that the coercivity of Mn_3O_4 plays a role: Mn_3O_4 gets gradually magnetized when its temperature-dependent coercivity is exceeded by the measuring field (100 Oe). Of course, in the FC process, this is not of relevance as the measuring field always exceed $H_c(Mn_3O_4)$ when Mn_3O_4 gets ordered (at $\approx$ 48 K) and its magnetic moment at every temperature below T_c in the FC process is always fully saturated. When further warming, the magnetization in ZFC of the film gets progressively more positive until approaching the FC data at room temperature. Again, the most plausible scenario is that Co gets gradually magnetized as 100 Oe surpasses its coercive field.

Data in Fig. A2 illustrates the complex interplay among different magnetic signals coexisting in the LuMnO₃ when ferromagnetic electrodes are used. The presence of the magnetic contribution of Co can be also evidence by comparing *m-T* data collected without any magnetic field preparation in the SQUID magnetometer: that is residual trapped magnetic fields and remnant magnetization at Co electrodes may contribute to the measurement. To minimize these contributions, new measurements were performed after a "demag process" in which the magnet and sample are submitted to magnetic field loops of decreasing amplitude and sign from H = 70 kOe down to H = 0. Subsequently, H = 100 Oe was used to perform ZFC-FC measurements as in Fig. A2(a). The results are displayed in Fig. A3. It is obvious that the *m-T* data recorded after a "demag process" shifted to larger positive values compared to measurements without "demag process" [Fig. A2(a)], thus implying that a negative magnetization was pre-existing in the measurement without "demag". Now, the positive $m > 0$ contributions largely override any diamagnetic substrate contribution.
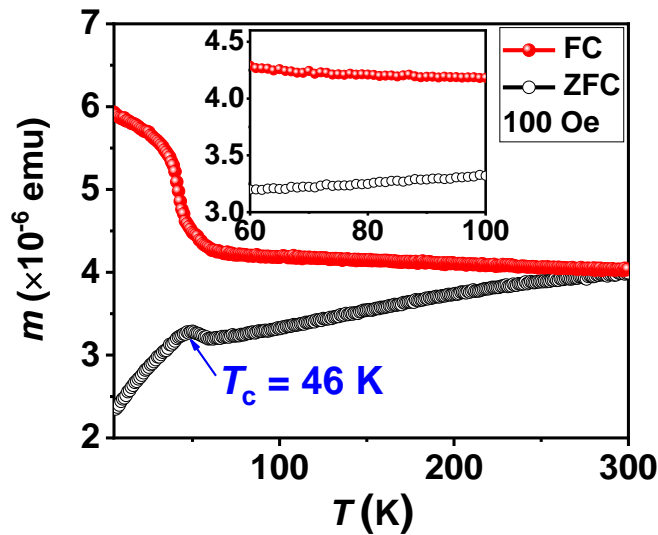
Fig. A3. ZFC-FC temperature-dependent magnetic moment of the sample Al₂O₃//Pt/LMO(70 nm)/M (M = Pt, Co and Ti) recorded under 100 Oe field, after proper demagnetization process. It can be appreciated that now the magnetization abruptly varies at about 46 K, and the magnetic contribution of the Co electrode is also evident at $T > 46$ K.

All in all, these magnetic data illustrate how magnetic measures in LuMnO₃ films allows unveil the presence of spurious phases virtually imperceptible in XRD data, although in

Chapter 5.2 the STEM measurements gave first indications of their presence. As a final example we show in Fig. A4, magnetic data corresponding to different films (with non-magnetic electrodes electrodes) grown under identical nominal conditions, where magnetic data reflect the presence of of Mn_3O_4 in both of them, which is in contrast to XRD data where the Mn_3O_4 peak is almost invisible.
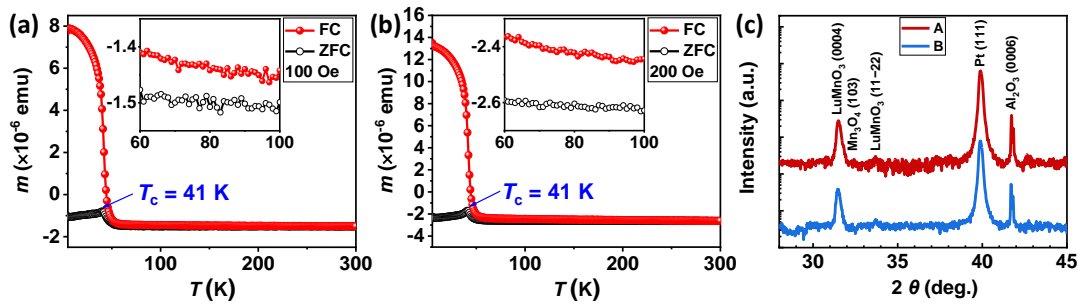

Fig. A4. ZFC-FC temperature-dependent magnetic moment of (a) sample A: Al_2O_3//Pt/LMO(120 nm)/Pt and (b) sample B: Al_2O_3//Pt/LMO(130 nm)/Pt. (c) θ-2θ scans of sample A and sample B.

Bibliography

[1] H. Iida, T. Koizumi, and Y. Uesu, Phase Transitions **84**, 747 (2011).

[2] P. Murugavel, J.-H. Lee, D. Lee, T.W. Noh, Y. Jo, M. Jung, Y.S. Oh, and K.H. Kim, Appl. Phys. Lett. **90**, 142902 (2007).

[3] W. Wang, Growth and Characterization of Hexagonal Lu-Fe- O Multiferroic Thin Films, 2012.

[4] Y.K. Jeong, J. Lee, S. Ahn, and H.M. Jang, Chem. Mater. **24**, 2426 (2012).

[5] J.-H. Lee, P. Murugavel, H. Ryu, D. Lee, J.Y. Jo, J.W. Kim, H.J. Kim, K.H. Kim, Y. Jo, M.-H. Jung, Y.H. Oh, Y.-W. Kim, J.-G. Yoon, J.-S. Chung, and T.W. Noh, Adv. Mater. **18**, 3125 (2006).

[6] H. Han, S. Song, J.H. Lee, K.J. Kim, G.-W. Kim, T. Park, and H.M. Jang, Chem. Mater. **27**, 7425 (2015).

[7] H. Han, D. Kim, K. Chu, J. Park, S.Y. Nam, S. Heo, C.-H. Yang, and H.M. Jang, ACS Appl. Mater. Interfaces **10**, 1846 (2018).

[8] H. Han, D. Kim, S. Chae, J. Park, S.Y. Nam, M. Choi, K. Yong, H.J. Kim, J. Son, and H.M. Jang, Nanoscale **10**, 13261 (2018).

[9] M.-M. Yang, D.J. Kim, and M. Alexe, Science (80-.). **360**, 904 (2018).

[10] X. Han, Y. Ji, and Y. Yang, Adv. Funct. Mater. **32**, 2109625 (2022).

[11] S. Nadupalli, J. Kreisel, and T. Granzow, Sci. Adv. **5**, 1 (2019).

[12] Y. Bai, Front. Mater. **8**, 1 (2021).

[13] J.E. Spanier, V.M. Fridkin, A.M. Rappe, A.R. Akbashev, A. Polemi, Y. Qi, Z. Gu, S.M. Young, C.J. Hawley, D. Imbrenda, G. Xiao, A.L. Bennett-Jackson, and C.L. Johnson, Nat. Photonics **10**, 611 (2016).

[14] R. Nechache, C. Harnagea, S. Li, L. Cardenas, W. Huang, J. Chakrabartty, and F. Rosei, Nat. Photonics **9**, 61 (2015).

[15] L. You, F. Zheng, L. Fang, Y. Zhou, L.Z. Tan, Z. Zhang, G. Ma, D. Schmidt, A. Rusydi, L. Wang, L. Chang, A.M. Rappe, and J. Wang, Sci. Adv. **4**, 1 (2018).

[16] T. Choi, S. Lee, Y.J. Choi, V. Kiryukhin, and S.-W. Cheong, Science (80-.). **324**, 63 (2009).

[17] V.M. Fridkin, Crystallogr. Reports **46**, 654 (2001).

[18] S.Y. Yang, J. Seidel, S.J. Byrnes, P. Shafer, C.H. Yang, M.D. Rossell, P. Yu, Y.H. Chu, J.F. Scott, J.W. Ager, L.W. Martin, and R. Ramesh, Nat. Nanotechnol. **5**, 143 (2010).

[19] A. Bhatnagar, A. Roy Chaudhuri, Y. Heon Kim, D. Hesse, and M. Alexe, Nat. Commun. **4**,

2835 (2013).

[20] Y. Sheng, I. Fina, M. Gospodinov, and J. Fontcuberta, Appl. Phys. Lett. **118**, 232902 (2021).

[21] V.M. Fridkin and B.N. Popov, Sov. Phys. - Uspekhi **21**, 981 (1978).

[22] S. Nakashima, R. Hayashimoto, H. Fujisawa, and M. Shimizu, Jpn. J. Appl. Phys. **57**, 11UF11 (2018).

[23] Y. Sheng, I. Fina, M. Gospodinov, A.M. Schankler, A.M. Rappe, and J. Fontcuberta, Phys. Rev. B **104**, 184116 (2021).

[24] M.-M. Yang, A. Bhatnagar, Z.-D. Luo, and M. Alexe, Sci. Rep. **7**, 43070 (2017).

[25] W.T.H. Koch, R. Munser, W. Ruppel, and P. Würfel, Solid State Commun. **17**, 847 (1975).

[26] W. Ji, K. Yao, and Y.C. Liang, Phys. Rev. B - Condens. Matter Mater. Phys. **84**, 1 (2011).

[27] Y. Sheng, I. Fina, M. Gospodinov, and J. Fontcuberta, Appl. Phys. Lett. **120**, 242901 (2022).

[28] J. Yu, Y. Chen, S. Cheng, and Y. Lai, Phys. E Low-Dimensional Syst. Nanostructures **49**, 92 (2013).

[29] M. Tian, Y. Li, G. Wang, and X. Hao, Sol. Energy Mater. Sol. Cells **224**, 111009 (2021).

[30] J. Chen, Z. Wang, H. He, J. Mao, Y. Zhang, Q. Zhang, M. Li, Y. Lu, and Y. He, Adv. Electron. Mater. **7**, 2100717 (2021).

[31] B.J. Rodriguez, C. Callahan, S. V Kalinin, and R. Proksch, Nanotechnology **18**, 475504 (2007).

[32] B. Boucher, R. Buhl, and M. Perrin, J. Phys. Chem. Solids **32**, 2429 (1971).

[33] W.S. Seo, H.H. Jo, K. Lee, B. Kim, S.J. Oh, and J.T. Park, Angew. Chemie Int. Ed. **43**, 1115 (2004).

[34] M. Alexe and A. Gruverman, editors , *Nanoscale Characterisation of Ferroelectric Materials* (Springer Berlin Heidelberg, Berlin, Heidelberg, 2004).

[35] W.S.M. Werner, K. Glantschnig, and C. Ambrosch-Draxl, J. Phys. Chem. Ref. Data **38**, 1013 (2009).

[36] M.N. Polyanskiy, Refractive index database. https://refractiveindex.info. (accessed on Aug. 29, 2022).

[37] X. Long, H. Tan, F. Sánchez, I. Fina, and J. Fontcuberta, Nat. Commun. **12**, 382 (2021).

[38] P. Chen, C. Paillard, H.J. Zhao, J. Íñiguez, and L. Bellaiche, Nat. Commun. **13**, 2566 (2022).

[39] T. Li, A. Lipatov, H. Lu, H. Lee, J.-W. Lee, E. Torun, L. Wirtz, C.-B. Eom, J. Íñiguez, A. Sinitskii,

and A. Gruverman, Nat. Commun. **9**, 3344 (2018).

[40] M.-M. Yang and M. Alexe, Adv. Mater. **30**, 1704908 (2018).

[41] L. Chen, G. Zheng, G. Yao, P. Zhang, S. Dai, Y. Jiang, H. Li, B. Yu, H. Ni, and S. Wei, ACS Omega **5**, 8766 (2020).

[42] S.R. Cowan, A. Roy, and A.J. Heeger, Phys. Rev. B **82**, 245207 (2010).

[43] Z. Sun, G. Sitbon, T. Pons, A.A. Bakulin, and Z. Chen, Sci. Rep. **5**, 10626 (2015).

[44] L. Madi, I. Bouchama, and N. Bouarissa, J. Sci. Adv. Mater. Devices **4**, 509 (2019).

[45] T. Singh and T. Miyasaka, Adv. Energy Mater. **8**, 1700677 (2018).

[46] N.K. Elumalai and A. Uddin, Energy Environ. Sci. **9**, 391 (2016).

[47] P. Lopez-Varo, L. Bertoluzzi, J. Bisquert, M. Alexe, M. Coll, J. Huang, J.A. Jimenez-Tejada, T. Kirchartz, R. Nechache, F. Rosei, and Y. Yuan, Phys. Rep. **653**, 1 (2016).

[48] R. Zhao, N. Ma, K. Song, and Y. Yang, Adv. Funct. Mater. **30**, 1906232 (2020).

[49] I. Visoly-Fisher, S.R. Cohen, A. Ruzin, and D. Cahen, Adv. Mater. **16**, 879 (2004).

[50] J. Chakrabartty, C. Harnagea, M. Celikin, F. Rosei, and R. Nechache, Nat. Photonics **12**, 271 (2018).

[51] K. Chu, B.-K. Jang, J.H. Sung, Y.A. Shin, E.-S. Lee, K. Song, J.H. Lee, C.-S. Woo, S.J. Kim, S.-Y. Choi, T.Y. Koo, Y.-H. Kim, S.-H. Oh, M.-H. Jo, and C.-H. Yang, Nat. Nanotechnol. **10**, 972 (2015).

[52] J. Fontcuberta, Comptes Rendus Phys. **16**, 204 (2015).

[53] D.G. Tomuta, S. Ramakrishnan, G.J. Niewenhuys, and J.A. Mydosh, J. Phys. Condens. Matter **13**, 4543 (2001).

[54] K. Dwight and N. Menyuk, Phys. Rev. **119**, 1470 (1960).

[55] D. Mukherjee, N. Bingham, M.-H. Phan, H. Srikanth, P. Mukherjee, and S. Witanachchi, J. Appl. Phys. **111**, 07D730 (2012).

Chapter 6. Distinguishing BPE and Fresnel contributions in the photovoltaic response

In previous Chapters, the Fresnel contribution to polarization-dependent photoresponse has been repeatedly mentioned. In this Chapter, the detail of Fresnel contributions will be presented and, particularly following up Chapter 5.2.7, we will report on attempts to untwine BPE and Fresnel contributions by comparing how the $V_{oc}(J_{sc})$ dependence evolves when changing the light intensity and light polarization.

The light polarization dependent $J_{sc}(\varphi)$ oscillations are fingerprints of BPE. However, when light propagates along the polar c-axis, $J_{sc}(\varphi)$ oscillations may be absent and thus other incidence angles, i.e. oblique incidence, are required to properly identify BPE. However, at oblique incidence, Fresnel reflectance/transmittance at interfaces is also dependent on the light polarization, which implies that the intensity of the transmitted and absorbed light will also be dependent on the polarization of the arriving light. Subsequently, any photocurrent can also be modulated by Fresnel reflectance/transmittance as much as BPE. Both contributions shall appear intertwined when measuring $J_{sc}(\varphi)$ and $V_{oc}(\varphi)$. We illustrate the complex interplay of BPE and Fresnel at oblique incidences by analyzing the $J_{sc}(I_p, \varphi)$ dependent $V_{oc}(I_p, \varphi)$ and more precisely $V_{oc}(J_{sc})$, in a series of ferroelectric LuMnO$_3$ (LMO) single crystals and films, YMnO$_3$ (YMO) films and compared to data that obtained when using non-ferroelectric LaFeO$_3$ (LFO) films. It will be shown that whereas in all cases $J_{sc}(\varphi)$ and $V_{oc}(\varphi)$ display similar dependences either originated from BPE or Fresnel, the observed $V_{oc}(J_{sc})$ differs in polar and nonpolar materials, which offers the possibility of disentangling BPE from Fresnel contributions.

6.1. Introduction

Photocurrent density (J_{sc}) in polar materials, other than conventional drift and diffusion terms (CPE), may contain a BPE contribution genuinely arising from the non-centrosymmetric character of ferroelectrics. Eq. [6.1] illustrates the BPE, drift and diffusion contributions to J_{sc}.

$$J_{sc} = J_{BPE} + J_E + J_D = I_0\alpha[G_{ij}e_ie_j + f(J_E, J_D)] \qquad [6.1]$$

In general, J_{BPE} manifests via a dependence of J_{sc} on the polarization angle φ of the impinging light, which give rise to Glass tensor related $J_{sc}(\varphi)$ oscillations. In general, for a given incidence angle θ and for a given light of incoming intensity I_0, $J_{sc}(\varphi)$ oscillations can be induced by BPE, but any polarization-dependent transmission/reflection (Fresnel) and/or polarization-dependent adsorption (dichroism), represented by $I_0(\varphi)$ and $\alpha(\varphi)$, respectively, may also introduce additional contributions to any observed $J_{sc}(\varphi)$.

Typically, f.i. in $BiFeO_3$ (001) thin films, $J_{sc}(\varphi)$ dependence is monitored at normal incidence to avoid the Fresnel contribution (*p/s*-polarized light reflection/transmission) and any dichroism contribution (light polarization dependent light absorption).[1,2] Indeed, in $BiFeO_3$ the rhombohedral symmetry imposes that, the polar axis (111) is not long the normal to film surface (001). Therefore, at normal incidence, an out-of-plane BPE photocurrent can be observed and the Fresnel and dichroism contributions must be either suppressed or much reduced. In sharp contrast, in hexagonal manganites, with the ferroelectric polar axes along the hexagonal *c*-axis,[3–5] at normal incidence, any out-of-plane photocurrent cannot be sensitive to light polarization and thus any J_{BPE} cannot display a oscillating φ-dependence. By the same token (symmetry nature), BPE cannot lead to any in-plane photocurrent (Supplementary information S4.7).[6] It follows that any attempt to evaluate BPE in hexagonal manganites ($LuMnO_3$, $YMnO_3$, etc) requires performing $J_{sc}(\varphi)$ measurements at oblique incidence or in-plane 90° incidence to visualize and evaluate the oscillating BPE signature. Under oblique incidence conditions, neither the Fresnel nor the dichroism can be in principle avoided.

The dichroism contribution was found to be insignificant in our LMO sample as the same cosine waveform of $J_{sc}(\varphi)$ was obtained and having the same phase, either using red and blue lase. If dichroism would have been significant ($\alpha_{\parallel} \neq \alpha_{\perp}$, Chapter 4.2.4) then one should have overserved a different sign of oscillations for these two wavelengths. Therefore, it was concluded that dichroisms were not relevant. However, at oblique incidence, the Fresnel contribution that mimics a genuine BPE contribution cannot be excluded.[1,7] The in-plane incidence[6] (Chapter 4.2.6) could be a good solution for the Fresnel contribution as in this case the reflectance of *p*- and *s*-polarized light is the same (normal to the lateral surface, Fig. 6.1), but when using thin films, perfect sample alignment with the light in the sample plane for lateral illumination is extremely difficult.

Consequently, it follows that the measured $J_{sc}(\varphi)$ at oblique incidence can be a superposition of BPE and Fresnel, that may challenge their disentangling and proper quantification. This seems to be facile at first sight as these two scenarios own distinct mechanisms that are not expected to show identical behaviors in their magnitudes, namely, the A_z and B_z coefficients in Eq. [4.3] (repeated here as Eq. [6.2]) are expected to be different as they come from different (BPE and Fresnel) origins.

$$J_{sc}(\theta, \varphi) = A_z(\theta) \cos2(\varphi - \varphi_0) + B_z(\theta) \qquad [6.2]$$

Correspondingly, we first attempted to: a) fitting the experimental $J_{sc}(\varphi)$ results by combining the BPE and Fresnel contributions, at each incidence angle θ (S6.1), and b) focusing on the background B_z values at every incidence angle θ and comparing the experimental B_z values to the expectations (constant for Fresnel but not for BPE) (S6.2). As lengthy discussed in Supplementary information S6.1 and S6.2, these analyses failed to provide a clear separation of both contributions. It follows that deconvolution of the BPE and Fresnel contributions cannot be done based on data-fitting analysis due to the close similarity of both contributions, neither by comparing B_z values due to the incomparable values obtained at different optical setups used when exploring the θ dependences.

Instead, as argued in Chapter 5.2.7, we considered the BPE controlled $J_{sc}(I_p, \varphi)$, according to Eq. [5.2] (repeated here for convenience as Eq. [6.3]),[8,9] should lead to a linear variation of $V_{oc}(J_{sc})$, while a Fresnel controlled $J_{sc}(I_p, \varphi)$ should give a logarithmic $V_{oc}(J_{sc})$ (Eq. [5.1]) (reaped here for convenience as Eq. [6.4])[10] dependence.

$$V_{oc} = \frac{J_{sc}l}{\sigma_d + \sigma_{pv}} \qquad [6.3]$$

$$V_{oc} = n\frac{kT}{q}\ln(1 + \frac{J_{sc}}{J_0}) \qquad [6.4]$$

Therefore, in principle the analysis of the $V_{oc}(J_{sc})$ dependencies given by Eq. [6.3] and [6.4], may be a tool to discriminate between the different physical origins of $J_{sc}(\varphi)$.

Accordingly, we have explored $V_{oc}(J_{sc})$ when varying the light intensity (I_p), light polarization angle (φ) or incidence angle (θ). Four different devices comprising polar and non-polar materials have been studied. It will be shown that the dependence of J_{sc} and V_{oc}

indeed differs in polar (LMO and YMO) and nonpolar (LFO) materials. However, as mentioned in Chapter 1.3, when the heterostructure of LSMO/LFO/Pt (in bulk, LFO is non-polar) displays a $J_{sc}(\varphi)$ and $V_{oc}(J_{sc})$ dependence, that would be compatible with the presence of a BPE contribution which may be related to interfacial effects, additional experiments with non-polar structures and materials would be required to further establish more solid conclusions. To this regard, currently the $V_{oc}(J_{sc})$ dependencies in Nb doped $SrTiO_3$ (Pt/Nb:STO/Pt) and Silicon (Pt/Si/Pt) samples are being studied. Results are beyond the scope of this Chapter.

6.2. Samples and experiments

Four samples were studied to make comparison among polar ($LuMnO_3$, $YMnO_3$) and nonpolar ($LaFeO_3$) materials: a) Cry-5 in Chapter 4.2, Pt(7 nm)/$LuMnO_3$ SC/Pt(7 nm), denoted as LMO SC; b) sample in Chapter 5.2, Al_2O_3//Pt(94 nm)/$LuMnO_3$ film(70 nm)/Co(20 nm Co + 10 nm Pt), denoted as LMO; c) Al_2O_3//Pt(90 nm)/$YMnO_3$ film(93 nm)/Pt(7 nm), denoted as YMO; and d) STO(110)//LSMO(27 nm)/$LaFeO_3$ film(100 nm)/Pt (7 nm), denoted as LFO.

To evidence the Fresnel contribution to subsequent measurements, we first set the light beam on the top contacts, the incident and reflected power were measured by mounting the power meter either perpendicular to the incident or reflected light path [Fig. 6.1(a)], while rotating φ and changing (θ). As varying the incidence angle requires significant changes in the optical setup, that may induce spurious artifacts (see Chapter 3.5.2), this θ dependence is introduced here for completeness but has not been studied systematically. The transmitted power indicated below was obtained by the incident power minus reflected power ($I_T = I_I - I_R$). Next, the samples were measured using the methodology described in Chapter 3.4.2. Under illumination of 405 nm laser ($S_d \approx 280\,\mu m$), the I_p dependence is measured at $\varphi = 0°$ ($\theta = 45°$), the φ dependence J_{sc} is measured at the maximum power ($I_p \approx 50\ W/cm^2$, $\theta = 45°$), and the θ dependence is measured using another 405 nm laser of larger beam ($S_d \approx 1.7\ mm$) at $\varphi = 0°$ ($I_p \approx 0.6\ W/cm^2$).

6.3. Fresnel contribution

The Fresnel equations/coefficients describe the reflection and transmission of light when incident on an interface between different optical media, and predict the differing behavior of waves of the *p* and *s* polarizations incident upon a material interface. As shown in Fig. 6.1(a), when light (intensity I_I) comes to an interface, the reflection (I_R) of *p*- and *s*-polarized (parallel and perpendicular to the incident plane, respectively) differs depending on the incidence angle and the contrast of refractive indexes at the interface. Therefore, the intensity of the transmitted light ($I_T = I_I - I_R$) depends on light polarization.
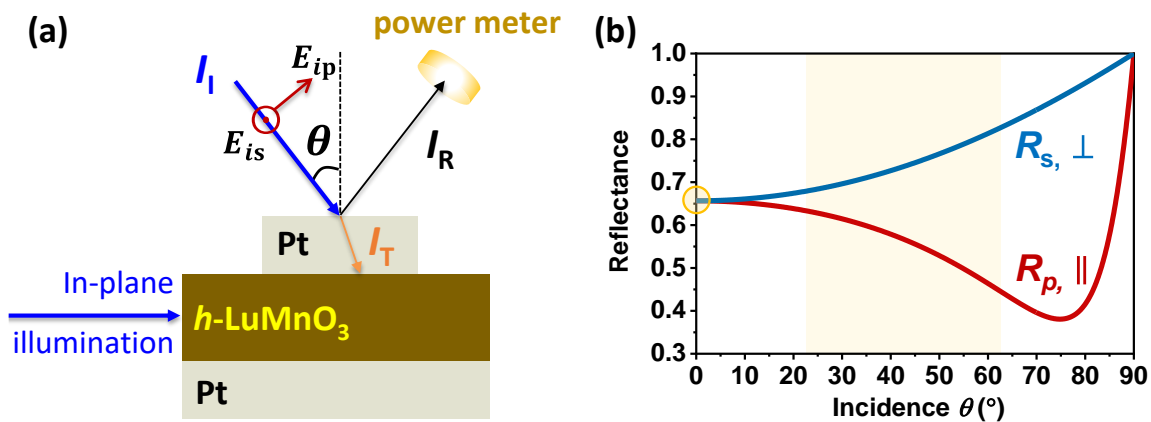

Fig. 6.1. (a) Sketch of an Pt/LMO/Pt sample under illumination, the power meter (yellow cylinder) is mounted perpendicular to the reflected light path to collect the reflected power. (b) The dependence of Reflectance of *p*, *s* polarized light (R_p, R_s) on incidence angle θ, with 405 nm light passing from Air to Pt, adapted from Refs [11,12]. At normal incidence, $R_p = R_s$ (yellow circle).

In Fig. 6.1(b) we show the Fresnel reflectance for *s*- and *p*-polarized light, on an interface air/Pt, as a function of incidence angle.[11,12] Within the angular range of incidence of relevance here, θ (22.5 - 65°, gray shadow), $R_p < R_s$, namely, $T_p (= 1 - R_p) > T_s (= 1 - R_s)$ and the difference $\Delta T (= T_p - T_s = R_s - R_p)$ increases with θ. That is, the light intensity (I_T) reaching to the absorbing layer depends on light polarization [identified by Fig. 6.2(a,b)], being maximum at $\varphi = 0°$ (T_p) and minimum at $\varphi = 90°$ (T_s). Besides, the light polarization state at $\varphi = 0°$ and 180° are identical (vibrating in the same plane), thus the transmitted light intensity should display a $I_T(\varphi) \propto \cos 2\varphi$, as experimentally observed [Fig. 6.2(a,b)]. Furthermore, it is obvious in Fig. 6.1(b) that in the angular range of interest, the amplitude of the $\cos 2\varphi$ dependence of the reflected/transmite light increases when increasing the

incidence angle. More precisely, (see Supplementary information S6.1, Fig. S6.1.1, the amplitude of $I_T(\varphi)$ is roughly proportional to $\sin^2(\theta)$ $[A_F = \frac{\Delta I_T}{2} \propto \sin^2(\theta)]$. Therefore, the Fresnel ruled $J_{sc}(\varphi, \theta)$, controlled by $I_T(\varphi, \theta)$ (Eq. [S6.1]), shows exactly the same angular (φ, θ) dependences than $J_{BPE}(\varphi, \theta)$ (Chapter 4.2, Eq. [4.7]). This is the origin of the difficulty to distinguish these two effects by observing the φ, θ dependence of the photocurrent.

6.4. Results

6.4.1. Light polarization dependent power and photocurrent
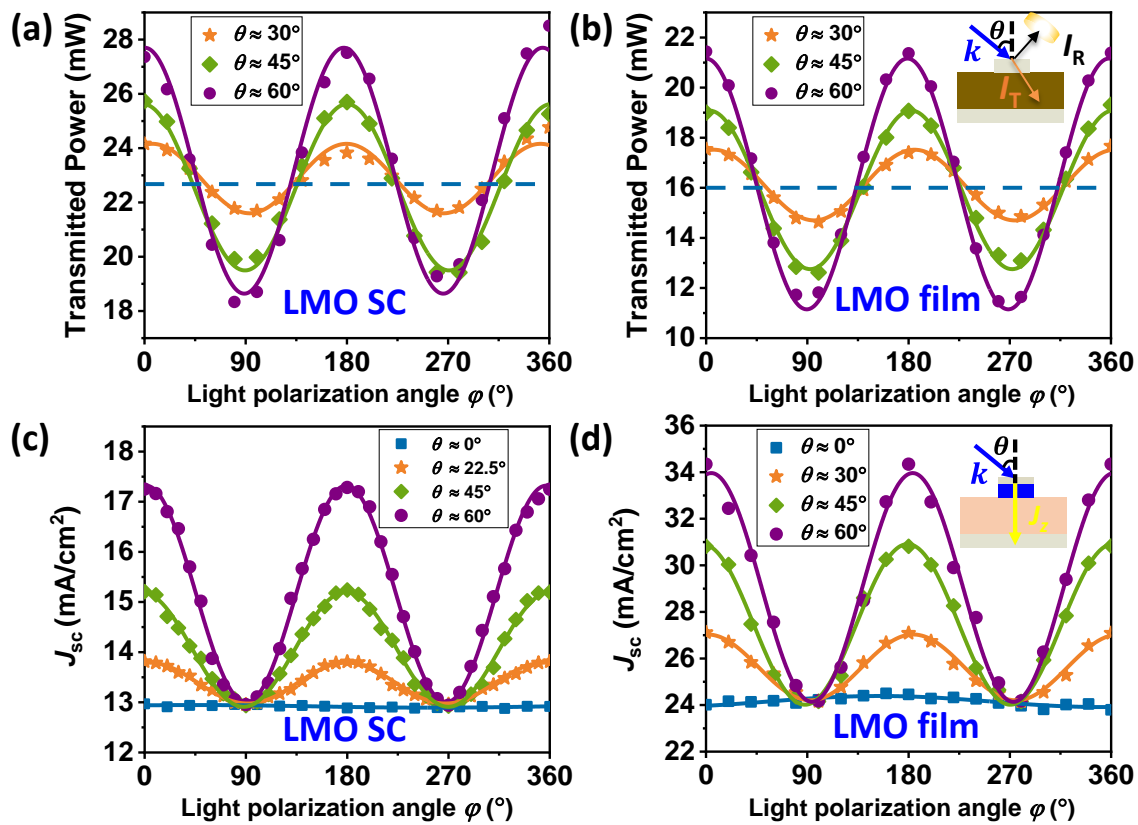
Fig. 6.2. Dependence of (a,b) transmitted power and (c,d) normalized photocurrent density $J_{sc}(\theta, \varphi)$ on the light polarization angles (φ) at various incident angles (θ), of (a,c) LMO SC and (b,d) LMO film. Light intensity I_p after optical plates is around (c) 45 W/cm^2 and (d) 50 W/cm^2. The blue dashes in (a,b) denote the power measured at θ = 0° and φ = 0°. The sketches illustrate the experimental arrangements (b) to detect the reflected power (then obtain transmitted power) and (d) to record the photocurrent J_z. Solid lines are sine fits of experimental data (symbols).

Figs. 6.2(a,b) show the dependence of the transmitted power ($I_T = I_I - I_R$) on the light polarization angles (φ) at various incident angles (θ), of LMO single crystal (SC) and film. It clearly indicates that, even with different top contacts and materials (Supplementary information S6.3), the transmitted power dependence [equivalent to transmitted light intensity $I_T(\theta, \varphi)$] show the Fresnel-predicted $\cos(2\varphi)$ and θ dependence. Notice that data recorded at diferent incidence angles closely matches at $\varphi = 45°$, as expected from the Fresnel contribution [Fig. 1(b), ($R_s + R_p$)/2 almost constant up to $\theta = 60°$].

In Figs. 6.2(c,d) we show $J_{sc}(\theta, \varphi)$. Data clearly show a $\cos(2\varphi)$. As discussed elsewhere (Supplementary information S4.4) the background photocurrent signal varies in an irregular manner due to the experimental artifacts when varying the incidence angle. For this reason, data in Fig. 6.2(c,d) have been shifted to merge at $\varphi = 90°$, because in the BPE scenario, $J_{sc}(\varphi=90°)$ should be independent on θ. Therefore, the prevalence of BPE is imposed here and the background signal in Figs. 6.2(c,d) cannot be used to infer any information regarding the BPE or Fresnel contributions. The background signal (B_z) plays an important role and can be a reference to discriminate BPE and Fresnel by comparing B_z at different θ to see whether they remain constant or not. While attempts are reported in Supplementary information S6.2, the mentioned difficulty of keeping the illumination geometry constant when changing θ, does not allow to obtain accurate and comparable photocurrent values when changing θ. This makes it difficult to evaluate properly the background current as the arbitrariness of the vertical shifting of $J_{sc}(\theta, \varphi)$ remains, hence the observation of the $\cos(2\varphi)$ alone cannot be used to claim an undisputable assignment to BPE or Fresnel.

6.4.2. Power and light polarization dependent photovoltaic response

Fig. 6.3 shows the J_{sc} and V_{oc} dependence on power density I_p and light polarization angle φ of YMO and LFO, measured using the same procedure as in Chapter 5.2.7. Data show the same trend as for LMO (Chapter 4.2.3 and 5.2.7). Indeed, the J-V curves [Figs. 6.3(a,d)] recorded with various intensities show an obvious increase of J_{sc} with light intensity, as summarized in Figa. 6.3(b,e) (left axis). On the other hand, at first sight it seems in Figs 6.3(a,d) that V_{oc} is independent on I_p, however, it can be appreciated in insets of Figs. 6.3(a,d) that there is a gradual minor increase of V_{oc} when increasing power. The extracted intensity dependence of J_{sc} and V_{oc} are depicted in Figs. 6.3(b,e), where it can be

appreciated that J_{sc} increases almost linearly with I_p (left axes) while V_{oc} roughly follows a logarithmic dependence in accordance with the typical V_{oc} [$\propto \ln(I_p)$] of conventional photovoltaic devices.[13–15]
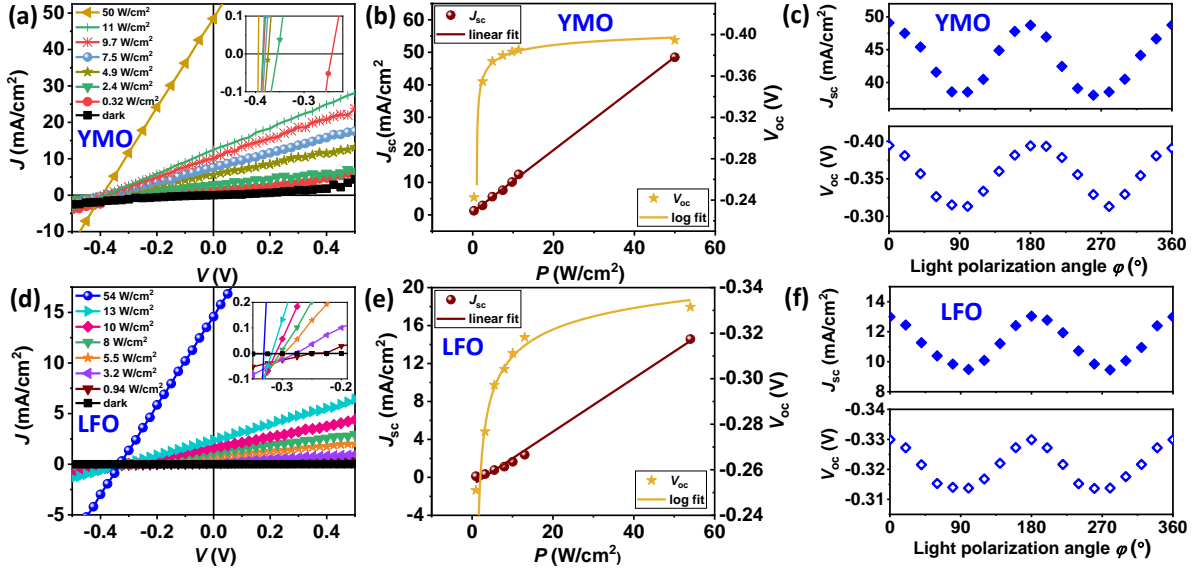

Fig. 6.3. (a, d) The *J-V* curves of (a) YMO and (d) LFO collected in dark and under illumination of various light intensities. Insets show zoom near V_{oc}. (b, e) Average values of J_{sc} and V_{oc} extracted from the *J-V* curves of three capacitors as a function of light intensity, of (b) YMO and (e) LFO. Brown and yellow solid lines are linear ($J_{sc} \propto I_p$) and logarithm [$V_{oc} \propto \ln(I_p)$] fits of the experimental data (symbols), respectively. (c, f) Dependence of the $J_{sc}(\varphi)$ and $V_{oc}(\varphi)$ of (c) YMO and (f) LMO on the light polarization angles (φ). The I_p after optical plates is around 50 W/cm² for YMO and 54 W/cm² of LFO, $\theta = 45°$.

Figs. 6.3(c) shows the light-polarization dependence of $J_{sc}(\varphi)$ and $V_{oc}(\varphi)$ observed in YMO-based samples, which as mentioned, could be taken as fingerprints of BPE as hexagonal YMO is ferroelectric.[6] In Fig. 6.3(f) we display the equivalent data collected on the LFO based heterostructures. The observation of a similar oscillations than in YMO [Fig. 6.3(c)] is striking as YMO is ferroelectric but LFO in bulk is not. Bulk LFO is supposed to be centrosymmetric and conventional photovoltaic response does not predict a dependence of J_{sc} on light polarization φ (unless the I_0 or α change with φ). Nevertheless, it is worth noticing that the amplitude of $V_{oc}(\varphi)$ in LFO is smaller than in YMO and LMO (Fig. 5.19), which could be a sign of slower variation of V_{oc} upon varying J_{sc}, and this may be a hint on their different origin from BPE.
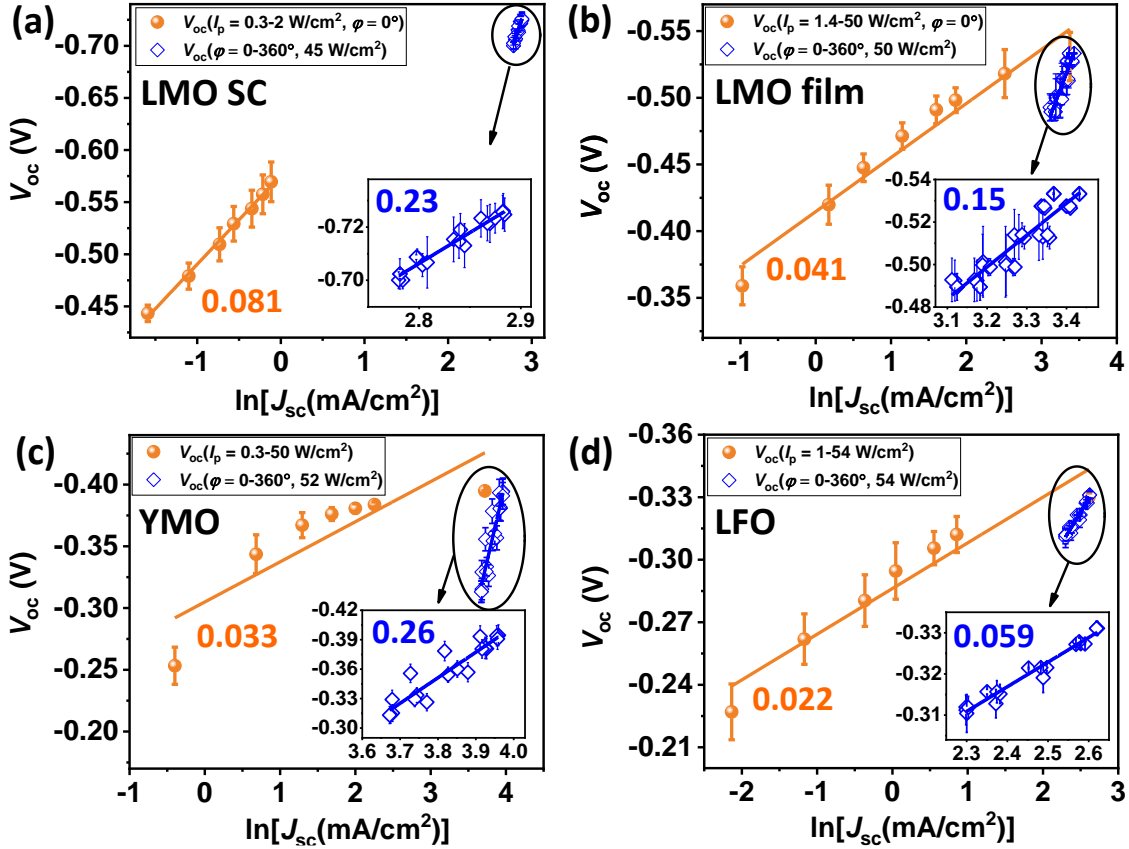
Fig. 6.4. Average values of V_{oc} among three capacitors as a function of $\ln(J_{sc})$ at various power [orange spheres] and light polarization angle φ [blue rhombi] of samples (a) LMO SC, (b) LMO film, (c) YMO and (d) LFO, $\theta = 45°$. The insets show the zoom of $V_{oc}(\varphi)$ vs. $\ln[J_{sc}(\varphi)]$. Solid lines are linear fits of experimental data (symbols), numbers are slopes of the linear fits, error bars indicate the spread (SD) of values.

Fig. 6.4 displays the dependence of $V_{oc}(I_p)$ vs. $\ln[J_{sc}(I_p)]$ (orange spheres) derived from $J_{sc}(I_p)$ and $V_{oc}(I_p)$, that is, when varying the laser intensity for a given polarization angle ($\varphi = 0°$), for all samples (polar and non-polar). It is clear that for all samples, except YMO, the experimental data display a linear dependence of V_{oc} on $\ln(J_{sc})$, which is in agreement with Eq. [6.4]. In Figure 6.4 we also include the $V_{oc}(\varphi)$ vs. $\ln[J_{sc}(\varphi)]$ data (blue rhombi) collected when varying the polarization angle at a fixed laser intensity ($I_p \approx 50$ W/cm^2). Data also show a linear relation of $V_{oc}(\varphi)$ vs. $\ln[J_{sc}(\varphi)]$, but interestingly enough, the slope of the linear fit of $V_{oc}[\ln(J_{sc})]$ is definitively larger when $V_{oc}(J_{sc})$ data are obtained from light-polarization dependent data $V_{oc}(\varphi)$ vs. $\ln[J_{sc}(\varphi)]$ (blue rhombi) than from light intensity variation $V_{oc}(I_p)$

vs. $\ln[J_{sc}(I_p)]$ (orange spheres). These slopes, indicated by the numbers in the plots and partly summarized in Table 6.1, are sample dependent.

The discrepancy of slopes of $V_{oc}(I_p, \varphi)$ vs. $\ln[J_{sc}(I_p, \varphi)]$ depending on if they are extracted from light intensity or light polarization is intriguing. Actually, within the CPE, any dependence of V_{oc} on J_{sc} comes from the light intensity absorbed into the sample. Accordingly, one should not expect any φ dependence. Only in case a Fresnel contribution occurs, the actual intensity reaching the sample varies with φ. But in this case, the observed slopes of $V_{oc}(I_p, \varphi)$ vs. $\ln[J_{sc}(I_p, \varphi)]$ should be the same irrespectively if measurements are done varying φ or I_p. Fig. 6.4 shows that the $V_{oc}(\varphi)$ vs. $\ln[J_{sc}(\varphi)]$ data have a slope larger than $V_{oc}(I_p)$ vs. $\ln[J_{sc}(I_p)]$, suggesting that the polarization sensitive photocurrent does not only come from conventional photoresponse, even if Fresnel is considered.

An additional insight into the $V_{oc}(\varphi)$ vs. $\ln[J_{sc}(\varphi)]$ dependence can be obtained from Fig. 6.5 where we plot the $V_{oc}(\varphi)$ vs. $J_{sc}(\varphi)$ in a linear scale. Obviously, a linear fit describes the observed variation which is as expected from BPE scenario (Eq. [6.3]). The small range of variation of $J_{sc}(\varphi)$ when varying polarization φ explains why $V_{oc}(\varphi)$ data can be described both as linear (Fig. 6.5) or logarithmic in $J_{sc}(\varphi)$ (blue rhombi in Fig. 6.4). Within BPE scenario (Eq. [6.3]), $V_{oc}(\varphi)$ is proportional to $J_{sc}(\varphi)$ with a slope ($Q_1 = \frac{l}{\sigma_d + \sigma_{pv}}$) depending on the effective length between electrodes l and the dark and photovoltaic conductivities ($\sigma_d + \sigma_{pv}$). As seen in Fig. 6.5, LMO SC shows the largest slope (≈ 0.014) of $V_{oc}(\varphi)$ vs. $J_{sc}(\varphi)$, probably owing to the thicker crystal (≈ 100 µm) than films (≈ 90 nm). LMO and YMO films show very similar slope (≈ 0.0057). LFO film shows the smallest slope (≈ 0.0051).

The logarithmic relation and linear relation of V_{oc} vs. J_{sc} found in power density variation (orange spheres in Fig. 6.4) and light polarization variation (Fig. 6.5) suggest the CPE dominates in a wide range when varying I_p, while the BPE dominates in a smaller region when varying φ, in the studied polar and probably also nonpolar LFO samples.
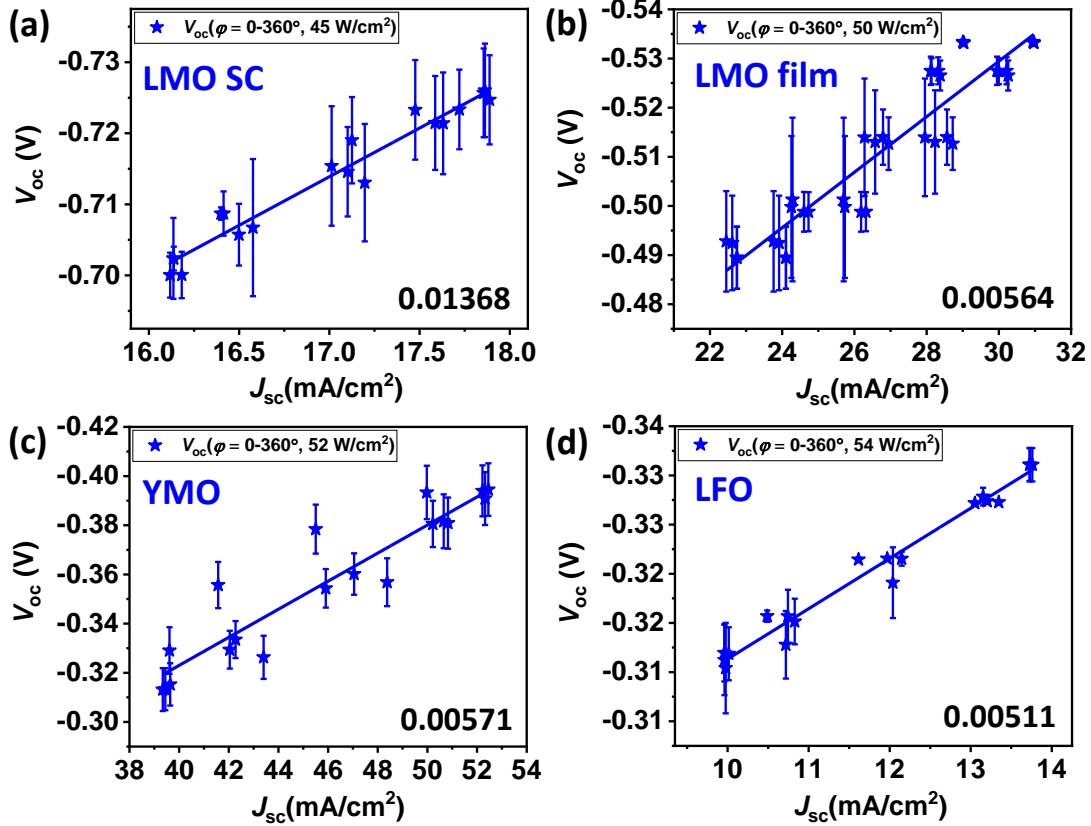
Fig. 6.5. Average values of $V_{oc}(\varphi)$ among three capacitors as a function of $J_{sc}(\varphi)$ of samples (a) LMO SC, (b) LMO film, (c) YMO and (d) LFO, $\theta = 45°$. Solid lines are linear fits of experimental data (symbols), numbers on the bottom right are slopes of the linear fits, error bars indicate the spread (SD) of values.

We turn now back to Fig. 6.4 and discuss in more detail of the implications of the measured slopes, included in Table 6.1. For CPE the slope (Q_2) obtained from the linear fits of $V_{oc}(I_p)$ vs. $\ln[J_{sc}(I_p)]$ is given by $Q_2 = n \left(\frac{kT}{q}\right)$ (Eq. [6.4]), where n is the ideality factor of the photovoltaic junction. Interestingly, for non-polar LFO using the measured slope Q_2 one gets $n \approx 0.85$ which is significantly close to the ideal $n = 1$ value, in good agreement within the conventional photovoltaic framework. In contrast, for the polar samples n is larger and even exceeds the typical variation range ($1 \leq n \leq 2$). Again, this observation suggests that in polar samples other ingredients other than the conventional photoresponse indeed contribute to V_{oc} vs. $\ln[J_{sc}]$.

Samples	Slope Q_2 of $V_{oc}(I_p)$ vs. $\ln[J_{sc}(I_p)]$ [V/ln(mA/cm²)]	n
LuMnO₃ SC	0.081	3.12
LuMnO₃ film	0.041	1.58
YMnO₃ film	0.033, nonlinear	1.27
LaFeO₃ film	0.022	0.85

Table 6.1. Slopes and ideality factors derived from the linear fits of $V_{oc}(I_p)$ vs. $\ln[J_{sc}(I_p)]$, $\theta = 45°$.

Finally, we show in Fig. 6.6 the *J-V* curves of LMO SC and LFO, measured at 55° and 65° incidence angle. Here we use a laser with larger beam size ($S_d \approx 1.7$ mm) to minimize the artifacts from different optical installation and illumination state, hence the obtained photocurrent is much smaller due to the smaller light intensity applied. It clearly shows that the V_{oc} varies more with J_{sc} in LMO SC than in LFO, which supports the assumption that the polar LMO SC is mainly dictated by BPE (Eq. [6.3]) and nonpolar LFO is mainly dictated by Fresnel effect (Eq. [6.4]).
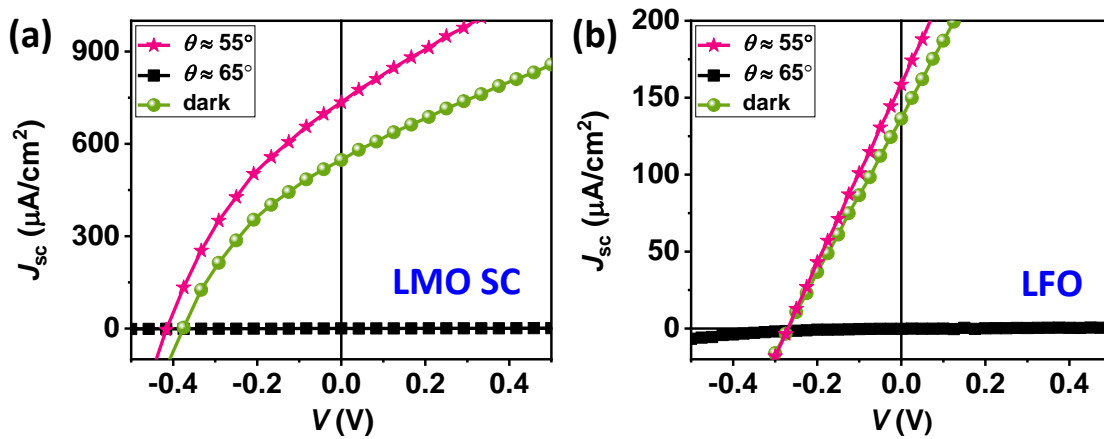
Fig. 6.6. The *J-V* curves of (a) LMO SC and (b) LFO collected in dark and under illumination of various incidence angle. The I_p after optical plates is around 0.6 W/cm².

6.5. Conclusions

In summary, we first showed that due to the Fresnel effect, the transmitted light intensity follows the same light polarization angle and incidence angle dependence than BPE, thus the Fresnel controlled CPE is entangled with BPE. To discriminate these two effects by the relation of V_{oc} vs. J_{sc}, we have measured the photovoltaic response depending on power density I_p and light polarization angle φ of ferroelectric LuMnO$_3$, YMnO$_3$ and non-ferroelectric LaFeO$_3$. The I_p dependence follows a logarithmic relation of V_{oc} vs. J_{sc} [$V_{oc} \propto \ln(J_{sc})$], with an ideality factor n close to 1 in LFO as found in conventional photodiodes, but larger n (> 1.5) in LMO suggesting a different physics could be involved, e.g., BPE. In the φ dependence, a linear relation of $V_{oc} \propto J_{sc}$ is also found, compatible with its logarithmic relation, which can happen within a small spread of values. The linear relation of $V_{oc} \propto J_{sc}$ indicates contribution from BPE. The larger slope of $V_{oc}[\ln(J_{sc})]$ deduced from $V_{oc}[J_{sc}(\varphi)]$ than from $V_{oc}[J_{sc}(I_p)]$ is found in both polar LMO, YMO and nonpolar LFO, although the two slopes are closer in LFO as expected for a conventional photovoltaic response. To further prove this, performing measurements in purely nonpolar Nb:STO and intrinsic Si with symmetric contacts are under preparation. Overall, there is a synergetic contribution of both Fresnel controlled conventional photovoltaic and bulk photovoltaic effects in the studied materials. As expected, the preliminary conclusion (remaining to be further explored though) is that BPE weighs more in ferroelectric LMO and YMO, and Fresnel contribution weighs more in non-ferroelectric LFO.

Supplementary information

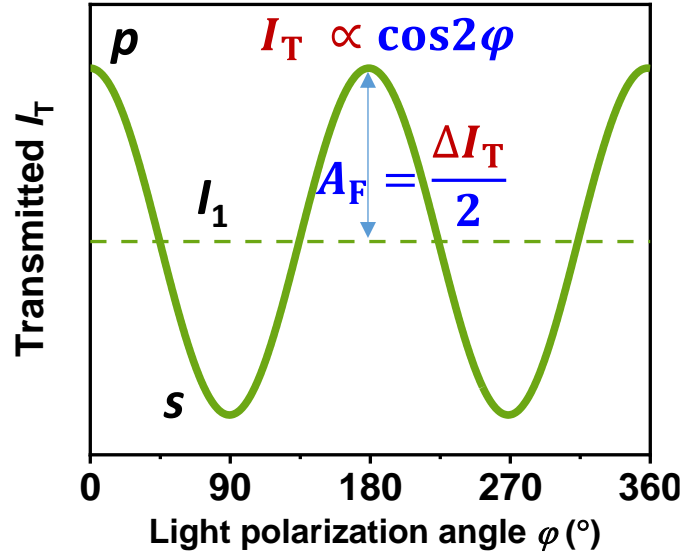S6.1. Fitting $J_{sc}(\varphi)$ by the equation combining BPE and Fresnel

Fig. S6.1.1. An example of transmitted light intensity I_T on the light polarization angles (φ) at oblique incidence.

By Figs. 6.2(a,b), we know the transmitted light intensity $I_T \propto \cos2\varphi$ (Fig. S6.1.1), and the amplitude of the transmitted power oscillation A_T is extracted and shown in Fig. S6.1.2, which shows clear that A_T is proportional to $\sin^2(\theta)$. This dependence conforms well to the photocurrent amplitude A_z dependence on $\sin^2(\theta)$ [Fig. 4.6(b)] as expected from BPE (Eq. [4.7]), which makes it difficult to distinguish BPE and Fresnel by qualitative analysis (observing the $\cos2\varphi$ dependence of J_{sc} or amplitude A_z variation among θ) but only by quantifying their contributions. According to the Fresnel equations, for the air/Pt interface and up to the Brewster angle ($\theta_B \approx 75°$ for air/Pt), $(R_s + R_p)/2$ (at $\varphi = 45°$) is roughly constant [identified by the constant background in Figs. 6.2(a,b)], implying that the light transmitted through the electrode can be represented by:

$$I_T(\theta, \varphi, t) = I_1 e^{-\alpha_m t}(1 + A_F \sin^2\theta \cos2\varphi) \qquad [\text{S6.1}]$$

where I_1 is the background of $I_T(\varphi)$ oscillation (Fig. S6.1.1); α_m is the absorption coefficient of the top contact, t is the thickness of the top contact, A_F is the amplitude of the $I_T(\varphi)$ oscillation basically depending on the contrast of refractive index at the interface and the

absorption coefficient of the material. The value of A_F can be derived experimentally by the slope of the linear fits in Fig. S6.1.2 and the background (blue dashes) in Figs. 6.2(a,b), that is, A_F = 6.108/22.88 = 0.267 for LMO SC, A_F = 6.71/16 = 0.419 for LMO film.
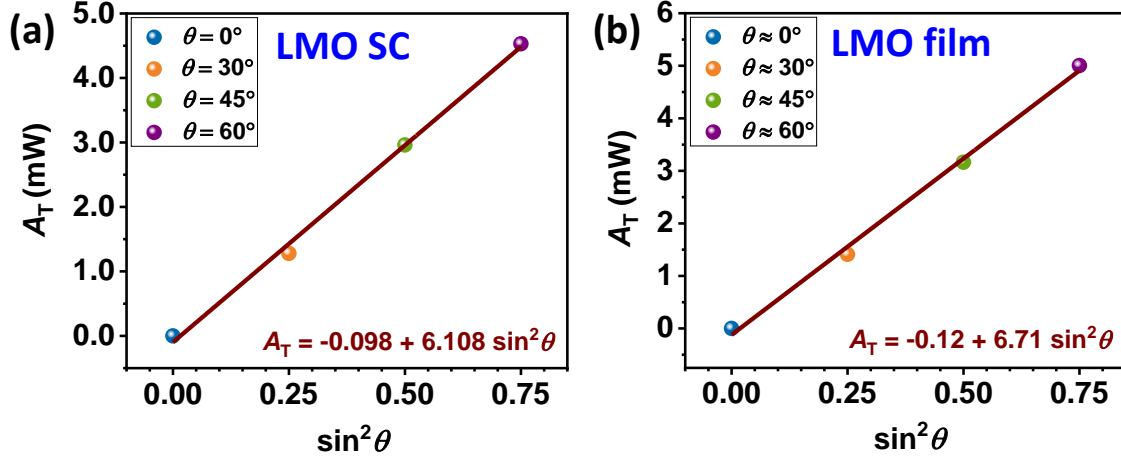

Fig. S6.1.2. Dependence of the amplitude $A_T(\theta)$ on $\sin^2(\theta)$ of (a) LMO SC and (b) LMO film. Solid lines are linear fits of experimental data (symbols).

By Eqs. [6.1], [S6.1] and [4.7], photocurrent generated by BPE and Fresnel effect can be written as:

$$J_{sc} = J_{BPE} + J_E + J_D = I_T\alpha[G_{ij}e_ie_j + f(J_E, J_D)]$$

$$= I_1e^{-\alpha_m t}\alpha(1 + A_F\sin^2\theta\cos2\varphi)\left[\left(\frac{G_{33}-G_{31}}{2}\sin^2\theta\cos2\varphi + \frac{G_{33}-G_{31}}{2}\sin^2\theta + G_{31}\right) + f(J_E, J_D)\right]$$

$$= I_1e^{-\alpha_m t}\alpha\left[\frac{G_{33}-G_{31}}{2}A_F\sin^4\theta(\cos2\varphi)^2 + \left(\frac{G_{33}-G_{31}}{2}\sin^2\theta + \frac{G_{33}-G_{31}}{2A_F} + G_{31} +\right.\right.$$

$$\left.\left.f(J_E, J_D)\right)A_F\sin^2\theta(\cos2\varphi) + \frac{G_{33}-G_{31}}{2}\sin^2\theta + G_{31} + f(J_E, J_D)\right]$$

$$= C(\cos2\varphi)^2 + D(\cos2\varphi) + E \qquad\qquad\qquad\qquad\qquad\qquad [S6.2]$$

Then there are three possibilities:

a) BPE is dominant (A_F = 0), $J_{sc} = A_1\sin^2\theta(\cos2\varphi) + B_1$ $\qquad\qquad\qquad$ [S6.3]

b) Fresnel contribution is dominant (G_{ij} = 0), $J_{sc} = A_2*A_F\sin^2\theta(\cos2\varphi) + A_2$ $\qquad$ [S6.4]

c) Both Fresnel and BPE exist, $J_{sc} = C(\cos2\varphi)^2 + D(\cos2\varphi) + E$ [S6.5]

We experimentally observe $J_{sc} = A_0\sin^2\theta(\cos2\varphi) + B_0$ which seems that only one contribution dominates. Nevertheless, note that here $D > C$, in which case the $(\cos2\varphi)^2$ behavior is easily hidden and only the $\cos2\varphi$ oscillation is shown. Thus, we try to fit the experimental results with Eq. [S6.5], taking the data of LMO film at 60° incidence (more evident oscillation beneficial for compensating the precision in the experimental setup) as an example shown in Fig. S6.1.3.
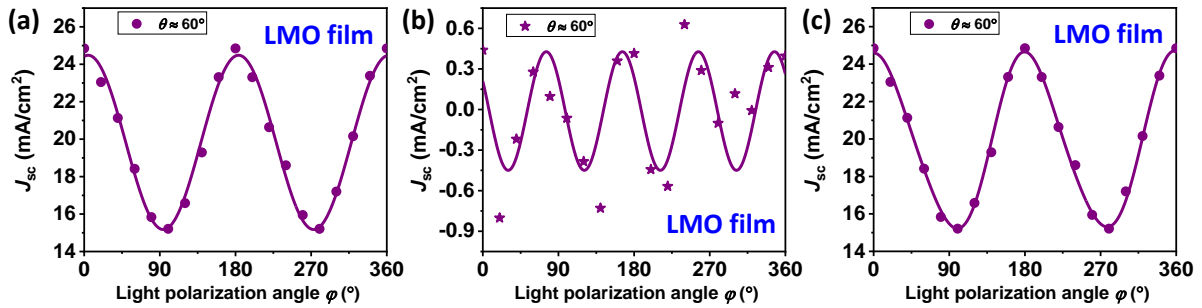

Fig. S6.1.3. (a,c) Experimental $J_{sc}(\varphi)$ raw data (circle symbols) of LMO film measured at $\theta = 60°$, I_p after optical plates is around 50 W/cm^2. Solid line in (a) is a fit of $J_{sc}(\varphi)$ data using Eq. [6.2] [$A\cos2\varphi + B$]. Solid line in (c) is a fit of $J_{sc}(\varphi)$ data using Eq. [S6.5] [$C(\cos2\varphi)^2 + D(\cos2\varphi) + E$]. (b) The difference $\Delta J_{sc}(\varphi)$ (star symbols) between the measured data and the fits of $J_{sc}(\varphi)$ in (a), solid line is a fit of $\Delta J_{sc}(\varphi)$ using Eq. [6.2].

It can be appreciated in Fig. S6.1.3(a) that $J_{sc}(\varphi)$ can be described as $J_{sc}(\varphi) \approx A\cos2\varphi + B$, implying $J_{sc}(\varphi)$ is larger for *p*-light than for *s*-light. However, detailed inspection in Fig. S6.1.3(b) where we plot the difference $\Delta J_{sc}(\varphi)$ between the raw $J_{sc}(\varphi)$ data and the results of [$A\cos2\varphi + B$] fit in (a) reveals deviation of the fit. By checking all the available data in LMO SC and film (not shown here), a tinny but systematic $\Delta J_{sc}(\varphi)$ departure can be observed. The fit of $\Delta J_{sc}(\varphi)$ suggests the presence of an additional [$A\cos2\varphi + B$] contribution to $J_{sc}(\varphi)$, namely, $J_{sc}(\varphi)$ possesses a double period of [$(\cos2\varphi)^2$]. Therefore, not surprisingly, $J_{sc}(\varphi)$ data can be better described by $J_{sc}(\varphi) \approx C(\cos2\varphi)^2 + D(\cos2\varphi) + E$ as shown in Fig. S6.1.3(c). This fitting in Fig. S6.1.3(c) allows to extract C, D and E values and from them the evaluation of $(G_{33} - G_{31})$ and [$G_{31} + f(J_E, J_D)$] can be obtained (with A_F fixed as 0.267 for LMO SC and 0.419 for LMO film), as shown in Table. S6.1.

Samples	Fresnel + BPE		BPE	
	$G_{33} - G_{31}$	$G_{31} + f(J_E, J_D)$	$G_{33} - G_{31}$	$G_{31} + f(J_E, J_D)$
	(pm/V)	(pm/V)	(pm/V)	(pm/V)
LMO SC	27.7	189.5	41	116
LMO film	1003	3837	1066	1360

Table. S6.1. Parameters of $(G_{33} - G_{31})$ and $[G_{31} + f(J_E, J_D)]$ extracted by the fitting of $J_{sc}(\varphi)$ data using Eq. [S6.5] recorded from LMO SC and thin films (considering the top contact absorption).

The Glass coefficients obtained by Eq. [S6.5] is reasonable comparing with the values obtained only considering BPE contribution (Chapters 4.2 and 5.2), which supports that both BPE and Fresnel contribute to the measured $J_{sc}(\varphi)$. Nevertheless, we find this method a bit tricky as the extracted values can be different depending on how the fitting is processed. For example, fitting the $J_{sc}(\varphi)$ data by using Eq. [S6.5] directly, or by the equivalent Eq. [$A\cos4\varphi + B\cos2\varphi + C$], or by setting associated parameters as C, D, E are dependent (Eq. [S6.2]), or by fixing A_F, the results obtained by different process can be totally different and some are not reasonable. Moreover, the fitting in Fig. S6.1.3(a) is already good, and it naturally goes better when introducing more parameters to fit [Fig. S6.1.3(c)]. Therefore, even some of the fitting in Fig. S6.1.3(c) makes sense and proves the contribution from both BPE and Fresnel, the experimental data is not necessary to be fitted with Eq. [S6.5] as it is well described by a single contribution (Eq. [S6.3] or [S6.4]) as well.

S6.2. Comparing the experimental B_z to the expectations in BPE and Fresnel

BPE and Fresnel can also be discriminated by observing the characteristics of the background B_z values. As can be seen in Fig. 6.2 and by Eqs. [S6.1-6.4], a main difference of BPE and Fresnel is, $J_{BPE} = I_0 \alpha G_{31}$ at $\varphi = 90°$ while $J_F = I_0 \alpha f(J_E, J_D)$ at $\varphi = 45°$, no matter at which incidence angle. Therefore, we repeated the $J_{sc}(\theta, \varphi)$ measurements using a bigger laser ($S_d \approx 1.7$ mm) with more cautions at each incidence trying to minimize artifacts

(Chapter 3.5.2) and get more effective and meaningful B_z values. Some of the results are shown in Fig. S6.2.
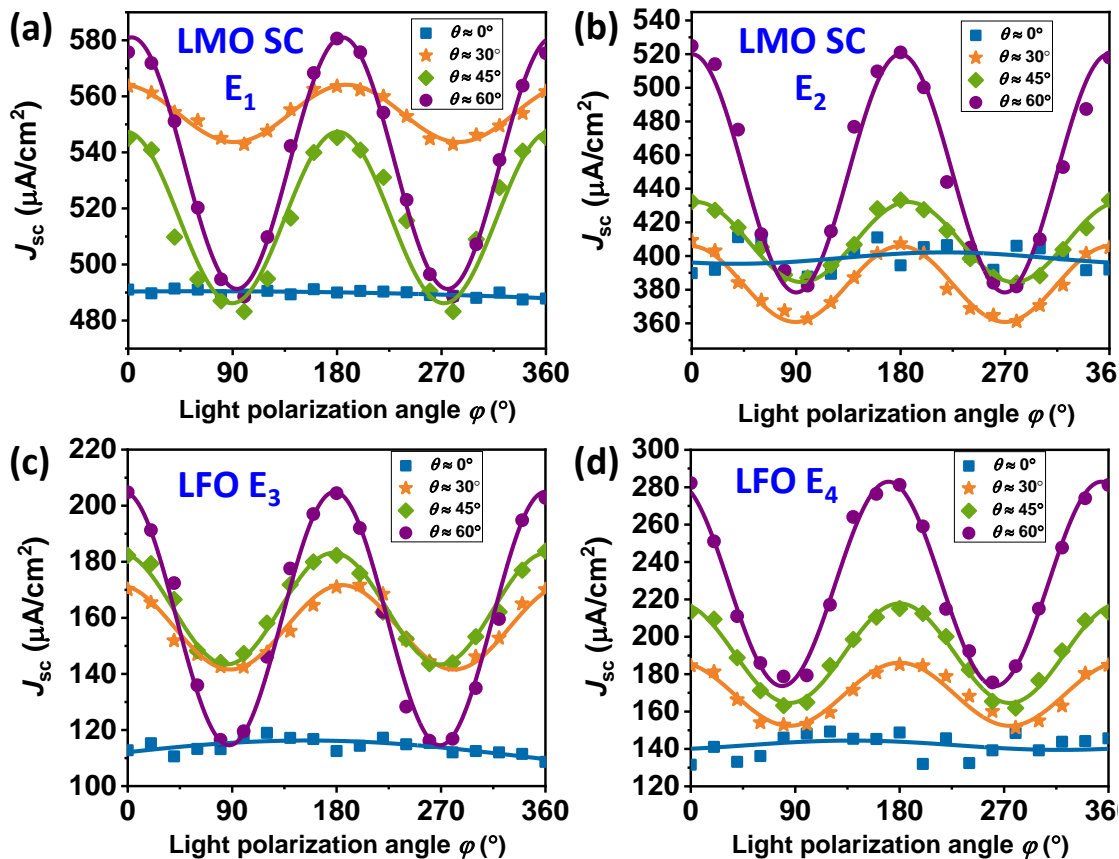
Fig. S6.2. Dependence of raw $J_{sc}(\theta, \varphi)$ on the light polarization angles (φ) at various incident angles (θ), of (a,b) capacitor E_1 and E_2 in LMO SC and (c,d) capacitor E_3 and E_4 in LFO. Solid lines are sine fits of experimental data (symbols). The I_p after optical plates is around 0.6 W/cm^2.

It can be appreciated from Fig. S6.2(a) that in capacitor E_1 of LMO SC, the curves measured at $\theta = 0°$, 45° and 60° overlap at $\varphi = 90°$, indicating that BPE dominates, while in capacitor E_2 [Fig. S6.2(b)] the curves are more random and show a tendency of merging at $\varphi = 45°$. Similarly, in capacitor E_3 of LFO [Fig. S6.2(c)], the curves of $\theta = 30°$, 45° and 60° match at $\varphi = 45°$, implying that Fresnel dominates, while in capacitor E_4 [Fig. S6.2(d)] the curves tend to merge at $\varphi = 90°$. These observations indicate either both contributions existed and competing, or more probably the randomness of the measured J_{sc} and B_z values. As J_{sc} and B_z strongly depend on the optical setup and illumination state at different θ, unlike

154

the I_p and φ dependences which can be performed at identical illumination state without changing any optical setup.

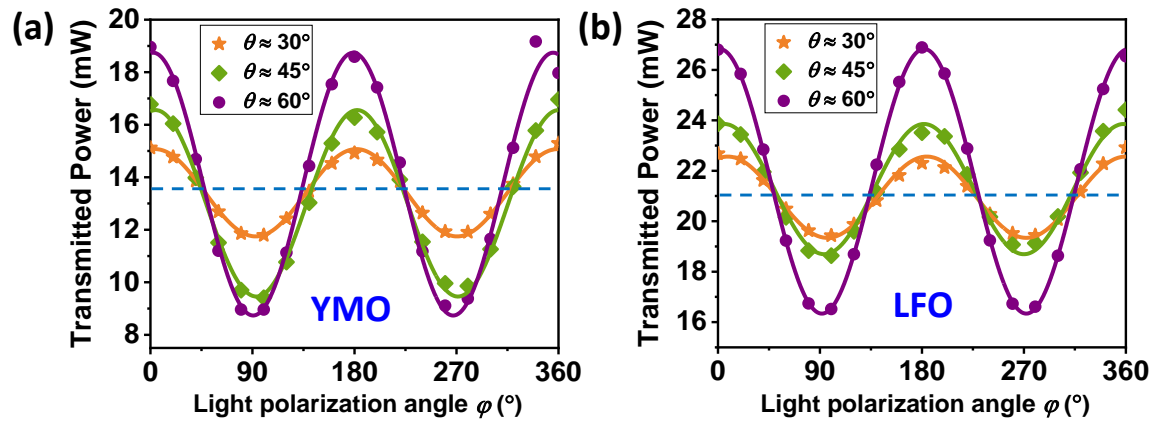S6.3. Dependence of transmitted power on φ and θ of LFO film

Fig. S6.3. Dependence of transmitted power on the light polarization angles (φ) at various incident angles (θ), of (a) YMO and (b) LFO films. Blue dashes denote the power measured at $\theta = 0°$ and $\varphi = 0°$. Solid lines are sine fits of experimental data (symbols).

Bibliography

[1] M.-M. Yang, D.J. Kim, and M. Alexe, Science (80-.). **360**, 904 (2018).

[2] W. Ji, K. Yao, and Y.C. Liang, Phys. Rev. B - Condens. Matter Mater. Phys. **84**, 094115 (2011).

[3] Y.K. Jeong, J.-H. Lee, S.-J. Ahn, and H.M. Jang, Chem. Mater. **24**, 2426 (2012).

[4] M.-A. Oak, J.-H. Lee, H.M. Jang, J.S. Goh, H.J. Choi, and J.F. Scott, Phys. Rev. Lett. **106**, 047601 (2011).

[5] B.B. Van Aken, T.T.M. Palstra, A. Filippetti, and N.A. Spaldin, Nat. Mater. **3**, 164 (2004).

[6] Y. Sheng, I. Fina, M. Gospodinov, A.M. Schankler, A.M. Rappe, and J. Fontcuberta, Phys. Rev. B **104**, 184116 (2021).

[7] J. Yu, Y. Chen, S. Cheng, and Y. Lai, Phys. E Low-Dimensional Syst. Nanostructures **49**, 92 (2013).

[8] A. Bhatnagar, A. Roy Chaudhuri, Y. Heon Kim, D. Hesse, and M. Alexe, Nat. Commun. **4**, 2835 (2013).

[9] P. Lopez-Varo, L. Bertoluzzi, J. Bisquert, M. Alexe, M. Coll, J. Huang, J.A. Jimenez-Tejada, T. Kirchartz, R. Nechache, F. Rosei, and Y. Yuan, Phys. Rep. **653**, 1 (2016).

[10] T. Singh and T. Miyasaka, Adv. Energy Mater. **8**, 1700677 (2018).

[11] M.N. Polyanskiy, Refractive index database. https://refractiveindex.info. (accessed on Aug. 29, 2022).

[12] W.S.M. Werner, K. Glantschnig, and C. Ambrosch-Draxl, J. Phys. Chem. Ref. Data **38**, 1013 (2009).

[13] S.R. Cowan, A. Roy, and A.J. Heeger, Phys. Rev. B **82**, 245207 (2010).

[14] Z. Sun, G. Sitbon, T. Pons, A.A. Bakulin, and Z. Chen, Sci. Rep. **5**, 10626 (2015).

[15] L. Madi, I. Bouchama, and N. Bouarissa, J. Sci. Adv. Mater. Devices **4**, 509 (2019).

Chapter 7. Band alignment and photovoltaic response of LaFeO₃-based heterojunctions

In Chapter 6, the non-ferroelectric LaFeO$_3$ (LFO) with narrow bandgap is introduced to compare the BPE [$J_{sc}(\varphi)$, $V_{oc}(\varphi)$] with the ferroelectric materials. In this Chapter, epitaxial LaFeO$_3$ thin film-based photovoltaic devices, of different thicknesses (50 - 200 nm), have been grown on cubic LSAT (001) single crystalline substrates, using a common LSMO bottom electrode and different top electrodes [Pt, BLSO], to determine their photoresponse. The measured photocurrent (I_{sc}) first increases with LFO thickness and then decreases, and it is larger/smaller, when Pt/BLSO electrodes are used, respectively. The corresponding photovoltage (V_{oc}) displays the opposite trend, being smaller/larger for Pt/BLSO, respectively, which is in excellent agreement with the electronic band alignments determined by XPS and also consistent with the rectifying character of the dark current-voltage (I-V) data. It turns out that the films display a complex microstructure containing different variants, strained and relaxed, of the orthorhombic LaFeO$_3$, that evolves with film thickness and entails the presence of strain gradients and, possibly, flexoelectric fields. We discuss these data and propose that the unavoidable grain boundaries between differently textured LaFeO$_3$ crystallites play a significant role on the observed responsivity (2.6 x 10^{-4} A/W), found to be larger than in related LFO-based structures.

The work presented in this Chapter is to be submitted. Some of the work, i.e., the structural characterization (XRD, XRR, AFM), optical properties (α) and XPS, had been done and included in the thesis (Chapter 8) of Dr. M. Mirjolet.[1] His great contribution is highly acknowledged.

7.1. Introduction

Narrow band oxides are receiving a tremendous attention in different areas of research and technology, which range from photoconversion and water splitting to novel spintronics.[2] To reach an efficient charge extraction, thin films of these oxides are usually grown between a bottom electrode or conducting substrate and a top metallic layer. The band alignment among the different layers is instrumental for device operation, as it determines the presence of valence band/conduction band offsets (VBO/CBO), implying the

presence of built-in potentials across the structure. Selection of the electrodes is the simplest tool to adjust band alignments, via their work function. However, the interfaces between consecutive layers, metallic electrodes and photoabsorbing layer, are not electronically rigid but are by themselves a device, where electronic reconstructions and interfacial dipoles may exist largely impacting the band alignment. For instance, focusing on narrow band gap transition metal perovskites, such as $LaFeO_3$ (LFO), it was proposed that when LFO is grown on a large band gap $SrTiO_3$ (STO) perovskite, a polar//non-polar interface exists and thus charge discontinuity may arise at the interface. Indeed, Nakamura et al.[3,4] first observed that the photocurrent in LFO//STO heterostructures could be reversed by changing the atomic termination of the STO substrate and proposed the existence of an interface-induced polarization contributing to the photocurrent. Subsequent experiments did not allow to obtain evidence of an atomic termination-dependent built-in dipole at LFO//STO interface[5] but rather the presence of chemical instabilities at this interface.[6] It follows that details of growth are capital on the properties of interfaces.

In recent years, a new aspect of epitaxial heterostructure has emerged. Indeed, while the possible presence of strain gradients in thin films was well understood,[7] the impact of the associated flexoelectric fields (E_f) on the photoresponse is now under scrutiny. The presence of strain gradients implies the presence of charge polarization in the dielectric layer and the associated flexoelectric field. In thin films, the contribution of E_f may be dramatic, as strain gradients can be exceedingly large (up to 10^7 m^{-1}), and could lead to voltages across the device comparable to built-in potentials and thus largely impacting band alignment. It follows that charge extraction could be governed by strain gradients. Illustrative examples include ferroelectric $HoMnO_3$ thin films, where strain gradient-related flexoelectric fields produce remarkable shifts of the ferroic loops[8] and, subsequently, modify the rectifying character of charge transport,[9,10] or even the tunnel transport across dielectric barriers.[11]

While $HoMnO_3$ in the above examples is ferroelectric, flexoelectricity is not restricted to polar materials but it should also exist in any centrosymmetric system under strain gradient, as nicely evidenced by the observation of the so-called flexo-photovoltaic response in tip-deformed silicon.[12] The presence of the flexoelectric field has also been recently invoked to explain the relatively large photoresponse of ultrathin LFO films grown

on substrates imposing a compressive strain (LaAlO$_3$, LAO) and attributed to a reduction of the height of the Schottky barrier at dielectric/metal interface which favors charge extraction.[13] Interestingly, the benefiting effect of E_f were found to be maximal for ultrathin films (≤ 35 nm), where the largest short-circuit current density (J_{sc} = 1.5 mA/cm^2) was measured, but reducing at larger thicknesses, presumably due to a detrimental effect of dislocations and other plastic deformations resulting from strain relaxation and limiting the photocarrier mean free path. By the same token, E_f is argued to be negligible in films grown on well matched substrates (i.e., STO), where strain gradients should be minimal. In a further twist on photovoltaic-flexoelectric possible synergy, Jiang et al. reported on tunable photoresponse of LFO films grown on flexible substrates (mica), proposing that the effect was due to strain gradient-controlled bending of the films.[14] While at first sight the possible effect of strain-gradients on the modulation of interfacial Schottky barriers seems well supported by the observed changes of J_{sc}, still questions arise regarding the open-circuit voltage V_{oc} values in strain-graded samples. The flexoelectric field E_f along a given direction (e.g.; z) is roughly:

$$E_f \approx N \frac{q}{a\,\varepsilon_0} \frac{\partial \epsilon}{\partial z},$$

where N is a scale factor depending on the material (≈ 1 in perovskite oxides),[15] q is the elementary charge, a is the cell parameter, ε_0 is the vacuum permittivity, and the derivative term is the gradient of strain (ϵ) along the z-axis. Using N = 1, and the reported strain gradient $\frac{\partial \varepsilon}{\partial z}$ ≈ 10^6 for a 35 nm LFO film on LAO,[13] it turns out that E_f ≈ 4.5 x 10^7 V/m, corresponding to a contribution to the built-in potential of about V_f ≈ 1.6 eV. In these structures, V_{oc} is primarily bounded by the built-in potential V_{bi} and consequently depends on the metal electrodes, which is typically much smaller (V_{bi} ≈ 0.2 - 0.8 eV)[13] than V_f. As V_f is sensitively larger than V_{bi}, it follows that V_{oc} should be dramatically modified by E_f and even the sign could be reversed depending on strain gradient. However, reported data in strain-graded structures evidence minor variations of V_{oc} with strain gradient,[13,14] suggesting that the scenario is more intricate.

Here, aiming at getting a deeper understanding of the complex interplay of different effects contributing to band alignment and photoresponse in narrow band oxides, we

report on the conductivity, band alignment and photoresponse of LSMO/LFO/M heterostructures where the LFO layer is 50-200 nm thick, and M are different top metallic layers (Pt and BLSO), and La$_{2/3}$Sr$_{1/3}$MnO$_3$ (LSMO) is a common bottom electrode in the structure. As a substrate, we selected LSAT which is cubic and has a cell parameter intermediate to those of the above mentioned STO and LAO and that should give rise to different strain gradient pattern in LFO films. As the bulk LFO cell is orthorhombic in nature, the growth of LFO on relatively well-matched cubic substrates is expected to lead to crystallites with different orientations of the longest orthorhombic axis with respect to the substrate and, concomitantly, the film microstructure should be relatively complex, as we shall report. It is found that the charge transport across the heterostructure and the photoresponse are mainly controlled by the band alignments, that set both the interfacial built-in potential V_{bi} across the various interfaces and the observed open circuit voltage (V_{oc}), with obvious differences depending on the work function of the top metallic electrodes. Remarkably, it is found that the J_{sc} of these structures can be larger than in ultrathin LFO films where flexoelectric contribution was invoked.[13] We suggest a different scenario in which grain boundaries, as seen in BiFeO$_3$,[10] largely contribute to the observed enhanced photoresponse.

7.2. Samples and experiments

Sample preparation: Single layers of LaFeO$_3$ (LFO) were first deposited by pulsed laser deposition (PLD) on Nb:SrTiO$_3$ (001) substrates to determine the optimal growth conditions. Optimal LFO films were obtained using a laser fluence of $F \approx 2$ J/cm^2, frequency of $f = 5$ Hz, a deposition temperature of $T = 700$ °C, a dynamic oxygen pressure of $PO_2 = 0.01$ mbar and cooling under the same PO_2. In these conditions, the growth rate is about ≈ 0.14 Å/pulse. The number of laser pulses were adjusted to the required thickness after proper calibration. Some structural and morphologic, and optical properties of bare LFO films on Nb:STO are included in Supplementary information S7.1 and S7.2.

Next, LFO metal-insulator-metal heterostructures were grown, where the photoabsorbing LFO (insulator) was sandwiched between the bottom electrode: La$_{2/3}$Sr$_{1/3}$MnO$_3$ (LSMO), and a top metallic electrode (M). Two different materials were investigated: semitransparent Pt[16] and transparent Ba$_{0.95}$La$_{0.05}$SnO$_3$ (BLSO).[1] For

photoresponse measurements the thickness of each electrode was kept constant (27 nm for LSMO, 7 nm for Pt and 40 nm for BLSO), while three LFO thicknesses were explored: t_{LFO} = 50, 100 and 200 nm. The whole LSMO/LFO/M structures were deposited onto (001) LSAT single-crystal substrates. The bottom electrode (LSMO) was deposited at T = 725°C, F = 2 J/cm², and f = 5 Hz, PO_2 = 0.1 mbar and cooling under the same PO_2 (see ref. 17). The top Pt electrodes were sputtered ex-situ at room temperature through a shadow mask (60 x 60 μm²). The top BLSO electrodes were deposited by PLD by using a suitable mask (200 x 200 μm²) using the conditions of T = 725°C, F = 2 J/cm², f = 5 Hz, PO_2 = 0.1 mbar and cooling under PO_2 = 200mbar**.**

Structural characterization and surface morphology: phase purity, film thickness and cell parameters (out-of-plane and in-plane) were measured by X-ray diffraction (XRD) using a X'Pert Pro MRD diffractometer, Malvern-Panalytical [θ-2θ scans, reciprocal space maps (RSM)]. Film thickness of LFO single layers was determined from X-ray reflectivity (XRR) data and from the fitting of Laue fringes, using a Bruker A25 D8 Discover. The 2θ-χ scans were measured with a Bruker D8 Advance GADDS using a 2D Vantec-500 detector. Topographic images were collected by AFM in dynamic mode. Details and structural characterization of the LSMO/LFO/Pt and LSMO/LFO/BLSO heterostructures are given in Supplementary information S7.3.

Electrical measurements and photoresponse: Two-point-measured *I-V* characteristics, with or without illumination, were performed in top-bottom configuration (the LSMO bottom electrode was connected to the ground), using gold-plated tungsten probe tips of 10 μm radius. A Keithley 6517B Electrometer/High Resistance Meter was used to apply a bias voltage *V*+/− (performing a loop between -1 V and +1 V) to the top electrode (TE) and measure the resulting current *I* flowing through the structure, where positive current corresponds to positive charges flowing from TE towards the bottom electrode (BE). Current density was evaluated using the area of the TE identified under a microscope. Dark *I–V* characteristics were measured either in complete darkness, i.e. that the sample was covered by an opaque box for several hours (overnight) prior measurements, or at ambient dark conditions without observing significant changes. *I-V* characteristics under illumination were collected mainly using a monochromatic blue laser (λ = 405 nm, $h\upsilon$ = 3.06 eV),

operating with a power of about 33 mW calibrated with a power meter (PM16-401 thermal sensor, Thorlabs). Considering the approximate diameter of the laser spot ($S_d \approx 280$ μm), the corresponding power density was estimated to be $I_p \approx 54$ W/cm^2. The photoresponse dependence on wavelength (λ) was recorded by using a STEC multiwavelength system (Blue Sky Research), with a parallel laser beam of $\lambda = 405, 450, 520,$ and 638 nm ($S_d \approx 1.7$ mm, $I_p \approx 0.55$ W/cm^2). The lasers were fed by a CPX400SA DC power source (AimTTi Co.). The incidence angle was fixed at 45°. For a given sample, at least 6 contacts were measured to monitor data dispersion and the reproducibility of the measurements.

Spectroscopic *ellipsometry:* Variable-angle spectroscopic ellipsometry measurements were performed using a SOPRALAB GES5E ellipsometer in reflection mode, at an angle of incidence of 65°. The ellipsometric angles (Δ, Ψ) were collected over the 230 - 990 nm spectral range, and data were analyzed using the WinElli II software.

X-ray photoelectron spectroscopy (XPS) measurements: XPS measurements were performed with a PHOIBOS 150 hemispherical electron analyzer (SPECS GmbH) at a base pressure of 4 x 10^{-10} mbar, with a monochromatic Al K_α X-ray source (1486.6 eV), irradiating a sample surface of about 0.5 x 3.5 mm². The reported binding energies are referred to the Fermi level (E_F) of the analyser, which is periodically determined by measuring the photoelectron energies from an atomically clean reference Au(111) sample. All spectra were acquired at normal emission. After deposition, the sample was exposed to air for transfer to the XPS chamber, where it was fixed to the sample holder by metallic screws ensuring an electrical contact between the sample surface and the ground. Survey spectra are shown in Supplementary information S7.4. Data analysis was performed with the CasaXPS processing software.[18]

Band alignment *determination:* The band alignment at the metal-insulator (or insulator-metal) interfaces were determined by XPS combined with ellipsometry measurements for bandgap evaluation. The valence band offset (VBO) is determined by measuring energy differences associated to two different core levels characteristic of each material and their relative position to the corresponding valence band maximum (VBM).[19,20] Details on the technique are given in Supplementary information S7.5.

For XPS measurements different sets of films were grown *on-purpose,* as follows: a) a thick film of LFO (35 nm) was grown on a conducting Nb:SrTiO$_3$ substrate to mitigate charging effects during XPS measurements, a thick film of LSMO (27 nm) was grown on LSAT, and ultrathin LFO films of thicknesses 1 nm, 3 nm and 5 nm were grown on LSAT//LSMO (27 nm); b) a thick film of Pt (20 nm) was grown on Si, and ultrathin Pt films of 1 nm, 2 nm and 3 nm were grown on LSAT//LFO (50 nm); c) a thick film of BLSO (64 nm) was grown on STO, and ultrathin BLSO films of 2 nm, 3 nm and 5 nm were grown on LSAT//LFO(50 nm).

STEM measurements*:* Cross-sectional scanning transmission electron microscopy (STEM) analysis of LSAT//LSMO/LFO heterostructures has been performed using a probe aberration corrected Jeol ARM 200cF STEM with a cold field emission source operated at 200 kV. Electron diffraction micrographs were obtained in a JEOL 1210 transmission electron microscope operating at 120 kV, equipped with a side-entry 60º/30º double tilt GATAN 646 specimen holder. Specimens for TEM observations were prepared by conventional methods, by grinding, dimpling and Ar ion milling.

7.3. Results

7.3.1. Structural data
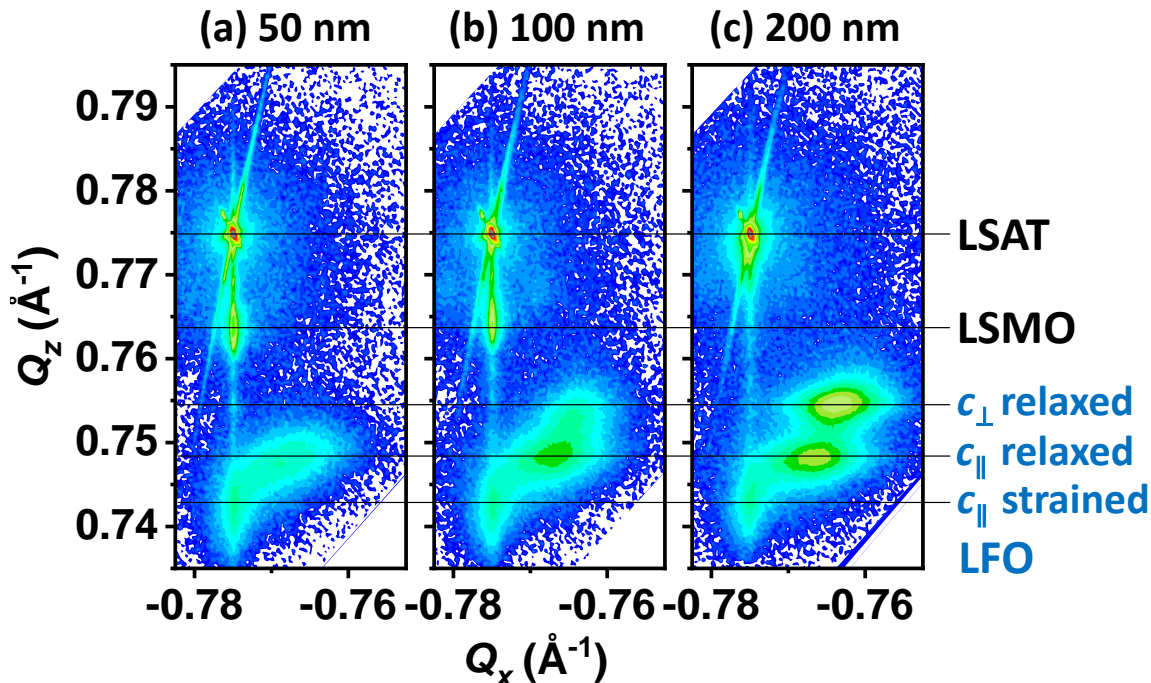

Fig. 7.1. (a, b, c) Reciprocal space maps around the (-303) reflection of LSAT of LSMO/LFO/Pt heterostructures having t_{LFO} = 50 nm, 100 nm and 200 nm, respectively. Horizontal lines indicate out-of-plane position of the diffracting planes of LSAT, LSMO, and the position of the observed fully strained and relaxed $c_∥$ crystallites, and relaxed $c_⊥$ ones, of LFO.

X-ray diffraction $θ$-$2θ$ scans and reciprocal space maps (RSM) were collected on LSMO/LFO/Pt and LSMO/LFO/BLSO heterostructures, having different thicknesses of the LFO (t_{LFO}) photoabsorbing layer. The RSM (Fig. 7.1) clearly show that LSMO is fully epitaxial and coherently grown on LSAT (001). In contrast, LFO displays more complex diffraction patterns that arise from the coexistence of fully strained and gradually relaxing crystallites of LFO differently textured on LSAT//LSMO. Bulk LFO has an orthorhombic structure *Pbnm* (62) with room-temperature cell parameters a = 5.5544 Å, b = 5.5659 Å and c = 7.8534 Å,[21] that correspond to pseudo-tetragonal c(LFO) = 3.9267 Å and a(LFO) = 3.9316 Å interplanar distances. The cell parameter of LSAT is 3.868 Å, and accordingly the mismatch is only marginally smaller (-1.5 %) when c(LSAT)//c(LFO) than when a(LSAT)//c(LFO) (-1.6 %). Accordingly, it can be expected that LFO film grows with its c-axis in the (001) plane of

LSAT//LSMO (denoted as $c_\parallel$), either clamped to the substrate or gradually relaxing when increasing thickness, somehow mixed with LFO crystallites with c(LSAT)//a(LFO) (denoted as $c_\perp$). The RSM of the $t_{LFO} \approx 50$ nm film, that displays a fraction of coherently grown LFO crystallites (horizontal line in Fig. 7.1), as mentioned most likely with their c-axis in-plane ($c_\parallel$), and a fraction of relaxed phase (horizontal line in Fig. 7.1). The relative fraction of the relaxed phase increases when the film thickness increases, as appreciated in the $t_{LFO} \approx 100$ nm. For the thickest films ($t_{LFO} \approx 200$ nm) a new additional diffraction spot appears in the RSM that fits well with the expected position of d(002) indicating a $c_\perp$-textured crystallite (Supplementary information S7.3.1).

Therefore, the growth of relatively thick (50 - 200 nm) films of LFO on LSAT leads to a subtle coexistence of epitaxial crystallites of different texture, either coherently grown or relaxed as observed in Figs. 7.1(a, b, c), where the corresponding RSM are shown. The LFO microstructure observed in LSAT//LSMO/LFO structures having Pt and BLSO electrodes were found to be virtually identical (Supplementary information S7.3.2).
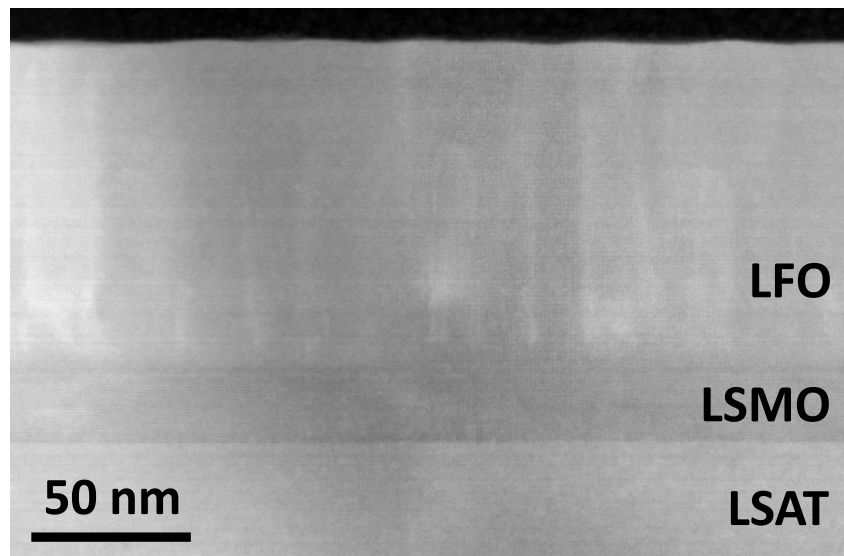
Fig. 7.2 An HAADF-STEM image of the LSAT//LSMO/LFO (100nm) sample, revealing a columnar structure. There is a dimmer and brighter contrast along the LFO films, which is consistent with the existence of crystallographic domains with boundaries that propagate along the LFO layer.

Fig. 7.2 shows a low-magnification high angle annular dark field STEM (HAADF-STEM) images of the LSMO(27nm)/LFO(100nm) heterostructures. Films show a columnar

morphology, where continuous lines of low-angle grain boundaries propagate across the LFO layer. In addition, the LFO film shows misfit dislocations (see Fig. 7.3), suggesting these relatively thick films are relaxed. These results are in agreement with both X-Ray measurements and electron diffraction patterns (see Supplementary information S7.6).
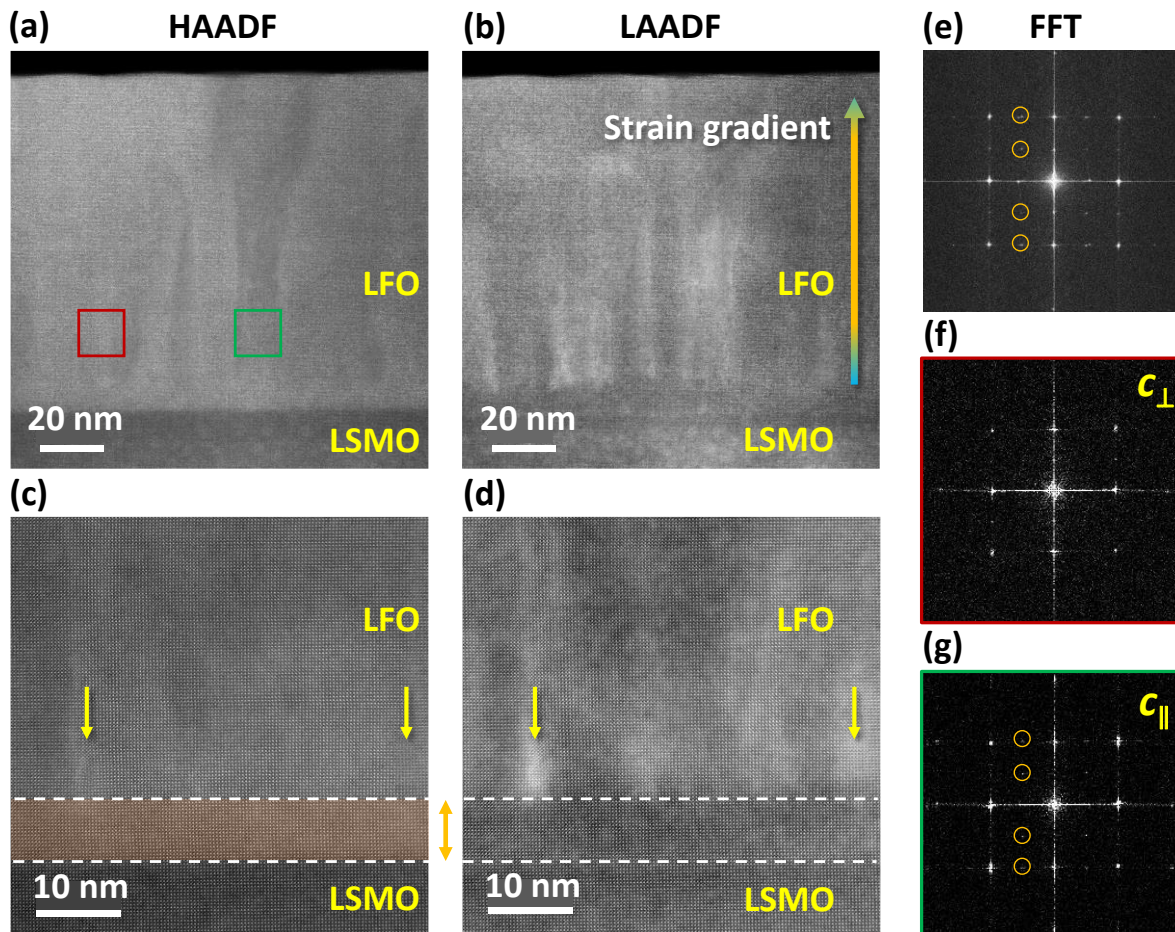

Fig. 7.3. (a) HAADF-STEM and (b) LAADF-STEM images of a LSAT//LSMO(27 nm)/LFO(100nm) heterostructure, respectively. As the contrast in a LAADF-STEM image contains information of strain, the image shows that near the LSMO/LFO interface the LFO is more distorted and that this distortion diminishes near the top surface. Notice that the contrast in the HAADF-STEM image is constant throughout the LFO film, and the minor variations in contrast are due to the existence of different crystallographic domains. Higher magnification(c) HAADF-STEM and (d) LAADF-STEM images, respectively. LAADF-STEM image shows a brighter contrast at the base of the LFO columns just above a thin and strained LFO layer, delimited with dashed white lines and an orange shadow in (c). The yellow arrows point at misfit dislocations located atop the strained LFO layer. FFT's

belong to the (e) whole LFO film and to the (f) red and (g) green squares shown in (a), respectively. The orange circles in (e) and (g) mark the reflections that appear when *c*-axis lays in-plane.

A careful study of the microstructure of the LFO films grown on LSAT reveals a rather complex structure. Fig. 7.3(a) shows a HAADF-STEM image where different crystallographic domains propagate along the LFO layer. The domains can be distinguished using a local Fourier Transform (FT) as well. The red and green squares mark the areas from which FT's have been obtained, and they correspond to domains with *c* perpendicular [Fig. 7.3(f)] and *c* parallel [Fig. 7.3(g)], to the interface, respectively. The orange circles of Fig. 7.3(g) mark the reflections that appear when *c*-axis lays in-plane and allow for distinguishing different crystallographic domains (see also Supplementary information S7.6). One would expect that the high number of domain boundaries would generate local strain and defects throughout the LFO film, and to investigate it low angle annular dark field (LAADF) images were acquired, see Fig. 7.3(b). Notice that the LAADF-STEM image shows a bright contrast that progressively fades away near the surface of the film. Since the LAADF contrast contains information of the strain,[22,23] the images suggest that the lattice of the LFO film grown on LSAT present depth-wise deformations, or in other words, the lattice is much more relaxed away from the interface. Interestingly, the LAADF-STEM image also shows a homogeneous contrast at the bottom of the LFO film, which suggest a fully strained 8 - 9 nm thick LFO layer that grows coherently with the LSMO buffer layer. A higher magnification HAADF and LAADF-STEM images, Fig. 7.3(c) and 3(d), show that the brighter contrast at the base of the LFO columns appear just above this fine and strained LFO layer, and also that there are misfit dislocations atop this region. These results are in good agreement with the X-Ray analysis of the strain of the LSAT films, which unveiled not only a domain structure but also strained and relaxed regions within the LFO layer.

7.3.2. J-V characteristics and LFO thickness dependence

In Figs. 7.4(a) and 7.4(c), we show the *J-V* curves of the LSMO/LFO/Pt and LSMO/LFO/BLSO heterostructures, respectively. These *J-V* curves are clearly not ohmic and display an asymmetric conductivity between negative and positive bias voltage, indicating a rectifying behavior that becomes more perceptible when increasing LFO thickness and more pronounced in LSMO/LFO/BLSO than in LSMO/LFO/Pt. Moreover, it can be

appreciated that the conductivity decreases when the thickness of LFO increases, indicating that above some threshold voltage the conductivity is bulk-limited. Interface limited conductivity, as dictated by interfacial Schottky barriers at LSMO/LFO and LFO/(Pt,BLSO) interfaces, of height Φ_2 and Φ_1, would be prevalent at low voltages. In the interface-dominated regime, the LSMO/LFO/(Pt,BLSO) devices can be viewed as a back-to-back association of Schottky diodes[24] with a *p*-type (LFO) semiconductor, with an internal resistance R_i representing the carrier transport across the semiconducting LFO.[25] Inclusion of the R_i term is dictated by the observation that at relatively large voltages, the conductivity of the capacitors is clearly dependent on the thickness of the LFO layer. This model allows to replicate [Figs, 4(c,d)] the experimental data for the thinnest LFO layer, to deduce the $\Phi_{1,2}$ energy barriers and, under the assumption that $\Phi_{1,2}$ are independent of the LFO thickness, to estimate the contribution of R_i. It turns out that Φ_1(LFO/Pt) ≈ 0.63 eV, Φ_1(LFO/BLSO) ≈1.1 eV and Φ_2(LSMO/LFO) ≈ 0.83 eV (Supplementary information S7.7.1). These results clearly confirm the presence of a larger and dissimilar Schottky barriers in LSMO/LFO/BLSO than in LMO/LFO/Pt, and account for the larger rectifying character of the former.

At high voltage, the space charge limited conduction (SCLC) mechanism predicts that J ≈ V^2 and a power dependence on the LFO thickness, which is consistent with the observed variation with t_{LFO} of the extracted R_i values (Supplementary information S7.7.2).
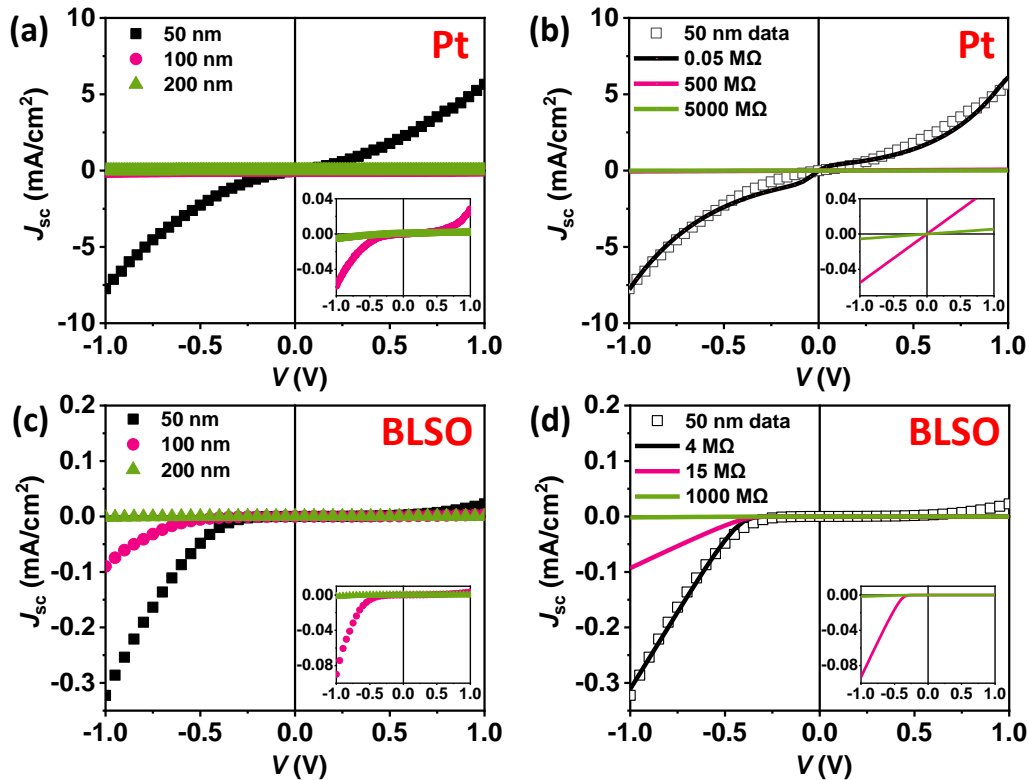
Fig. 7.4. *J-V* characteristics measured in dark of (a) LSMO/LFO/Pt and (c) LSMO/LFO/BLSO heterostructures, with varying LFO thickness of 50, 100 and 200 nm. Simulations of *J-V* curves in (a,c) using the back-to back diode model with an internal resistance (R_i) with varying LFO thickness are shown in (b) LSMO/LFO/Pt and (d) LSMO/LFO/BLSO. Black lines are the simulations of the experimental data (empty symbols) of the thinnest device (t_{LFO} = 50 nm), red and green lines are obtained with the same Schottky barrier parameters but increasing R_i.

The observed asymmetric *J-V* curves reflect the presence of a nonzero built-in potential V_{bi} through the LSMO/LFO/Pt and LSMO/LFO/BLSO structures. According to data in Figs. 7.4(a,c), and as deduced from the numerical analysis of the *J-V* curves, presumably V_{bi}(LSMO/LFO/BLSO) > V_{bi}(LSMO/LFO/Pt). When an insulating (or semiconducting) material is sandwiched between two metallic electrodes having work functions φ_1 and φ_2, a built-in potential V_{bi} emerges, that in the simple electron *affinity-rule* (EAR, Anderson-Mott) approach,[26] is given by: $V_{bi} = (\varphi_1 - \varphi_2)/q$,[27] with q the positive elementary charge. Using the reported work function of LSMO (φ_{LSMO} = 4.8 eV)[28–30] and Pt (φ_{Pt} = 5.6 eV),[31–36] EAR predicts a built-in potential $V_{bi,th}$ = − 0.8 eV for LSMO/LFO/Pt. Using the reported electronic affinity of LFO (χ_{LFO} = 3.3 eV[37]) and measured indirect band gap of our LFO films [E_g(indirect) ≈ 2.4 eV] (Supplementary information S7.2). The band alignment for LSMO/LFO/Pt derived

within the electron affinity rule model is depicted in Fig. 7.5(a), where a rigid fully-depleted flat band model is assumed. Similarly, using the φ_{BLSO} = 4.2 eV[38,39], EAR predicts $V_{bi,th}$ = + 0.6 eV and using the optically-determined indirect band gap of $BaSnO_3$ (≈ 3 eV[40,41]), the band alignment predicted within AER in LSMO/LFO/BLSO is shown in Fig. 7.5(b), where the Fermi level in BSO has been shifted up above the conduction band minimum by δ to illustrate the *n*-doping induced in BLSO.

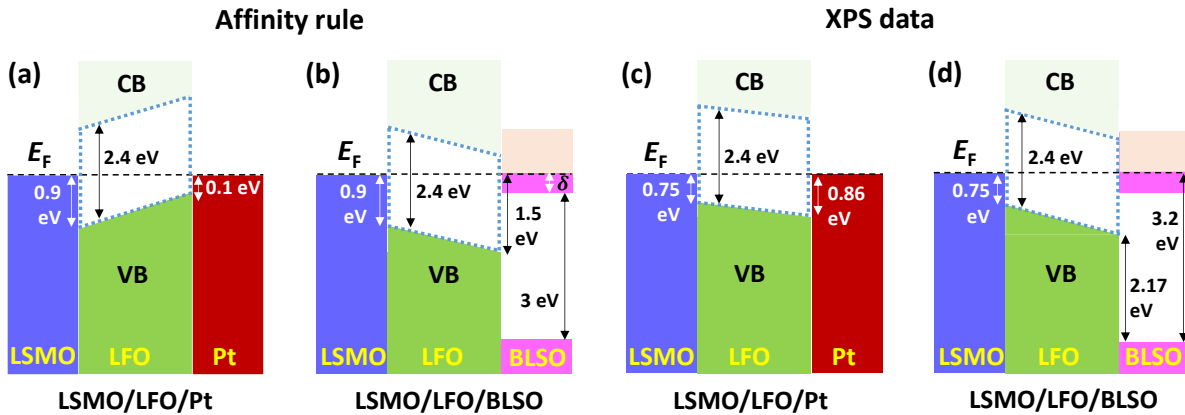**Affinity rule**   **XPS data**

Fig. 7.5. Schematic energy band diagrams based of:(a,c) LSMO/LFO/Pt and (b,d) LSMO/LFO/BLSO heterostructures, as inferred from the electron affinity rule (a,b) and as deduced from XPS data (c,d). The LFO layer is assumed to be fully depleted (flat bands) for sake of clarity. The band gaps of LFO and BLSO are indicated. The position of the Fermi level in BLSO, which is depending on the doping level (La^{3+}), is indicated in (b) by δ.

It follows that the band alignment derived from AER display an opposite slope for LSMO/LFO/Pt and LSMO/LFO/BLSO capacitors that would imply a rectifying character of opposite sign, which is not observed. However, the AER model does not include electronic reconstructions arising from chemical bonding across the interfaces nor the presence of interfacial dipoles of Fermi level pinning, it assumes sharp interfaces and no chemical interdiffusion, etc., has been largely criticized.[26,34] Similarly, the back-to-back diode model and the inclusion of the internal series resistance is far from unambiguous and energy barriers extracted from transport measurements may not be accurate enough.[42] Therefore, the valence band offsets (VBOs) at the interfaces between the different consecutive bilayers, namely LSMO/LFO, LFO/Pt and LFO/BLSO interfaces, need to be directly measured to account for the *I-V* curves recorded in dark and for the photoresponse to be described latter. We have used XPS and followed the methodology introduced by Kraut et al.[19,43]

widely used to determine the VBO at oxide/oxide interfaces,[5,40,44–48] or the Schottky barrier height at oxide/metal interfaces.[42,49,50]

7.3.3. Band alignments

(a) LSMO/LFO/Pt

To determine the VBOs at LSMO/LFO and LFO/Pt interfaces, we measured the valence band maxima (E_{VBM}) of the different layers (LSMO, LFO and Pt), first when separated and then when in intimate contact, using as reference the core levels (CLs) of various elements of the layers, to evaluate $\Delta E_{VBM}^{LSMO/LFO} = E_{VBM}^{LFO} - E_{VBM}^{LSMO}$ and $\Delta E_{VBM}^{LFO/Pt} = E_{VBM}^{Pt} - E_{VBM}^{LFO}$ respectively. By knowing the bandgap of the materials, the relative position of their conduction band minima E_{CBM} can also be deduced.
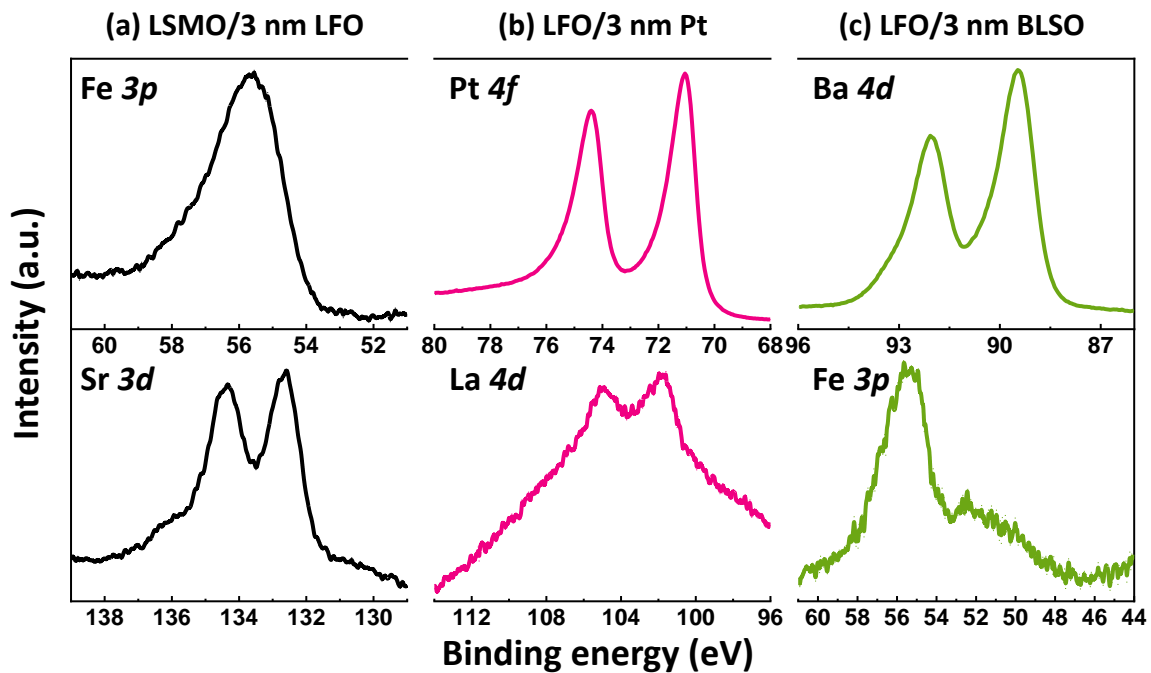
Fig. 7.6. High-resolution XPS spectra of the selected pairs of core level lines for the determination of the corresponding band offsets for 3 nm thick films of (a) LSMO (Sr*3d*)/LFO (Fe*3p*) (left), (b) LFO (La*4d*)/Pt (Pt*4f*) (middle) and (c) LFO (Fe*3p*)/BLSO (Ba*4d*) (right). The energies are referred to the Fermi level of the analyzer.

The LSMO/LFO interface was first investigated. To this aim, the position of various CLs relative to the corresponding valence band maxima, in LSMO and LFO thick films (27 nm

and 35 nm, respectively) grown on STO and Nb:STO substrates respectively, were determined. Subsequently, the spectra of ultrathin LFO films (1, 3, 5 nm) on LSMO were collected and the energy position of CLs of the capping layer (LFO) and the bottom one (LSMO) were compared. Examples for Fe*3p* lines and Sr*3d* lines of LSMO/LFO(3 nm) are shown in Fig. 7.6(a). Next, XPS data of ultrathin Pt films (1, 3, 5 nm) grown on LFO were similarly measured and the position of the corresponding CL were compared. Figs. 7.6(b,c) show, as illustrative data, the Pt*4f* and La*4d* lines collected on LFO/Pt(3 nm) and the Ba*4d* and Fe*3p* lines collected on LFO/BLSO(3 nm), respectively. Data for other CLs and film thicknesses are in Supplementary information S7.5. By collecting the values for two CLs of LFO (Fe*2p* and Fe*3p*) and two CLs of LSMO (Mn*2p*, Sr*3d*), up to four different VBOs values can be extracted, by using Eq. [7.1].

$$\Delta E_{\text{VBM}} = (E_{\text{LFO–CL}} - E_{\text{VBM}})^{\text{thick–LFO}} - (E_{\text{LSMO–CL}} - E_{\text{VBM}})^{\text{thick–LSMO}} - (E_{\text{LFO–CL}} - E_{\text{LSMO–CL}})^{\text{interface}}$$

[7.1]

Table 7.1 gathers the VBO (ΔE_{VBM}) values obtained using Eq. [7.1], for LSMO/LFO(3 nm), LFO/Pt(3nm) and LFO/BLSO(3nm). It is remarkable that the distribution of ΔE_{VBM} values around the mean value is notably narrow for LSMO/LFO and LFO/Pt.

LSMO/LFO	ΔE_{VBM} (eV)	Fe*2p*-Mn*2p*	Fe*2p*-Sr*3d*	Fe*3p*-Mn*2p*	**Fe*3p*-Sr*3d***	Average
		−0.70	−0.72	−0.77	**−0.79**	−0.75 (0.04)
LFO/Pt	ΔE_{VBM} (eV)	Pt*4f*-La*3d*		Pt*4f*-Fe*2p*	**Pt*4f*-La*4d***	Average
		0.89		X	**0.82**	0.86 (0.05)
LFO/BLSO	ΔE_{VBM} (eV)	Fe*3p*-Ba*3d*		Fe*3p*-Sn*3d*	**Fe*3p*-Ba*4d***	Average
		−2.50		−2.45	**−2.17**	XX

Table 7.1. Summary of VBOs measured at the LSMO/LFO(3 nm), LFO/Pt(3 nm) and LFO/BLSO(3 nm) interfaces as a function of LFO, Pt and BLSO coverages. The VBOs are extracted from each pair of CLs, indicated by the corresponding column headings. Bold data correspond to spectra shown in Fig. 7.6. Last column gives the average values and data in brackets indicate the standard deviation

of the average value. "X" symbol indicates that a CL line is not perceptible in the XPS spectrum, and :XX" indicates that averaging is not appropriate due to differential charging effects.

The negative sign of ΔE_{VBM} ($\Delta E_{VBM} < 0$) for the bottom interface (LSMO/LFO) indicates that the $(E_{VBM})_{LFO}$ is below $(E_{VBM})_{LSMO}$. This result is in agreement with predictions made above on the basis of the electron affinity rule[26] applied to the band alignment at the LSMO/LFO interface [Fig. 7.5(a)]. ΔE_{VBM} data collected for other LFO thicknesses (Supplementary information S7.5, Table S7.5) consistently display this trend with minor variations on thickness.

Next, we analyzed the top interface (LFO/Pt) using the same methodology. The PLD-deposited LFO (50 nm) film was transferred under UHV to the sputtering chamber for Pt deposition to avoid surface contamination. Different LFO/Pt (1 nm, 2 nm, 3 nm) heterostructures were deposited, and XPS was used to determine the position of several CL energies: Pt*4f*, La*3d*, Fe*2p* and La*4d.* Use of Eq. [7.2] allows to extract up to three VBOs values for each sample (Table 7.1).

$$\Delta E_{VBM} = (E_{Pt-CL} - E_{VBM})^{thick-Pt} - (E_{LFO-CL} - E_{VBM})^{thick-LFO} - (E_{Pt-CL} - E_{LFO-CL})^{interface} \quad [7.2]$$

For LFO/Pt(3nm) the Fe*3p* CL was found to be imperceptible in the XPS spectrum because the inelastic mean free path of electrons originating from this CL is shorter than the Pt thickness, thus precluding its use to determine ΔE_{VBM} (indicated by X symbol in Table 7.1). It can be appreciated in Table 7.1 that all data indicate a systematical shift between Pt and LFO CLs, with $\Delta E_{VBM} \approx 0.86$ (0.05) eV. The positive sign of ΔE_{VBM} ($\Delta E_{VBM} > 0$) indicates that the Fermi energy of Pt is above the VBM of LFO. ΔE_{VBM} data collected for other Pt thicknesses (Supplementary information S7.5, Table S7.5) consistently display this trend.

Using the VBO of LSMO/LFO and LFO/Pt (Table 7.1), the band alignment of the LSMO/LFO/Pt structure is sketched in Fig. 7.5(c). Notice that according to the XPS data, there is a small build-in potential ($V_{bi,XPS}$) across the LSMO/LFO/Pt heterostructure with a value of $V_{bi,XPS} \approx (0.86\ eV - 0.75\ eV) \approx + 0.11$ eV. Notice the XPS determined $V_{bi,XPS}$ ($\approx + 0.11$ eV) radically differs in sign from that obtained from the electron-affinity rule ($V_{bi,th} \approx - 0.8$ eV) [Fig. 7.5(a)]. Such discrepancy of band alignment estimates using the electron-affinity rule and the experimental determinations is commonly observed when using Pt (or other

metals) as top electrode onto some oxide layers.[42,49,50] Of greatest interest here is that the band alignment measured in LSMO/LFO/Pt [Fig. 7.5(c)], indicating a small built-in potential is in agreement with the shape of *J*−*V* curves [Fig. 7.4(a)], which displays a rather symmetric behavior with minor rectification at *V* < 0.

(b) LSMO/LFO/BLSO

A similar protocol has been used to determine the band-alignment in LSMO/LFO/BLSO. As the LSMO/LFO interface is identical to that explored in LSMO/LFO/Pt heterostructures described above, only additional measurements have been done to deduce VBOs at the LFO/BLSO interface. With this aim a thick BLSO (40 nm) film and ultrathin LFO/BLSO(2nm, 3nm and 5 nm) films were measured. Several CLs were measured in BLSO (Ba*3d*, Sn*3d* and Ba*4d*) and LFO (Fe*2p* and Fe*3p*). Illustrative CLs for LFO/BLSO(3 nm) are shown in Fig. 7.6(c). Data for other BLSO thicknesses are in Supplementary information S7.5.4. The VBOs were calculated using Eq. [7.3] and are included in Table 7.1.

$$\Delta E_{VBM} = (E_{BLSO-CL} - E_{VBM})^{thick-BLSO} - (E_{LFO-CL} - E_{VBM})^{thick-LFO} - (E_{BLSO-CL} - E_{LFO-CL})^{interface} \quad [7.3]$$

The fact that the energy shift for all CLs lines is not constant for all CLs illustrates residual charging effects in the BLSO (3 nm) film grown on insulating LFO, which is negligible when evaluating the conducting LSMO/LFO/Pt interfaces. Indeed, charging effects are expected to be more evident when comparing CLs with a large difference in energies (for instance Fe*3p*-Ba*3d*) than for more reduced differences (Fe*3p*-Ba*4d*). Consequently, ΔE_{VBM} values in LFO/BLSO data in Table 7.1 are not averaged and ΔE_{VBM} (Fe3*p*-Ba*4d*) ≈ −2.17 eV is used for subsequent discussion. Charging is exacerbated in the thinnest BLSO film (2 nm, not shown) and reduced in the 5 nm film (Supplementary Information S7.5.4). The negative sign of ΔE_{VBM} ≈ −2.17 eV indicates that $(E_{VBM})_{BLSO}$ is below $(E_{VBM})_{LFO}$, as already anticipated from the affinity rule [$V_{bi,th}$(LFO/BLSO) ≈ − (1.5 + δ) eV, Fig. 7.5(b)]. On the other hand, the position of the valence-band maximum (VBM) in BSLO with respect to the Fermi level is found E_{VBM} ≈ −3.2 eV (Fig. S7.5.4), which is a good agreement with earlier reports [51,52] and the indirect gap determined from optical measurements.[40,41] Using these values, the experimentally determined band alignment is shown in Fig. 7.5(d), indicates $V_{bi,XPS}$ ≈ + 0.28 eV for LSMO/LFO/BLSO. These results confirm the presence of a built-in potential in the

LSMO/LFO/BLSO, of the same sign, slightly larger than in LSMO/LFO/Pt, that would induce a stronger rectification and higher conductance at $V < 0$ as observed in Fig. 7.4(c).

7.3.2. Photoresponse

(a) Wavelength dependence of the photocurrent

The *J-V* characteristics in dark and under illumination of LSMO/LFO (100 nm)/Pt heterostructures recorded using different wavelengths are shown in Fig. 7.7(a). One can observe the emergence of a short circuit photocurrent and the presence of an open circuit voltage, which are fingerprints of photovoltaic effect. As observed, J_{sc} largely increases when increasing the photon energy [left axis in Fig. 7.7(b)]. The abrupt increase of J_{sc} around 2.4 - 2.8 eV indicates that the bandgap of LFO is within this range, which is in excellent agreement with energy-dependent absorption coefficient [yellow line, right axis in Fig. 7.7(b)] as derived from optical transmission experiments (Supplementary information S7.2) and literature data.
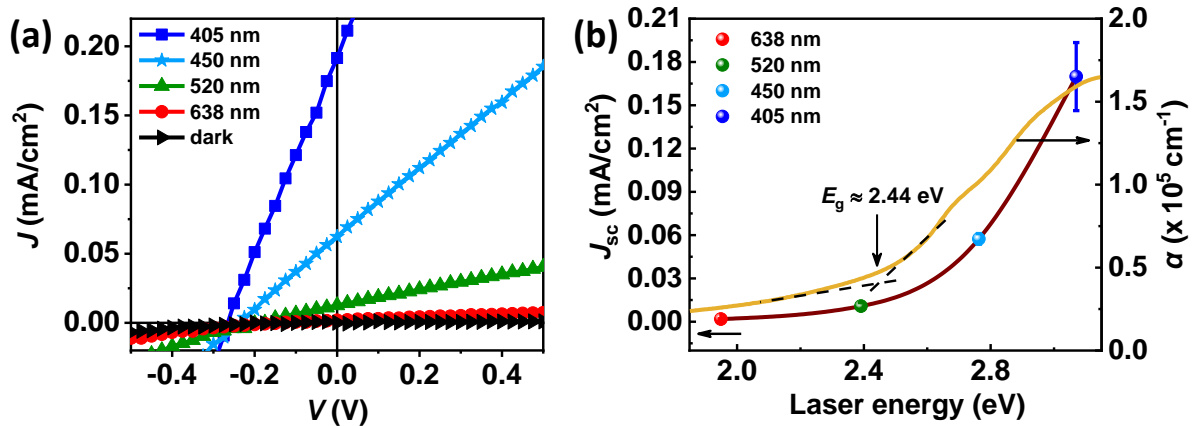
Fig. 7.7. (a) Photocurrent of LSMO/LFO(100 nm)/Pt measured in dark and using 0.55 W/cm² lasers of different wavelength as indicated. (b) Dependence of the short-circuit photocurrent (left) and absorption coefficient α (right) on photon energy. Error bar indicates the spread of values recorded in various electrodes (up to 6) of the same diameter.

(b) Photoresponse of LSMO/LFO/Pt and LSMO/LFO/BLSO

The photoresponse recorded using 405 nm laser of LSMO/LFO/Pt and LSMO/LFO/LBSO heterostructures of different thickness of the LFO photoabsorber (50 nm, 100 nm and 200

nm) are shown in Figs. 7.8(a-c) and Figs. 7.8(d-f), respectively. The thickness dependence of V_{oc} and J_{sc} are summarized in Figs. 7.9(a,b), respectively. We first notice in Figs. 7.8(a-f) and in Figs. 7.9(a,b) that, irrespectively on the thickness of LFO, J_{sc} and V_{oc} remain the sign ($J_{sc} > 0$, $V_{oc} < 0$) for both electrodes, and the V_{oc} is definitely larger for BLSO than Pt. These observations are fully consistent with the VBOs derived from XPS data [Figs. 7.5(c, d)]. That is, the positive $V_{bi,XPS}$ values in both LSMO/LFO/Pt and LSMO/LFO/BLSO means a built-in field pointing downwards from top electrode to bottom electrode, thus the photocurrent should flow downwards and be measured as positive value. V_{oc} is essentially, the voltage required to cancel the net current flowing in the circuit (open circuit voltage) and therefore it should have a sign opposite to V_{bi}. Therefore, as we determined $V_{bi} > 0$ for both devices, V_{oc} should also be negative, which is in agreement with experimental data (Fig. 7.8) as observed.
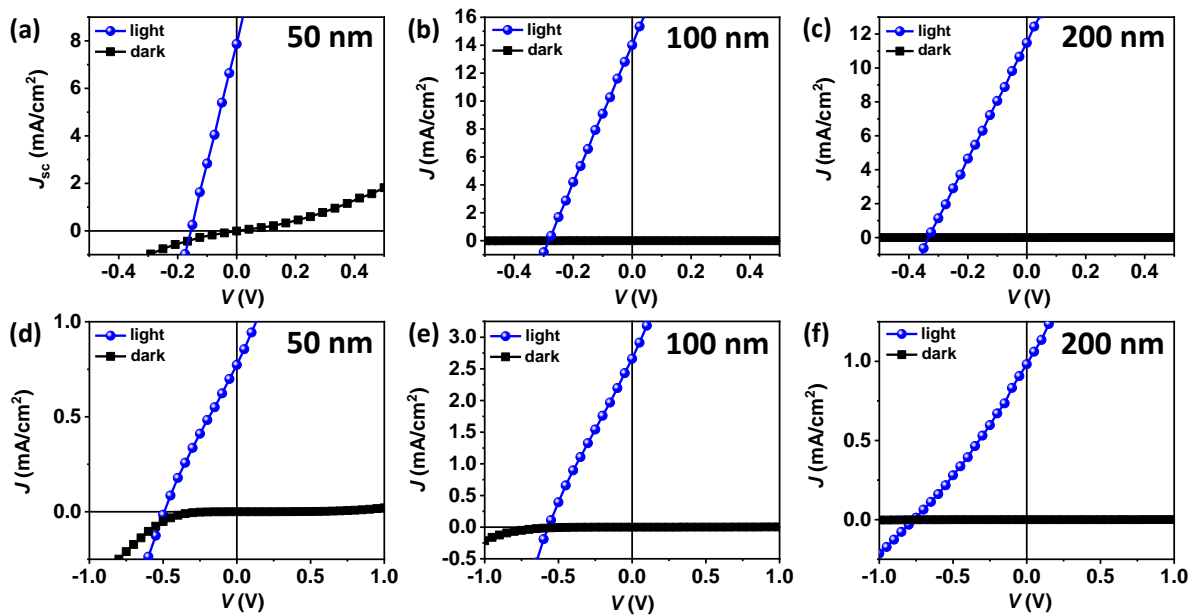

Fig. 7.8. *J-V* characteristics recorded in dark and under illumination on: (a-c) LSMO/LFO/Pt and (d-f) LSMO/LFO/BLSMO where (a,d) t_{LFO} = 50 nm, (b,e) t_{LFO} = 100 nm, and (c,f) t_{LFO} = 200 nm respectively.

From Fig. 7.5(c, d) it should be expected that V_{oc} values are roughly given by:[53]

V_{oc}(LSMO/LFO/Pt) ≈ V_{bi}(LSMO/LFO) − V_{bi}(LFO/Pt)

[7.4]

V_{oc}(LSMO/LFO/BLSO) ≈ V_{bi}(LSMO/LFO) − [E_{VBM} − V_{bi}(LFO/BLSO)]

[7.5]

where E_{VBM} is the measured VBM energy of BLSO (≈ −3.2 eV, Fig. S7.5.4) referred to the Fermi level, and using the experimentally determined band alignment values V_{bi}(LSMO/LFO) ≈ −0.75 eV, V_{bi}(LFO/Pt) ≈ 0.86 eV and V_{bi}(LFO/BLSO) = −2.17 eV, we deduce V_{oc}(LSMO/LFO/Pt) = −0.11 eV and V_{oc}(LSMO/LFO/BLSO) = −0.28 eV. The measured [Fig. 7.9(a)] and the predicted V_{oc} values (eq. [7.4,7.5]) [dashed lines in Fig. 7.9(a)] reveal some discrepancies, most noticeable for BLSO. They may have different sources. Most obvious is that V_{oc} has been measured from photoresponse in LSMO/LFO/Pt and LSMO/LFO/BLSO devices where the active LFO layer and top electrodes have radically different thickness than those used for XPS, and therefore the determined VBO and E_{VBM} may not represent accurately enough the actual values in the devices. On the other hand, as mentioned, residual charging effects in LFO/BLSO band alignment derivation (Table 7.1) may still be present and lead to a spuriously large ΔE_{VBM} (≈ −2.17 eV) that leads to an underestimation of the V_{oc} (Eq. [7.5]). On the other hand, in the derivation of the band alignment from XPS data, we have omitted a possible role of a photovoltage induced by the X-ray beam, as documented in some metal/semiconductor heterostructures, that may contribute to the measured V_{bi}.[42]
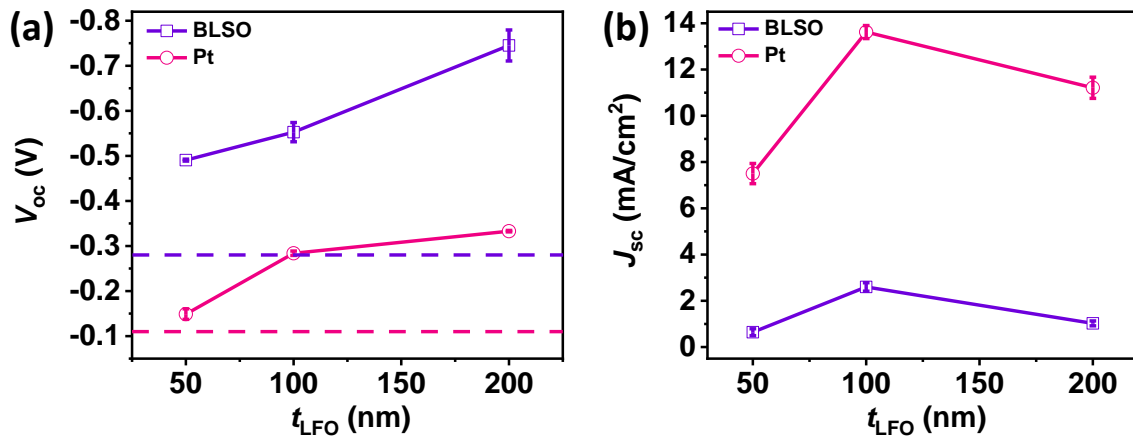

Fig. 7.9. Dependence of the (a) V_{oc} and (b) J_{sc} in LSMO/LFO/Pt (red circles) and LSMO/LFO/BLSO (purple squares), as a function of the thickness of LFO (t_{LFO}). The red (LSMO/LFO/Pt) and purple (LSMO/LFO/BLSO) dashed lines in (a) indicate corresponding the predicted V_{oc} as estimate from built-in voltages deduced from XPS data.

On the other hand, in XPS band alignment experiments, ultrathin LFO layers (1, 3, 5 nm) have been used. These ultrathin epitaxial films can be safely assumed to be homogeneous strained and thus any flexoelectric contribution to the internal field should be null and not contributing to the band alignment. In contrast, the photoresponse was measured in thicker LFO films (50, 100, 200 nm) where X-ray diffraction and STEM data confirmed the presence of various possible sources of strain gradients. Moreover, the strain gradients may generate a potential of the same direction with V_{bi} and contribute to the measured V_{oc}. The sign agreement between the relative VBOs values derived from XPS and V_{oc} obtained from *J-V* indicates that band alignment in LSMO/LFO/Pt and LSMO/LFO/BLSO is dictated by intrinsic electronic effects rather by flexoelectric fields (maybe affected by flexoelectric fields).

Data in [Fig. 7.9(b)] indicates that irrespectively on the top electrode, initially J_{sc} increases with t_{LFO} until reaching maxima at $t_{LFO} \approx 100$ nm: J_{sc}(Pt) ≈ 14 mA/cm^2 and J_{sc}(BLSO) ≈ 2.6 mA/cm^2. From Fig. 7.7(b), the absorption coefficient at 405 nm laser is $\alpha \approx 16$ μm^{-1} thus the light attenuates to ≈ 20 % in 100 nm light path. Accordingly, this initial increase of J_{sc} with t_{LFO} is attributed to the photoabsorption in LFO that itself increases with t_{LFO} until saturation. A further increase of t_{LFO} shall lead to a decrease to J_{sc} due to charge recombination within LFO, as observed. Data also indicates that J_{SC} is definitely larger when using Pt electrodes than when using BSLO. This difference, which cannot be accounted for by the different optical transparency of the electrodes (Pt is semitransparent but BLSO is virtually transparent at visible light), suggest that electron-hole recombination at LFO/BLSO interface is larger than at LFO/Pt interface, precluding efficient charge extraction in the former. The high temperature growth of BLSO on top LFO compared to the room-temperature growth of Pt, can easily explain this difference.

Finally, it is observed in Fig. 7.9(a) that, V_{oc} systematically increases with t_{LFO}. While some increase of V_{oc} with t_{LFO} is expected as in diode-like solar cells by $V_{oc} \approx$ Ln(J_{sc}),[54] the absence of saturation in $V_{oc}(t_{LFO})$ suggests other contributions to V_{oc} that we shall comment in the following.

7.4. Discussions and Conclusions

It has been shown here that the photovoltaic response of LFO films of different thickness (50 nm, 100 nm and 200 nm) grown on well matched and identical substrates (LSAT) and bottom electrodes (LSMO), largely differs depending on the top electrode used (here, Pt and BLSO). Band alignment measurements strongly indicate that the V_{oc} is directly related to the built-in voltage at the top LFO/Pt and LFO/BLSO interfaces, that already manifests in the measured *J-V* curves in dark. Consistent with built-in potential profiles, BLSO electrodes establish larger built-in potential. In contrast, they lead to a relatively smaller J_{sc} that we plausibly attribute to unavoidable chemical interdiffusion at LFO/BLSO interface occurring during the high temperature growth which is absent in room-temperature grown LFO/Pt interface. On the other hand, the growth of LaFeO₃ (orthorhombic in bulk) thin films on cubic substrates leads to a complex microstructure where crystallites of different texture and strain state coexist and which relative abundance depends on thickness. Despite the minor epitaxial mismatch of LFO films grown on LSAT substrates (< 0.2 %) epitaxial strain and strain relaxation is observed.

However, available data does not suggest any relevant impact of epitaxial strain gradients on the relative values of J_{sc}(LFO/Pt) and J_{sc}(LFO/BLSO) nor on the relative values of V_{oc}(LFO/Pt) and V_{oc}(LFO/BLSO) as microstructure of the underlying LFO is virtually identical. However, strain gradients may affect the absolute measured values V_{bi}(LFO/Pt) and V_{bi}(LFO/BLSO), as these data were collected using ultrathin LFO films whereas photoresponse was determined using thicker films where the presence of flexoelectric voltages cannot be excluded. In any event, it is remarkable that the measured J_{sc} value for LSMO/LFO(100)/Pt device [J_{sc}(Pt) ≈ 14 mA/cm²] corresponds to a responsivity *R* (≈ J_{sc}/I_p) of 2.6 x 10⁻⁴ A/W. This responsivity value is larger than reported for thinner LFO films on LaAlO₃ substrates, where epitaxial strain and inhomogeneous strain relaxation were claimed to assist band-bending and charge extraction via flexoelectric fields.[13] The excellent room-temperature responsivity of LSMO/LFO/Pt heterostructures reported here, even larger than in the celebrated BiFeO₃ (*R* = 1.5 x 10⁻⁴ A/W[55] and comparable to the responsivity of BiFeO3 recorded at high temperature (66.1 °C),[56] suggesting that there is room for improvement and potential in application. Interestingly, the coexistence of differently textured crystallites in the LFO thin film does not appear to be detrimental but on the contrary, they may be to

boost responsivity. Although at first sight counterintuitive, similar behavior has been documented in CdTe solar cells and other materials.[57,58] In this scenario, even higher responsivity could be obtained if film microstructure and strain gradients can be engineered and combined with appropriate electrode and substrate selection.

Supplementary information

S7.1. Growth of LaFeO₃ single layers.

Bulk LaFeO₃ (LFO) has an orthorhombic perovskite structure with a = 5.5544 Å, b = 5.5659 Å and c = 7.8534 Å (ICDD Powder Diffraction File 04-011-7994), corresponding to pseudocubic unit cell with a_{LFO} ≈ 3.92998 Å. Nb-doped (5%) STO (001) substrates (Nb:STO) are cubic with a_S = 3.905Å. Therefore, a compressive mismatch $f = [a_S-a_{LFO}]/a_S$ = −0.64 % exist with LFO. We used a laser fluence of ≈ 2 Jcm⁻² and frequency of 5 Hz and the number of laser pulses were adjusted to the required thickness after proper calibration. We used a deposition temperature of 700 °C and an oxygen pressure of PO_2 = 0.01 mbar. In these conditions, the growth rate is about ≈ 0.14 Å/pulse.

An example of the X-ray reflectivity and narrow θ-2θ region of a film of 2500 pulses is shown below (Fig. S7.1.1), where the reflectivity intensity oscillations and the Laue fringes are well visible evidencing the film quality.
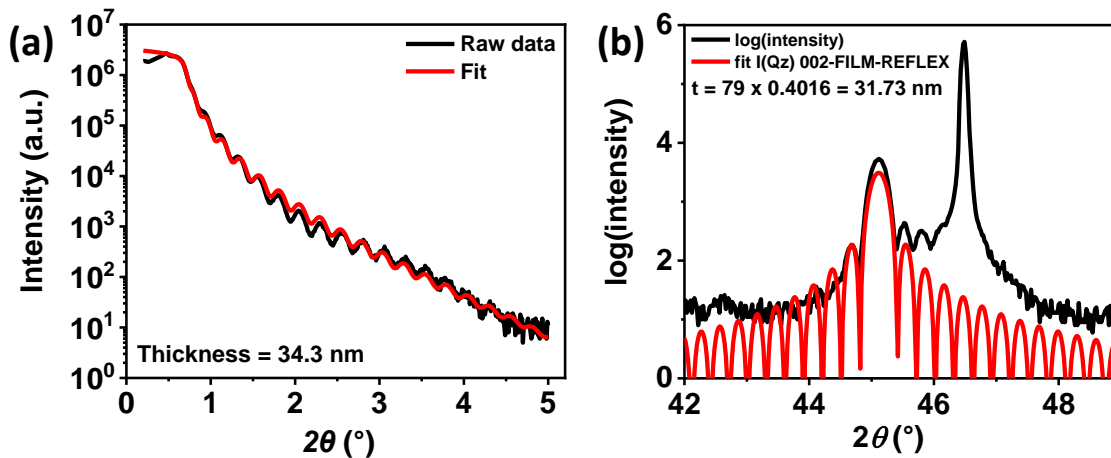
Fig. S7.1.1. (a) X-ray reflectivity scan of a Nb:STO//LFO film. Raw data were fitted using GenX software,[59] and the thickness is 34.3 nm. (b) Fitting of the Laue fringes of the (002) reflection of the same sample. The extracted thickness is 31.7 nm.

A broader angular range XRD θ-2θ scan is shown in Fig. S7.1.2. All (00*l*) reflections (*l* = 1,2,3,4) of film and substrate are well visible.[3] The out-of-plane parameter of LFO deduced from this plot is (c ≈ 4.016 Å), which is larger than that expected from bulk LFO (pseudo tetragonal cell parameters are c ≈ 3.9267 Å and a ≈ 3.9316 Å. From the 2θ-χ scans [Fig.

S7.1.2(c)], no spurious phase was detected and well-defined LFO round spots were observed next to the substrate reflections. The RSM recorded with GADDS diffractometer suggests that the film is in-plane strained films [Fig. S7.1.2(c)], coherent with the observed *c*-axis elongation of LFO, that we attribute to volume conservation.
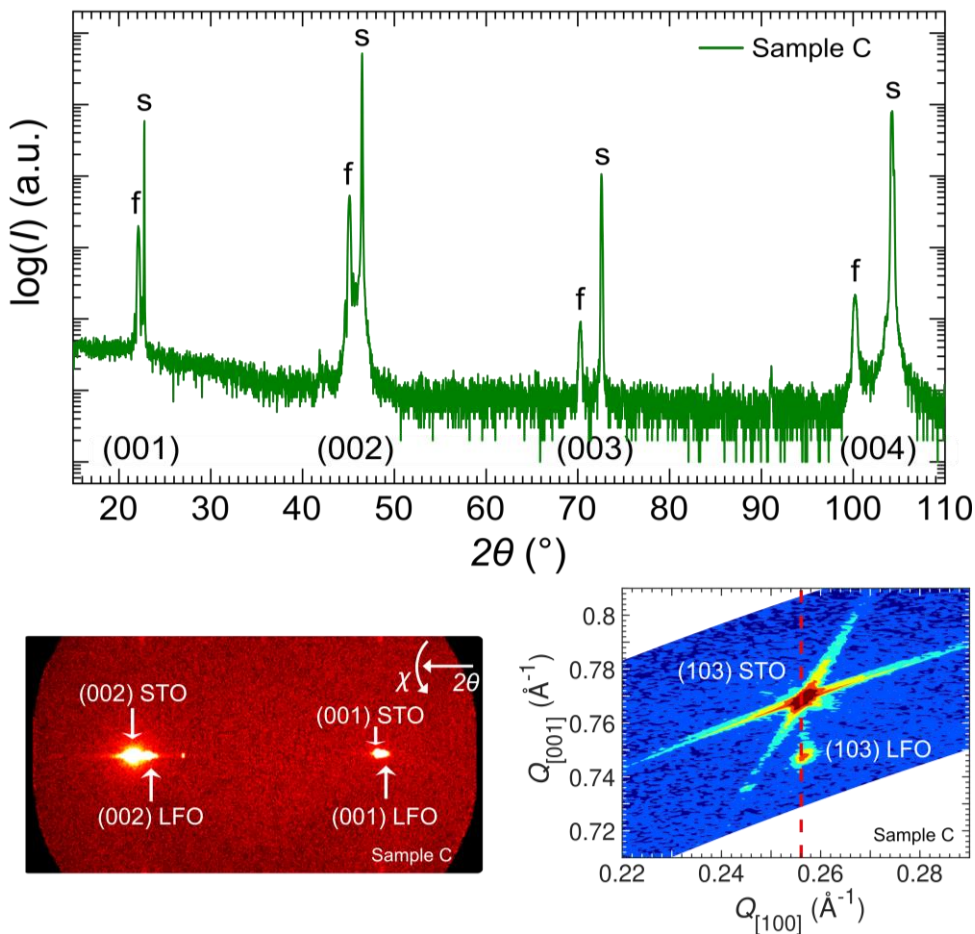
Fig. S7.1.2. XRD measurements performed on Nb:STO//LFO (Nb:STO//LFO (≈ 35 nm) films. (a) θ-2θ scan. (b) 2θ-χ scan and (c) RSM around the (103) reflection.

The surface morphology was measured by AFM (see Fig. S7.1.3). One can observe a very flat surface with low roughness of RMS ≈ 2.8 Å (≈ 1 uc).
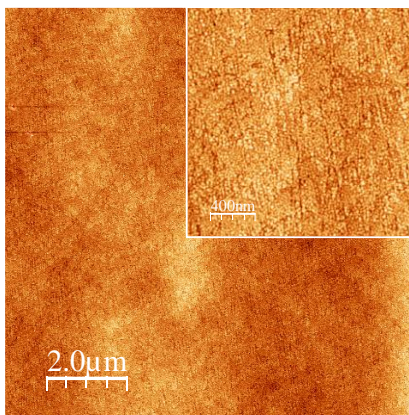
Fig. S7.1.3. AFM topographic image of the surface of Nb:STO//LFO.

S7.2. Optical properties of LFO single layers.

The optical properties of LFO films were investigated by spectroscopic ellipsometry. In Fig. S7.3(a), we show illustrative extracted (n, k) of the Nb:STO//LFO film. From its extinction coefficient k, we have plotted in Fig. S7.2(b) the absorption coefficient α (defined as α = $4\pi k/\lambda$). One can observe an onset of absorption at ≈ 2.5 eV. From the Tauc plots [Fig. S7.2(c)], we have determined an indirect bandgap of ≈ 2.4 eV, with an extrapolated α = 0 crossing at about 2.0 eV, and a direct bandgap of ≈ 2.6 eV. Both values are in good agreement with earlier reports, either LFO films[4,5,60] and polycrystalline samples.[61,62]
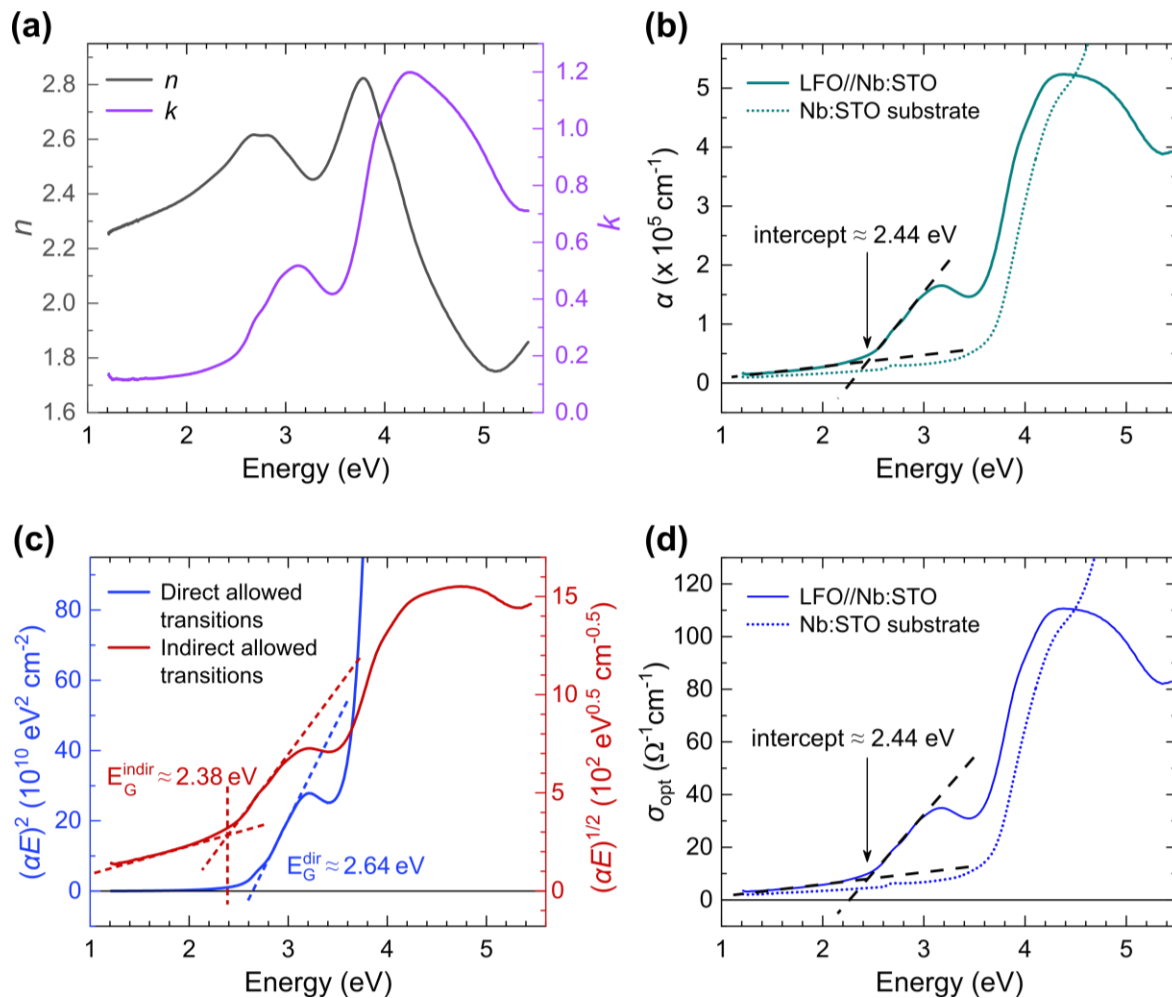
Fig. S7.2. Optical properties of an illustrative LFO film. (a) Optical constants (refractive index n and extinction coefficient k). (b) Absorption coefficient α. (c) Tauc plots for direct and indirect transitions. (d) Optical conductivity σ_{opt}.

S7.3. Structural data on LSAT//LSMO/LFO/Pt and LSAT//LSMO/LFO/BLSO heterostructures

The evolution of the cell parameters of the different LFO crystallites contributing to the RSM in Fig. 7.1, in LSAT//LSMO/LFO/Pt as a function of LFO thickness are shown below.
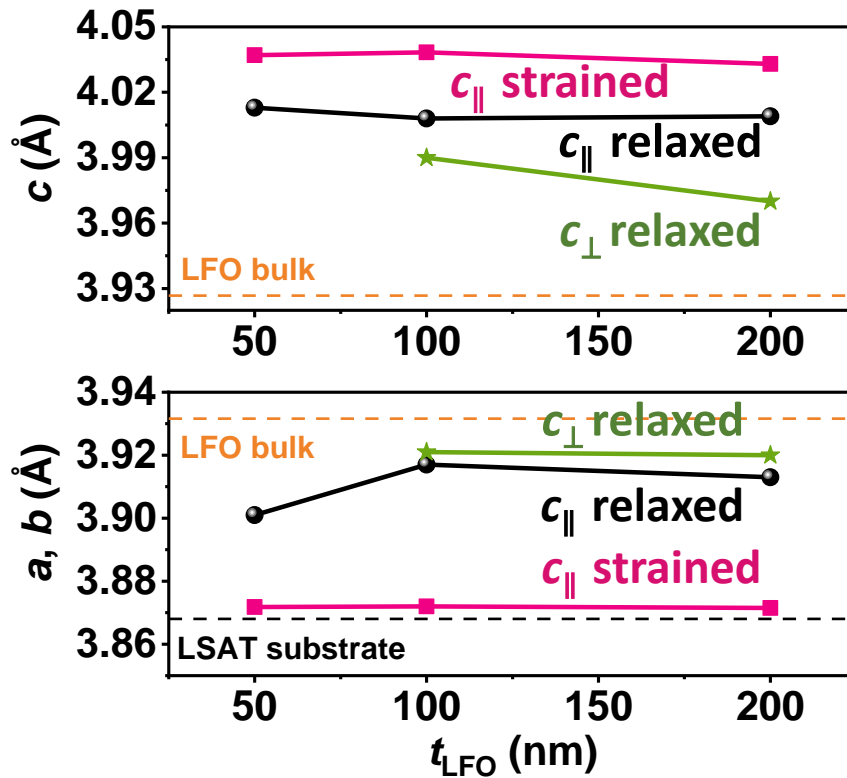
Fig. S7.3.1. Evolution of cell parameters of LFO in LSAT//LSMO/LFO/Pt with thickness. Each symbol corresponds to a particular type of domain (fully strained, relaxed $c_\parallel$, and relaxed $c_\perp$), as indicated.

The RSM of the LSAT//LSMO/LFO/BLSO samples are shown in Fig. S7.3.2. Comparison with the corresponding data of LSAT//LSMO/LFO/Pt (Fig. 7.1), shows that the growth of the top BLSO electrode has not modified at all the microstructure of the LFO films compared to LSAT//LSMO/LFO/Pt. An identical coexistence of strained and relaxed $c_{\parallel}$ and $c_{\perp}$ crystallites can be observed.
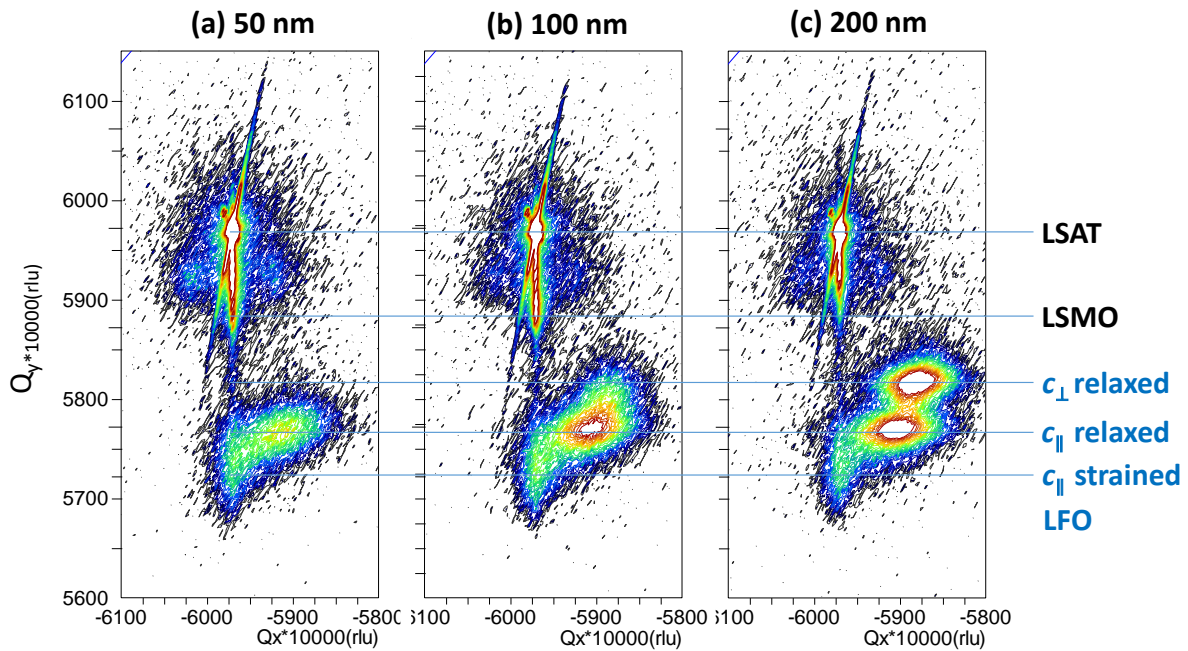
Fig. S7.3.2 (a, b, c) Reciprocal space maps around the (-303) reflection of LSAT of LSAT//LSMO/LFO/BLSO heterostructures having t_{LFO} = 50 nm, 100 nm and 200 nm, respectively. Horizontal lines indicate out-of-plane position of the diffracting planes of LSAT, LSMO and the position of the observed fully strained and relaxed $c_{\parallel}$ crystallites and relaxed $c_{\perp}$ ones, of LFO.

S7.4: Survey XPS spectra and charging effects

In Fig. S7.4 below we show survey spectra of thick LSMO, LFO and BLSO films.
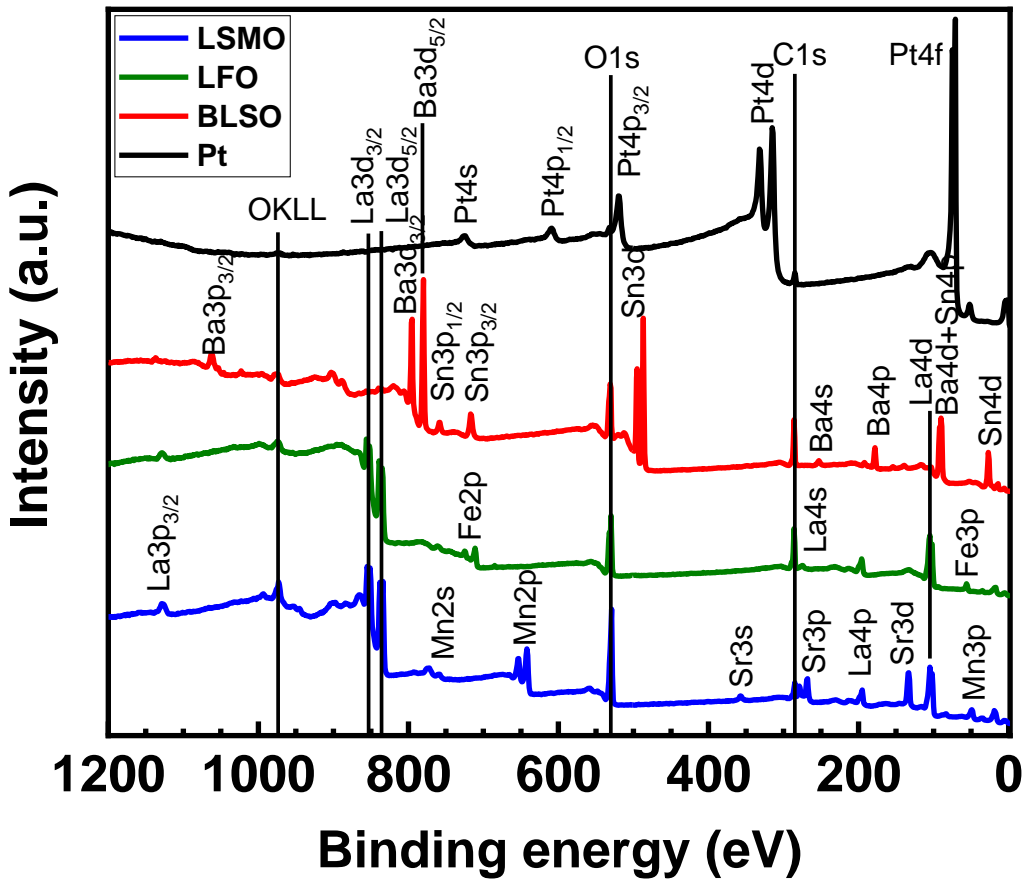
Fig. S7.4. Survey XPS spectra of LSMO (blue), LFO (olive), BLSO (red) and Pt (black) films. The main XPS and Auger lines are identified in the spectra. Spectra have been shifted for clarity.

S7.5: Valence band offset (VBO) measured by X-ray photoelectron spectroscopy

In Fig. S7.5.1 below, we illustratively show the different CLs used to evaluate VBO at LSMO/LFO interface.
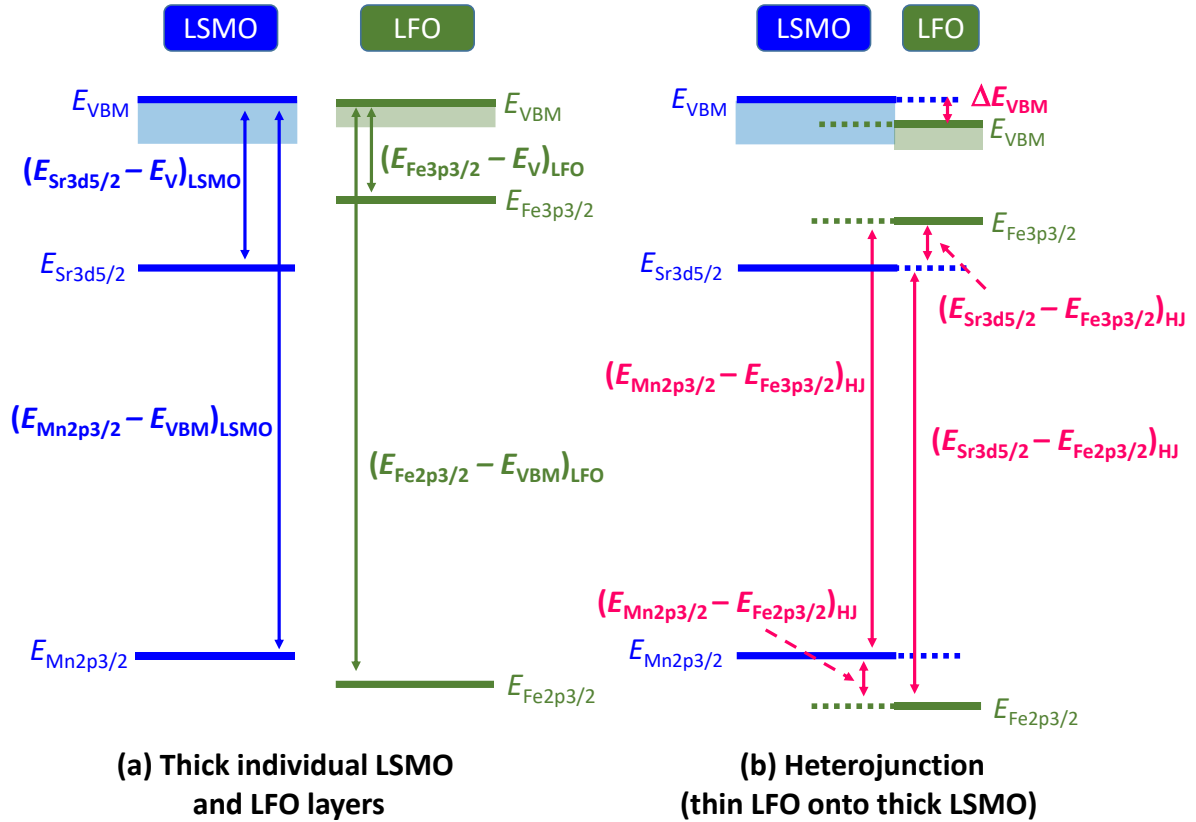
Fig. S7.5.1: Sketch illustrating the core levels and valence band measured by XPS, in: (a) LSMO and LFO thick single layers, and (b) LSMO/LFO interface. The formula above illustrates how the valence band offset is calculated.

$$\Delta E_{\text{VBM}} = (E_{\text{LFO–CL}} - E_{\text{VBM}})^{\text{thick–LFO}} - (E_{\text{LSMO–CL}} - E_{\text{VBM}})^{\text{thick–LSMO}} - (E_{\text{LFO–CL}} - E_{\text{LSMO–CL}})^{\text{interface}}$$

LSMO/LFO	Fe2p-Mn2p	Fe2p-Sr3d	Fe3p-Mn2p	**Fe3p-Sr3d**	Average ± STDEV
1 nm LFO	-1.0	-0.96	-0.94	**-0.90**	-0.95±0.04
3 nm LFO	-0.70	-0.72	-0.77	**-0.79**	-0.75±0.04
5 nm LFO	X	-0.80	X	**-0.85**	-0.83±0.04

LFO/Pt	Pt4f-La3d	Pt4f-Fe2p	**Pt4f-La4d**	Average ± STDEV
1 nm Pt	0.44	0.60	**0.64**	0.56±0.11
2 nm Pt	0.81	1.29	**1.05**	1.05±0.24
3 nm Pt	0.89	X	**0.82**	0.86±0.05

LFO/BLSO	Fe3p-Ba3d	Fe3p-Sn3d	**Fe3p-Ba4d**	Average ± STDEV
3 nm BLSO	-2.50	-2.45	**-2.17**	XX
5 nm BLSO	-2.34	-2.37	**-2.19**	XX

Table S7.5. Summary of VBOs measured at the LSMO/LFO, LFO/Pt and LFO/BLSO interfaces as a function of LFO, Pt and BLSO coverages. The VBOs are extracted from each pair of CLs, indicated by the corresponding column headings. Bold data correspond to spectra shown in Figs. S7.5.2-S7.5.4. Last column gives the average values. "X" symbol indicates that a CL line is not perceptible in the XPS spectrum. "XX" symbol indicates that average is not appropriate as charging effects are perceptible in the data. The units of energies are eV.
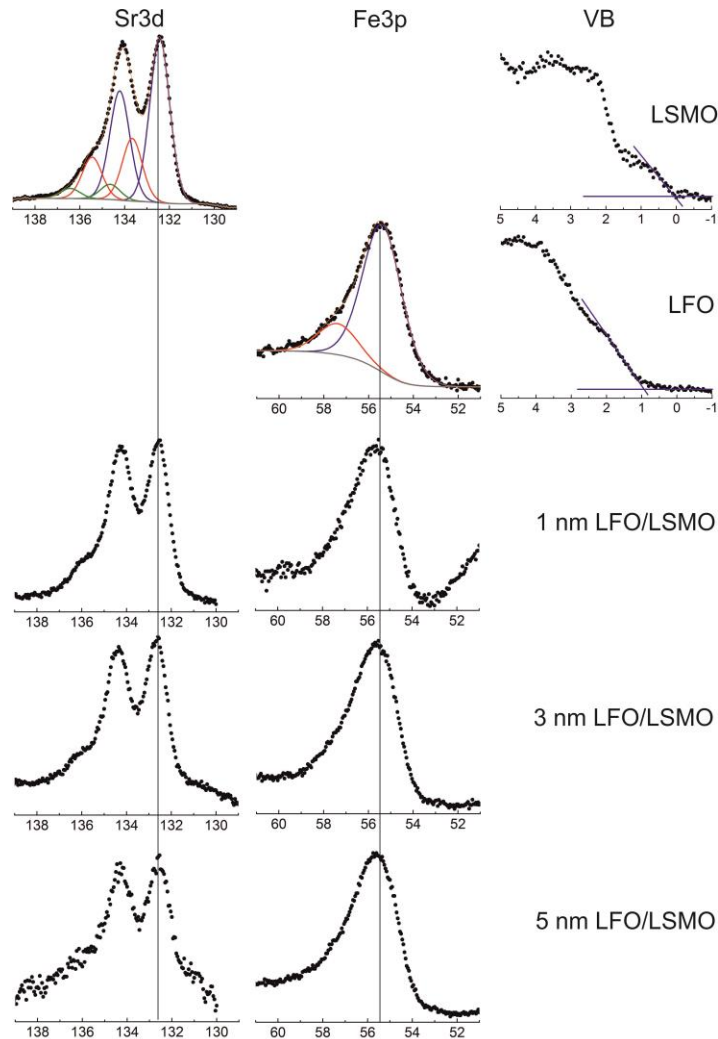
Fig. S7.5.2. High-resolution XPS Sr3d and Fe3p core level and valence band spectra corresponding to LSMO and LFO films and to LFO/LSMO heterostructures for different LFO thickness (1 nm, 3 nm and 5 nm). The energies are referred to the Fermi level of the analyzer. The valence band maxima for the LSMO and LFO films are obtained by a linear extrapolation (blue straight lines) of the leading edges in the valence band spectra. Least-squares fits of the Sr3d and Fe3p lines using a Shirley-type background subtraction and a combination of Gaussian and Lorentzian functions are shown for the LSMO and LFO films. In the case of the Sr3d lines the $3d_{3/2}/3d_{5/2}$ branching ratio is fixed to 2/3. The Sr3d line shows three doublets with binding energies of the $Sr3d_{5/2}$ lines of 132.43 eV (blue), 133.66 eV (red) and 134.64 eV (olive). The $3d_{5/2}$-$3d_{3/2}$ spin orbit splitting is 1.79 eV and the full width at half maximum (FWHM) for all components is 1.05 eV. The 132.43 eV component corresponds to lattice Sr in LSMO while the 133.66 and 134.64 eV lines has been assigned to the presence of carbonates and oxidized Sr.[63] The deconvolution of the Fe3p line gives two

lines at 55.39 eV (blue) and 57.38 eV (red) with a common FWHM of 2.06 eV. The 55.39 eV feature corresponds to lattice Fe in LFO. The line observed at 57.38 eV line could be attributed to contamination-related Fe-derivatives (e.g.; $Fe_2(SO_4)_3$).[64] The continuous vertical lines are guides to the eye.


Fig. S7.5.3. High-resolution XPS La4d and Pt4f core level and valence band spectra corresponding to LFO and Pt films and to LFO/Pt heterostructures with different Pt thickness (1 nm, 2 nm and 3 nm). The energies are referred to the Fermi level of the analyzer. The valence band maxima for the LFO film are obtained by a linear extrapolation (blue straight lines) of the leading edge in the valence band spectra (as in Fig. S7.5.2) and for the Pt film the energy is referred to the Fermi level. Least-squares fits of the La4d and Pt4f lines using a Shirley-type background subtraction are shown

for the LFO and Pt films. In the case of the La4d lines the 4d$_{3/2}$/4d$_{5/2}$ branching ratio is fixed to 2/3. The La4d line shows three doublets with binding energies of the La4d$_{5/2}$ lines of 101.76 eV (blue), 103.83 eV (red) and 105.61 eV (olive). The 4d$_{5/2}$-4d$_{3/2}$ spin orbit splitting is 3.04 eV and the full width at half maximum (FWHM) for all components is 1.89 eV. The 101.76 eV feature corresponds to lattice La in the ground state and the 103.83 eV and 105.61 eV components represent the associated final-state satellites.[65] The deconvolution of the Pt4f line gives a doublet at 70.85 eV (4f$_{7/2}$) and 73.93 eV (4f$_{5/2}$) with a common FWHM of 1.02 eV using a Gelius-type asymmetric line shape. The continuous vertical lines are guides to the eye.
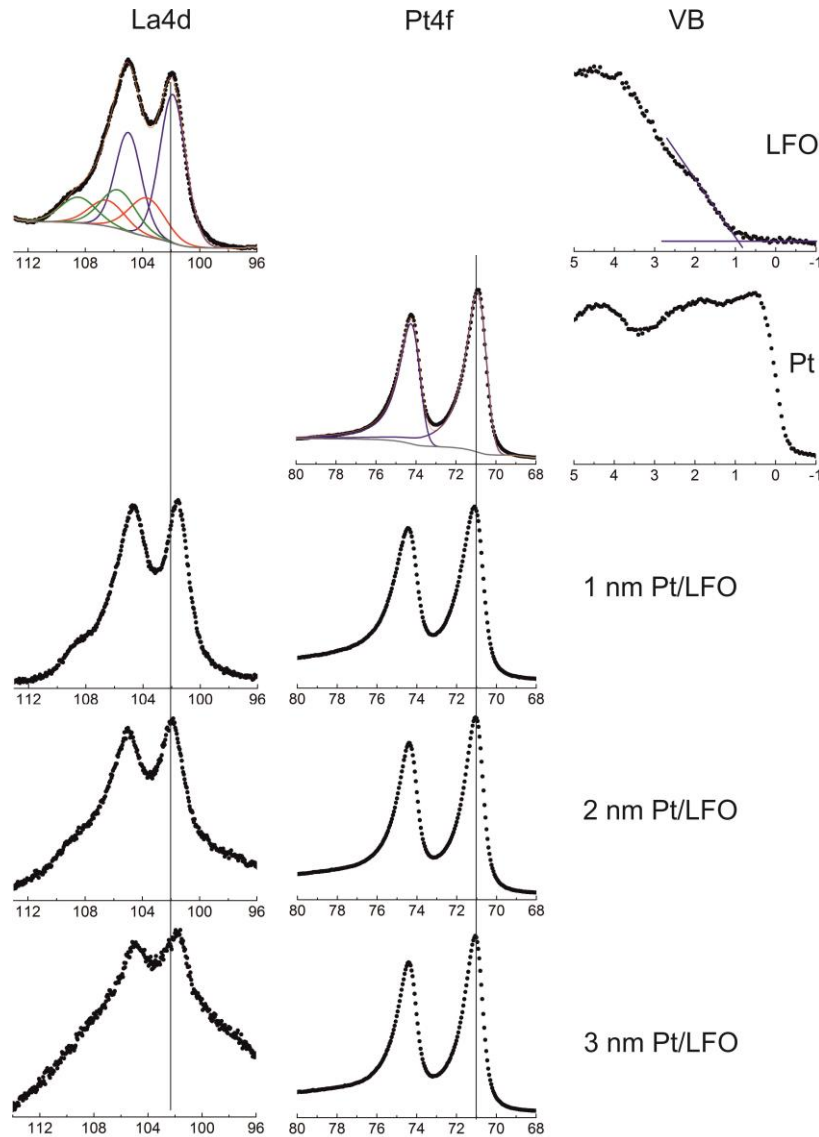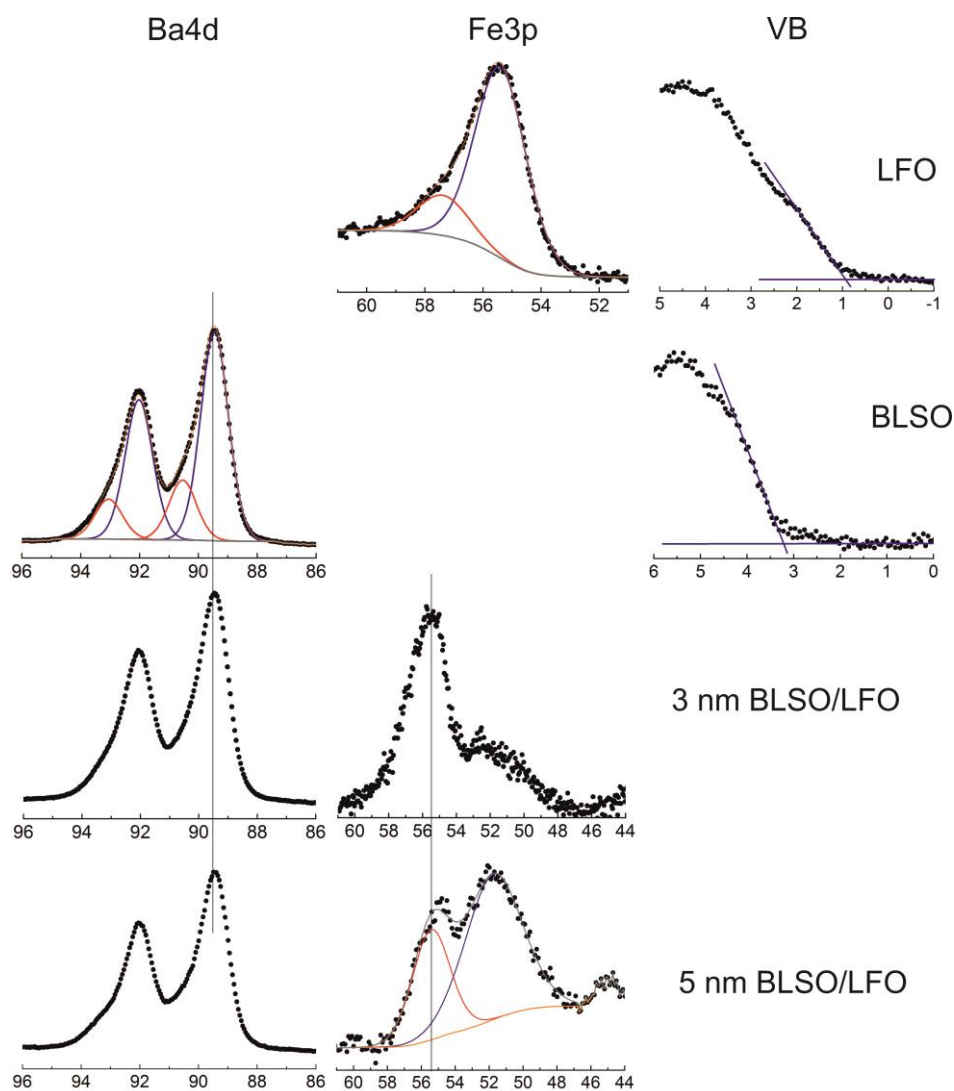

Fig. S7.5.4. High-resolution XPS Ba4d and Fe3p core level and valence band spectra corresponding to BLSO and LFO films and to LFO/BLSO heterostructures with different BLSO thickness (3 nm and 5 nm). The energies are referred to the Fermi level of the analyzer. The valence band maxima for

the BLSO and LFO films are obtained by a linear extrapolation (blue lines) of the leading edges in the valence band spectra. Least-squares fits of the Ba4d and Fe3p lines using a Shirley-type background subtraction and a combination of Gaussian and Lorentzian functions are shown for the BLSO and LFO films. In the case of the Ba4d lines the $4d_{3/2}/4d_{5/2}$ ratio is fixed to 2/3. The Ba4d line shows two doublets with binding energies of the Ba4d$_{5/2}$ lines of 89.45 eV (blue) and 90.52 eV (red). The position of the lower binding energy of the doublet is made to coincide for 3 nm and 5 nm films with that of the thick and metallic BLSO. The $4d_{5/2}$-$4d_{3/2}$ spin orbit splitting is 2.57 eV and the full width at half maximum (FWHM) for all components is 1.11 eV. The more intense 89.45 eV feature corresponds to lattice Ba while the 90.52 eV feature has been assigned to barium oxide, hydroxide and/or carbonate upon exposure to air.[40] The deconvolution of the Fe3p line for the LFO film gives two lines at 55.39 eV (blue) and 57.38 eV (red) with a common FWHM of 2.06 eV (see Fig. S7.5.3). The position of the Fe3p line for the 5 nm film is indicated by the red component of the corresponding fit.

S7.6. Transmission electron microscopy
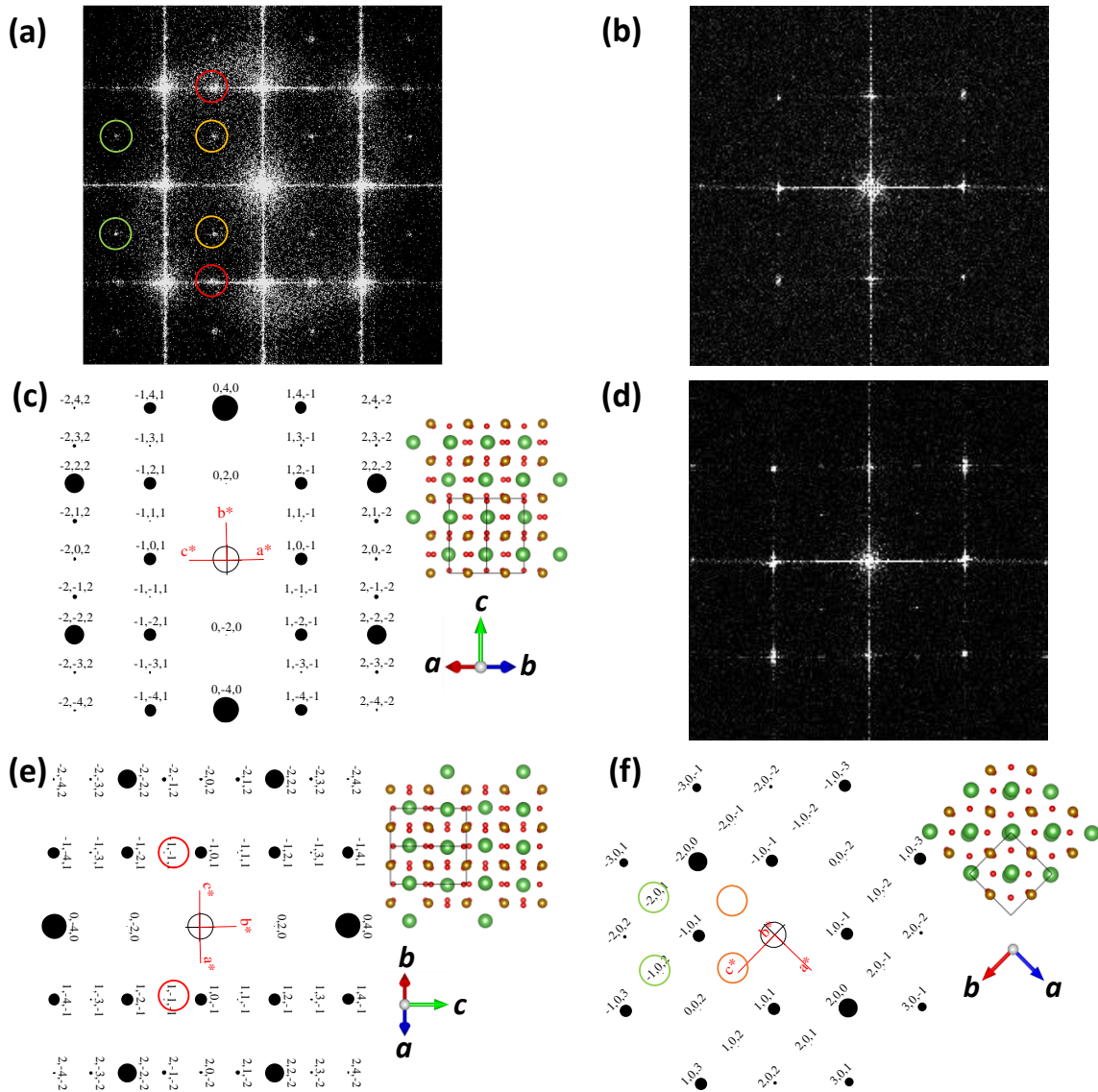
Fig. S7.6.1. (a) Fourier Transform (FT) obtained from a high resolution HAADF-STEM image of the LSAT//LSMO(27 nm)/LFO(100nm) heterostructure. The circles mark different diffraction spots of the FT that belongs to different crystallographic domains. (b) FT that belongs to a LFO column grown along the *c*-axis perpendicular to the interface. (c) Simulated diffraction pattern obtained along the [-1-10] zone axis, this is, with *c*-axis perpendicular to the LFO/LSMO interface. The inset shows the structure viewed along this zone axis. (d) FT that belongs to LFO columns grown with the *c*-axis parallel to the interface, either parallel or perpendicular to the plane of the image, as depicted in (e) and (f), respectively, which show two simulated diffraction patterns. The insets show the structure viewed along these crystallographic directions. The circles in (e) and (f) mark

those diffraction spots signalled in (a). Notice that the spots marked with red circles would correspond to forbidden reflections in X-Ray but that may be allowed in a FT. These features in FT's allowed us to distinguish between crystallographic domains found in LFO films. Notice that the b^* and c^* axes in the simulated diffraction patterns are switched as they are differently defined in the file used to generate them.
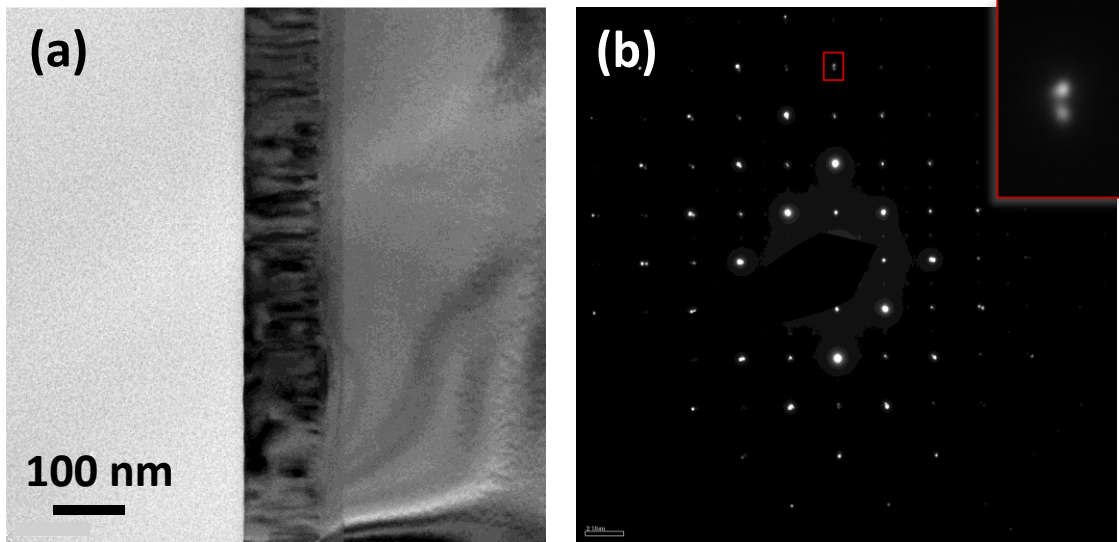
Fig. S7.6.2. (a) and (b) show a TEM image and its corresponding diffraction pattern of a LSAT//LSMO(27 nm)/LFO(100nm) heterostructure, respectively. There is no rotation between the TEM images and the diffraction patterns. The diffraction pattern shown in (b) presents splitting of several diffraction spots, which would be indicate the presence of a relaxed LFO film, as observed in RSM. The inset shows a zoom of the in-plane spot marked in red.

S7.7. Bulk limited transport across LSMO/LFO((Pt, BLSO) heterostructures

S7.7.1. A back-to-back Schottky model for the LaFeO₃-based device

As shown in Fig. S7.7.1 the structure of the device (Metal-Semiconductor-Metal, M-S-M), the semiconductor with Schottky barriers (SBs) at both metal/semiconductor interfaces can be modeled with two Schottky diodes connected back-to-back separated by a series resistance R_i, where the reverse saturation current of the reverse-biased diode plays a crucial role in the electrical transport behavior.[24,25]
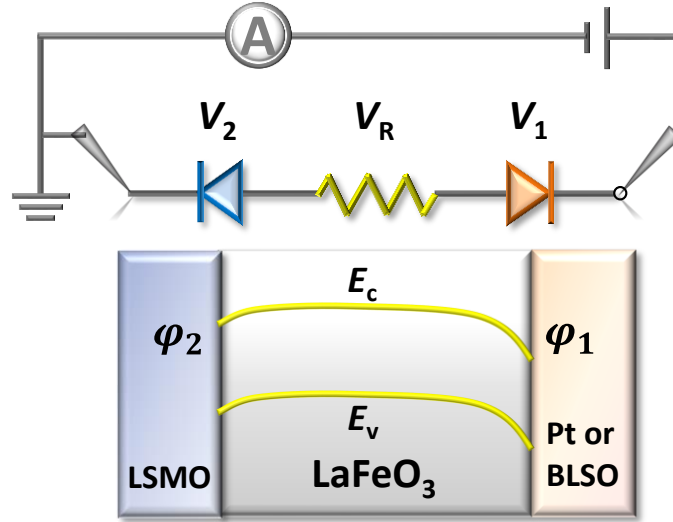
Fig. S7.7.1. A back-to-back Schottky diode model for two-terminal semiconducting device with an inner series resistance R. It shows the schematic diagram of the M-S-M structure and its equivalent circuit. The band diagram shows the bending of the bands at the metal-semiconductor interfaces, Φ_1 and Φ_2 denote the corresponding Schottky barrier heights.

Based on thermionic emission theory, the current at the two contacts of a metal and a *p*-type semiconductor can be written as:[66]

$$I_1 = -I_{A1}\left[\exp\left(-\frac{qV_1}{kT}\right) - 1\right]$$

$$I_2 = I_{A2}\left[\exp\left(\frac{qV_2}{kT}\right) - 1\right]$$

where

$$I_{A1,A2}(V) = A_{1,2}A^*T^2\exp\left(-\frac{\phi_{1,2}}{kT}\right)$$

are the reverse saturation currents, *A** is the Richardson constant (we use the value of a free electron in this text), *T* is the temperature, *k* is the Boltzmann constant, and $A_{1,2}$ are the areas of the contacts. While there can be various effects (defects, inadvertent oxide layers, etc.) that makes the SB height dependent on the applied voltage and causes deviation from the ideal thermionic emission, an ideality factor *n* can be introduced to indicate the effective SBs by:

$$\phi_1 = \phi_1^0 - eV_1(1 - \frac{1}{n_1})$$

$$\phi_2 = \phi_2^0 + eV_2(1 - \frac{1}{n_2})$$

For the continuity of the current, the total current I can be expressed as $I = I_1 = I_2$, while the applied potential is $V = V_1 + V_2 + V_R$ [$V_R = IR_i$] and assuming $V_1 = V_2 = (V-IR_i)/2$]. By merging the Eqs. above one can obtain the expression below:

$$I = \frac{2I_{A1}I_{A2}\sinh\left[\frac{q(V-IR)}{2kT}\right]}{I_{A1}e^{\frac{-q(V-IR)}{2kT}} + I_{A2}e^{\frac{q(V-IR)}{2kT}}} \qquad [S7.7.1]$$

Figs. 7.4(a,c) display the *J-V* characteristics measured in dark on LSMO/LFO/Pt and LSMO/LFO/BLSO devices. The back-to-back Schottky with a series resistance model, Eq. [S7.7.1] can be used to calculate the current at each *V*-bias and simulate the *J-V* curves. Results were shown in Figs. 7.4(b,d). The parameters leading to optimal simulation obtained are shown in the table below. Results from simulations evidence the series R_i largely increases with the LFO thickness. However, a word of caution should be given regarding the extracted SB values. The ultimate reason is that the model used to describe the *I-V* is that of thermionic emission across the barrier, a mechanism that in the model, is assumed to be valid over all explored voltage range (-1 V to +1 V). While as shown below, the SCLC appears to dominate at around *V* > 0.1 V. Therefore, the values of Φ extracted from the wide range may not be accurate though.

Top contact	t_{LFO} (nm)	R_i (MΩ)	Φ_1 (eV)	Φ_2 (eV)	n_1	n_2
Pt	50	0.05	0.63 (0.01)	0.83 (0.01)	1.19 (0.06)	1.14 (0.02)
	100	500				
	200	5000				
BLSO	50	4	1.1	0.83	1.06	1.2

100	15	(0.1)	(0.2)	(0.2)	(0.3)
200	1000				

Table S7.6. Summary of R_i, SBs and n obtained by simulation of *J-V* curves using Eq. [S7.7.1], where Φ_1 and Φ_2 denote the barriers at the top (LFO/Pt,BLSO) and bottom (LSMO/LFO) interfaces, respectively. Numbers in brackets means the precision allowed to obtain similar simulated results.

S7.7.2. Space Charge limited conduction.

Most generally, while at low voltages the motion of thermally activated carriers inside the dielectric gives rise to an ohmic behavior, above some threshold voltage (V_{tr}) the space charge limited conduction (SCLC) mechanism predicts that the SCLC current varies with V^2 as:

$$J = \frac{9\varepsilon n_0 \mu V^2}{8t^3}$$ [S7.7.2]

where ε is the permittivity of the insulating material, μ its carrier mobility, t is the film thickness, and n_0 is the ratio of free carriers to the total carrier concentration (free plus trapped) in the dielectric.[67,68]

In Fig. S7.7.2 we show a plot of Log $|J|$ *vs.* $|V|$ (for the $V < 0$) of LFO (200 nm)/Pt sample. A roughly ohmic behaviour ($J \approx V$) is observed in the low voltage regime, changing to a quadratic $J \approx V^2$ dependence at $V_{tr} \approx 0.1$ V. Using $\varepsilon \approx 35$ for LFO,[4] and Eq. [S7.7.2] we derive an effective mobility $\mu n_0 \approx 6 \times 10^{-9}$ cm²V⁻¹s⁻¹. The remarkably small value μn_0 reflects the presence of a large concentration of trap centers in the LFO film, as commonly found in the related oxides.[69,70]
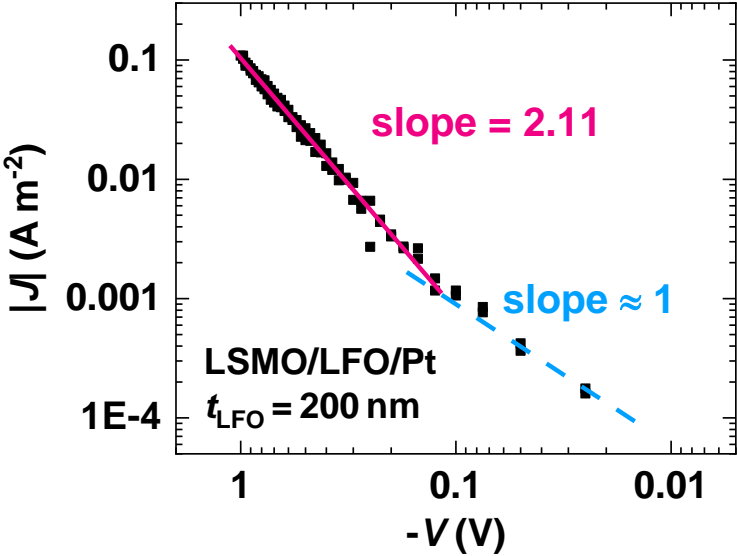
Fig. S7.7.2. The log-log plot of *J-V* characteristics (negative bias) of LSMO/LFO (200 nm)/Pt measured in dark.

Annex B: Photoresponse of LaFeO₃ films influenced by strain

As mentioned in previous discussions, strain and strain gradients may have a double effect on the photoresponse of photo absorbing thin films. Focusing on LaFeO₃: a) Epitaxial strain can modify the electronic structure of the LFO film which in turn may change the built-in potential at interfaces and thus the band alignment with the used electrodes, b) Strain gradients can induce the presence of internal electric fields which can also modify the band alignment. Films grown on different substrates could have relaxed, compressive and extensive strain, depending on the cell parameters of the substrates and subsequent films. To study the influence of strain on the photoresponse of LFO, following up the LSAT(001)//LFO in Chapter 7, further exploration using different substrates [SrTiO₃(110), SrTiO₃(001), LaAlO₃(001), LSAT(001)] and ultrathin LFO films (10 nm) to prevent strain relaxation inside the film layer is under way. Preliminary results are shown as follows.

B1: Samples and experiments

The bottom LSMO and top Pt electrodes, and LFO film were deposited using the same protocol than in Chapter 7.2 (Chapter 3). The architecture of the sample is: Substrate//LSMO(27 nm)/LFO/Pt(7 nm). The *J-V* curves were collected in dark and under illumination using a 405 nm laser with intensity of 54 W/cm² at 45° incidence. The surface topography of the films was investigated by atomic force microscopy (AFM) using an Asylum Research MFP-3D microscope (Oxford Instrument Co.) in tapping mode.

B2: Photoresponse of ultrathin LaFeO₃ films on SrTiO₃ and LaAlO₃ substrates

In previous Chapter 7, it was explicitly mentioned that LFO films thicker than $t_{LFO} \geq 50$ nm were assumed, for simplicity, that strain was basically relaxed and thus the band alignment was taken as independent of t_{LFO}. However, reciprocal space maps (RSM) of the LFO films of thicknesses t_{LFO} = 50 nm, 100 nm and 200 nm (Fig. 7.1), shows that films display a complex microstructure where relaxed and non-relaxed crystallites coexist and crystallites of different textures also coexist, in amount that varies with thickness. Namely, available data did not allow to go deeper on the analysis of the role of strain nor strain gradients.

Therefore, we have undertaken the exploration of ultrathin films of LFO (10 nm) grown on different substrates. For the exploratory study reported below, we restricted ourselves

to the use of $SrTiO_3$ [STO(001)] and $LaAlO_3$ [LAO(001)] substrates to impose different strain on films, indicates that results could be potentially very interesting. Films of 10 nm LFO were grown on STO and LAO simultaneously on the same batch.

The AFM images of the (STO, LAO)/LSMO/LFO(10 nm) films are shown in Fig. B1. The terraces from the substrate can be well appreciated in the STO sample, reflecting the good quality of the film. Unfortunately, the image of the film on LAO was not collected on fresh sample, shows some dusts but still with small roughness.

(a) RMS: 0.177 nm **(b)** RMS: 0.218 nm
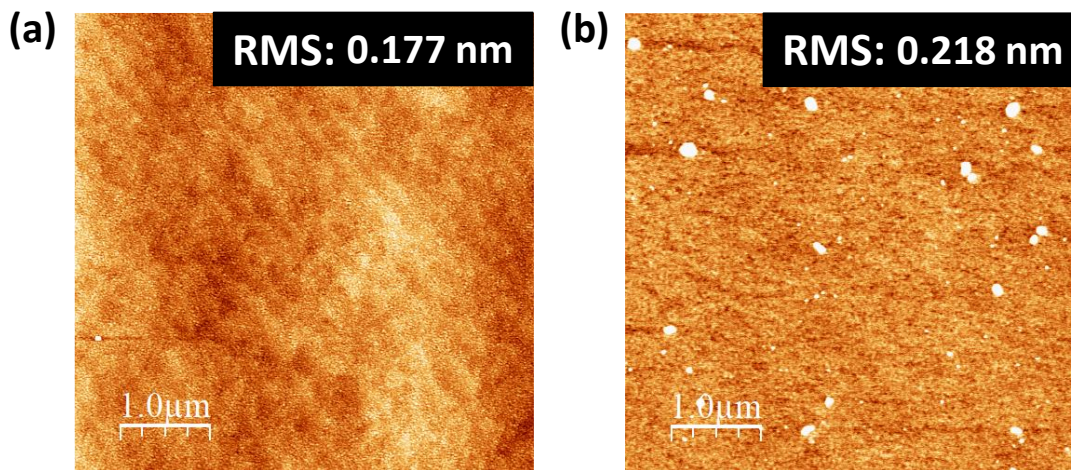
Fig. B1. AFM topographic images, 5 μm× 5 μm in size (top images), of LSMO/LFO(10 nm) grown on (a) STO(001) and (b) LAO(001) substrates. The roughness RMS (root mean square of a surface peaks and valleys) is shown.

The RSM are shown in Fig. B2. It can be clearly appreciated that the 10 nm LFO grown on STO is fully strained and the out-of-plane-axis ($c_\parallel$) responds relaxed accordingly, while the LFO signal is weak in film grown on LAO. From Fig. 2.2, the cell parameters of LFO(10nm) were evaluated, on STO: in-plane $c_\perp \approx 3.9057$ Å and out-of-plane $c_\parallel \approx 4.0257$ Å, on LAO: $c_\perp \approx 3.83$ Å and $c_\parallel \approx 4.073$ Å, that correspond to unit cell volumes of 61.41 Å^3 and 59.75 Å^3, respectively. Interestingly, and at variance with the growth of thicker films described in Chapter. 7 [Figs. 7.1 and S7.3.2], data in Fig. B2 indicates that within the experimental resolution only a single family of crystallites exist. Data does not yet allow to conclude the strain inside the layer is homogenous or not.
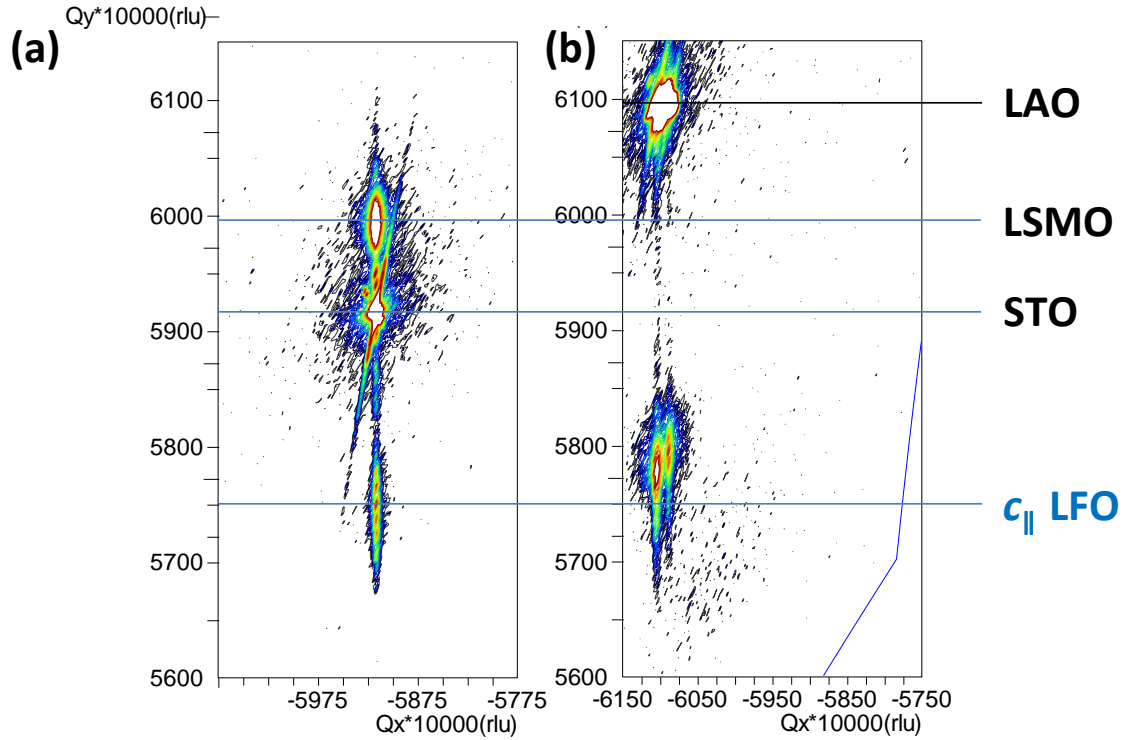
Fig. B2. RSM around the (-303) reflection of heterostructures of LSMO/LFO(10 nm) grown on (a) STO(001) and (b) LAO(001) substrates.

Fig. B3 shows the illustrative *J-V* curves recorded on a set of capacitors on LFO, either grown on STO (E_1-E_3, top panel) or on LAO (E_4-E_6, bottom panel). First observation is that in spite that results display some disparity between different capacitors due to the leaky ultrathin films, some trends appear to be clear: a) both J_{sc} and V_{oc} are larger in films on STO than on LAO; b) in dark, the films on LAO are generally more conducting than films on STO.

The observations J_{sc}(STO) > J_{sc}(LAO) and J_{dark}(LAO) > J_{dark}(STO) are interesting because it was earlier reported by M. Wu et al.,[13] the opposite behavior, that is: the photocurrent was larger in LFO grown on LAO than STO, and in dark the STO sample is more leaky than the LAO. In films with $t_{LFO} \geq 50$ nm, the reverse behavior is also found (not shown). In any case, the fact both J_{sc} and V_{oc} are found to be dependent on substrate -and presumably- on the epitaxial strain or strain gradients, indicate that a new physics may emerge.

Furthermore, the data for STO substrates lead to conclude that $J_{sc} \approx 73$ mA/cm², collected using 405 nm laser with a power density of 54 W/cm². This value corresponds to

a responsivity **R** = 1.35 mA/W, which is significant larger than early reports on LFO of similar thickness.[13]
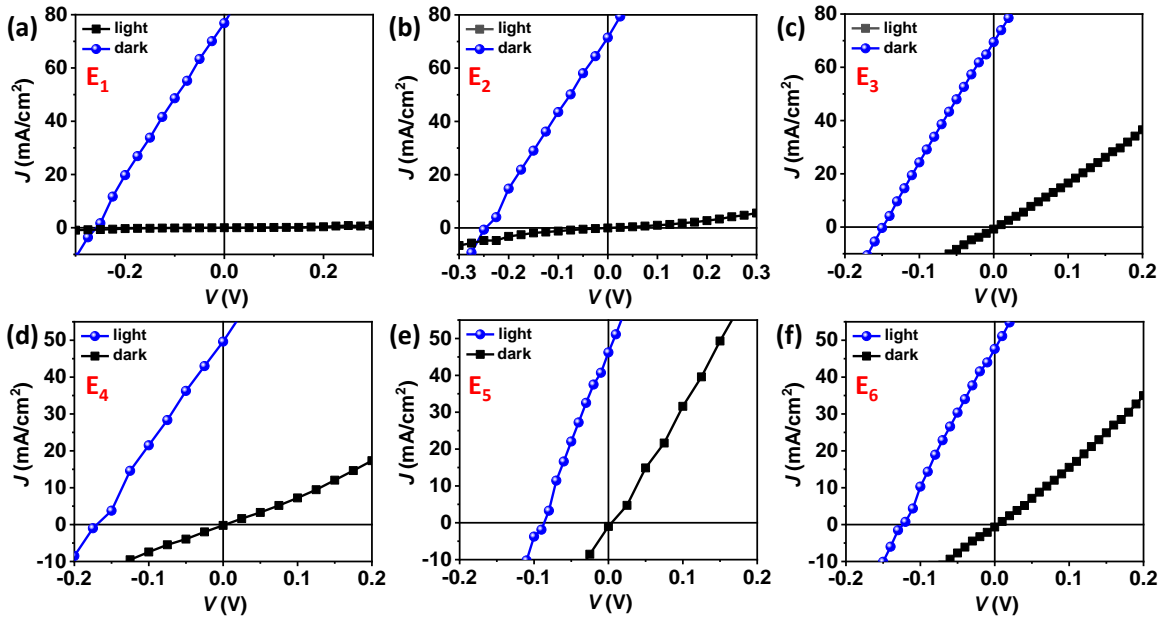
Fig. B3. A collection of *J-V* curves collected in dark and under illumination, on capacitors formed by LSMO/LFO(10 nm)/Pt gown on (a-c) STO(001) and (d-f) LAO(001) substrates.

In summary, the photoresponse on 10 nm LFO films indicates that there is a lot of room for improvement and for understanding the role of strain and potentially strain gradients on the photoresponse of LFO. To consolidate results and to get a deeper insight of LFO(10nm), a new series of 10 nm films have been recently grown on the same batch on LSAT(001), STO(001), STO(110) and LAO(001) substrates hoping to get a newer view on reproducibility, epitaxial mismatch and presumably epitaxial strain on the photoresponse. Measurements are currently being performed.

B3: Exploration of polarity mismatch of STO/LFO interfaces on the photoresponse

It was earlier mentioned, that research on the photoresponse of LFO was motivated by the fact that this oxide has a narrow bandgap and it was discovered that the photoresponse of LFO films on STO was dependent on the polarity selection of the STO substrate surface. It was also suggested that the polarity mismatch at TiO_2/LaO or SrO/FeO_2 interfaces could be the reason for this effect as it may induce an interface dipole, introducing an asymmetry and may be leading to some sort of BPE.[4,71] Although subsequent experimental data (XPS) failed to observe any electric field at interfaces,[5] experimental data is there and the ultimate reasons remain unknown.

To get a new light into the interface issue while avoiding differences in mismatch and strain, here some preliminary data of the photoresponse of 50 nm LFO films, grown on STO(001) and STO(110) (not from the same batch) is reported. It is emphasized that there are no earlier literature reports on the photoresponse of LFO with (110) texture.

Fig. B4 presents the AFM image of the film grown on STO(110). It can be appreciated that the roughness is small, illustrating a high-quality film.
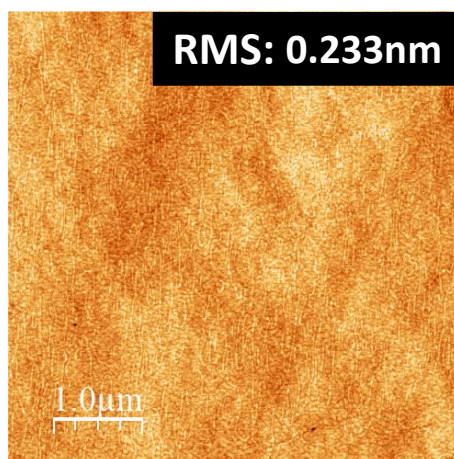
Fig. B4. AFM topographic image, 5 μm× 5 μm in size (top images), of STO(110)//LSMO(27 nm)/LFO(50 nm). The roughness RMS is shown.

The *J-V* curves measured in dark and under illumination of this film on STO(110) is displayed in Fig. B5(a). For comparison the corresponding data collected using nominally identical conditions on a device grown on STO(001) (previous sample, not grown in the

same batch) is also included. Obviously data show that LFO (50 nm) films grown on STO(110) substrates display a photocurrent that is about one order of magnitude larger than when grown on STO(001). This dramatic enhancement is astonishing. In films with t_{LFO} = 100 and 200 nm, the difference between STO(110) and STO(001) is reduced (not shown). To dig on the physical mechanism behind this superb result, requires first to repeat experiments and use LFO films grown simultaneously on different substrates. These films have already been grown and are ready to be tested. Results are beyond the timeline of this thesis.
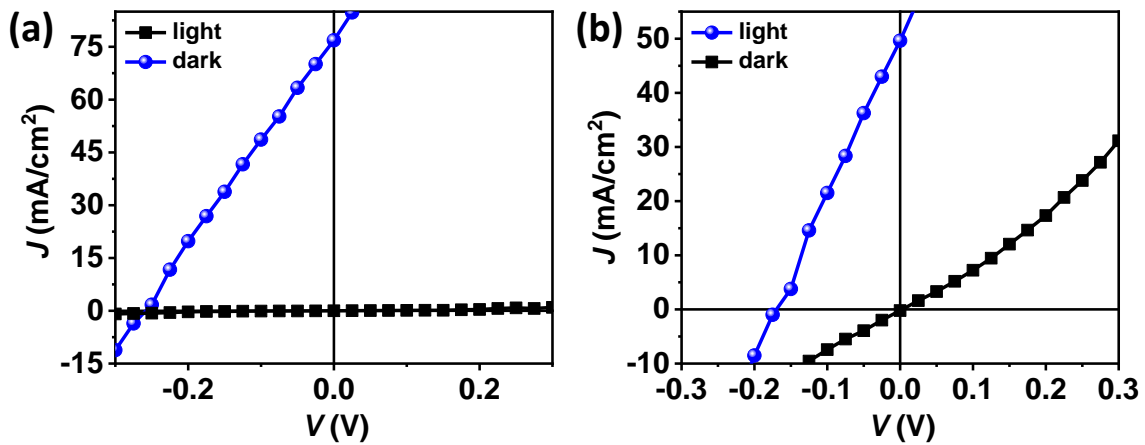
Fig. B5. *J-V* curves collected in dark and under illumination of LSMO/LFO(50 nm)/Pt grown on (a) STO(110) and (b) STO(001).

Bibliography

[1] M. Mirjolet, Transparent Conducting Oxides Based on Early Transition Metals : - Dipòsit Digital de Documents de La UAB, n.d.

[2] W. Lin, J. He, B. Ma, M. Matzelle, J. Xu, J. Freeland, Y. Choi, D. Haskel, B. Barbiellini, A. Bansil, G.A. Fiete, J. Zhou, and C.L. Chien, Nat. Phys. **18**, 800 (2022).

[3] K. Nakamura, H. Mashiko, K. Yoshimatsu, and A. Ohtomo, Appl. Phys. Lett. **108**, 211605 (2016).

[4] M. Nakamura, F. Kagawa, T. Tanigaki, H.S. Park, T. Matsuda, D. Shindo, Y. Tokura, and M. Kawasaki, Phys. Rev. Lett. **116**, 156801 (2016).

[5] R. Comes and S. Chambers, Phys. Rev. Lett. **117**, 226802 (2016).

[6] S.R. Spurgeon, P. V. Sushko, S.A. Chambers, and R.B. Comes, Phys. Rev. Mater. **1**, 063401 (2017).

[7] P. Zubko, G. Catalan, and A.K. Tagantsev, Annu. Rev. Mater. Res. **43**, 387 (2013).

[8] D. Lee, A. Yoon, S.Y. Jang, J.-G. Yoon, J.-S. Chung, M. Kim, J.F. Scott, and T.W. Noh, Phys. Rev. Lett. **107**, 057602 (2011).

[9] D. Lee, S.M. Yang, J. Yoon, and T.W. Noh, Nano Lett. **12**, 6436 (2012).

[10] K. Chu, B.-K. Jang, J.H. Sung, Y.A. Shin, E.-S. Lee, K. Song, J.H. Lee, C.-S. Woo, S.J. Kim, S.-Y. Choi, T.Y. Koo, Y.-H. Kim, S.-H. Oh, M.-H. Jo, and C.-H. Yang, Nat. Nanotechnol. **10**, 972 (2015).

[11] S. Das, B. Wang, T.R. Paudel, S.M. Park, E.Y. Tsymbal, L.-Q. Chen, D. Lee, and T.W. Noh, Nat. Commun. **10**, 537 (2019).

[12] M. Yang, D.J. Kim, and M. Alexe, Science (80-.). **360**, 904 (2018).

[13] M. Wu, Z. Jiang, X. Lou, F. Zhang, D. Song, S. Ning, M. Guo, S.J. Pennycook, J. Dai, and Z. Wen, Nano Lett. **21**, 2946 (2021).

[14] Z. Jiang, Z. Xu, Z. Xi, Y. Yang, M. Wu, Y. Li, X. Li, Q. Wang, C. Li, D. Wu, and Z. Wen, J. Mater. **8**, 281 (2022).

[15] S.M. Park, B. Wang, T. Paudel, S.Y. Park, S. Das, J.R. Kim, E.K. Ko, H.G. Lee, N. Park, L. Tao, D. Suh, E.Y. Tsymbal, L.-Q. Chen, T.W. Noh, and D. Lee, Nat. Commun. **11**, 2586 (2020).

[16] M.N. Polyanskiy, Refractive index database. https://refractiveindex.info. (accessed on Aug. 29, 2022).

[17] D. Pesquera, Strain and Interface-Induced Charge, Orbital and Spin Orderings in Transition-Metal Oxide Perovskites, Universitat Autònoma de Barcelona, 2014.

207

[18] J. Walton, P. Wincott, N. Fairley, and A. Carrick, *Peak Fitting with CasaXPS: A Casa Pocket Book* (Accolyte Science, 2010).

[19] E.A. Kraut, R.W. Grant, J.R. Waldrop, and S.P. Kowalczyk, Phys. Rev. Lett. **44**, 1620 (1980).

[20] E.A. Kraut, R.W. Grant, J.R. Waldrop, and S.P. Kowalczyk, Phys. Rev. B **28**, 1965 (1983).

[21] S.M. Selbach, J.R. Tolchard, A. Fossdal, and T. Grande, J. Solid State Chem. **196**, 249 (2012).

[22] Z. Yu, D.A. Muller, and J. Silcox, J. Appl. Phys. **95**, 3362 (2004).

[23] P.J. Phillips, M. De Graef, L. Kovarik, A. Agrawal, W. Windl, and M.J. Mills, Ultramicroscopy **116**, 47 (2012).

[24] A.J. Chiquito, C.A. Amorim, O.M. Berengue, L.S. Araujo, E.P. Bernardo, and E.R. Leite, J. Phys. Condens. Matter **24**, 225303 (2012).

[25] Z. Zhang, K. Yao, Y. Liu, C. Jin, X. Liang, Q. Chen, and L.-M. Peng, Adv. Funct. Mater. **17**, 2478 (2007).

[26] A. Klein, Thin Solid Films **520**, 3721 (2012).

[27] P. Lopez-Varo, L. Bertoluzzi, J. Bisquert, M. Alexe, M. Coll, J. Huang, J.A. Jimenez-Tejada, T. Kirchartz, R. Nechache, F. Rosei, and Y. Yuan, Phys. Rep. **653**, 1 (2016).

[28] M. Minohara, I. Ohkubo, H. Kumigashira, and M. Oshima, Appl. Phys. Lett. **90**, 132123 (2007).

[29] M. Minohara, R. Yasuhara, H. Kumigashira, and M. Oshima, Phys. Rev. B **81**, 235322 (2010).

[30] H.-S. Lee and H.-H. Park, Adv. Condens. Matter Phys. **2015**, 1 (2015).

[31] G.N. Derry, M.E. Kern, and E.H. Worth, J. Vac. Sci. Technol. A Vacuum, Surfaces, Film. **33**, 060801 (2015).

[32] R. Schlaf, C.D. Merritt, L.A. Crisafulli, and Z.H. Kafafi, J. Appl. Phys. **86**, 5678 (1999).

[33] B.E. Nieuwenhuys, O.G. Van Aardenne, and W.M.H. Sachtler, Chem. Phys. **5**, 418 (1974).

[34] A. Klein, J. Am. Ceram. Soc. **99**, 369 (2016).

[35] A. Ohta, H. Murakami, S. Higashi, and S. Miyazaki, J. Phys. Conf. Ser. **417**, 012012 (2013).

[36] D.R. Lide, *Handbook of Chemistry and Physics, 84th Edition* (CRC Press LLC, 2004).

[37] E.Y. Tsymbal and I. Žutić, *Spintronics Handbook: Spin Transport and Magnetism, Second Edition* (CRC Press, Second Edition. | Boca Raton : Taylor & Francis, CRC Press, 2018. |, 2019).

[38] K. Krishnaswamy, L. Bjaalie, B. Himmetoglu, A. Janotti, L. Gordon, and C.G. Van de Walle, Appl. Phys. Lett. **108**, 083501 (2016).

[39] J.D. Baniecki, T. Yamazaki, D. Ricinschi, Q. Van Overmeere, H. Aso, Y. Miyata, H. Yamada, N. Fujimura, R. Maran, T. Anazawa, N. Valanoor, and Y. Imanaka, Sci. Rep. **7**, 41725 (2017).

[40] S.A. Chambers, T.C. Kaspar, A. Prakash, G. Haugstad, and B. Jalan, Appl. Phys. Lett. **108**, 152104 (2016).

[41] S. Lee, H. Wang, P. Gopal, J. Shin, H.M.I. Jaim, X. Zhang, S.-Y. Jeong, D. Usanmaz, S. Curtarolo, M. Fornari, M. Buongiorno Nardelli, and I. Takeuchi, Chem. Mater. **29**, 9378 (2017).

[42] R. Schafranek, S. Payan, M. Maglione, and A. Klein, Phys. Rev. B **77**, 195310 (2008).

[43] J.R. Waldrop, R.W. Grant, S.P. Kowalczyk, and E.A. Kraut, J. Vac. Sci. Technol. A Vacuum, Surfaces, Film. **3**, 835 (1985).

[44] S.A. Chambers, M.H. Engelhard, V. Shutthanandan, Z. Zhu, T.C. Droubay, L. Qiao, P.V. Sushko, T. Feng, H.D. Lee, T. Gustafsson, E. Garfunkel, A.B. Shah, J.-M. Zuo, and Q.M. Ramasse, Surf. Sci. Rep. **65**, 317 (2010).

[45] S.A. Chambers, L. Qiao, T.C. Droubay, T.C. Kaspar, B.W. Arey, and P. V. Sushko, Phys. Rev. Lett. **107**, 206802 (2011).

[46] R. Schafranek, S. Li, F. Chen, W. Wu, and A. Klein, Phys. Rev. B **84**, 045317 (2011).

[47] K.J. May, D.P. Fenning, T. Ming, W.T. Hong, D. Lee, K.A. Stoerzinger, M.D. Biegalski, A.M. Kolpak, and Y. Shao-Horn, J. Phys. Chem. Lett. **6**, 977 (2015).

[48] F. Chen, R. Schafranek, S. Li, W.B. Wu, and A. Klein, J. Phys. D. Appl. Phys. **43**, 295301 (2010).

[49] S. Li, C. Ghinea, T.J.M. Bayer, M. Motzko, R. Schafranek, and A. Klein, J. Phys. Condens. Matter **23**, 334202 (2011).

[50] F. Chen, R. Schafranek, W. Wu, and A. Klein, J. Phys. D. Appl. Phys. **44**, 255301 (2011).

[51] A.P.N. Tchiomo, E. Carleschi, A.R.E. Prinsloo, W. Sigle, P.A. van Aken, J. Mannhart, P. Ngabonziza, and B.P. Doyle, arXiv:2205.07726 (2022).

[52] Z. Lebens-Higgins, D.O. Scanlon, H. Paik, S. Sallis, Y. Nie, M. Uchida, N.F. Quackenbush, M.J. Wahila, G.E. Sterbinsky, D.A. Arena, J.C. Woicik, D.G. Schlom, and L.F.J. Piper, Phys. Rev. Lett. **116**, 027602 (2016).

[53] V.D. Mihailetchi, P.W.M. Blom, J.C. Hummelen, and M.T. Rispens, J. Appl. Phys. **94**, 6849 (2003).

[54] W. Peter and W. Uni, *Physics of Solar Cells: From Principles to New Concepts* (2016).

[55] J. Xing, E.-J. Guo, J. Dong, H. Hao, Z. Zheng, and C. Zhao, Appl. Phys. Lett. **106**, 033504 (2015).

[56] R. Zhao, N. Ma, K. Song, and Y. Yang, Adv. Funct. Mater. **30**, 1906232 (2020).

[57] J. Chakrabartty, C. Harnagea, M. Celikin, F. Rosei, and R. Nechache, Nat. Photonics **12**, 271 (2018).

[58] I. Visoly-Fisher, S.R. Cohen, A. Ruzin, and D. Cahen, Adv. Mater. **16**, 879 (2004).

[59] M. Björck and G. Andersson, J. Appl. Crystallogr. **40**, 1174 (2007).

[60] M.D. Scafetta, Y.J. Xie, M. Torres, J.E. Spanier, and S.J. May, Appl. Phys. Lett. **102**, 081904 (2013).

[61] T. Arima, Y. Tokura, and J.B. Torrance, Phys. Rev. B **48**, 17006 (1993).

[62] T. Arima and Y. Tokura, J. Phys. Soc. Japan **64**, 2488 (1995).

[63] P. Decorse, E. Quenneville, S. Poulin, M. Meunier, A. Yelon, and F. Morin, J. Vac. Sci. Technol. A Vacuum, Surfaces, Film. **19**, 910 (2001).

[64] M. Descostes, F. Mercier, N. Thromat, C. Beaucaire, and M. Gautier-Soyer, Appl. Surf. Sci. **165**, 288 (2000).

[65] M.F. Sunding, K. Hadidi, S. Diplas, O.M. Løvvik, T.E. Norby, and A.E. Gunnæs, J. Electron Spectros. Relat. Phenomena **184**, 399 (2011).

[66] A. Grillo and A. Di Bartolomeo, Adv. Electron. Mater. **7**, 2000979 (2021).

[67] F.-C. Chiu, Adv. Mater. Sci. Eng. **2014**, 1 (2014).

[68] C.-P. Kwan, M. Street, A. Mahmood, W. Echtenkamp, M. Randle, K. He, J. Nathawat, N. Arabchigavkani, B. Barut, S. Yin, R. Dixit, U. Singisetti, C. Binek, and J.P. Bird, AIP Adv. **9**, 055018 (2019).

[69] F.-C. Chiu, H.-W. Chou, and J.Y. Lee, J. Appl. Phys. **97**, 103503 (2005).

[70] A. Goldenblum, I. Pintilie, M. Buda, A. Popa, T. Botila, A. Dimoulas, and G. Vellianitis, Appl. Phys. Lett. **86**, 203506 (2005).

[71] K. Nakamura, H. Mashiko, K. Yoshimatsu, and A. Ohtomo, Appl. Phys. Lett. **108**, (2016).

Chapter 8. Summary and outlook

Aiming to get a new understanding of the photoresponse of non-centrosymetric materials and heterostructures comprising narrow bandgap oxides, in this PhD thesis I have explored ferroelectric hexagonal oxides (LuMnO₃ and YMnO₃) either thin films or single crystals, as well as and non-ferroelectric LaFeO₃. Central to the work has been my aim to reach deeper insight on the relevance of bulk photovoltaic effect (BPE) to the measured photoresponse, compared to conventional photovoltaic effect (CPE) contribution.

8.1. Summary

Along this thesis we first learned that measuring the photoresponse of single crystals and thin films entails understanding and controlling the different contributions that may affect the measured photocurrent. Indeed, CPE comprises, photocurrent of diffusive origin associated to photogenerated charge gradients, and drift photocurrents associated to the presence of electric fields, either due to interfacial Schottky barriers (built-in field) or others (for example depoling or imprint fields in ferroelectric materials, or more generally flexoelectric fields in strain graded films). When dealing with non-centrosymmetric structures, these contributions to the photocurrent can coexist and be intertwined with the genuine BPE that only relates to the symmetry nature of the used material.

It turned out, that the interplay between these factors depends on samples and measuring configuration and thus there is not a unique rule to disentangle these effects. It follows that different measuring protocols should be adapted and optimized to each particular situation before conclusions can be derived on their relative weight, and this step is necessary to obtain quantitative measurement and for the understanding of BPE and its connection to the electronic properties and symmetry of the materials under study.

For the first time, the photoresponse of *h*-LuMnO₃ single crystals is reported. We used Pt contacts and we observed that the out-of-plane short-circuit photocurrent density J_{sc} is modulated by the ferroelectric polarization **P** (up to 25 %). We also observed an oscillatory dependence of $J_{sc}(\theta, \varphi)$ on the light polarization angle φ measured at various incidence angle θ, using lasers of different wavelength. Data revealed a contribution arising from BPE, coexisting with a drift term originated from Schottky barriers or depoling field, both

contributing to the photoresponse. As a result of this double contributions, we could not derive precise values of the photovoltaic (PV) tensor elements neither Glass coefficients (β_{ij} and G_{ij}) representing the genuine BPE response of the materials, but only some bounds of the BPE coefficients could be extracted. Still, it was found that the bounds of $\underline{\beta_{ij}}$ and G_{ij} are larger than other photoferroelectrics, such as $BiFeO_3$, suggesting possible advantages of hexagonal manganites for photoconversion.

Furthermore, we discovered that the amplitude of $J_{sc}(\varphi)$ oscillations are largely affected by the polarization back-switching and depoling processes. This pioneering observation implies that the accurate extraction of the intrinsic Glass coefficients (related to the amplitude of $J_{sc}(\varphi)$ oscillations), is even more challenging. Not only the simple contribution from drift and diffusion affects the data but the inherent instability of the saturated ferroelectric state adds a new difficulty.

Aiming at minimizing diffusion contributions, research was directed to h-$LuMnO_3$ thin films. After optimizing their epitaxial growth, it was shown that $LuMnO_3$ films have good ferroelectricity and photovoltaic response with a responsivity up to 2×10^{-3} A/W when using thin Pt top contacts. The photocurrent (≤ 100 mA/cm^2) and responsivity reported here are larger than observed in other ferroelectric oxide films (e.g., $BiFeO_3$), including earlier $LuMnO_3$ films or even isostructural ferroelectric ferrites, and definitely larger than in $LuMnO_3$ single crystals ($\approx 3 \times 10^{-4}$ A/W). This last observation suggests that charge extraction in thin films is more efficient than in bulky single crystals. Even more, the presence of grain boundaries in our thin films does not impede reaching a larger responsivity, but it may even boost it, as known to occur in some II-VI semiconductors.

When exploring the dependence of J_{sc} and V_{oc} on the intensity of the laser, it was observed that J_{sc} increases roughly linearly with light intensity, as expected both within BPE and CPE. V_{oc} is found to increase logarithmically with light intensity and J_{sc} [$V_{oc} \propto \ln(J_{sc})$]. This observation is intriguing as this is the expected dependence in CPE, while $V_{oc} \propto J_{sc}$ was expected within BPE. In contrast, the $V_{oc}(\varphi)$ was found to be linear on $J_{sc}(\varphi)$ [$V_{oc} \propto J_{sc}$] which is best interpreted arising from BPE. It follows that BPE is a relatively small modulation to the overall photoresponse.

Overall, a large responsivity has been obtained in vertical capacitors using ferroelectric LuMnO$_3$ thin films, displaying a <u>synergetic contribution of conventional photovoltaic and bulk photovoltaic effects (CPE and BPE).</u>

An additional feature, not yet mentioned above, is that the intensity of light penetrating the sample and ultimately being absorbed in it, is dependent on its polarization as described by <u>Fresnel</u> classical equations. It follows that any absorbed light and subsequently any photocurrent, should display a <u>(φ, θ) dependence similar to BPE</u> and thus these polarization-dependences are entangled in the observed photoresponse. In an attempt to discriminate between BPE and CPE contributions to the $J_{sc}(\varphi)$ oscillations, experiments have been designed to compare $J_{sc}(\varphi, \theta)$ oscillations in polar and nonpolar films where BPE should be absent in principle. LaFeO$_3$ films has been selected as an example of nonpolar material to compare the $J_{sc}(\varphi, \theta)$ data with that of polar materials. Preliminary results suggest that although <u>Fresnel contribution cannot be avoided in any material when measuring at oblique incidence, the BPE in polar materials appears to dominate $J_{sc}(\varphi)$</u> <u>while Fresnel governs the nonpolar LaFeO$_3$ response.</u>

The structures involving in LaFeO$_3$ have further offered the possibility to study in detail the role of electrodes in the CPE. Different electrodes have been explored [Pt and (Ba,La)SnO$_3$]. Starting from the earlier results obtained within the PhD work of Dr. M. Mirjolet within our MULFOX group, the band alignment in these structures has been carefully analyzed. I have been able to derive <u>a close connection between the observed V_{oc} and the built-in potential (V_{bi}) in the measured capacitors.</u> The responsivity is measured to be larger than in earlier reports on LaFeO$_3$. Although some strain relaxation is observed in the measured LaFeO$_3$ films, we have argued that V_{oc} is mainly dictated by band alignment related to the selected electrodes, with negligible contribution, if any, from flexoelectric fields. We have proposed new ways to engineer larger responsivity.

8.2. Outlook

1. A critical issue that emerged is the difficulty to disentangle BPE from Fresnel contributions to the measured polarization-dependent photocurrent in hexagonal ferroelectrics. As mentioned in Chapter 6, in principle $LaFeO_3$, which in bulk is not polar, was considered for benchmark experiments. However, the suggested polar reconstruction at interfaces in $LaFeO_3$ still may cast difficulties. To cross check results and methodology, further measurements in purely nonpolar Nb:STO and intrinsic Si with symmetric contacts are under preparation.

2. Another critical effect in the photocurrent of nonpolar material is as mentioned, even in nominally symmetric structures, the presence of strain fields can be a source of polar-like response (including BPE and drift currents). To address this point, the photoresponse characterization of $LaFeO_3$ having a controlled strain relaxation is a must. As mentioned, films of different thicknesses (including ultrathin films) grown on different substrates are required and if possible, using symmetric electrodes.

3. The measurements of the BPE in our polar materials has been restricted to the measurement of out-of-plane photocurrent, as so, a limited number of Glass coefficients were accessible. In-plane measurements are required to determine all the Glass coefficients. Higher quality films are needed.

4. It is interesting to note that in any of the polar materials measured in this thesis, the open voltage circuit has been found smaller than the corresponding band gap, which is contrary to some BPE expectations. Although several prospects have been suggested, a definitive answer is lacking.

5. Finally, it would be nice to have first principle calculation of the PV tensor elements and Glass coefficients in hexagonal manganites to rationalize the observation of a larger BPE (upper bounds) than in related $BiFeO_3$.

List of publications

1. **Y. Sheng**, I. Fina, M. Gospodinov, and J. Fontcuberta. *Back-switching of polarization and bulk photovoltaic effect in ferroelectrics*. Appl. Phys. Lett. 120, 242901 (2022).

2. **Y. Sheng**, I. Fina, M. Gospodinov, A. Schankler, A. M. Rappe, and J. Fontcuberta. *Bulk photovoltaic effect in hexagonal LuMnO$_3$ single crystals*. Phys. Rev. B 104, 184116 (2021).

3. **Y. Sheng**, I. Fina, M. Gospodinov, and J. Fontcuberta. *Switchable photovoltaic response in hexagonal LuMnO$_3$ single crystals*. Appl. Phys. Lett. 118, 232902 (2021).

4. **Y. Sheng**, H. Tan, A. Quintana, M. Villa, J. Gázquez, I. Fina, and J. Fontcuberta. *Untwining polar contributions from light-polarization dependent photovoltaic response of LuMnO$_3$-based ferroelectric capacitors*. (Acta Mater. Under review).

5. **Y. Sheng**[§], M. Mirjolet[§], M. Villa, J. Gazquez, J. Santiso, A. Klein, J. Fraxedas, and J. Fontcuberta. *Band alignment and photoresponse of LaFeO$_3$-based heterojunctions.* ([§] Equal contribution, To be submitted).

6. H. Tan, J. Lyu, **Y. Sheng**, P. Machado, T. Song, A. Bhatnagar, M. Coll, F. Sánchez, J. Fontcuberta and I. Fina. *A transversal approach to predict surface charge compensation in piezoelectric force microscopy.* (Appl. Surf. Sci., Accepted)

List of communications

1. **Oral.** *Bulk Photovoltaic Effect in Hexagonal LuMnO$_3$ Single Crystals.* IEEE International Symposium on Applications of Ferroelectrics, ISAF/PFM/ECAPD2022 (Jun. 27th - Jul. 1st 2022).

2. **Poster and Flash Talk**. *Disentangling bulk photovoltaic effect (BPE) from the intricate photoresponse of strongly absorbing hexagonal LuMnO$_3$.* II Annual Congress of Nanoscience and Nanotechnology, IIICANN2021 (Nov. 18th, 2021)

3. **Poster and Flash Oral**. *Disentangling bulk photovoltaic effect from the intricate photoresponse of strongly absorbing polar material.* International School of Oxide Electronics, ISOE2021 (Aug. 24th - Sep. 3rd, 2021)

4. **Flash Poster**. *First evidence of bulk photovoltaic effect in hexagonal manganites.* Quantum Oxide Research Online Meeting, QUOROM-2, (Nov. 12nd, 2020)

5. **Oral**. *The modulation of photocurrent by light polarization on ferroelectric hexagonal LuMnO$_3$ single crystal.* The 5th Scientific Meeting of PhD Students at UAB Campus, JPhD2020, (Sep. 17th - 18th 2020).

6. **Poster (awarded prize)**. *The modulation of photocurrent by light wavelength and polarization on ferroelectric hexagonal LuMnO$_3$ single crystal*. Condensed Matter Division, CMD2020GEFES, (Aug. 31st - Sep. 4th 2020)

7. **Poster**. *The synergistic effect of ferroelectric and light polarization on the photovoltaic response of hexagonal LuMnO$_3$ single crystal.* The 4th Scientific Meeting of BNC-b Students, JPhD2019, (June 6th - 7th 2019).

List of symbols and acronyms

α	Absorption coefficient
α_m	Absorption coefficient of the top contact
$\alpha_\parallel, \alpha_\perp$	α along the direction parallel (op), perpendicular(ip) to c-axis
A^*	Richardson constant
$A_{1,2}$	Areas of the contacts
A_F	Amplitude of the $I_T(\varphi)$ oscillation
A_T	Amplitude of the transmitted power oscillation among φ
A_z, B_z	Amplitude, background of the sinusoidal oscillation $J_{sc}(\varphi)$
β_{ij}	Linear photovoltaic tensor element
$\varepsilon, \varepsilon_0$	Permittivity, vacuum permittivity
ϵ	strain gradient
$\mathbf{E}$	Light electric field / light polarization
E_{bi}, V_{bi}	Built-in electric field, voltage
E_c, V_c	Coercive electric field, voltage
E_d	Depolarization electric field
E_g	Bandgap
E_f, V_f	Flexoelectric electric field, E_f induced potential
E_F	Fermi level
E_{im}	Imprint electric field
E_n	Capacitor number n
E_w, V_w	Writing electric field, writing voltage
f	Laser repetition rate / frequency
F	Laser fluence
φ	Light polarization rotating angle
$\varphi_{1,2}$	Work functions
$\Phi_{1,2}$	Heights of the interfacial Schottky barriers
G_{ij}	Glass coefficient
h, o	Hexagonal, orthorhombic pahse
H, H_c	Magnetic field, coercive magnetic field

$h\upsilon$	Photon energy
I_0	Light intensity reaching to the absorbing layer
I_p	Laser power density / light intensity
I_I, I_R, I_T	Incident, reflected, transmitted light intensity
$I_T(\varphi)$	I_T oscillating dependence on φ
ΔI_T	The difference of I_p and I_s
$I(V)$	Ferroelectric current *vs.* voltage hysteresis loop
I-V, J-V	Current, current density vs. voltage characteristics
I_{sc}	Short circuit current / photocurrent
J_{sc}	Short circuit current density / photocurrent density,
J_{sc}^+, J_{sc}^-	J_{sc} measured after applying pre-polarizing V^+, V^-
$J_{sc}(\varphi)$, $V_{oc}(\varphi)$	J_{sc}, V_{oc} oscillating dependence on φ
J_D, J_E, J_{BPE}	Diffusion, drift, bulk photovoltaic current density
$J_{E\text{-}sw}$, $J_{E\text{-}usw}$	Switchable, unswitchable drift current density
J_{sw}, J_{usw}	Switchable, unswitchable photocurrent density
k	Boltzmann constant
l	Distance between electrodes, effective device length
λ, $\lambda/2$	Wavelength, half wave
m	Magnetic moment
M	Mirror symmetry transformation
$m(H)$	Magnetic moment *vs.* magnetic field hysteresis loop
m-T	Temperature-dependent magnetic moment
M_T, M_B	Top, bottom metallic electrodes
μ	Carrier mobility
n	Ideality factor
n_0	Ratio of free carriers to the total carrier concentration
N	Scale factor
p, s	Parallel, perpendicular to the incident plane
$\boldsymbol{P}$	Ferroelectric polarization
$P^\uparrow$, $P^\downarrow$	Upward (from BE to TE), downward ferroelectric polarization
P_r, P_s	Remanent, spontaneous ferroelectric polarization

P_r^+, P_r^-	Retention measured after saturation with V^+, V^-
$P_{r,rel}^+$, $P_{r,rel}^-$	Relaxation polarization at remanence after saturation with V^+, V^-
$\delta P_{r,rel}$	The difference between $P_{r,rel}^+$ and $P_{r,rel}^-$
$P(V)$, $P(E)$	Ferroelectric polarization *vs.* voltage, electric field hysteresis loop
PO_2	Dynamic oxygen pressure
Pt_{top}, Pt_{bot}	Top, bottom Pt electrode
q	elementary charge
Q	Slope
R	Responsivity
R	Roughness
R_p, R_s	Reflectance of p, s polarized light
S_1, S_2	Electrode length along x, y-axis
S_d	Laser spot diameter
σ_d, σ_{pv}	Dark, photo conductivity
θ	Light incidence angle
t	Thickness
T	Temperature
T_c, T_N	Curie temperature, Néel temperature
T_p, T_s	Transmittance of p, s polarized light
ΔT	The difference of T_p and T_s
τ, τ_d, τ_r, τ_w	Time, delay time, delay to read time, writing time
v	Volume
V	Voltage
V^+, V^-	Positive, negative applied voltage
V_c^+, V_c^-	Positive, negative coerceive voltage
V_{oc}	Open circuit voltage / photovoltage

AFM, PFM	Atomic, Piezoresponse force microscopy
APE	Anomonous photovoltaic effect
BPE	Bulk photovoltaic effect
CPE	Conventional photovoltaic effect
BFO	$BeFeO_3$
BLSO	$Ba_{0.95}La_{0.05}SnO_3$
Cry-n	Crystal number n
DC	Direct current
DHM	Dynamic Hysteresis Mode
DLCC	Dynamic Leakage Current Compensation
DW	Domain wall
FC, ZFC	field-cooled, zero-field-cooled
FE	Ferroelectric photo-absorbers
FFT	Fast Fourier transform
G, NG	Grounded, non-grounded
ip, op	in-plane, out-of-plane
JCPDS	Joint Committee on Powder Diffraction Standards
LAO	$LaAlO_3$
LMO, YMO	$LuMnO_3$, $YMnO_3$
LFO	$LaFeO_3$
LSAT	$(LaAlO_3)_{0.3}(Sr_2TaAlO_6)_{0.7}$
LSMO	$La_{2/3}Sr_{1/3}MnO_3$
LAADF, HAADF	Low, high angle annular dark field
PCE	Power conversion efficiency
PLD	Pulsed laser deposition
PUND	Positive-Up-Negative-Down
PV, PVE	Photovoltaic, hotovoltaic effect
RMO, RFO	Rare earth manganites, ferrites
RMS	Root mean square of a surface microscopic peaks and valleys
RSM	Reciprocal space map
RT	Room temperature

SB	Schottky barrier
SC	Single crystal
SD	Standard deviation
SEM	Scanning electron microscopy
STEM	Scanning transmission electron microscopy
STO, Nb:STO	$SrTiO_3$, Nb doped STO
TE, BE	Top, bottom electrode
VBO	Valence band offset
VBM	Valence band maximum
XPS	X-ray photoelectron spectroscopy
XRD	X-ray diffraction
XRR	X-ray reflectometry/reflectivity